8-2022

Studying Electron Dynamics for Quantum Materials with Real Space Resolution: A Wannier Orbital Approach to Spectroscopy using High-Performance Supercomputers

Casey J. Eichstaedt
University of Tennessee, Knoxville, ceichsta@vols.utk.edu

To the Graduate Council:

I am submitting herewith a dissertation written by Casey J. Eichstaedt entitled "Studying Electron Dynamics for Quantum Materials with Real Space Resolution: A Wannier Orbital Approach to Spectroscopy using High-Performance Supercomputers." I have examined the final electronic copy of this dissertation for form and content and recommend that it be accepted in partial fulfillment of the requirements for the degree of Doctor of Philosophy, with a major in Physics.

Adolfo G. Eguiluz, Major Professor

We have read this dissertation and recommend its acceptance:

Hanno Weitering, Steven Johnston, Tom Berlijn, David Mandrus

Accepted for the Council:

Dixie L. Thompson

Vice Provost and Dean of the Graduate School

(Original signatures are on file with official student records.)

Studying Electron Dynamics for Quantum Materials with Real Space Resolution: A Wannier Orbital Approach to Spectroscopy using High-Performance Supercomputers

A Dissertation Presented for the

Doctor of Philosophy

Degree

The University of Tennessee, Knoxville

Casey James Eichstaedt

August 2022

This dissertation is dedicated to my two daughters Layla and Bradley and to my step-brother, Senior Airman Earl R. Cartrette Jr.

Acknowledgements

I would like to first thank my research advisor, Professor Adolfo G. Eguiluz for the wisdom he bestowed upon me throughout my tenure at the University of Tennessee, Knoxville. Without his leadership and guidance, I would not be the physicist I am today.

I would also like to thank Anton Kozhevnikov for the development of the density response code that was used throughout my thesis. Without his hard work in developing a nice computation foundation, my research would have been focused on implementing what he already has done. I would like to thank Robert Van Wesep for his assistance in my early year as a doctoral student. I was lucky to have him around to get started with my research. I would like to give a special thank you to Dr. Eduardo D'Azevedo. It was a great pleasure to work with him who assisted our porting of the density response code to the GPU. In addition, Dr. Piotr Luczceck and Dr. Stanimire Tomov from Jack Dongarra's Innovative Computational Laboratory were very gracious and helpful with offering advice and working with our research group in the porting of density response code to the GPUs.

I owe a lot and have learned a great deal from Mr. Wileam Phan. He has been a great colleague and an even greater friend through my later years as a doctoral student. I hope our relationship continues through both of our professional careers.

I owe a great debt of gratitude to the department head and one of my committee members Dr. Hanno Weitering. Through his support throughout my tenure as a doctoral student, I was able to pursue research that I put forth in this dissertation.

Finally, I would like to thank Mr. Michael Ownby for insightful conversations late at night in my office. It really made working late at night worthwhile.

Abstract

Quantum materials have a promising future for energy and security applications which will lay the bedrock for material science research for decades to follow. Particularly, 'one-dimensional' Mott-insulating cuprates such as $SrCuO_2$ and $(Ca)Sr_2CuO_3$ have been deemed to fall under a 'fractionalization' paradigm in which the electrons disintegrate into bosonic collective excitations of their fundamental constituents— spin, charge, and 'orbital' degrees of freedom— due to the anisotropic crystalline structure, deeming them outside the band theory of solids.

Here, I provide *ab initio* theory for the 'one-dimensional' cuprates $SrCuO_2$ and $(Ca)Sr_2CuO_3$ using no adjustable parameters with excellent agreement in *absolute units* with optical conductivity, dielectric function, and loss function measurements. In addition, we i) notice an overlooked 'discontinuity' in the loss dispersion at the antiferromagnetic zone boundary and provide theory to fill this void; ii) predict a novel Mott-gapped *longitudinal* spin excitation that can be verified via inelastic neutron scattering measurements; and iii) predict a re-emergence of the charge density excitations in higher Brillouin zones which can be validated with *non-resonant* inelastic X-ray scattering measurements.

To understand the microscopic physics, it was necessary to downfold *exact* time-dependent density functional theory to a low energy space of Wannier orbitals. This required developing a rigorous disentanglement procedure to partition the Wannier basis from the rest of the Hilbert space, a necessity for the cuprates due to the strong entanglement between the oxygen p and copper d derived content of the band

structure. By doing so, I attest that the Mott-gapped collective excitations require a proper treatment of the solid state chemistry inherit to the electronic structure, and they are triggered by the *long-ranged* dynamically screened Coulomb interaction. In addition, the calculations strongly suggest the 'fractionalization' paradigm is not compatible with these materials due to the indiscrimination of the orbital and spin degree of freedom of the Coulomb interaction, in which the collective modes do not simply separate into charge-only, spin-only, and 'orbital'-only degrees of freedom.

Table of Contents

List of Tables

List of Figures

Chapter 1

Introduction

Quantum materials have enormous potential for paving the road for material science in the twenty-first century. Quantum materials are loosely defined [4] as materials which require a rigorous treatment in a quantum mechanical framework to describe their properties. Materials that fit this nomenclature are the consolidation of many classes of materials, such as correlated-electron and topological materials. It is usually the case that these materials possess properties outside that of seminal solid state physics textbooks [5, 6].

By understanding the properties of these materials, future generations will benefit greatly from the development we make in our understanding and the progress we make today. For example, one could have transmission of dissipationless electrical energy from the discovery of an ambient temperature superconductor [7]. Additionally, one's digital information could completely be encrypted forbidding undesired intruders from obtaining it with the development of materials to be used in quantum computation and quantum information applications [8–10].

The principal method for studying these materials quantum mechanically is by diagonalizing a many-body Hamiltonian. Often, an effective low energy Hamiltonian, e.g. Hubbard's narrow band Hamiltonian [11], expanded in a Hilbert space of so-called Wannier orbitals is introduced since the Hilbert space size of the material

grows exponentially with the number of degrees of freedom. Alternatively, one can circumvent this issue by using Kohn-Sham density functional theory [12, 13] and its time-dependent extension [14] which gives the ability to calculate physical quantities of interest without knowledge of the many-body eigenvectors from the *exact* Hamiltonian via a functional of the density of particles.

The 'claim to fame' of this thesis is to gain insight into the microscopic physics in a low energy Hilbert space of Wannier orbitals and how it propagates to the physics from the entire Hilbert space. To achieve this, I downfold the linear response formalism of time-dependent density functional theory to a low energy space of *exactly-disentangled* Wannier orbitals from the Kohn-Sham band structure using methods introduced within our research group. From there, I 'carve out' a density response function computed via the Wannier orbitals, which is referred to as the target space, to understand the microscopic physics which otherwise would be masked behind a black box calculation. Once the response of the Wannier orbitals is well-understood, it can be put in its place in the exact *physical* response function from the entire Hilbert space to compare with experiments in *absolute* units, and determine how well the calculation from the Wannier orbitals captures the features from the exact calculation apart from intensity differences and small changes in line shapes of computed spectra.

I used this formalism to study the 'one-dimensional' Mott-insulating cuprates $(Ca)Sr_2CuO_3$ and $SrCuO_2$. These materials have attracted much attention since the discovery of high temperature superconductivity found in the electron- and hole-doped two-dimensional cuprates in 1987 [15] in which Phil Anderson argued that the properties of the one-dimensional cuprates could underlie a lot of the rich physics behind understanding the two-dimensional compounds [16]. These materials also possess strong non-linear optical properties which could be useful in opto-electronic devices [17–20]. To this day, the 'one-dimensional' cuprates are a class of quantum materials which are proposed as being a realization of a system in which the electrons 'fractionalize', meaning the fundamental quantities such as spin and charge separate into collective excitations [21, 22]. These collective (bosonic) excitations are primarily

used in explaining the features and properties of spectroscopic experiments such as angle-resolved photoemission spectroscopy [2, 23–27], inelastic neutron scattering [1, 28–30], reflectivity [31, 32], electron energy-loss spectroscopy [33], and resonant inelastic X-ray scattering [3, 34, 35].

In addition to studying the one-dimensional cuprates, I also constructed an effective low energy Hamiltonian within the random phase approximation of time-dependent density functional theory for t_{2g} Wannier orbitals for the potential quantum spin liquid candidate α-$RuCl_3$. In collaboration with Dr. Tom Berlijn, Dr. Satoshi Okamoto, Dr. Pontus Laurell, Dr. Yi Zhang, and my advisor Dr. Adolfo Eguiluz; we used second order perturbation theory in the strong-coupling limit to construct a low-energy Kitaev-Heisenberg-Γ spin Hamiltonian to give the first fully *ab initio* based Hamiltonian for this material.

Before I delve into the details of the research I performed, I deem it beneficial to introduce a few of the concepts and tools I use and compare with. First, I give a brief introduction to the notion of an *ab initio* and an *effective* Hamiltonian. Second, I introduce spectroscopy and linear response theory for its use in determining material properties. Third, I introduce the current interpretation to several experiments for the one-dimensional cuprates where the underlying theme of 'fractionalization' of the electron appears to be the consensus in its interpretations. Finally, I give an overview of high-performance computation and give a broad picture on how it has been an essential tool to the research I have performed.

1.1 *Ab initio* and an Effective Hamiltonian

The theory of the solid state of matter has evolved into an extremely rich subject over the last twelve decades. Generally speaking, the solid state of matter is a state in which the atoms *break* the continuous translational symmetry that is present in both the gas and liquid states. Solids can be further classified in whether there is an underlying repeating structure. If it does not have a repeating structure, then we

use the term amorphous solid such as glass and plastics. If the material *does* have a repeating structure, then we call these crystalline solids such as silicon[1], quartz, diamond, and iron. The focus of this thesis is studying properties of crystalline solids in the bulk where the role of surfaces is irrelevant.

To describe material properties from a theoretical standpoint without invoking any bias, one must have a *universal* method for calculating quantities from the interacting many-atom problem. To obtain such high fidelity in the calculation quantum mechanically, one must have the ability to handle all the constituents of the material. To achieve this, one must have the ability to diagonalize the Hamiltonian of the solid $\hat{H}_{solid}$, i.e. solve the eigenvalue equation

$$\hat{H}_{solid} \left|\psi_n\right\rangle_{solid} = E_n \left|\psi_n\right\rangle_{solid}. \tag{1.1}$$

By knowing all the eigenvalues $\{E_n\}$ and eigenvectors $\{\left|\psi_n\right\rangle_{solid}\}$, any ground state observable O can be computed by taking the average value of the ground state $O = \langle\hat{O}\rangle_0$ for $T = 0K$ or by taking a thermal average in the grand canonical ensemble $O = \mathrm{Tr}\hat{\rho}\hat{O}$ using the density matrix $\hat{\rho} = e^{-\beta(\hat{H}_{solid}-\mu\hat{N})}$ for finite temperatures. In addition to ground state properties, excited state properties are of great interest due to their application in many technological devices such as solar cells [36], transistors [37], atomic clocks, and automatic garage door openers.

As previously mentioned, $\hat{H}_{solid}$ involves all of the atoms interacting in a solid, however, it is more convenient to divide the atoms into their ionic and electronic contribution due to the drastically different energy scales they often acquire in the solid state. Hence, $\hat{H}_{solid}$ takes the general form[2]

$$\hat{H}_{solid} = \hat{T}_{el} + \hat{V}_{el-el} + \hat{T}_{ion} + \hat{V}_{ion-ion} + \hat{V}_{el-ion}. \tag{1.2}$$

[1] It should be mentioned that silicon can be amorphous.

[2] Neglecting effects from special relativity. These effects for solids can often be treated perturbatively and are relevant for the chapter 4.

where $\hat{T}_{el(ion)}$ is the operator associated with the kinetic energy of the electrons (ions), and the terms with $\hat{V}$ are the operators representing the Coulombic interaction among the electrons and ions. For the solid state, the ions are primarily located in a fixed equilibrium location and slightly deviate about these positions[3] making it convenient to expand the contributions from the ions about these fixed locations. Utilizing this fact, operators involving the ions can be recast as

$$\hat{T}_{ion} \to \delta\hat{T}_{ion}, \tag{1.3}$$

$$\hat{V}_{ion-ion} \to E_M + \delta\hat{V}_{ion-ion}, \tag{1.4}$$

and

$$\hat{V}_{el-ion} \to \hat{V}_{ext} + \delta\hat{V}_{el-ion}, \tag{1.5}$$

where I have used a δ in front of operators that will be associated with very low energy scales. E_M is referred to as the Madelung energy which is the *classical* electrostatic interaction of the ionic crystal in its equilibrium configuration, $\hat{V}_{ext}$ represents the interactions of the electrons with an *effective* classical *external* potential from the fixed ionic crystal, $\delta\hat{T}_{ion} + \delta\hat{V}_{ion-ion}$ represent the Hamiltonian for the *vibrating* lattice, and finally $\delta\hat{V}_{el-ion}$ gives the coupling between the electrons and the *fluctuations* of the ions about their equilibrium point.

By setting the reference energy such that $E_M = 0$, the Hamiltonian 1.2 has the equivalent form[4]

$$\hat{H}_{Solid} = \hat{T}_{el} + \hat{V}_{el-el} + \hat{V}_{ext} + \delta\hat{T}_{ion} + \delta\hat{V}_{ion-ion} + \delta\hat{V}_{el-ion}. \tag{1.6}$$

Any attempt to calculate observables from any or all the terms in equation 1.6 are considered to be *ab initio*, or from first principles. Without knowing the solution a priori, which we do not, it impossible to do so by direct and exact methods such as

[3]Except when the material is approaching its melting point.

[4]The first five operators in this expression are known as the Born-Oppenheimer Hamiltonian [38].

exact diagonalization (ED) or quantum Monte Carlo. While the last three terms in equation 1.6 are important for describing material properties such as conventional, and potentially unconventional, superconductivity, it is the focus of this thesis is to strictly consider the electronic structure aspect of the problem corresponding to the first three terms in equation 1.6.

We therefore can introduce the electronic Hamiltonian $\hat{H}_{el}$ as

$$\hat{H}_{el} = \hat{T}_{el} + \hat{V}_{el-el} + \hat{V}_{ext}. \tag{1.7}$$

Using second quantization in terms of electron field operators $\hat{\psi}_\sigma(\vec{x})$, the terms in this Hamiltonian are explicitly given as

$$\hat{T}_{el} = -\frac{\hbar^2}{2m} \sum_\sigma \int d^3x \hat{\psi}^\dagger_\sigma(\vec{x}) \nabla^2 \hat{\psi}_\sigma(\vec{x}), \tag{1.8}$$

$$\hat{V}_{el-el} = \frac{1}{2} \sum_{\sigma\sigma'} \int d^3x \int d^3x' \hat{\psi}^\dagger_\sigma(\vec{x}) \hat{\psi}^\dagger_{\sigma'}(\vec{x}') \left(\frac{e^2}{|\vec{x} - \vec{x}'|} \right) \hat{\psi}_{\sigma'}(\vec{x}') \hat{\psi}_\sigma(\vec{x}), \tag{1.9}$$

and

$$\hat{V}_{ext} = \int d^3x V^{ext}(\vec{x}) \hat{n}(\vec{x}), \tag{1.10}$$

where the operator for the electron density $\hat{n}(\vec{x})$ is

$$\hat{n}(\vec{x}) = \sum_\sigma \hat{\psi}^\dagger_\sigma(\vec{x}) \hat{\psi}_\sigma(\vec{x}). \tag{1.11}$$

Even at the level of $\hat{H}_{el}$, without an analytic solution to the problem, this task is impossible with current and most likely future computational capabilities even for extremely small systems. To understand how difficult this problem is, let us consider the case for just *one* neon atom which has 10 electrons. To numerically approach the amplitude $\psi_{Ne}(\vec{x}_1, \vec{x}_2, \vec{x}_3, \vec{x}_4, \vec{x}_5, \vec{x}_6, \vec{x}_7, \vec{x}_8, \vec{x}_9, \vec{x}_{10})$ on a discrete grid of size $10 \times 10 \times 10$, the disk space required[5] to store this would be, using the IEEE

[5]Of course I am making the argument for a classical computer. Quantum computers may be able to get this problem size down substantially, but this may be a long time from now to realize this.

standard of 16 bytes for a double-precision complex number, $(16 \times 10 \times 10 \times 10)^{10} = 16000^{10} \approx 10^{30}$ Terabytes, far exceeding all of the storage we have on our entire planet! Furthermore, there are $\sim 10^{23}$ atoms per cubic centimeter in a typical solid, so simulating a small piece of a material would make the unobtainable problem of a neon atom seem like a 'walk in the park'. There is a caveat to circumvent this unfeasible task through density functional theory (DFT) [12] which is introduced in chapter 2 and is the primary tool used for my research. While DFT is exact, it is often implemented using the Kohn-Sham formalism [13] which relies on approximating the exchange-correlation potential for its accuracy.

Besides DFT, to mitigate this computational problem, the notion of an *effective* low energy Hamiltonian for a solid is often invoked making the problem tractable. These effective Hamiltonians are expanded in a basis $\{|i\rangle\}$ and take the general form[6],

$$\hat{H}_{eff} = \sum_{\sigma} \sum_{ij} h_{ij}^{\sigma} c_{i\sigma}^{\dagger} c_{j\sigma} + \frac{1}{2} \sum_{\sigma\sigma'} \sum_{ijkl} V_{ijkl}^{\sigma\sigma'} c_{i\sigma}^{\dagger} c_{j\sigma'}^{\dagger} c_{k\sigma} c_{l\sigma}$$

$$+ \frac{1}{3!} \sum_{\sigma\sigma'\sigma''} \sum_{ijklmn} V_{ijklmn}^{\sigma\sigma'\sigma'''} c_{i\sigma}^{\dagger} c_{j\sigma'}^{\dagger} c_{k\sigma''}^{\dagger} c_{l\sigma''} c_{m\sigma'} c_{n\sigma} + \ldots, \tag{1.12}$$

but most modelling uses only the first two terms in this series. One advantage of using an effective Hamiltonian is the ability to exactly treat difficult aspects of the Hamiltonian, such as correlation effects, using current computational capabilities. Another advantage is that it can give microscopic insight into the active ingredients of a material which can help physicists search for materials with particular properties, assuming the microscopics are well understood and valid. A disadvantage to these effective Hamiltonians is their lack of universality in describing a wide variety of materials. This can lead to using an effective Hamiltonian to describe properties of materials outside their realm of validity.

[6] In general, the low energy Hamiltonian will be dependent on the entire energy spectrum, but this obviously defeats the purpose since it involves knowing the full spectrum of the full Hamiltonian.

The effective Hamiltonians have a rigorous origin in the renormalization group[7] [41–44] by 'integrating' out the higher energy states greatly reducing the size of the Hilbert space, but this problem is very difficult, if not impossible, for real materials. One potential issue that accompanies this is the low energy Hamiltonian can inherit retardation effects manifesting itself through time dependence in the Hamiltonian, causing the Hamiltonian to no longer represent conservation of energy.

For practicality, the material dependent quantities in the models are often fit to or from experiments to obtain the best agreement with experimental results. In conjunction to greatly reducing the Hilbert space size, these Hamiltonians are further simplified by diagonalizing on a discrete grid of lattice sites, as opposed to a numerical grid, greatly reducing the computational cost of the calculation. If the electrons primarily reside on a site of the discrete lattice, this may be a valid approximation, however if it does not, the modeling lacks unpixelated *real space resolution* which is required for accurately describing material properties.

1.2 Spectroscopy and Linear Response Theory

To genuinely understand material properties, the spectrum of the material, both the ground state and excited states, must be known. The spectrum can be inferred through both theoretical *calculations* and experimental *measurements* by the means of *thermodynamic* and *spectroscopic* quantities. Thermodynamic quantities, such as specific heat, bulk moduli, and thermal conductivity; are quantities that come from derivatives of the total *free energy* with respect to thermodynamic variables such as temperature, number of particles, and pressure. Spectroscopy, on the other hand, offers much more microscopic information about the excitation spectrum of a material. Spectroscopy involves having a source that can produce a beam of particles whose

[7] There are methods to construct these Hamiltonians via first-principles calculations on current high-performance supercomputers by using the random-phase approximation [39], and I will discuss the theory behind this in chapter 2 and provide an example for α-$RuCl_3$ in chapter 4 which was published in Physical Review B [40].

properties are well understood; which could be light, electrons, or neutrons; that are prepared in an initial state. This beam interacts with the material through scattering and absorption processes, and the outgoing particles[8] interact with a detector which can discern their properties within a given resolution.

When an external probe, such as the beam of particles in a spectroscopic experiment, interact with the material, the material will *respond* in a particular manner. In the case of a weak coupling between the probe and material, then the response can be well-described within *linear response* theory. Linear response theory is centered around the linear response function which gives a linear relation between the external potential produced by the probe and an *induced* observable of a system. Linear response functions are very useful because they are *entirely* determined by material properties in the absence of the external probe. Spectroscopic experiments often have a differential cross section which measures correlation functions defined as

$$S_{AB}(t) = \langle \hat{A}(t)\hat{B}(0)\rangle_0 \,. \tag{1.13}$$

Through the powerful nature of the fluctuation-dissipation theorem [45] can be directly related to the imaginary part of the linear response functions.

Spectroscopy

Spectroscopy entails the coupling of the beam of particles to the material via an *external* electric $\vec{E}^{ext}(\vec{x},t)$ or magnetic field $\vec{B}^{ext}(\vec{x},t)$, which may or may not have explicit time dependence. These fields are related to the scalar potential $\phi^{ext}(\vec{x},t)$ and vector potential $\vec{A}^{ext}(\vec{x},t)$ through the relations

$$\vec{E}^{ext}(\vec{x},t) = -\nabla\phi^{ext}(\vec{x},t) - \frac{1}{c}\frac{\partial \vec{A}^{ext}}{\partial t}(\vec{x},t) \qquad \vec{B}(\vec{x},t) = \nabla \times \vec{A}^{ext}(\vec{x},t). \tag{1.14}$$

[8]The outgoing particles do not need to be the same as the incoming beam of particles used to probe the material.

Here, due to the non-uniqueness of the potentials, I *choose* to work in the Coulomb gauge $\vec{\nabla} \cdot \vec{A}^{ext}(\vec{x},t) = 0$. In the presence of these potentials, the time-dependent Hamiltonian[9] leads to a modication[10] for the operator associated with the kinetic energy of the electrons to

$$\hat{T}_{el}(t) = \frac{1}{2m} \sum_{\sigma\sigma'} \int d^3x \hat{\psi}^\dagger_\sigma(\vec{x}) \left(\vec{\sigma}_{\sigma\sigma'} \cdot \left(\frac{\hbar}{i} \vec{\nabla} + \frac{e}{c} \vec{A}^{ext}(\vec{x},t) \right) \right)^2 \hat{\psi}_{\sigma'}(\vec{x}). \tag{1.15}$$

In addition, there is a coupling between the electron density and the scalar potential. It follows that the original electronic Hamiltonian is modified as

$$\hat{H}_{el} \to \hat{H}_{el}(t) = \hat{H}_{el} + \hat{V}^{(1)}_{ext}(t) + \hat{V}^{(2)}_{ext}(t) + \hat{V}^{(3)}_{ext}(t) + \hat{V}^{(4)}_{ext}(t), \tag{1.16}$$

where the four additional terms are given as

$$\hat{V}^{(1)}_{ext}(t) = -e \int d^3x \hat{n}(\vec{x}) \phi^{ext}(\vec{x},t), \tag{1.17}$$

$$\hat{V}^{(2)}_{ext}(t) = \frac{e\hbar}{2mic} \int d^3x \hat{\psi}^\dagger_\sigma(\vec{x}) \vec{A}^{ext}(\vec{x},t) \cdot \vec{\nabla} \hat{\psi}_\sigma(\vec{x}), \tag{1.18}$$

$$\hat{V}^{(3)}_{ext}(t) = \frac{e^2}{2mc^2} \int d^3x \hat{n}(\vec{x}) \vec{A}^{ext}(\vec{x},t) \cdot \vec{A}^{ext}(\vec{x},t), \tag{1.19}$$

and

$$\hat{V}^{(4)}_{ext}(t) = - \int d^3x \hat{\mathbf{m}}(\vec{x}) \cdot \left(\vec{\nabla} \times \vec{A}^{ext}(\vec{x},t) \right), \tag{1.20}$$

where I have introduced the magnetization density from the spin of an electron[11] $\hat{\mathbf{m}}(\vec{x})$ as

$$\hat{\mathbf{m}}(\vec{x}) \equiv \mu_B \sum_{\sigma\sigma'} \hat{\psi}^\dagger_\sigma(\vec{x}) \vec{\sigma}_{\sigma\sigma'} \hat{\psi}_{\sigma'}(\vec{x}) \tag{1.21}$$

[9] The notion of a Hamiltonian representing the conservation of energy is lost here due to the breaking of time translational symmetry.

[10] Here, I am only considering modifications up to $1/c^2$ since it will cover all the interactions between the material and probe pertaining to this thesis.

[11] There is also a contribution from the orbital magnetic moment defined as $\hat{\mathbf{m}}_L(\vec{x}) \equiv \mu_B \sum_\sigma \hat{\psi}^\dagger_\sigma(\vec{x}) \left(\vec{x} \times \vec{\nabla} \right) \hat{\psi}_\sigma(\vec{x})$

and the Bohr magneton $\mu_B \equiv e\hbar/2mc$.

It is often the case that the external probe will interact weakly with the material. We can then invoke results from perturbation theory where the transition probability for a system[12] from an initial state $|\psi_I\rangle$ to a final state $|\psi_F\rangle$ is given through Fermi's Golden rule [46]

$$w_{I\to F} = \frac{2\pi}{\hbar}\left|\langle\psi_F|\,\hat{V}_{ext}\,|\psi_I\rangle\right|^2\delta(E_F - E_I). \tag{1.22}$$

Experiments prepare the initial state of the probe, so a more relevant quantity is the differential cross section $d\sigma/d\Omega$, which is the transition probability subtended by a detector with solid angle $d\Omega$ divided by the incoming current flux density of particles[13] denoted by $j(\vec{k})$ [47]

$$\left.\frac{d\sigma}{d\Omega}\right|_{I\to F} = \frac{2\pi}{\hbar}\frac{1}{j(\vec{k})}\left|\langle\psi_F|\,\hat{V}_{ext}\,|\psi_I\rangle\right|^2\delta(E_F - E_I). \tag{1.23}$$

The physical transition *rate* is given by multiplying the differential cross section with the density of states of the outgoing beam and summing over final states of the outgoing beam [48] which depend on the dispersion relation of said particles. When the energy difference between the incoming and outgoing beam of particles is $\hbar\omega$, the double differential cross section (DDCS) is given by [47, 48]

$$\frac{d^2\sigma}{d\Omega d(\hbar\omega)} = \sum_f \frac{2\pi}{\hbar}\frac{\rho(\varepsilon_f)}{j(\vec{k})}\left|\langle\psi_F|\,\hat{V}_{ext}\,|\psi_I\rangle\right|^2\delta(E_f - E_i - \hbar\omega), \tag{1.24}$$

which can be thought of as [48]

$$\frac{d^2\sigma}{d\Omega d(\hbar\omega)} = \frac{\text{current of scattered particles in range}\,[\Omega, d\Omega]\,\text{into energy range}[\hbar\omega, d(\hbar\omega)]}{\text{current density of incoming particles} \times d\Omega \times d(\hbar\omega)}$$

[12] Here the system is the combination of the material and the external probe

[13] The current flux density depends on the dispersion of the scattering probe. For non-relativistic electrons and neutrons (in a volume L^3), $j(\vec{k}) = \hbar k/(mL^3)$ where m is the mass of the particle. For light sources, $j(\vec{k}) = \hbar\omega/(cL^3)$.

For finite temperatures, one must average over initial states weighted by a Boltzmann factor. For the case of weakly interacting probes such as *non-resonant* X-rays, thermal neutrons, and fast electrons, the DDCS will *directly* measure dynamical structure factors which are the Fourier transform of correlation functions over space and time. For the case of fast electrons and non-resonant X-rays, the quantity of interest is the dynamical charge structure factor and is given by [48]

$$S_{nn}(\vec{q},\omega) = \int d^3x \int d^3x' e^{-i\vec{q}\cdot(\vec{x}-\vec{x}')} \int_{-\infty}^{\infty} dt' e^{i\omega t'} \langle \hat{n}(\vec{x}',t')\hat{n}(\vec{x},0)\rangle \tag{1.25}$$

which involves a density-density probe-system coupling. A measurement obtained from thermal neutrons gives the dynamical spin structure factor[14] [49]

$$S_{\alpha\beta}(\vec{q},\omega) = \int d^3x \int d^3x' e^{-i\vec{q}\cdot(\vec{x}-\vec{x}')} \int_{-\infty}^{\infty} dt' e^{i\omega t'} \langle \hat{S}_{\alpha}(\vec{x}',t')\hat{S}_{\beta}(\vec{x},0)\rangle \tag{1.26}$$

which involves spin-spin probe-system coupling.

It can be shown rigorously through the *fluctuation-dissipation* theorem [45] these correlation functions can be related to the imaginary part of linear response functions. For the dynamical charge structure factor we have

$$S_{nn}(\vec{q},\omega) = -\frac{2\hbar}{1-e^{-\beta\hbar\omega}}\chi_{nn}(\vec{q},\omega) \tag{1.27}$$

and for the dynamical spin structure factor we have

$$S_{\alpha\beta}(\vec{q},\omega) = -\frac{2\hbar}{1-e^{-\beta\hbar\omega}}\chi_{S_\alpha S_\beta}(\vec{q},\omega). \tag{1.28}$$

1.2.1 'The' Dielectric Function

One of the most important properties, along with the one-particle Green function, of a material [50] is the *dynamical* screening in a material, which can be obtained via

[14] It should be noted that neutrons can also couple to the electron and lattice motion, but here I am isolating just the coupling to the spin degree of freedom.

the dielectric function. For 'linear' dielectric materials[15], the effective potential that determines an electron's motion inside the material from an external *scalar* potential are related through the inverse dielectric function

$$v_{tot}(\vec{x},t) = \int_{-\infty}^{\infty} dt' \int d^3x' \varepsilon^{-1}(\vec{x},\vec{x}';t-t')v_{ext}(\vec{x}',t'). \tag{1.29}$$

The *inverse* dielectric function is given through the density-density response function χ_{nn} through the relation

$$\varepsilon^{-1}(\vec{x},\vec{x}';t-t') = \delta(\vec{x}-\vec{x}')\delta(t-t') + \int d^3x_1 \int_{-\infty}^{\infty} dt_1 v(\vec{x}-\vec{x}_1)\chi_{nn}(\vec{x}_1,\vec{x}';t_1-t'), \tag{1.30}$$

where $v(\vec{x}-\vec{x}_1) = e^2/|\vec{x}-\vec{x}_1|$ is the bare Coulomb interaction.

It would be very insightful to examine $\varepsilon^{-1}(\vec{x},\vec{x}';t-t')$ as a function of space and time arguments $(\vec{x},t)$, however, we often examine their Fourier transform in terms of momentum and frequency space $(\vec{q},\omega)$. The double Fourier transform of the inverse dielectric function is given by

$$\varepsilon^{-1}(\vec{k},\vec{k}';\omega) = \int_{-\infty}^{\infty} d(t-t')e^{i\omega(t-t')} \int d^3x \int d^3x' e^{-i\vec{k}\cdot\vec{x}} \varepsilon^{-1}(\vec{x},\vec{x}';t-t')e^{i\vec{k}'\cdot\vec{x}'}. \tag{1.31}$$

For a *homogeneous* system, the inverse dielectric function is equivalent when translated by any displacement $\vec{y}$, i.e. $\varepsilon^{-1}(\vec{x}+\vec{y},\vec{x}'+\vec{y};t-t') = \varepsilon^{-1}(\vec{x},\vec{x}';t-t')$, therefore, the inverse dielectric function is a function of only the *difference* of $\vec{x}-\vec{x}'$. This allows the double Fourier transfrom to only depend on one wave vector $\vec{k}$

$$\varepsilon^{-1}(\vec{k};\omega) = \int_{-\infty}^{\infty} d(t-t')e^{i\omega(t-t')} \int d^3(x-x')e^{-i\vec{k}\cdot(\vec{x}-\vec{x}')}\varepsilon^{-1}(\vec{x}-\vec{x}';t-t'). \tag{1.32}$$

For a system with that has a *discrete* translational symmetry such as a periodic crystal, the inverse dielectric function has the symmetry $\varepsilon^{-1}(\vec{x}+\vec{R},\vec{x}'+\vec{R};t-t') =$

[15] By linear, I mean the repsonse of the 'internal' fields that the electrons respond to is proportional to the external potential which is probing the material.

$\varepsilon^{-1}(\vec{x},\vec{x}';t-t')$, the double Fourier transform is given by a wave vector in the first Brillouin zone $\vec{q}$ and two reciprocal lattice vectors $\vec{G}$ and $\vec{G}'$, which is shown in appendix E,

$$\varepsilon^{-1}(\vec{q}+\vec{G},\vec{q}+\vec{G}',\omega)=\int_{-\infty}^{\infty}d(t-t')e^{i\omega(t-t')}\int d^3x\int d^3x' e^{-i(\vec{q}+\vec{G})\cdot\vec{x}}\varepsilon^{-1}(\vec{x},\vec{x}';t-t')e^{i(\vec{q}+\vec{G}')\cdot\vec{x}'}, \tag{1.33}$$

which can be cast in a convenient matrix form as

$$\varepsilon^{-1}_{\vec{G}\vec{G}'}(\vec{q},\omega)\equiv\varepsilon^{-1}(\vec{q}+\vec{G},\vec{q}+\vec{G}',\omega). \tag{1.34}$$

This allows equation 1.30 to be cast as

$$\varepsilon^{-1}_{\vec{G}\vec{G}'}(\vec{q},\omega)=\delta_{\vec{G}\vec{G}'}+v(\vec{q}+\vec{G})\chi_{\vec{G}\vec{G}'}(\vec{q},\omega) \tag{1.35}$$

where $v(\vec{q}+\vec{G})$ is the Fourier transform of the Coulomb interaction

$$v(\vec{q}+\vec{G})=\frac{4\pi e^2}{|\vec{q}+\vec{G}|^2}. \tag{1.36}$$

To obtain the inverse dielectric *function* $\varepsilon^{-1}(\vec{k},\omega)$ for an arbitrary wave vector $\vec{k}$, one must take the diagonal matrix element for a reciprocal lattice vector $\vec{G}$ which translates $\vec{k}$ to the first Brillouin zone

$$\varepsilon^{eff}(\vec{k},\omega)\equiv\varepsilon^{-1}_{\vec{G}_{\vec{q}}\vec{G}_{\vec{q}}}(\vec{q},\omega) \tag{1.37}$$

where $\vec{k}=\vec{q}+\vec{G}$. The effective dielectric function $\varepsilon^{eff}(\vec{k},\omega)$ is obtained from the arithmetic inverse of the inverse dielectric function

$$\varepsilon^{eff}(\vec{k},\omega)\equiv\frac{1}{\varepsilon^{-1}(\vec{k},\omega)}=\frac{1}{\varepsilon^{-1}_{\vec{G}_{\vec{q}}\vec{G}_{\vec{q}}}(\vec{q},\omega)}. \tag{1.38}$$

1.3 'Fractionalization' Paradigm for 'One Dimensional' Cuprates

One dimensional cuprates have been used as a prototype to search for the exotic physics which results from the highly anisotropic crystalline structure. This exotica entails the concept of electron fractionalization, where the fundamental quantities of an electron separate into collective density waves, one carries charge $\pm e$ and one carries spin $S = \hbar/2$, when the system is excited [21, 22]. For example, the particle-hole excitations of the material replace elementary collective excitations such as the magnon from linear spin wave theory [5] of the Heisenberg model or the plasmon from the random phase approximation [51] of the electron gas model with a *continuum* of pairs of these fractionalized bosons [52].

Despite being one of the prime candidates that should encompass fractionalization, it is still ambiguous if the one-dimensional cuprates are hosts to this phenomenon beyond the INS measurements. This murkiness is partially due to the wide variety of modeling that is used to describe experimental data and a lack of a universal model that can describe all the data. For example, some experiments utilize a simple one band Hubbard model in one dimension to justify the experimental data such as ARPES [2, 23–27] and INS [1, 28–30]. Others find it a requirement to add a nearest neighbor interaction to describe exitonic effects which is the case for EELS [33] and reflectivity [32] measurements. In contrast to my previous statement, some argue that the inclusion of the oxygen degrees of freedom in a multi-orbital description of EELS [53, 54] and reflectivity [31] is needed. For RIXS experiments using the copper L_3 edge [3], a multi-orbital Hilbert space is introduced which inhibits examination of the gapped *dipole-forbidden* $d-d$ transitions which culminated in further fractionalization of the electron in terms of 'spin-orbital' separation to reconcile the spectrum.

Here, I summarize the primary literature that supports the claim of electron fractionalization to give an overview of the current modeling that is used. In chapter 3, I propose an *ab initio* perspective on explaining some of the experiments previously

mentioned, that is not compatible with some of the *interpretation* of the modeling that I introduce here.

1.3.1 Inelastic Neutron Scattering (INS)

Magnetic inelastic neutron scattering (INS) is the most direct way for measuring the magnetic excitations of a material. The external magnetic field $\vec{B}^{ext}(\vec{x},t)$ couples to both the orbital magnetization from the motion of the electrons and the spin magnetization from the intrinsic angular momentum. If we just consider the spin magnetization, the interaction between the magnetic field from the beam of neutrons and the magnetization of the material is

$$\hat{V}^{(4)}_{ext}(t) = -\int d^3x \hat{\mathbf{m}}(\vec{x}) \cdot \left(\vec{\nabla} \times \vec{A}^{ext}(\vec{x},t)\right). \tag{1.39}$$

If we assume that the neutron cannot flip an electron's spin orientation, then the DDCS is [55]

$$\frac{d^2\sigma}{d\Omega d\hbar\omega} = (\gamma r_0)^2 |F(\vec{q})|^2 \sum_{\alpha\beta}(\delta_{\alpha\beta} - \frac{q_\alpha q_\beta}{q^2}) S_{\alpha\beta}(\vec{q},\omega), \tag{1.40}$$

where $\gamma = 1.913$ is the gyromagnetic ratio of the neutron, $r_0 \equiv e^2/mc^2 = 2.818\times10^{-13}$ cm is the classical electron radius, $\vec{F}(\vec{q}) = \int d^3x e^{-i\vec{q}\cdot\vec{x}}\vec{m}(\vec{x})$ is the magnetic form factor which is the Fourier transform of the ground state magnetization, and $S_{\alpha\beta}(\vec{q},\omega)$ is the dynamical spin structure factor [49]

$$S_{\alpha\beta}(\vec{q},\omega) = \int d^3x \int d^3x' e^{-i\vec{q}\cdot(\vec{x}-\vec{x}')} \int_{-\infty}^{\infty} dt e^{i\omega t} \langle \hat{S}_\alpha(\vec{x},t)\hat{S}_\beta(\vec{x}',0)\rangle. \tag{1.41}$$

For the one dimensional cuprates, the low energy gapless magnetic excitations offer the best justification where the theory of a one-dimensional material matches that observed in experiment. Since the cuprates are considered strongly correlated materials, the low energy modeling is often assumed to be well-described via spin models where the itineracy of the electrons in the material can be integrated out or

treated perturbatively. For materials that have an anisotropic chain of atoms such as the cuprates, the dimensionality of the materials is often inferred from the ratio of the interchain to the intrachain 'exchange integrals' denoted $J_\perp$ and $J_\parallel$ respectively. For any *finite* value of this ratio, calculations performed in reference [56] suggest the material to have Néel order whose ordering temperature T_N is determined by this ratio. One of the first and most studied realization of a $S = 1/2$ spin chain is $KCuF_3$, whose ratio $J_\perp/J_\parallel \sim 10^{-2}$ [57]. Later measurements of the magnetic excitations were performed in reference [58], and better measurements followed in reference [59, 60].

The one dimensional cuprates were a game changer as far as idealized one-dimensional magnetic systems. There are some ambiguities on the estimated values for $J_\parallel$. Early magnetic susceptibility measurements [28] and muon spin rotation μSR measurements [61, 62] estimated $J_\parallel \approx 0.11eV$ for Sr_2CuO_3 and Ca_2CuO_3, while later susceptibility measurements [29] estimated $J_\parallel \approx 0.18$eV and $J_\parallel \approx 0.19$eV for Sr_2CuO_3 and $SrCuO_2$ respectively, while midinfrared absorption measurements [63] estimate a higher $J_\parallel \approx 0.26$eV. Reference [62] estimates a Néel temperature of $T_N = 5K$ and $T_N = 11K$ for Sr_2CuO_3 and Ca_2CuO_3 with an estimated *ordered* magnetic moment of 0.06 μ_B and 0.15 μ_B respectively, and reference [64] estimated $T_N = 5K$ for $SrCuO_2$. The ratio is estimated to be $J_\perp/J_\parallel \sim 10^{-5}$ for these compounds making them 'superstar' [65] materials to examine $S = 1/2$ Heisenberg antiferromagnets.

Due to the low estimate of $J_\perp$, the magnetic ground state and excitations for these cuprates are often modeled by the one dimensional Heisenberg model [65]

$$\hat{H}_{Heisenberg} = -J_\parallel \sum_{<i,j>} \hat{\mathbf{S}}_i \cdot \hat{\mathbf{S}}_j. \tag{1.42}$$

As a consequence of the low dimensionality and the sufficiently short range interactions, a magnetically ordered ground state above T_N is strongly suppressed [66] due to 'strong quantum fluctuations' which are claimed to be the origin of the low *ordered* magnetic moment for these materials [62]. This lack of ordering also has consequences in the inelastic magnetic neutron scattering cross section. Without a magnetically

ordered ground state, the spin dynamical structure factor $S_{\alpha\beta}(\vec{q},\omega) = 0$ if $\alpha \neq \beta$ and $S_{xx}(\vec{q},\omega) = S_{yy}(\vec{q},\omega) = S_{zz}(\vec{q},\omega)$. This behavior dictates that the *transverse* and *longitudinal* dynamical spin structure factors of the one dimensional Heisenberg model are *equivalent*. Therefore, for wave vectors along the chain, the DDCS for the one dimensional cuprates has the form

$$\frac{d^2\sigma}{d\Omega d\hbar\omega} = (\gamma r_0)^2 |F(\vec{q})|^2 2S_{zz}(\vec{q},\omega). \tag{1.43}$$

The one dimensional Heisenberg model was realized as a low energy effective model of Hubbard's model by P.W. Anderson [67] using second order perturbation theory for the strong-coupling limit $U \gg t$. The 'exchange integral' is given by $4{t_\parallel}^2/U$ of the Hubbard model at half-filling, in which the exact solution was proposed by Hans Bethe [68] called the Bethe-ansatz. Similar to the case of the Lieb-Wu solution for the one dimensional Hubbard model [69], it is extremely difficult to calculate magnetic correlation functions from the Bethe-ansatz solution [70]. The current interpretation of the gapless excitation spectrum has its roots in the so-called Müller ansatz [71] which gives the dynamical magnetic form factor, for the *longitudinal* dynamical structure factor $S_{zz}(\vec{q},\omega)$, in terms of the lower [72] $E_L(\vec{q})$ and upper bounds [73] $E_H(\vec{q})$ of the 'two-spinon continuum' given by

$$S_{M\ddot{u}ller}(\vec{q},\omega) = \frac{A\Theta(\hbar\omega - E_L(\vec{q}))\Theta(E_H(\vec{q}) - \hbar\omega)}{2\pi\sqrt{(\hbar\omega)^2 - {E_L}^2(\vec{q})}} \tag{1.44}$$

where the lower and upper bounds for the spinon continuum are given by

$$E_L(\vec{q}) = \frac{\pi J}{2}|\sin(\vec{q})| \qquad E_H(\vec{q}) = \pi J|\sin(\frac{\vec{q}}{2})|. \tag{1.45}$$

In the Müller ansatz A is an adjustable parameter that should be between 1 and 1.5 [71, 74] to satisfy f-sum rules.

Due to the solvability of the model, theorists sought to compute the INS cross section as accurate as possible and in exact units. Since the magnetic excitations are made up of even integer multiples of spinon continua[16], the contribution from each of these are possible to calculate quantitatively. Jean-Sébastien Caux et al. had computed [75] the four-spinon contribution to the dynamical structure factor and together with the two-spinon continuum can determine 98% of the total spectral weight seen in experiments for $S = 1/2$ Heisenberg antiferromagnets. This has been verified experimentally in reference [76] for $CuSO_4 \cdot 5D_2O$.

However, there was a problem with the missing *intensity* even with four-spinon contribution for Sr_2CuO_3. The values that best fit the data, $A \in (0.4, 0.6)$ were not in agreement with what they should be [71, 74]. Alternative fits which included itineracy through the extended Hubbard model [77] were not sufficient to explain this missing intensity [74]. This issue also existed in the INS measurements of $SrCuO_2$ [30] and also was an issue in the two dimensional cuprates [78]. The issue with the missing intensity was not in the calculations for the dynamical structure factor, but rather in the magnetic form factor $F(\vec{q})$. $F(\vec{q})$ is often fit from an *ionic* perspective, but the nature of the *covalency* in the cuprates was the culprit for the missing intensity [1] which can be seen in figure 1.1. In panel b) of figure 1.1, the strong *hybridization* tails can be seen in the Wannier function which shows the covalent departure from the ionic picture which is seen in panel c) of figure 1.1. By including the form factor with covalency, Walters et al. [1] were able to resolve $\sim$ 80% of the INS intensity and attributed the remaining $\sim$ 20% to the Debye-Waller factor $W(\vec{q})$ from the attenuation of coherent neutrons that modified the DDCS from equation 1.40 through an exponential $e^{-2W(\vec{q})}$ [55]. In reference [81], the sum rule was satisfied by integrating to several eV and through the explicit inclusion of oxygen degrees of freedom in the model Hamiltonian.

[16]The spinons have to be created in pairs since the neutron scattering processes involve $\Delta S = 1$ excitations.

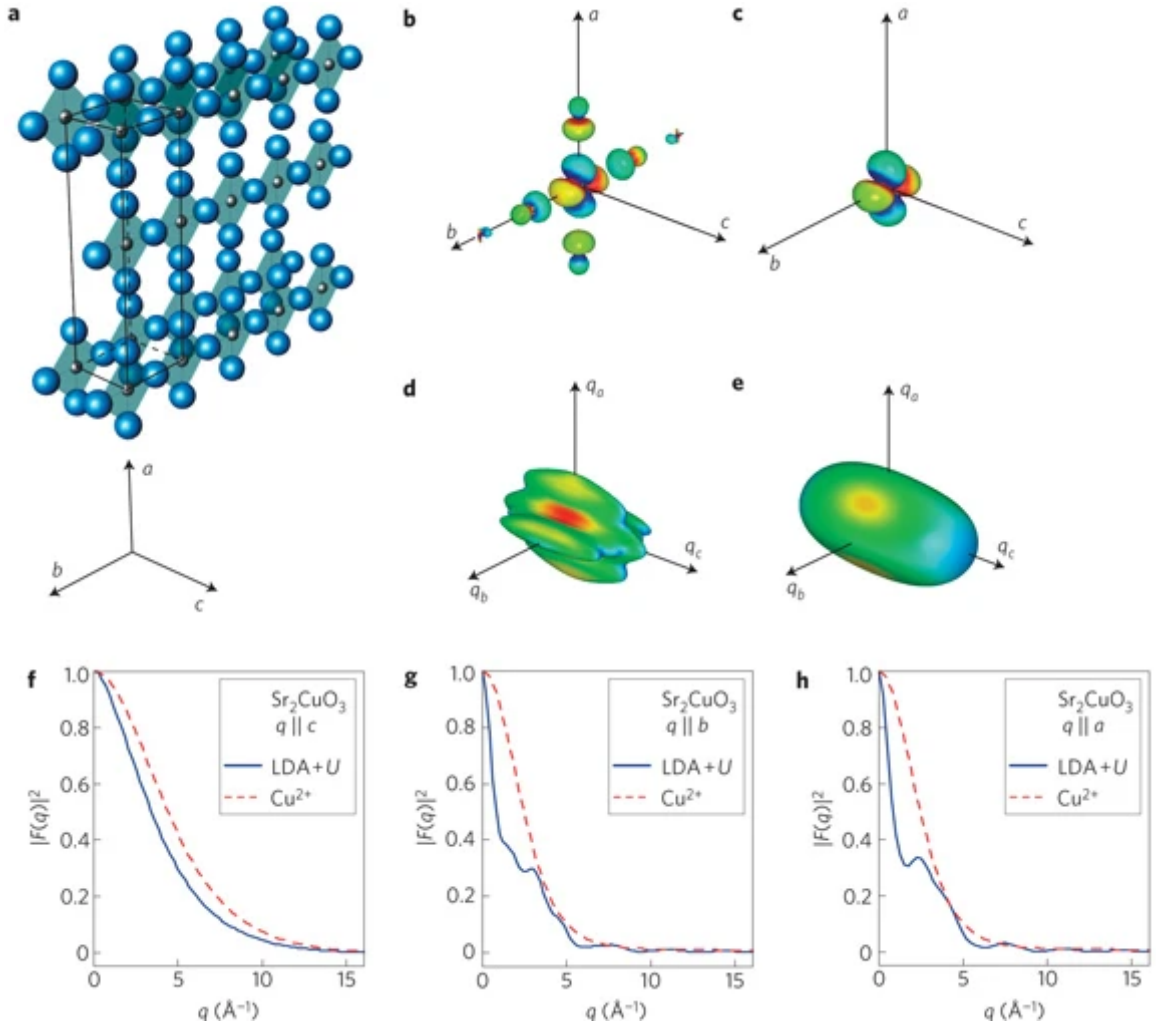

Figure 1.1: Magnetic form factors from reference [1]. a) Crystal structure of Sr_2CuO_3. b) The Wannier orbital from the density functional theory calculation. c) The atomic x^2-y^2 orbital that was used in calculating the form factor. d) Contour plot of the form factor from the Wannier orbital. e) Contour plot of the form factor from the atomic orbital. f)-h) $|F(\vec{q})|^2$ along all three axes.

1.3.2 Angle-Resolved Photoemission Spectroscopy (ARPES)

The intensity of the ARPES experiment using the sudden approximation in the long wavelength measures the spectral function modulated by the matrix element of the dipole operator[17] between the initial and final state of the photoelectron

$$I \propto \frac{2\pi e A_0}{\hbar m} \sum_f \left| \vec{\varepsilon} \cdot \langle \vec{k}_f | \hat{\mathbf{p}} | \vec{k}_i \rangle \right|^2 \left| \langle \Psi_f^{N-1} | \Psi_0^{N-1} \rangle \right|^2 \delta(\hbar\omega - E_{KE} - (E_f^{N-1} - E_0^N)). \quad (1.46)$$

To obtain this result, the ground state of the electronic degrees of freedom is approximated as a direct product of an $N-1$ electon state with the photoelectron

$$|\psi^N\rangle_0 \approx |\vec{k}_i\rangle \otimes |\psi^{N-1}\rangle_0 \quad (1.47)$$

The important quantity that ARPES measures is the spectral function $A(\vec{q},\omega)$ which is proportional to the imaginary part of the retarded one-particle Green function.

$$A(\vec{q},\omega) = -f_{FD}(-\hbar\omega)\frac{1}{\pi} Im G^{ret}(\vec{q},\omega) \quad (1.48)$$

of the N-electron system where $f_{FD}(-\hbar\omega)$ is the Fermi-Dirac distribution function.

The INS measurements seem to strongly support that the low-energy[18] magnetic excitations can be well-described in a one-dimensional framework, and since the charge excitations are above the Mott gap for these materials, this gives a very trivial interpretation of spin-charge separation in terms of energy scales. However, this is not a direct probe to observe this spin-charge separation paradigm. The best proposed method for observing spin-charge separation is through ARPES measurements. The justification for this originates when an electron is ejected from the system, the hole left behind will disintegrate into its two *collective* excitations, one which carry charge $-e$ called holons and one which carry spin $\hbar/2$ called spinons—*spin-charge separation*

[17] The dipole operator being used is due to the wavelength of light extending over several unit cells of the material

[18] By low energy I mean the meV scale

This was claimed to be the case in photoemission measurements for $SrCuO_2$ in 1996 by C. Kim et al. [23]. In this experiment, using a synchrotron radiation light source, photons of energy $\hbar\omega = 22.4$ eV were used with energy resolution of 75 meV and angular resolution of $\pm 1^\circ$. Here, the experimental evidence for spin-charge separation was justified by the difference in the spectra from the two-dimensional compound Sr_2CuO_2Cl, where the total dispersion of $SrCuO_2$ was ~ 1 eV while the dispersion for Sr_2CuO_2Cl was ~ 0.3 eV. Since a tight-binding parameterization of a one-dimensional lattice should be half that of a two-dimensional lattice, the argument of the opposite occuring was a strong suggestion that this was indicitive of spin-charge separation.

The notion for spin-charge separation was based on modeling using the one band Hubbard model in the strong-coupling limit $U \gg t$ which results in an effective[19] $t-J$ Hamiltonian. Using exact diagonalization, the calculated spectral function had two dispersing features, one scaled by t and one by J, which were compared with the charge and spin dynamical structure factors, $S_{nn}(\vec{q},\omega)$ and $S_{zz}(\vec{q},\omega)$ respectively, for the N-1 electron systems which was the justification for the association of each branch to a charge and spin excitation. The justification for comparing to the particle-hole spectrum was rationalized in reference [79] with no references why these *two-particle* structure factors for be used[20]. In addition, the theoretical calculation had a large spectral weight in the higher energy region at the zone boundary which was absent in the experiment. The claim for the discrepracy between theory and experiment was blamed on the experiment due to the experimental cross section was masked by elastic and inelastic scattering.

In a follow up paper [24] from the same group, it was further argued that this phenomena was outside the band theory by comparing their results to density

[19] At half filling (the initial state before the photoelectron is ejected), this gives the antiferromagnetic Heisenberg model. Once the photoelectron is ejected, the electrons are not completely frozen and can 'hop' to a neighboring site.

[20] It also should be noted in reference [79] that the two peak structure in the spectral function also exists for the two-dimensional modeling of the $t-J$ modeling bringing into question if this observed spin-charge separation is just an artifact of the modeling used to compute the spectral function.

functional theory calculations [80] using the local density approximation. However, this comparison should not have been made due to the lack of physical interpretation of the Kohn-Sham DFT band structure, and a Green function calculation should have been performed to compute the spectral function. They also mentioned of a step-like structure at the zone boundary which was attributed to isotropic elastic and inelastic scattering and was subtracted from the data as background. Later in ARPES measurements of Sr_2CuO_3 by H. Fujisawa et al. [26], this was claimed to be an effect of surface degradation.

It was argued in reference [25] H. Fujisawa et al. argued the measurements in [23] might have matrix element effects in the cross section due to the polarized light produced from the synchrotron source. Additionally [23] had a charging-up effect that was removed with an electron flood gun. To test the reliability of previous measurements, H. Fujisawa et al. used an unpolarized light source from the He I resonance line (21.2 eV) with energy resolution of 100 meV and angular resolution of $\pm 1^\circ$. They also used a low photon flux to minimize the charging-up effect. They also noticed discrepancies between theory and experiment having to do with the spinon dispersion, namely the experimental 'spinon' has finite weight in the second half of 1BZ and much less spectral weight than predicted in the first half of the 1BZ.

In 2004, S. Suga et al. performed ARPES measurements [27] using high energy photons $\sim$ 700 eV photons with with energy resolution of $\sim$ 100 meV and angular resolution of $\pm 3^\circ$ to study the spectral function of $SrCuO_2$. They claim that using such high incident energy photons were to penetrate deeper within the material measuring bulk properties as opposed to seeing effects from the surface for the low energy ARPES. In addition, these measurements were claimed to be less sensitive to the matrix element effects. The two branches seen in reference [23] were absent in the valence band for these measurements. They also used more reasonable modeling with quantum Monte Carlo simulation of the Hubbard model, and claim that the $t - J$ model interpretation is inconsistent with the high energy ARPES measurements.

In 2006, B.J. Kim et al. performed another measurement on $SrCuO_2$ [2]. In this seminal paper, with new developments in the ARPES technology and using photons with energy $\hbar\omega = 85$ eV, they were able to distinctly see the two branches proposed in the 1996 paper which is shown in figure 1.2. The two peak structure was deemed more consistent with the Bethe-Ansatz solution as opposed to two separate peaks due to the large spectral weight seen between the two peaks. There still was the issue of the lack of spectral weight at the zone boundary which now was attributed to the oxygen $2p$ character which appears consistent with DDMRG calculations in reference [81]. In addition, they could not rectify the wide broadening of the square root singularities from the Bethe-ansatz solution and attributed this to large effects from phonons.

I would like to make a few comments here before proceeding. There has been no *realistic* comparison to conventional band theory to these experiments. The comparisons made were from the band structure from density functional theory which should not be used for analysis. A realistic comparison would involve a Green function calculation using a conserving[21] approximation [82] where the spectral function can sincerely be computed for direct comparison. Not only would this calculation be 'comparing apples to apples', but it would also include many body effects such as satellites [83–85] from the plasmon in the two-particle Green function that feed back into the one-particle Green function. While plasmons for simple metals usually occur at several eV, the Cuprates have plasmonic excitations that occur slightly above the Mott gap, which will be seen in section 1.3.3, which could cause a very noticeable change between the computed spectral function and the DFT band structure. Additionally, the plasmonic behavior is different in the one dimensional cuprates than the two dimensional cuprates which could explain why the ARPES measurements are different in these two compounds. I hope this thesis motivates work to be done in the future on this front.

[21] By conserving, I am referring to the conservation laws that are obeyed by the system. This is achieved by the self-energy being a functional derivative of the generating functional with respect to the self-consistent one-particle Green function.

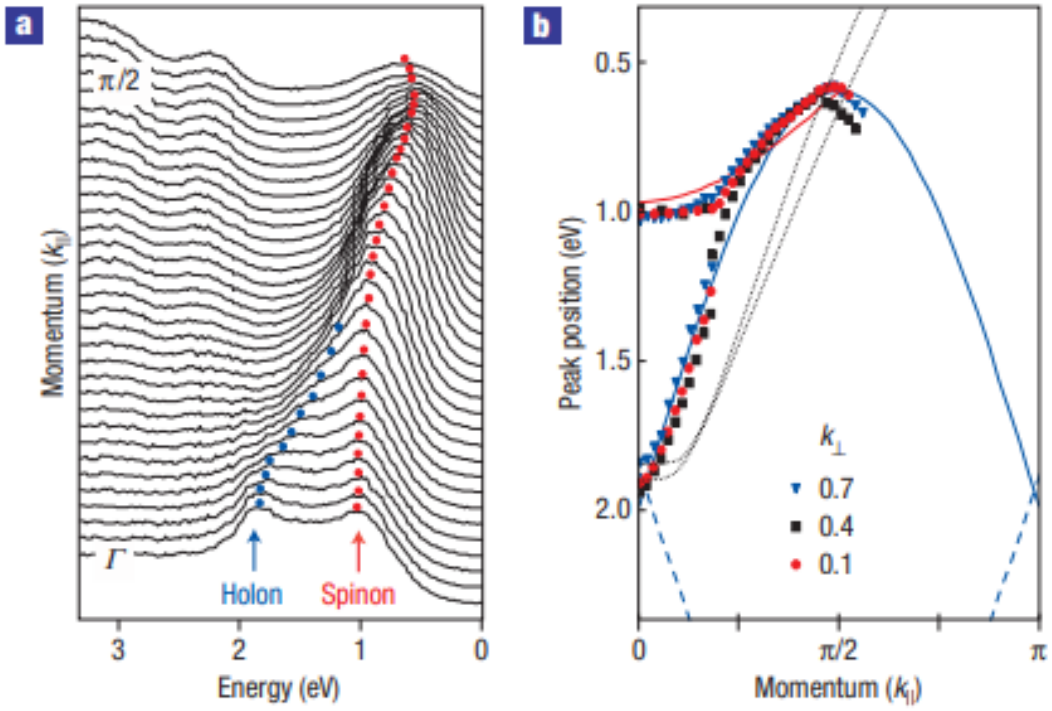

Figure 1.2: Evidence for spin-charge separation for $SrCuO_2$ from reference [2]. a) Energy distribution curves for wave vector parallel to Cu-O chain showing the low energy valence bands measured by the ARPES experiemnt At the zone center Γ, there are two peaks which are interpretted as the spinon and holon band. b) Peak positions of for various out of plane wave vectors $k_\perp$ (circle, square, and triangle) and dispersion from $t - J$ model (solid lines).

1.3.3 Electron Energy Loss Spectroscopy (EELS)

Fast electrons (∼100 keV) are an excellent probe for the long wavelength particle-hole charge excitations of the material i.e. the plasmons [86]. The beam of fast electrons couple to the electrons in the material through the Coulomb interaction giving rise to a Hamiltonian

$$\hat{H}_{int} = -e^2 \int d^3x \int d^3x' \frac{\hat{n}(\vec{x})\hat{n}_{el}(\vec{x}')}{|\vec{x} - \vec{x}'|} \tag{1.49}$$

where $\hat{n}_{el}(\vec{x})$ corresponds to the electron density from the beam of electrons and $\hat{n}(\vec{x})$ corresponds to the electron density in the material. The initial state and final states are a direct product of the the initial and final state of the electrons in the material and the incoming and outgoing momentum of the electron beam i.e. $|I\rangle = |i\rangle \otimes |\vec{k}_i\rangle$ and $|F\rangle = |f\rangle \otimes |\vec{k}_f\rangle$. To single scattering events, the DDCS is determined strictly by the momentum transfer $\vec{q} = \vec{k}_f - \vec{k}_i$ and the DDCS is given by [87]

$$\frac{d^2\sigma}{d\Omega d\hbar\omega} = \frac{m^2}{2\pi^3\hbar^5}\frac{k'}{k}v^2(\vec{q})S_{nn}(\vec{q},\omega) \tag{1.50}$$

where $v(\vec{q}) = \frac{4\pi e^2}{|\vec{q}|^2}$ is the Fourier transform of the Coulomb interaction and $S_{nn}(\vec{q},\omega)$ is the dynamical charge structure factor

$$S_{nn}(\vec{q},\omega) = \int d^3x \int d^3x' e^{-i\vec{q}\cdot(\vec{x}-\vec{x}')} \int_{-\infty}^{\infty} dt e^{i\omega t} \langle \hat{n}(\vec{x},t)\hat{n}(\vec{x}',0)\rangle \tag{1.51}$$

which is the Fourier transform of the Van Hove formula [49]. Another form of the DDCS can be cast using the loss function Im(-1/ε) [87]

$$\frac{d^2\sigma}{d\Omega d\hbar\omega} = \frac{m^2}{\pi^3\hbar^4}\frac{k'}{k}v(\vec{q})Im(-1/\varepsilon(\vec{q},\omega)). \tag{1.52}$$

The first EELS measurement for a one-dimensional cuprate was performed by Jörg Fink et al. [33] to examine the manifestation of spin-charge separation in the loss function for wave vector transfer in the first Brillouin zone. The modeling used

was the extended one band Hubbard model with a nearest-neighbor interaction. The density response function was not directly computed using the Hubbard model, but rather a 'Lindhard' function $\chi_0(\vec{q},\omega)$ was computed in the strong coupling limit using an effective *spinless* $t-J$ model consisting of a single occupied site (holon) and a doubly occupied site (doublon). From there, the density response function $\chi_{nn}(\vec{q},\omega)$ was computed within the 'random-phase approximation' using the *bare* Coulomb interaction[22]

$$\chi_{nn}(\vec{q},\omega) = \frac{\chi_0(\vec{q},\omega)}{1-\frac{4\pi e^2}{|\vec{q}|^2}\chi_0(\vec{q},\omega)}. \tag{1.53}$$

It was argued that similar spectra could be reproduced without the long-range screening by using a 'screened' value of the nearest-neighbor interaction V.

The results of this calculation and experiment are shown in figure 1.3a. The justification for seeing spin-charge separation in this data was rationalized from the lack of a *spin-dependent* background in the effective spinless $t-J$ model of holons and doublons interacting with an *attractive* nearest neighbor interaction V which produce a *continuum* of 'interband plasmons'. The explanation of the line shape of the experiment was argued in the optical limit, the continuum of excitations induced a broad excitation from the interband transitions from the 'band' dispersion of the holon and doublon while at the zone boundary a sharp bound exciton formed since it is outside the continuum. For small wave vectors, the bound exciton is inside the continuum, so its features were not seen in this regime.

This exciton seen as a narrowing of the line shape in the theory for increasing wave vector that gives a sharp peak at the zone boundary is not consistent with experiment since after *halfway* to the zone boundary the line shape starts to broaden which can be seen in the left panel of 1.3a. This broadening was attributed to total enhanced background from multiple scattering, as opposed to being inconsistent with

[22]It will be shown in section 2.2.3 that working in a low energy Hilbert space, the bare interaction should be dynamically screened.

theory. It was also pointed out that changing the parameters by $\sim 10\%$ caused a very noticeable disagreement with experiment.

In 2000, J. Richter et al. in reference [53] argued that the role of the oxygen orbitals was necessary to accurately describe the dispersion seen in the loss function. The model Hamiltonian involved only oxygen↔oxygen and oxygen↔copper hoppings with an onsite interaction between the copper orbitals. They concluded that the loss dispersion was composed of two *separate* excitations which were due to the formation of a Zhang-Rice singlet [88] which were then convolved to get the final loss function. In the optical limit, the Zhang-Rice singlet was argued to be rather delocalized and for larger wave vector, the Zhang-Rice singlet was to be rather local, i.e. within the CuO_4 plaquette. It was argued that the nearest-neighbor interaction was not needed and its role in the single band model was to adjust the energy positions.

One year later, it was argued by A. Hübsch et al. in reference [54] that the *interaction* between copper and oxygen degrees of freedom is needed to obtain a realistic description of the EELS spectrum. As in reference [33], they used the RPA, however, they realized that the *bare* Coulomb interaction needed to be screened in the density response function 'RPA' equation. To do so, they used the value estimated from reference [33] which used Kramers-Kronig analysis to obtain $\varepsilon(\vec{q}, \omega = 0) = 8$. The spectrum they calculated is shown in figure 1.3b.

A.S. Moskvin et al. in reference [89] were the first to try and explain the shoulder at ~ 2 eV that appears for larger wave vector appearing in the loss dispersion seen in figure 1.3. Here they argued that there were two types of excitonic transitions, a one- and two-center exciton. The one-center exciton had a π bonding configuration while the two-center exciton had a σ bonding configuration of orbitals. In this paper, the one-center exciton was claimed to be responsible for the shoulder that appeared at ~ 2 eV for larger wave vector seen in the second panel of figure 1.3a since this excitation was also seen in wave vector transfer perpenduclar to the chain, and the two-center exciton was responsible for the dispersive excitation which dispersed from $\sim$2.6 eV to ~ 3.2 eV.

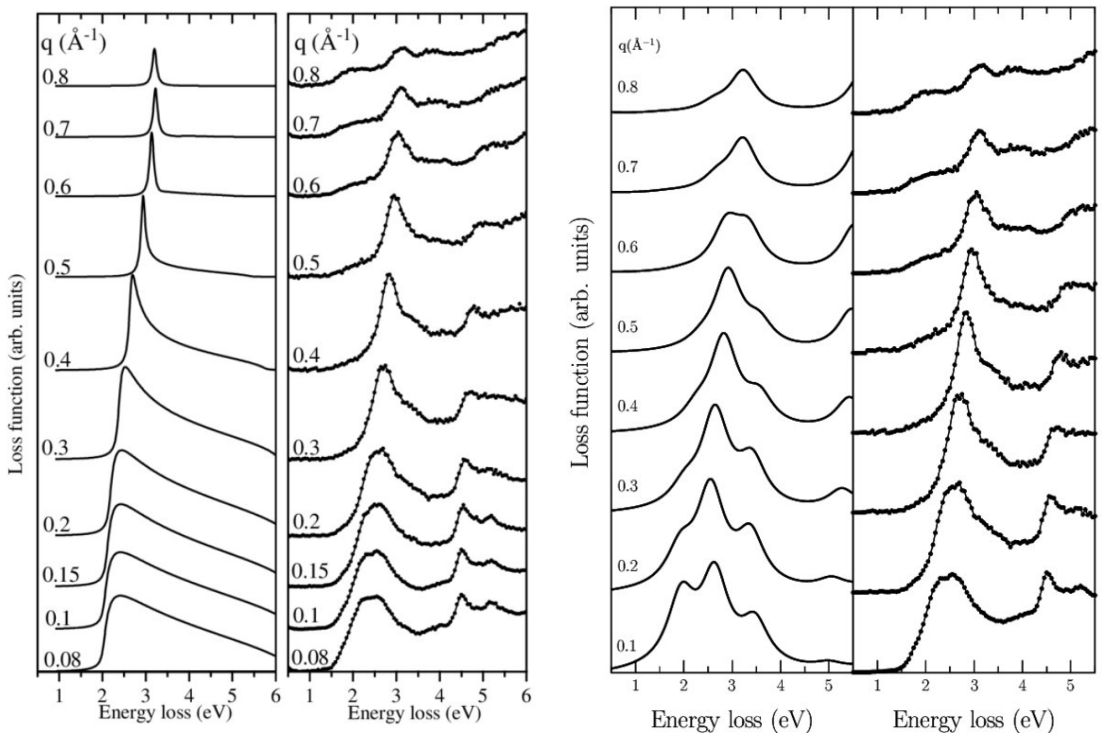

(a) Loss function from one band extended Hubbard model. **(b)** Loss function from three band Hubbard model.

Figure 1.3: Loss function from experiment and Hubbard models. a) Theory from one band extended Hubbard model (left) and loss function obtained from EELS measurement reproduced from reference [33]. b) Theory from three band extended Hubbard model (left) and loss function obtained from EELS measurement reproduced from reference [54].

1.3.4 Optical Conductivity

The optical properties of one dimensional cuprates have struck great interest in the condensed matter community due to their nonlinear optical properties [17–20] that can be used in opto-electronic devices for ultra-fast switching. Measurements for optical conductivity can be obtained from several method. It can be obtained from using the Kramers-Kronig relations from the long wavelength limit of the EELS cross section to obtain the dielectric function. Then the real part of the optical conductivity can be obtained from the relation

$$\sigma_1(\omega) = \frac{\omega}{4\pi}\varepsilon_2(\omega). \tag{1.54}$$

for complex dielectric function and optical conductivity

$$\tilde{\varepsilon}(\omega) = \varepsilon_1(\omega) + i\varepsilon_2(\omega) \qquad \tilde{\sigma}(\omega) = \sigma_1(\omega) + i\sigma_2(\omega) \tag{1.55}$$

Alternatively, the dielectric function can directly be obtained from ellipsometry measurements in which elliptically polarized light is shined upon a sample and the phase shift of the reflected light is used to obtain the dielectric function. Another method is using reflected light from a synchrotron source which can be used in conjunction with Kramers-Kronig relation to obtain the optical conductivity.

In 2008, reflectivity measurements were performed [32] for one dimensional cuprate Sr_2CuO_3. In their letter, they indicated that their exists a bound exciton at the edge of the optical gap which was inferred through sharp peaks where they had to look at the first derivative to show this feature. They used the one-dimensional extended Hubbard model which has a bound exciton of holons and doublons in the strong coupling limit for $V > 2t$ [90], however, this was not in the parameter range used in reference [33]. Additionally, the line shape for the bound exciton in this measurement was not the same as the one that occurs in the extended Hubbard model [91]. This led them to conclude the 'missing ingredient' was the inclusion of the *long range*

Coulomb interaction which is key to our interpretation given in chapter 3. It was also mentioned that the line shape was very dependent on the nearest neighbor interaction V.

In 2009, a different interpretation of these measurements were proposed in reference [31] with the inclusion of the oxygen degrees of freedom. In this paper, they tried to attribute features in the loss function from features in optical conductivity. The interpretation involved using the notion that peaks A and B in figure 1.4 were due to Zhang-Rice excitations from the hole in the electron-hole process introduced by the charge-neutral excitation. One problem that they had was they were not able to attribute the excitations seen in the loss A' and B' could not be attributed to the fits from peaks A and B from optical conductivity, nor could they be fit by the sum of the fits. This message is also consistent with our interpretation of the optical data in chapter 3 where we agree in both peak position and *intensity* with experiment. In the calculations I performed, the higher energy spectrum feeds back to the lower energy spectrum through the Kramers-Kronig relation, so peaks in the optical conductivity cannot be attributed to peaks seen in the loss function.

There is also modeling of the optical conductivity based on the dynamical density matrix renoralization group (DDMRG) [92]. Here, the model Hamiltonian is the extended Hubbard model. In reference [90], they use the relation of the optical conductivity to the density-density response obtained from lattice models, and in reference [92] they relate optical conductivity to the current-current response function which yields

$$\sigma_1(\omega) = \omega \lim_{\vec{q}\to\vec{0}} \frac{\chi_{nn}(\vec{q},\omega)}{|\vec{q}^2|} = \omega\chi_{jj}(\omega). \tag{1.56}$$

Due to the different locations of the measured peaks in optical conductivity and density response, this could not yield a consistent framework to give an accurate description of both. In addition, reference [35] gives agreement in *absolute* units with the optical conductivity for $SrCuO_2$ which should *not* be the case for working in a low energy Hilbert space as seen in section 2.2.3 and with reference [5].

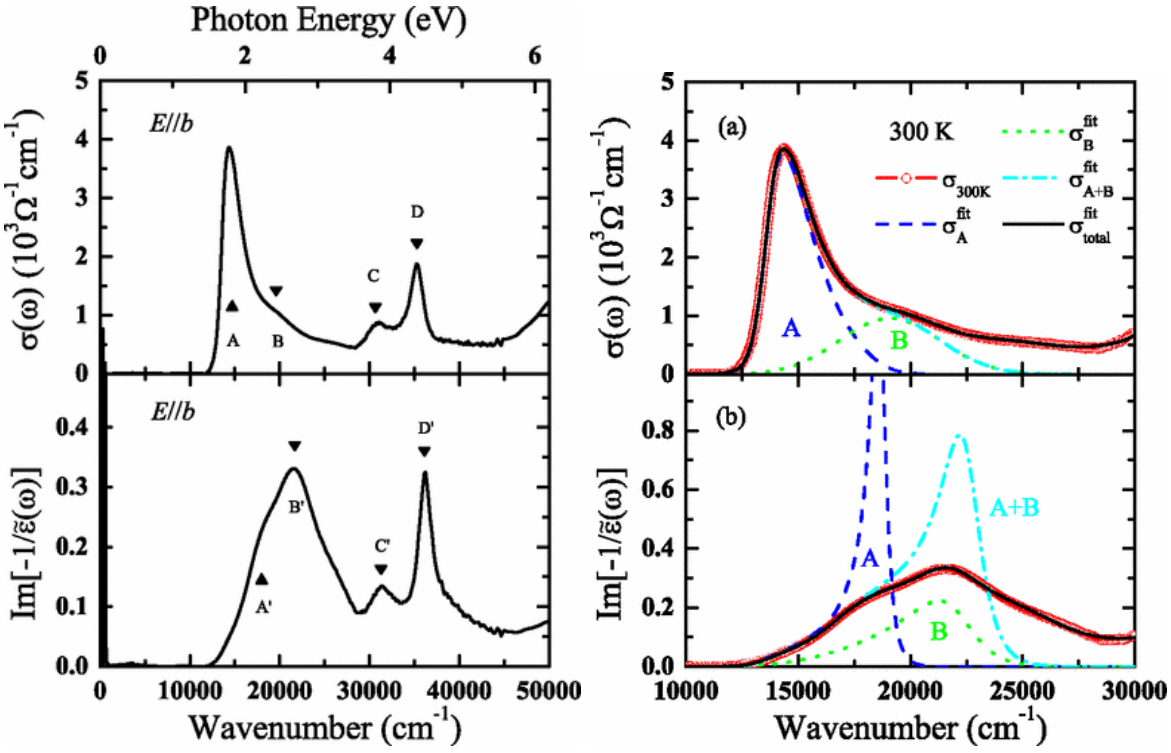

Figure 1.4: Optical conductivity from reference 1.4. Top-left: Optical conductivity where four features were isolated and fit with Gaussians. Bottom-left: Loss function where four peaks were identified. Top right: Gaussian fits for features A and B from top left panel. Bottom-right: Loss function with additional curves showing the loss function obtained from Gaussian fits from A, B, and A+B. It can be seen that using these fits *cannot* produce the loss spectrum.

1.3.5 Resonant Inelastic X-ray Scattering (RIXS)

Resonant inelastic X-ray scattering (RIXS) has acquired great popularity as a probe for examining excitations of materials. With the increase of brilliance in the synchrotron sources, RIXS has recently become extremely popular for studying correlated electron materials since they can probe charge, spin, and orbital degrees of freedom [93]. For a RIXS experiment, the X-ray is *tuned* to a resonant energy between a core electron deep inside an atom with a valence electron state. The tuning of different resonances can unveil different cross sections which can shed light on different excitations within the material. These resonances are categorized in terms of absorption edges and have different atomic transition character. For the transition metals in correlated electron materials, The K edge refers to a $1s \rightarrow 3d/4p$ atomic transition, the L edge refers to $2p \rightarrow 3d$ atomic transitions, and the M edge corresponds to $3p \rightarrow 3d$ atomic transitions.

Unlike *non-resonant* X-rays which interact with the material to first order in $\hat{V}^{(3)}_{ext}(t) = e^2/2mc^2 \int d^3x \hat{n}(\vec{x})\vec{A}^{ext}(\vec{x},t) \cdot \vec{A}^{ext}(\vec{x},t)$, the *resonant* X-rays are dominated by the interaction where the light couples to the current of electrons to second order in $\hat{V}^{(2)}_{ext}(t) = e\hbar/2mic \sum_\sigma \int d^3x \hat{\psi}^\dagger_\sigma(\vec{x})\vec{A}^{ext}(\vec{x},t) \cdot \vec{\nabla}\hat{\psi}_\sigma(\vec{x})$.

In principle, a resonant probe should have a cross section that should be expanded to *infinite* order in the interaction, but due to the core-hole lifetime Γ_n and a low photon flux, the transition probability is evaluated to *second* order

$$w_{I\rightarrow F} = \frac{2\pi}{\hbar}\left|\sum_n \frac{\langle\psi_F|\,\hat{V}^{(2)}_{ext}\,|n\rangle\,\langle n|\,\hat{V}^{(2)}_{ext}\,|\psi_I\rangle}{E_I - E_n + i\Gamma_n}\right|^2 \delta(E_F - E_I), \tag{1.57}$$

which is the Kramers-Heisenberg formula [94]. The RIXS amplitudes that contribute to the cross section are divided into two individual processes which are referred to as direct and indirect RIXS. In direct RIXS, the core-hole does not play a main role in the scattering process while for indirect RIXS, the core-hole does play a prominent role. Since the RIXS cross section is expanded to second order, it does not *directly*

probe the elementary excitations of a material, but there has been work to relate the cross section to that of probes which do [95, 96].

Since RIXS can be tuned to shed light on certain excitations it has played a crucial role in the fractionalization paradigm for quantum materials. In 2002, M. Z. Hasan et al. performed a RIXS measurement [35] tuned to the copper K edge with incident energy $E_i = 8996$ eV on $SrCuO_2$. The interpretation was the excitations seen originated from the holons due to the comparison from the one dimensional Hubbard model [97–99] where the measurement used the onset of the spectrum as opposed to the 'center of gravity'. Further justification of fractionalization, similar to the case of the ARPES, was the dispersion of the onset for $SrCuO_2$ was about twice as large as for the two dimensional compound $Ca_2CuO_2Cl_2$ measured in reference [100].

In 2004, Young-June Kim et al. also performed measurements on the copper K edge of $SrCuO_2$ [34]. Since RIXS measures charge neutral processes, it was argued the electron is moved to a neighboring site creating a hole and a doubly occupied site. Subsequently, the hole decays into a holon and a spinon while the doubly occupied site decays into an antiholon and spinon. They then argued that since the X-ray couples much stronger to the charge than the spin degree of freedom, the broad sinusoidal dispersive feature ~ 1.1 eV, was a *continuum* comprised of holon and antiholons. They also made comments that there were two additional features in the measurement, the onset of the holon-antiholon continuum with dispersion ~ 0.4 eV which is indicative of the spinon dispersion relation $E(q) = (\pi/2)J|\sin(qa)|$ 'shifted' by a constant value of 1.9 eV. The second feature was a broader more dispersive remnant of a strong-coupling exciton which was in contradiction to the EELS measurement [33].

The main tour de force of realizing fractionalization in the RIXS experiments was that performed by J. Schlappa et. al. [3]. Here, they performed measurements on the copper L_3 edge ($E_i \approx 931$ eV) of Sr_2CuO_3 where both gapped and gapless excitations were both observed. The gapless features were consistent with the two-spinon continuum and they were able to estimate the exchange integral $J = 0.249$ meV, consistent with other measurements. Since the magnetic sector was well

established to be made of even integer spinon continua, the gapped excitations *must* be remnants of the other fragmentations of the electron.

The gapped spectrum's interpretation utilized the fact that within the strong coupling limit of these materials, the electrons in the crystal are bound to the ions giving them an inherit orbital degree of freedom. Therefore, the electron can be thought of as a bound state, similar to the quarks in a nucleus, of three fundamental quantities spin, charge and orbital constituents referred to as the spinon, holon, and orbiton respectively. The numerical work behind this was based on a multi-orbital (all copper d and oxygen p) calculation modelled using the complete-active-space self-consistent field (CASSCF) and supplemented with configuration interaction (CI), i.e. a multiple Slater determinant basis, to get the correct multiplet structure. From here, using strong-coupling perturbation theory with respect to the charge transfer energy Δ, they were able to obtain a Kugel-Khomskiĭ-like Hamiltonian [101] where the details of the synthesis of the Hamiltonian are given in reference [102]. This Hamiltonian resembles in its form the $t-J$ model where the hopping parameter t is replaced with the orbital super-exchange integral J_0. Here spin-orbital separation is said to occur in the so-called J_0-J model.

The spectrum obtained in the measurement involved a gapless dispersive feature which were a continuum of spinons, a Mott-gapped intensity at $\sim$ 1.8 eV which was attributed to an xy 'orbiton', a strong, broad dispersive feature with its center of gravity at $\sim$ 2.3 eV which was attributed to xz and yz 'orbitons', and a weaker feature at $\sim$ 3 eV which was attributed to the $3z^2-r^2$ 'orbiton' as seen in figure 1.5. I would like to point out that I introduce a Mott gapped longitudinal spin excitation in section 3 that overlaps in the energy region of the xy 'orbiton' and a plasmonic loss seen at slightly above the energy of the xz and yz 'orbitons' which disperses into the region of the $3z^2-r^2$ 'orbiton' in chapter 3. While a direct comparison of my calculations to that of RIXS cannot be directly made since I am unable to compute a cross-section, it is conspicuous that the spectrum in my calculation has a drastically different origin.

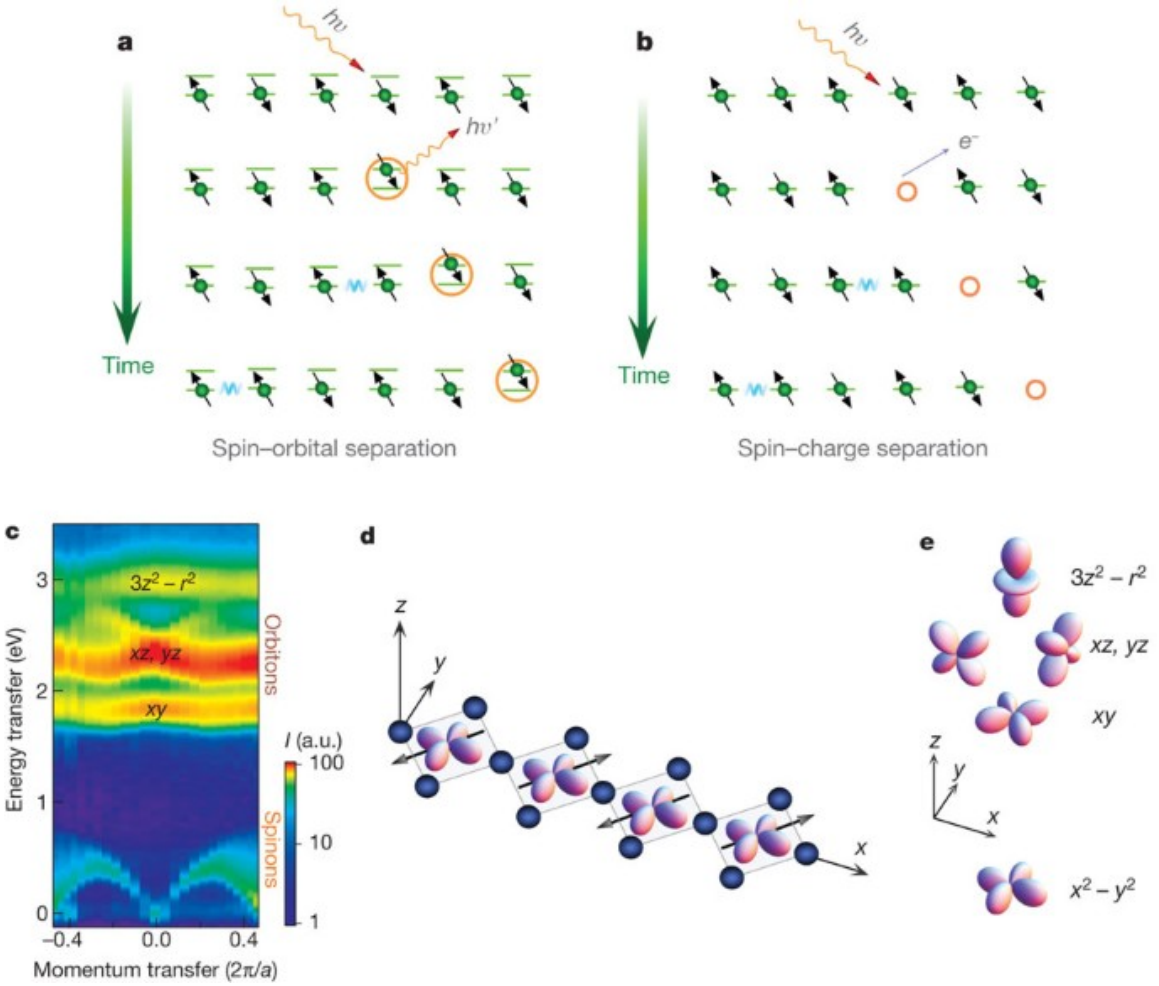

Figure 1.5: Evidence for spin-orbital separation for Sr_2CuO_3 from reference [3]. a) Cartoon for spin-orbital separation. b) Cartoon for spin-charge separation. c) RIXS spectrum for copper L_3 edge. d) Cartoon for xy 'orbiton'. e) Atomic d ($l = 2$) Hydrogenic orbitals.

High-Performance Computation

The main tool that we use in our research group are state-of-the-art high-performance supercomputers to compute material properties. Previous generations of physicists did not have the luxury of being to exploit such excellent machinery, leaving them to a more 'pencil and paper' approach to calculations and often relied on the solvability, whether exact or approximate, of simple toy models with aspiration that these calculations could be realized in *real* materials.

The current state of high-performance supercomputers are the implementation of many central processing units (CPUs) located on what are referred to as compute nodes performing calculations in parallel over several nodes. Additionally, the CPUs are often equipped with accelerators which often are graphic processing units (GPUs) that can perform computations much quicker than the CPUs. However, there is a drawback to using the GPUs. Since they are not stand-alone computational resources, they require the transfer of data from the CPUs, but the current transfer rate is quite slow. This latency can be become less of an issue if the calculations are quite demanding, and the GPUs can be kept busy with computations.

In our research group, we require the use of high-performance computers to compute density response functions and interaction parameters to enter effective models from *ab initio* electronic structure. To do so requires the computation of charge fluctuation matrix elements within the linearized augmented plane wave basis. The code we use within our research group is based on the elk (ver 1.0.17) [103] ground state density functional theory code. A former postdoctoral researcher in our research group, Anton Kozhevnikov who is currently at the ETH in Zurich, Switzerland, extended the capabilities to compute density response functions on massively parallel CPU environments over a two-dimensional message-passing interface (MPI) grid which won a Gordon-Bell prize for scalability in 2009 [104]. Further developments were done in Wileam Phan's thesis [105] to port the charge fluctuation matrix elements using the full-potential linearized augmented plane

wave basis to the CPU-GPU environment which gave $\sim$12$\times$ speedup from Dr. Kozhevnikov's implementation. Without these optimizations for high-performance computation, the research I performed would not have been possible. The calculations performed during my thesis were run on the Cray XC-30 (Darter) supercomputer under project UT-TENN0105, the Cray XK7 (Titan) supercomputer under a director's discretionary allocation granted by Dr. Bobby Sumpter, and the IBM AC922 (Summit) supercomputer under projects MAT168 and MAT201.

Overview

My thesis is organized in the following manner. In chapter 2, I introduce the theoretical tools that I use for my research. I introduce density functional theory for systems in a static external scalar potential and magnetic field. Then I discuss the Wannier orbital basis and the disentanglement technique implemented within our research group. Next, I introduce time-dependent density functional theory (TDDFT) in its linear response formalism and the technique developed within our research group to downfold it to a low energy Hilbert space. Then I discuss a method to construct a low energy effective Hamiltonian that can be used in many-body methods such as exact diagonalization, quantum Monte Carlo, dynamical mean field theory (DMFT), and the dynamical cluster approximation (DCA) to examine ground and excited state properties of materials.

In chapter 3, I present the main research I performed during my time as a Ph.D. student. This involves performing calculations for spectroscopic quantities to examine the charge and longitudinal spin particle-hole excitations for the Mott-insulating one-dimensional cuprates using our downfolding procedure introduced in chapter 2. Here, I show excellent agreement with dielectric spectroscopy in the optical and finite momentum transfer regimes. From here, I get inside the black box calculations using our downfolding implementation of TDDFT to unveil the microscopic ingredients that give rise to our spectra.

In chapter 4, I summarize work that was done with collaborators at Oak Ridge National Lab to construct a *fully ab initio*- based Hamiltonian to study potential quantum spin liquid candidate α-$RuCl_3$. To do this, I synthesized a multi-orbital extended Hubbard model where my collaborators performed calculations using strong-coupling perturbation theory upon exact diagonalization calculations to construct an effective Kitaev-Heisenberg-Γ spin Hamiltonian [40]. This Hamiltonian was used in reference [106] to compute the INS cross section and the specific heat associated with magnetic excitations. By changing one of the parameters from our model, it was shown that our Hamiltonian could describe both the INS and specific heat measurements which was shown in reference [106].

Chapter 2

Theory

In this chapter, I present the theory I use throughout my thesis which is based on Peter Hohenberg and Walter Kohn's ground state density functional theory (DFT) [12] in section 2.1. I then discuss the localized Wannier basis [107] in section 2.1.4 and the success of a new disentanglement procedure in section 2.1.4 that my advisor and myself have proposed and successfully implemented. This procedure is currently more successful than other state-of-the-art methods [108, 109] as far as enforcing what I will refer to as *unitarity* which means it can faithfully reproduce the underlying eigenvalues from the band structure. By strictly enforcing a unitary transformation, this will allow the band structure to *exactly* be partitioned into two subspace, the *target* space corresponding to the Wannier orbital basis and the *rest* space which are the orbitals not included in the Wannier projection. To extend the ground state methods to compute excited states, I introduce Erich Runge and Eberhard K. U. Gross's seminal time-dependent extension [14] to DFT and its application to linear response [110]. Finally, I describe our rigorous method for downfolding procedure for the density response function which systematically becomes exact. To do so, the band structure must *exactly* partition the Hilbert space into two subspaces which *requires* our disentanglement procedure for the Wannier orbital basis. This downfolding procedure will be insightful for constructing *ab initio* Hamiltonians [39]

introduced in section 2.2.4 because it introduces a reducible polarization function in the random phase approximation (RPA) for the rest space which *dynamically* screens the Coulomb interaction between the Wannier orbitals in the target space.

2.1 Density Functional Theory (DFT)

As mentioned in section 1.1, the ability to diagonalize the electronic Hamiltonian $\hat{H}_{el}$ for a material is by far too computationally expensive due to the storage required for the eigenvectors $|\psi_n\rangle_{el}$. DFT relies on the eigenvalues E_n inherently being *functionals* of the eigenvectors through $E_n[\psi_n] = \langle\psi_n|\,\hat{H}_{el}\,|\psi_n\rangle_{el}$. The energy functional $E_n[\psi_n]$ can be separated into two contributions

$$E_n[\psi_n] = F[\psi_n] + V_{ext}[\psi_n] \tag{2.1}$$

in which $F[\psi_n] = \langle\hat{T}_{el}\rangle_{el} + \langle\hat{V}_{el-el}\rangle_{el}$ is a *universal functional* of an interacting system of N electrons and $V_{ext}[\psi_n] = \langle\hat{V}_{ext}\rangle_{el}$ is a functional that depends on the ionic degrees of freedom in the problem. This allows one to see $V_{ext}[\psi_n]$ will *entirely* determine the properties of a particular system.

Hohenberg and Kohn *proved* in their seminal paper [12] that the energy, and more generally any ground state observable, is a *functional* of the *electron density* which is quite remarkable[1]. Specifically, they showed the external potential $V^{ext}(\vec{x})$ is completely *determined* by the electron density, hence the total energy is a unique functional of the electron density $n(\vec{x}) = \langle\hat{n}(\vec{x})\rangle_{el}$. This allowed for a rigorous mathematical framework to compute the total energy via a functional of a function of three variables, as opposed to 3^N, paving the way for an *ab initio* way of handling the *exact* interacting electron system. Furthermore, using the Rayleigh-Ritz variation principle, the ground state energy, and hence the *exact* ground state electron density, can exactly be determined by a global minimum of the energy functional.

[1]The theory proposed by Hohenberg and Kohn was proposed for $T = 0K$, but it was extended to finite temperatures by [111].

2.1.1 Hohenberg-Kohn Theorems

While it is obvious that for a system of N electrons, there is a map *from* the external potential $V^{ext}(\vec{x})$ *to* the ground state density $n_0(\vec{x})$ containing by solving the Schrödinger equation

$$V^{ext}(\vec{x}) \longrightarrow \psi_0(\vec{x}, \vec{x}_2 \dots \vec{x}_N) \longrightarrow n_0(\vec{x}) \tag{2.2}$$

where the ground state electron density is

$$n_0(\vec{x}) = \int d^3x_2 \dots \int d^3x_N |\psi_0(\vec{x}, \vec{x}_2 \dots \vec{x}_N)|^2, \tag{2.3}$$

it is by no means obvious the map is invertible; however, it is the case that this is indeed true. The proof of this claim relies on two theorems proposed by Hohenberg and Kohn put forth in 1964 known as the Hohenberg-Kohn theorems [12].

Hohenberg-Kohn Theorem 1: Given a Hamiltonian of the form of $\hat{H}_{el}$, there exists a one-to-one map between the external potential $V^{ext}(\vec{x})$ and the electron density $n(\vec{x}) \equiv \langle \hat{n}(\vec{x}) \rangle_{el}$. In other words, the external potential is *entirely* determined by the electron density.

The proof of the theorem is done in Appendix C. To ensure that the electron density entering this functional gives the exact electron density of N electrons, we must introduce a constraint to the total energy functional through a Lagrange multiplier[2] μ, so the functional that needs to be considered is

$$E[n] \longrightarrow E[n] - \mu \int d^3x n(\vec{x}). \tag{2.4}$$

[2]This Lagrange multiplier should not be interpreted as a chemical potential. It will be shown in the section on the Kohn-Sham equations the Lagrange multiplier will be replaced by the Kohn-Sham eigenvalues which also have no physical interpretation.

Hohenberg-Kohn Theorem 2: As a consequence of theorem 1, a *universal functional* of the electron density can be defined $E[n] \equiv \langle \hat{H}_{el} \rangle_{el}$. The *global* minimum of this functional yields the *exact* ground state energy E_0 and is determined by the *exact interacting* ground state density $n_0(\vec{x})$. The global minimum occurs at the first functional derivative of this functional through

$$\left.\frac{\delta E}{\delta n}\right|_{n=n_0} = \mu. \tag{2.5}$$

The proof of the theorem is shown in Appendix C.

Spin-density Functional Theory (sDFT)

The Hohenberg-Kohn theorems are of great importance because it gives a first-principles method of determining all ground state properties of a system of interacting electrons in the presence of an external scalar potential[3], however, it does not address the problem of magnetism in the ground state or if the system is in the presence of an external *static* magnetic field $\vec{B}^{ext}(\vec{x})$. Since the ground state density is a sum over the spin degree of freedom of the electrons

$$n_0(\vec{x}) = \sum_{\sigma} n_0^{\sigma}(\vec{x}), \tag{2.6}$$

there would be no way of determining if the ground state is magnetic using DFT à la Hohenberg and Kohn.

It was therefore determined that the Hohenberg-Kohn formalism of DFT needed to be extended to handle the material in the presence of a *static external* magnetic

[3]This external potential usually refers to the static potential of the ionic lattice, however it can consider the case where there is an external potential applied to the material, for example a voltage applied across the material.

field $\vec{B}^{ext}(\vec{x})$. Since magnetic fields can couple to both the orbital and spin degree of freedom, DFT needed to be extended to both of these cases. The former was proposed and proved by Giovanni Vignale and Mark Rosalt [112] referred to as current-density functional theory (cDFT), and the latter was introduced by Ulf Von Barth and Lars Hedin [113] called spin-density functional theory (sDFT). Here, I will introduce sDFT since magnetic fields couple stronger to the spin magnetization over the orbital magnetization[4], and this is the implementation I will need to discuss the antiferromagnetic ground state I use for the one-dimensional Mott insulating cuprates.

We are now considering an electronic Hamiltonian of the same form as equation 1.7

$$\hat{H}_{el} = \hat{T}_{el} + \hat{V}_{el-el} + \hat{V}_{ext} \tag{2.7}$$

where now the external potential adds a coupling of the external magnetic field to the magnetization from the spin degree of freedom i.e.

$$\hat{V}_{ext} = \int d^3x \left[V^{ext}(\vec{x})\hat{n}(\vec{x}) - \hat{\mathbf{m}}(\vec{x}) \cdot \vec{B}^{ext}(\vec{x}) \right]. \tag{2.8}$$

The theorems associated with the presence of an external magnetic field are slightly more restrictive than the original Hohenberg-Kohn theorems and are given below.

'Magnetic' Hohenberg-Kohn Theorem 1: Two different non-degenerate ground states $|\Psi_0\rangle$ and $|\Psi_0'\rangle$ from the set of *all* ground states resulting from Hamiltonians having the form of equation 2.7 using equation 2.8 always lead to two different sets of ground state densities $(n_0, \vec{m}_0)$ and $(n_0', \vec{m}_0')$ where at least one of the four density components differs. As a consequence, $|\Psi_0\rangle$ is a functional of n_0 and $\vec{m}_0$ so $|\Psi_0\rangle = |\Psi_0[n_0, \vec{m}_0]\rangle$.

The proof of the theorem is done in Appendix C. The second theorem for the magnetic case is similar to the second Hohenberg-Kohn theorem.

[4]This statement is made for the cuprates and the materials discused in this dissertation.

'Magnetic' Hohenberg-Kohn Theorem 2: As a consequence of 'magnetic' theorem 1, a *universal functional* of the electron density and magnetization density can be defined $E[n, \vec{m}] \equiv \langle \hat{H}_{el} \rangle_{el}$. The *global* minimum of this functional yields the *exact* ground state energy E_0 and is determined by the *exact interacting* ground state density $n_0(\vec{x})$ and magnetization $\vec{m}_0(\vec{x})$. The global minimum occurs at the first functional derivative of *four* functionals through

$$\left.\frac{\delta E}{\delta n}\right|_{n=n_0,\vec{m}=\vec{m}_0} = \mu \qquad \left.\frac{\delta E}{\delta \vec{m}}\right|_{n=n_0,\vec{m}=\vec{m}_0} = \vec{0}. \tag{2.9}$$

The proof of the theorem is done in Appendix C.

2.1.2 Kohn-Sham Equations

Hohenberg and Kohn provided the foundation to tackle the interacting electron system, but it did replace one problem with another. As previously mentionted, prior to Hohenberg-Kohn's DFT the problem stemmed from a computational dilemma of computing the eigenstates, however Hohenberg-Kohn's DFT relies on the knowledge of a functional form of the total energy $E[n]$. Very few functionals exist, such as in the Thomas-Fermi theory of screening [114], and their accuracy of application in DFT were often very poor. In 1965, Walter Kohn and Liu Sham proposed a method [13] to better construct the total energy functional. Kohn and Sham made the ansatz that the electron density could be computed via an *independent* electron orbital framework. Here, the electron density could be computed via the square of the modulus of these orbitals

$$n(\vec{x}) = \sum_{i}^{occ} |\phi_i(\vec{x})|^2, \tag{2.10}$$

where the summation is performed over all the occupied states to ensure the number of electrons are equal to the number of electrons of the system of interest. Here, the

dummy index i is a super index that represents the orbital type since DFT applies to a wide variety of interacting electronic systems; such as atoms, molecules, and condensed matter.

It is first convenient to recast the total energy functional given in equation 2.1 in the form

$$E[n] = T[n] + E_{el-el}[n] + E_{ext}[n]. \tag{2.11}$$

The kinetic energy functional $T[n]$, can be equivalently rewritten as $T[n] = T_s[n] + (T[n] - T_s[n])$, where $T_s[n]$ is the kinetic energy functional of the Kohn-Sham orbitals[5]

$$T_s[n] = -\frac{\hbar^2}{2m}\sum_i \int d^3x \phi_i^*(\vec{x})\nabla^2\phi_i(\vec{x}). \tag{2.12}$$

Additionally, the functional for the interaction among the electrons $V_{el-el}[n]$ can also be manipulated in a similar manner. Here the manipulation is to treat the direct interaction between electrons, also known as the Hartree interaction, exactly. It follows that the functional for the interaction electrons can be rewritten as $E_{el-el}[n] = E_{Hartree}[n] + (E_{el-el}[n] - E_{Hartree}[n])$, where the *nonlocal* Hartree functional $E_{Hartree}[n]$ takes the form

$$E_{Hartree}[n] = \frac{e^2}{2}\int d^3x \int d^3x' \frac{n(\vec{x})n(\vec{x}')}{|\vec{x} - \vec{x}'|}. \tag{2.13}$$

Using the above manipulations, the exact energy functional[6] $E[n]$ now has the form

$$E[n] = T_s[n] + E_{Hartree}[n] + E_{ext}[n] + (T[n] - T_s[n] + E_{el-el}[n] - E_{Hartree}[n]). \tag{2.14}$$

[5]It should be noted here that the form of $T_s[n]$ is an implicit functional of the density through the orbitals since the electron density $n(\vec{x})$ is not explicitly in this functional.

[6]Up to this point, the only assumption that has been made is the electron density can be computed via an independent electron framework.

Here, it is convenient to introduce the definition of the 'exchange-correlation' functional

$$E_{xc}[n] \equiv T[n] - T_s[n] + E_{el-el}[n] - E_{Hartree}[n] \tag{2.15}$$

which allows the total energy functional that needs to be minimized to take the more applicable form

$$E[n] = T_s[n] + E_{Hartree}[n] + E_{ext}[n] + E_{xc}[n]. \tag{2.16}$$

By using this construction, the constraint from the Lagrange multiplier μ to fix the electron density is replaced by N Lagrange multipliers

$$\mu \int d^3x n(\vec{x}) \rightarrow \sum_i^{occ} \varepsilon_i \int d^3x |\phi_i(\vec{x})|^2. \tag{2.17}$$

The variational condition in equation 2.5 is now replaced a functional derivative of Kohn-Sham orbitals given by

$$\delta E[n] = \sum_i \int d^3x \left(\frac{\delta E[n]}{\delta \phi_i^*(\vec{x})} \delta \phi_i^*(\vec{x}) + \frac{\delta E[n]}{\delta \phi_i(\vec{x})} \delta \phi_i(\vec{x}) \right) = 0. \tag{2.18}$$

Using the chain rule of functional differentiation, we can use the equivalent expression

$$\frac{\delta E[n]}{\delta \phi_i^*(\vec{x})} \delta \phi_i^*(\vec{x}) = \int d^3x' \frac{\delta E[n]}{\delta n(\vec{x}')} \frac{\delta n(\vec{x}')}{\delta \phi_i^*(\vec{x})} \delta \phi_i^*(\vec{x}) = 0. \tag{2.19}$$

After computing this functional derivative to equation 2.16, we obtain the variational equations

$$\sum_i \int d^3x \delta \phi_i^*(\vec{x}) \left[-\frac{\hbar^2}{2m} \vec{\nabla}^2 + v_s[n](\vec{x}) - \varepsilon_i \right] \phi_i(\vec{x}) = 0, \tag{2.20}$$

and a similar equation holds by interchanging $\phi_i(\vec{x})$ and $\phi_i^*(\vec{x})$. In equation 2.16, the Kohn-Sham potential $v_s[n](\vec{x})$ is a sum of the external potential, Hartree potential, and exchange correlation potential $v_s[n](\vec{x}) = V^{ext}[n](\vec{x}) + V^H[n](\vec{x}) + V^{xc}[n](\vec{x})$ where

the Hartree and exchange-correlation potential are given by

$$V^H[n](\vec{x}) = e^2 \int d^3x' \frac{n(\vec{x}')}{|\vec{x} - \vec{x}'|} \tag{2.21}$$

and

$$V^{xc}[n](\vec{x}) = \int d^3x' \frac{\delta E_{xc}[n(\vec{x})]}{\delta n(\vec{x}')} \tag{2.22}$$

respectively. Since the variations of the Kohn-Sham orbitals $\delta\phi_i^*(\vec{x})$ in equation 2.20 are arbitrary, the variational principle is satisfied by solving the *self-consistent* Kohn-Sham equations

$$\left[-\frac{\hbar^2}{2m}\vec{\nabla}^2 + v_s[n](\vec{x})\right]\phi_i(\vec{x}) = \varepsilon_i\phi_i(\vec{x}). \tag{2.23}$$

For the case of a spin-polarized system, equation 2.23 takes the form

$$\sum_{\sigma'}\left[-\frac{\hbar^2}{2m}\vec{\nabla}^2\delta_{\sigma\sigma'} + v_s^{\sigma\sigma'}[n_\uparrow, n_\downarrow](\vec{x})\right]\phi_{i\sigma'}(\vec{x}) = \varepsilon_{i\sigma}\phi_{i\sigma}(\vec{x}). \tag{2.24}$$

The Exchange Correlation Functional $E_{xc}[n]$

All the approximations that enter Kohn-Sham DFT are through the exchange-correlation functional $E_{xc}[n]$. It is possible to compute the electron-electron interaction functional $E_{el-el}[n] = E_{Hartree}[n] + (E_{el-el}[n] - E_{Hartree}[n])$ exactly [115] using coupling constant integration, however, it is not useful because a solution of the many-electron system must be known. Therefore, one needs to approximate $E_{xc}[n]$ to obtain a decent description of the *true* electron density. In general, $E_{xc}[n]$ is a *non-local* functional of the electron density, as in the Hartree functional, which takes the form

$$E_{xc}[n] = \int d^3x \int d^3x' n(\vec{x}) V_{xc}[n](\vec{x}, \vec{x}'). \tag{2.25}$$

However, the most popular ones are taken to be *local* functionals, i.e.

$$V_{xc}[n](\vec{x}, \vec{x}') = \delta(\vec{x} - \vec{x}')V_{xc}^{local}[n](\vec{x}). \tag{2.26}$$

The exchange-correlation potential $V_{xc}^{local}[n](\vec{x})$ are often parameterized by quantum Monte Carlo simulations of the homogeneous electron gas [116] where the electron density is uniform, i.e. $n(\vec{x}) \to \tilde{n}$, such as the local density approximation [117] (LDA) or including the spin polarization in the LSDA [118]. Since the electron density for real systems are not uniform, parameterizations based on the gradient of the density ∇n are invoked such as the generalized gradient approximation [119] (GGA).

For systems with d or f-like valence states, the LDA and GGA often 'fail' to treat this orbital content properly to produce an accurate electron density. To rectify this, the DFT+U [120] method is used which is an *orbital* dependent functional as opposed to a density functional, so it falls outside Kohn-Sham DFT. This is implemented by adding an *orbitally* dependent functional[7] in terms of a onsite interaction U and Hund's coupling J_H to equation 2.16 as

$$E_U[n_{m\sigma}] = \frac{1}{2}\left[U \sum_{mm'\sigma} n_{m\sigma} n_{m'-\sigma} + (U - J_H) \sum_{m \neq m'} n_{m\sigma} n_{m'\sigma}\right], \tag{2.27}$$

where $n_{m\sigma} = \langle n_{m\sigma} \rangle$ is the average value for a particular orbital content evaluated from the Kohn-Sham reference system. Upon taking the functional derivative, this adds a term to the Kohn-Sham equations

$$V_U^{m,\sigma}[n_{m\sigma}] = U \sum_{m'} n_{m-\sigma} + (U - J_H) \sum_{m' \neq m} n_{m'\sigma}. \tag{2.28}$$

However, this will double count contributions that are already in the Kohn-Sham potential. Therefore, one must attempt to subtract this contribution. One method is the 'around mean-field' [121] (AMF), which replaced the energy functional in equation

[7] Since the DFT+U functional is orbitally dependent functional, it falls outside the usual framework of Kohn-Sham DFT

2.27 with

$$E_U^{AMF}[n_{m\sigma}] = \frac{1}{2}\left[U\sum_{mm'\sigma}(n_{m\sigma}-\bar{n})(n_{m'-\sigma}-\bar{n}) + (U-J_H)\sum_{m\neq m'}(n_{m\sigma}-\bar{n})(n_{m'\sigma}-\bar{n})\right]. \tag{2.29}$$

However, it may be better to subtract the atomic contribution from the energy functional 2.27, and this is referred to as the 'fully localized limit' [122] (FLL). If we define the atomic contribution to the orbitals in terms of

$$N = \sum_\sigma N_\sigma \qquad N_\sigma = \sum_m n_{m\sigma}, \tag{2.30}$$

the double counting functional from the atomic limit is

$$E^{DC}[N_\sigma] = \frac{1}{2}\left[UN(N-1) - J_H N_\uparrow(N_\uparrow-1) - J_H N_\downarrow(N_\downarrow-1)\right], \tag{2.31}$$

so the DFT+U functional in the AMF double counting method is

$$E_U^{FLL}[n_{m\sigma}] = E_U[n_{m\sigma}] - E^{DC}[N_\sigma]. \tag{2.32}$$

2.1.3 Crystal Lattices, Bloch's Theorem, and the Bloch Basis

This section is a summary of that which can be found in most solid state physics textbooks such as [5, 6, 123]. Until this point, I have introduced DFT for an arbitrary system of interacting electrons. The focus of this dissertation is to simulate crystalline solids, so it will be beneficial to introduce a *good* basis for the Kohn-Sham orbitals. A perfect crystalline solid is modelled as a periodic repetition of a fundamental unit cell which may be comprised of one atom, such as aluminum or nickel, or a collection of atoms, such as Sr_2CuO_3 or $\alpha-RuCl_3$ where the latter is referred to as a lattice with a basis. To simulate the crystal, the unit cell generates a Bravais lattice by translation of an infinite number of lattice vectors $\{\vec{R}\}$ that tile the space indefinitely. Moreover, the lattice will appear the same irregardless from any unit cell. The lattice vectors

are expanded in *linear independent* primitive vectors[8] $\vec{a}_i$ in which any lattice vector can be expanded as integer multiples of, i.e. $\vec{R} = n_1\vec{a}_1 + n_2\vec{a}_2 + n_3\vec{a}_3$ where each n_i takes an integer value.

Like the case of the non-interacting electron gas with *continuous* space translational symmetry in a box of volume V with periodic boundary conditions whose eigenfunctions are planewaves $\psi_{\vec{k}}(\vec{x}) = \langle\vec{x}|\vec{k}\rangle = \frac{1}{\sqrt{V}}e^{-i\vec{k}\cdot\vec{x}}$, the eigenfunctions of a system with *discrete* space translational symmetry have a similar form. For simplicity, consider *one* electron in a periodic potential $v(\vec{x})$ which satisfies $v(\vec{x}+\vec{R}) = v(\vec{x})$. In the position basis, the time dependent Schrödinger equation has the usual form

$$\left(-\frac{\hbar^2}{2m}\nabla^2 + v(\vec{x})\right)\phi_i(\vec{x}) = \varepsilon_i\phi_i(\vec{x}). \tag{2.33}$$

Bloch's theorem states that the eigenfunctions of this system's quantum numbers are given by wave vectors $\vec{k}$ in the first Brillouin zone (1BZ) and spin index σ, i.e. $\phi_i(\vec{x}) \to \psi_{\vec{k}\sigma}(\vec{x})$ and $\varepsilon_i \to \varepsilon_{\vec{k}\sigma}$. The wave vectors $\vec{k}$ in 1BZ, can be expanded in reciprocal lattice basis vectors $\vec{b}_i$ as

$$\vec{k} = x_1\vec{b}_1 + x_2\vec{b}_2 + x_3\vec{b}_3 \tag{2.34}$$

which satisfy the orthogonality condition with the primitive lattice vectors $\vec{b}_i \cdot \vec{a}_j = 2\pi\delta_{ij}$.

Ideally, wave vectors $\vec{k}$ in the first Brillouin zone should be continuous variables, but this only holds in the limit where there are an infinite number of unit cells in the macrocrystal which is referred to as the *thermodynamic* limit. However, this is not feasible in practice due to finite computational resources. To mitigate this, one invokes periodic boundary conditions referred to as Born Van Karmen boundary conditions that satisfy

$$\psi_{\vec{k}\sigma}(\vec{x} + N_i\vec{a}_i) = \psi_{\vec{k}\sigma}(\vec{x}). \tag{2.35}$$

[8]The primitive vectors need to *span* the three dimensional space, however, they need not be orthonormal to each other.

Therefore, the expansion coefficients x_i of the reciprocal lattice basis vector $\vec{b}_i$ take the values

$$x_i = \frac{m_i}{N_i} \tag{2.36}$$

for integer value of m_i.

Like the Bravais lattice in real space, there exists a Bravais lattice in reciprocal space that is spanned by reciprocal lattice vectors $\vec{G}_i$ that satisfy the condition

$$e^{i\vec{G}\cdot(\vec{x}+\vec{R})} = e^{i\vec{G}\cdot\vec{x}}, \tag{2.37}$$

which is equivalent to the condition $\vec{G}\cdot\vec{R} = 2\pi n$ where n is an integer. Formally, Bloch's theorem states the eigenfunctions transform under discrete translation by a lattice vector $\vec{R}$ as

$$\psi_{\vec{k}\sigma}(\vec{x}+\vec{R}) = e^{i\vec{k}\cdot\vec{R}}\psi_{\vec{k}\sigma}(\vec{x}), \tag{2.38}$$

which is equivalent to the eigenfunctions having the form $\psi_{\vec{k}\sigma}(\vec{x}) = e^{i\vec{k}\cdot\vec{x}}u_{\vec{k}\sigma}(\vec{x})$ such that the periodic part u satisfies $u_{\vec{k}\sigma}(\vec{x}+\vec{R}) = u_{\vec{k}\sigma}(\vec{x})$. If there are several *independent* electrons, a band index j for each electron in the primitive unit cell must be added to the quantum numbers, i.e. $\psi_{\vec{k}\sigma}(\vec{x}) \to \psi_{\vec{k}j\sigma}(\vec{x})$ and $\varepsilon_{\vec{k}\sigma} \to \varepsilon_{\vec{k}j\sigma}$.

The Full-Potential Linearized Augmented Plane Wave (FP-LAPW) Basis

The eigenfunctions of an independent electron in a periodic potential are Bloch states as mentioned in the previous section. We therefore must choose a method to calculate them. This can either be done through a numerical grid or expanding in a complete basis set[9]. One of the most obvious choices would be to use a plane wave basis. This however requires an extremely large number of plane waves for convergence to describe the Bloch states near the ions in the crystal. The pseudopotential method [124–129] was introduced where the core and semi-core

[9]Sometimes the Bloch states are computed through fitting with several Gaussians, however this is not a complete basis set.

electronic states generate an effective potential that the valence electrons are solved with. This allows the $1/|\vec{R}|$ Coulombic potential felt by the electrons to feel a rather smoothly varying potential allowing convergence in a reasonable size of a plane wave basis. Other bases that are used are the linearized muffin-tin orbital (LMTO) [130, 131] and the linear combination of atomic orbital (LCAO) [132] basis.

While the psedupotential method allows the treatment in a plane wave basis in which integrals can be computed analytically, it has a few downfalls which makes it not an ideal choice to use. First, it requires the necessity to generate these pseudopotentials which one needs to be an expert in. Second, it does not allow a treatment of the semicore states which turn out to play an important role when calculating the self-energy for Green function methods [133]. To mitigate this, the full-potential linearized augmented plane wave basis was introduced to compute the Bloch functions. This involves dividing real space into two regions; an atomic sphere (AS) centered around each of the atoms in the unit cell, and an interstitial (IS) region which is the area of space outside these atomic spheres. Inside the atomic spheres, atomic-like basis functions are used and in the interstitial region, a plane wave basis is used. The form of the LAPW basis functions are of the form

$$\psi_{\vec{k}j\sigma}(\vec{x}) = \begin{cases} \sum_{\alpha} \sum_{lm} \sum_{\nu=1}^{N_l^{\alpha}} A_{lm\nu}^{\alpha,\sigma j}(\vec{k}) u_{l\nu}^{\alpha}(x) Y_{lm}(\hat{\mathbf{x}}), & \text{if } x \in \text{AS} \\ \frac{1}{\sqrt{V_{BvK}}} \sum_{\vec{G}} C_{\vec{G}}^{\sigma j}(\vec{k}) e^{(\vec{k}+\vec{G})\cdot\vec{x}}, & \text{if } x \in \text{IS} \end{cases}$$

where α represents the atomic sphere inside the unit cell, ν represents the type of APW basis function which corresponds to the usual APW basis function, local orbital (lo), Local orbital (LO), etc., $u_{l\nu}^{\alpha}(x)$ is the radial function, and $Y_{lm}(\hat{\mathbf{x}})$ represent real spherical harmonics. For a detailed description of the method, reference [134] is very informative. It is worthwhile mentioning that the contribution from the atomic spheres to the charge fluctuation matrix elements is the most expensive part of the

calculation of response functions which require high-performance supercomputing resources to compute for complex materials with several atoms in the unit cell.

2.1.4 Wannier Basis

While the Bloch basis is the ideal choice for a single-particle basis for a periodic system since they are the *eigenfunctions* of a single-particle perfectly periodic Hamiltonian, it is not always the best basis for expanding the Hamiltonian. This is indeed the case for a correlated-electron materials, where the local interactions between electrons must be treated as accurately as possible. It is convenient to introduce the *Wannier basis*, first introduced by Gregory Wannier in 1937 [107], which act as localized orbitals centered about a particular unit cell. For a unit cell located at position $\vec{R}$, the Wannier orbital is obtained from the Bloch functions via the transformation

$$w_{n\sigma}(\vec{x}-\vec{R}) \equiv \langle \vec{x}|W_{n\sigma}(\vec{R})\rangle = \frac{1}{\sqrt{N_{BvK}}}\sum_{\vec{k}} e^{-i\vec{k}\cdot\vec{R}} \sum_{j} a_{nj\sigma}(\vec{k})\psi_{\vec{k}j\sigma}(\vec{x}), \tag{2.40}$$

where n is a label that distinguishes the type of Wannier orbital.

The Bloch states are defined up to a phase since they are *eigenstates* of a Hermitian operator. This means there is no impact on the physics under the 'gauge' transformation $|\vec{k}j\sigma\rangle \rightarrow e^{i\Theta_{j\sigma}(\vec{k})}|\vec{k}j\sigma\rangle$. Therefore, the Wannier functions are not *uniquely* defined, and this ambiguity is absorbed into the expansion matrix $a_{nj\sigma}(\vec{k})$. Sixty years after Wannier functions were first introduced, physics and solid state chemists started getting serious about computing these quantities for real materials. Nicola Marzari and David Vanderbilt proposed *choosing* a gauge by the criterion of localizing the Wannier functions as much as possible [135]. This was done by minimizing the variance, or spread of the orbital Ω defined as

$$\Omega \equiv \sum_{n\sigma\vec{R}} \left(\langle W_{n\sigma}(\vec{R})|\,\hat{\mathbf{x}}\,|W_{n\sigma}(\vec{R})\rangle \right)^2 - \langle W_{n\sigma}(\vec{R})|\,\hat{\mathbf{x}}^2\,|W_{n\sigma}(\vec{R})\rangle \tag{2.41}$$

which was deemed to be the best 'gauge' due to being tailored for discrete lattice models.

Since the Wannier functions need to span a subspace of the entire Hilbert space, they should satisfy the orthonormality condition

$$\langle W_{n\sigma}(\vec{R})|W_{m\sigma'}(\vec{R}')\rangle = \int d^3x w^*_{n\sigma}(\vec{x}-\vec{R})w_{m\sigma'}(\vec{x}-\vec{R}') = \delta_{\sigma\sigma'}\delta_{nm}\delta_{\vec{R}\vec{R}'}. \tag{2.42}$$

The Wannier functions *should* also satisfy the *closure* relation within the subspace, which is stated mathematically as

$$\sum_{n\sigma\vec{R}} |W_{n\sigma}(\vec{R})\rangle \langle W_{n\sigma}(\vec{R})| = \hat{I}_{subspace} \tag{2.43}$$

To accomplish this, the transformation from the Bloch basis to the Wannier basis must be *unitary*. This translates mathematically to the transformation in equation 2.40 to be invertible meaning

$$\psi_{\vec{k}j\sigma}(\vec{x}) = \frac{1}{\sqrt{N_{BvK}}} \sum_{\vec{R}} e^{i\vec{k}\cdot\vec{R}} \sum_n c_{jn\sigma}(\vec{k}) W_{n\sigma}(\vec{x}-\vec{R}) \tag{2.44}$$

where the transformation matrices are *unitary* transformations of one another

$$c_{jn\sigma}(\vec{k}) = a^*_{nj\sigma}(\vec{k}). \tag{2.45}$$

If this condition holds, the Wannier functions will *exactly* reproduce the low energy band structure from the Bloch states that were used in the projection.

$$\hat{H}^t_{KS} = \sum_\sigma \sum_{nm} \sum_{\vec{R}\vec{R}'} \langle W_{n\sigma}(\vec{R})|\hat{h}^t_{KS}|W_{m\sigma}(\vec{R}')\rangle \, d^\dagger_{n\sigma\vec{R}} d_{m\sigma\vec{R}'} \tag{2.46}$$

$$= \frac{1}{N_{BvK}} \sum_{\sigma} \sum_{nm} \sum_{\vec{R}\vec{R}'} \sum_{\vec{k}\vec{k}'}^{1BZ} e^{i\vec{k}\cdot\vec{R}} e^{-i\vec{k}'\cdot\vec{R}'} \sum_{jj'} a^*_{jn\sigma}(\vec{k}) a_{mj'\sigma}(\vec{k}') \underbrace{\langle \vec{k} j\sigma | \hat{h}^t_{KS} | \vec{k}' j'\sigma \rangle}_{\delta_{\vec{k}\vec{k}'}\delta_{jj'}\varepsilon_{\vec{k}j\sigma}} d^\dagger_{n\sigma\vec{R}} d_{m\sigma\vec{R}'} \tag{2.47}$$

$$= \frac{1}{N_{BvK}} \sum_{\sigma} \sum_{nm} \sum_{\vec{R}\vec{R}'} \sum_{\vec{k}}^{1BZ} e^{i\vec{k}\cdot(\vec{R}-\vec{R}')} \sum_{j} a^*_{jn\sigma}(\vec{k}) a_{mj\sigma}(\vec{k}) \varepsilon_{\vec{k}j\sigma} d^\dagger_{n\sigma\vec{R}} d_{m\sigma\vec{R}'}. \tag{2.48}$$

Using the relations

$$d^\dagger_{n\sigma\vec{R}} = \frac{1}{\sqrt{N_{BvK}}} \sum_{\vec{k}_1}^{1BZ} e^{-i\vec{k}_1\cdot\vec{R}} \sum_{j_1} a_{nj_1\sigma}(\vec{k}_1) d^\dagger_{\vec{k}_1 j_1\sigma} \tag{2.49}$$

and

$$d_{n\sigma\vec{R}} = \frac{1}{\sqrt{N_{BvK}}} \sum_{\vec{k}_2}^{1BZ} e^{i\vec{k}_2\cdot\vec{R}'} \sum_{j_2} a^*_{j_2 m\sigma}(\vec{k}_2) d_{\vec{k}_2 j_2\sigma}, \tag{2.50}$$

then equation 2.48 becomes

$$\frac{1}{(N_{BvK})^2} \sum_{\sigma} \sum_{\vec{k}\vec{k}_1\vec{k}_2}^{1BZ} \sum_{nm} \sum_{\vec{R}} e^{i(\vec{k}-\vec{k}_1)\cdot\vec{R}} \sum_{\vec{R}'} e^{-i(\vec{k}-\vec{k}_2)\cdot\vec{R}'} \sum_{jj_1j_2} a^*_{jn\sigma}(\vec{k}) a_{nj_1\sigma}(\vec{k}_1)$$

$$\times \varepsilon_{\vec{k}j\sigma} a_{j_2 m\sigma}(\vec{k}_2) a^*_{mj\sigma}(\vec{k}) d^\dagger_{\vec{k}_1 j_1\sigma} d_{\vec{k}_2 j_2\sigma}. \tag{2.51}$$

We can now use the identity

$$\sum_{\vec{R}} e^{i(\vec{k}-\vec{k}_1)\cdot\vec{R}} = N_{BvK}\delta_{\vec{k}\vec{k}_1} \qquad \sum_{\vec{R}'} e^{-i(\vec{k}-\vec{k}_2)\cdot\vec{R}} N_{BvK}\delta_{\vec{k}\vec{k}_2} \tag{2.52}$$

to obtain the result

$$\hat{H}_{KS} = \sum_{\sigma} \sum_{\vec{k}}^{1BZ} \sum_{j} \sum_{nm} \sum_{j_1j_2} a^*_{jn\sigma}(\vec{k}) a_{nj_1\sigma}(\vec{k}) a^*_{j_2 m\sigma}(\vec{k}) a_{mj\sigma}(\vec{k}) \varepsilon_{\vec{k}j\sigma} d^\dagger_{\vec{k}j_1\sigma} d_{\vec{k}j_2\sigma}. \tag{2.53}$$

We can use the relations

$$a^*_{jn\sigma}(\vec{k}) a_{nj_1\sigma}(\vec{k}) = \delta_{jj_1} a^*_{jn\sigma}(\vec{k}) a_{nj\sigma}(\vec{k}) \tag{2.54}$$

and

$$a^*_{j_2m\sigma}(\vec{k})a_{mj\sigma}(\vec{k}) = \delta_{jj_2}a^*_{jm\sigma}(\vec{k})a_{mj\sigma}(\vec{k}) \tag{2.55}$$

to simplify equation 2.53 to

$$\hat{H}_{KS} = \sum_{\sigma}\sum_{\vec{k}}^{1BZ}\sum_{j}\varepsilon_{\vec{k}j\sigma}d^{\dagger}_{\vec{k}j\sigma}d_{\vec{k}j\sigma}\sum_{nm}\left[a^*_{jn\sigma}(\vec{k})a_{nj\sigma}(\vec{k})a^*_{jm\sigma}(\vec{k})a_{mj\sigma}(\vec{k})\right]. \tag{2.56}$$

If the Wannier orbitals are related to the Bloch states through a unitary transformation, the quantitiy

$$\sum_{nm}\left[a^*_{jn\sigma}(\vec{k})a_{nj\sigma}(\vec{k})a^*_{jm\sigma}(\vec{k})a_{mj\sigma}(\vec{k})\right] \tag{2.57}$$

will be unity for the bands used in the projection for each wave vector in the first Brillouin zone, but if they are not related via a unitary projection, then this quantity will give a number which differs from one which will create fake eigenvalues. This can be seen in the right panel of figure 2.1.

Constructing the Wannier Functions

To construct Wannier functions, one must define: a) an energy window[10] to project the Wannier orbitals and b) the 'orbital' character that is desired for said projection. The method used here is using the local orbitals defined strictly in the atomic spheres of the FL-LAPW basis functions first introduced by W. Ku et al. [136].

First, I will discuss the single-site projection. This involves projecting a local orbital with a particular symmetry corresponding to a particular (real) spherical harmonic which is labelled by $|\phi_n\rangle$. Then a non-orthogonal Wannier orbital $|\tilde{W}_{n\sigma}(\vec{R})\rangle$

[10]The energy window we use is defined by including a desired number of bands to be included in the projection. One of the goals my advisor Professor Adolfo Eguiluz and myself desired was to eliminate the energy window dependence of the Wannier orbital projection. This will be discussed when introducing our new method for constructing Wannier functions.

is computed through the relation

$$|\tilde{W}_{n\sigma}(\vec{R})\rangle = \frac{1}{\sqrt{N_{BvK}}} \sum_{\vec{k}} e^{-i\vec{k}\cdot\vec{R}} \sum_{j} \underbrace{\tilde{a}_{nj\sigma}(\vec{k})}_{\langle \vec{k}j\sigma|\phi_n\rangle} |\vec{k}j\sigma\rangle \,. \tag{2.58}$$

To require orthonormality 2.42, we take the inner product of the Wannier orbitals,

$$\langle \tilde{W}_{n\sigma}(\vec{R})|\tilde{W}_{m\sigma'}(\vec{R}')\rangle = \frac{1}{N_{BvK}} \sum_{\vec{k}\vec{k}'}^{1BZ} e^{i\vec{k}\cdot\vec{R}} e^{-i\vec{k}'\cdot\vec{R}'} \sum_{jj'} \tilde{a}^{*}_{jn\sigma}(\vec{k})\tilde{a}_{mj'\sigma'}(\vec{k}') \underbrace{\langle \vec{k}j\sigma|\vec{k}'j'\sigma'\rangle}_{\delta_{\vec{k}\vec{k}'}\delta_{jj'}\delta_{\sigma\sigma'}} \tag{2.59}$$

$$= \delta_{\sigma\sigma'} \frac{1}{N_{BvK}} \sum_{\vec{k}}^{1BZ} e^{i\vec{k}\cdot(\vec{R}-\vec{R}')} \sum_{j} \tilde{a}^{*}_{jn\sigma}(\vec{k})\tilde{a}_{mj\sigma}(\vec{k}). \tag{2.60}$$

Since $\sum_{\vec{k}}^{1BZ} e^{i\vec{k}\cdot(\vec{R}-\vec{R}')} = N_{BvK}\delta_{\vec{R}\vec{R}'}$, we would require that the overlap matrix $O_{mn}(\vec{k}) = \sum_j \tilde{a}^{*}_{jn\sigma}(\vec{k})\tilde{a}_{mj\sigma}(\vec{k})$ to be unity. To do so, we use the Löwdin orthonormalization procedure [137]. This entails redefining the matrix of the transformation using the inverse 'square root'[11] of the overlap matrix $\mathbf{S}(\vec{k}) = \mathbf{O}^{-\frac{1}{2}}(\vec{k})$. We therefore use a new definition

$$|W_{n\sigma}(\vec{R})\rangle \equiv \frac{1}{\sqrt{N_{BvK}}} \sum_{\vec{k}} e^{-i\vec{k}\cdot\vec{R}} \sum_{jn'} \tilde{a}_{n'j\sigma} S_{n'n}(\vec{k}) \, |\vec{k}j\sigma\rangle \,. \tag{2.61}$$

By taking the inner product between two Wannier orbitals using the new definition in equation 2.61,

$$\langle W_{n\sigma}(\vec{R})|W_{m\sigma'}(\vec{R}')\rangle \tag{2.62}$$

$$= \frac{1}{N_{BvK}} \sum_{\vec{k}\vec{k}'}^{1BZ} e^{i\vec{k}\cdot\vec{R}} e^{-i\vec{k}'\cdot\vec{R}'} \sum_{jj'} \sum_{n'm'} S^{*}_{nn'}(\vec{k})\tilde{a}^{*}_{jn\sigma}(\vec{k})\tilde{a}_{mj'\sigma'}(\vec{k}') S_{m'm}(\vec{k}') \underbrace{\langle \vec{k}j\sigma|\vec{k}'j'\sigma'\rangle}_{\delta_{\vec{k}\vec{k}'}\delta_{jj'}\delta_{\sigma\sigma'}} \tag{2.63}$$

[11] In general, it would be very difficult to take the square root of the matrix. To do so, we make a change of basis to diagonal form and take the inverse square root of each matrix element

$$= \delta_{\sigma\sigma'} \frac{1}{N_{BvK}} \sum_{\vec{k}}^{1BZ} e^{i\vec{k}\cdot(\vec{R}-\vec{R}')} \sum_{j} \sum_{n'm'} S^{*}_{nn'}(\vec{k}) \tilde{a}^{*}_{jn\sigma}(\vec{k}) \tilde{a}_{mj'\sigma'}(\vec{k}') S_{m'm}(\vec{k}'). \tag{2.64}$$

The quantity

$$\sum_{j} \sum_{n'm'} S^{*}_{nn'}(\vec{k}) \tilde{a}^{*}_{jn\sigma}(\vec{k}) \tilde{a}_{mj'\sigma'}(\vec{k}') S_{m'm}(\vec{k}') = \left(O^{-\frac{1}{2}}(\vec{k}) O(\vec{k}) O^{-\frac{1}{2}}(\vec{k}) \right)_{nm} = \delta_{mn}, \tag{2.65}$$

so we obtain the orthonormality condition

$$\langle W_{n\sigma}(\vec{R}) | W_{m\sigma'}(\vec{R}') \rangle = \delta_{\sigma\sigma'} \delta_{nm} \delta_{\vec{R}\vec{R}'}. \tag{2.66}$$

We can therefore equate the expansion matrix $a_{\sigma}(\vec{k})$ in equation 2.40 with the result in equation 2.61 to obtain the result

$$a_{nj\sigma}(\vec{k}) = \sum_{n'} \tilde{a}_{n'j\sigma} S_{n'n}(\vec{k}) \tag{2.67}$$

It is not necessarily the case that Wannier functions need to be projected on just one site and for one particular orbital. In chapter 3 and in figure 2.2 it is required that a molecular orbital picture is used to produce the orbitals in the low energy Hilbert space. For this type of projection, the local orbital $|\phi_n\rangle$ is replaced by a unitary matrix that sums over multilple orbitals and lattice sites, i.e.

$$|\phi_n\rangle = \sum_{n'} U_{nn'} |\phi_{n'}\rangle \tag{2.68}$$

which is put into equation 2.59 to obtain an orthonormal basis.

Wannier Functions for Entangled Band Structure

For certain materials, it is not trivial to satisfy the condition of unitarity as in equation 2.44. This is a consequence of having undesired bands crossing within the

desired energy window which will be used to project the Wannier functions and is referred to as an *entangled* band structure. This causes the transformation matrix $a_{nj\sigma}(\vec{k})$ to be rectangular for some are all of the wave vectors in the first Brillouin zone. Since rectangular matrices are not invertible, this causes the eigenvalues in equation 2.44 to produce eigenvalues which do not correspond to the eigenvectors used in the projection. This was an issue that was realized in the Wannier orbital community. To mitigate this, Marzari et al. proposed a 'disentanglement' procedure [138] to develop a method to fix this issue that relied on two energy windows, a frozen larger energy window and a smaller wave vector dependent energy window. While this was able to reproduce the band structure better than before, it still was not 100% successful as seen for the case of La_2CuO_4 in the right panel of figure 2.1.

In the left panel of figure 2.1, I showed the result which an anti-bonding Wannier[12] orbital was exactly disentangled from the rest of the Hilbert space using the method we proposed discussed in the next paragraph. To do so involved developing a new procedure of disentanglement developed by my advisor and myself. At the heart of the method, we had to enforce the matrices $a_{nj\sigma}(\vec{k})$ were *exactly* square matrices for each wave vector in the first Brillouin zone and each spin projection. This translates to choosing the same number of bands j as orbitals we want to project n. In addition to the matrices $\tilde{a}_{nj\sigma}(\vec{k})$ being square, we also want to not rely on energy dependent windows for the Wannier projections since we did not want to sacrifice poorly projected Wannier orbitals for the sake of obtaining a unitary transofrmation. We desire this because a Wannier orbital can faithfully reproduce the band structure it was derived from, but it may be a bit too 'man-made' in the sense that it will pick up band indices that are not a good depiction of the orbital that is being produced.

To satisfy the unitarity of transformation, we adopt the following procedure. First, we compute and tabulate all the overlaps $\tilde{a}_{nj\sigma}(\vec{k})$ before the orthonormalization procedure for all the orbitals we desire to project, all the band indices, and all the

[12] I have glossed over the details describing this orbital. Since the focus of this thesis is the one dimensional cuprates as opposed to the two dimensional cuprates, extensive details will be introduced in section 3.1.3 that shed light on what I had done here.

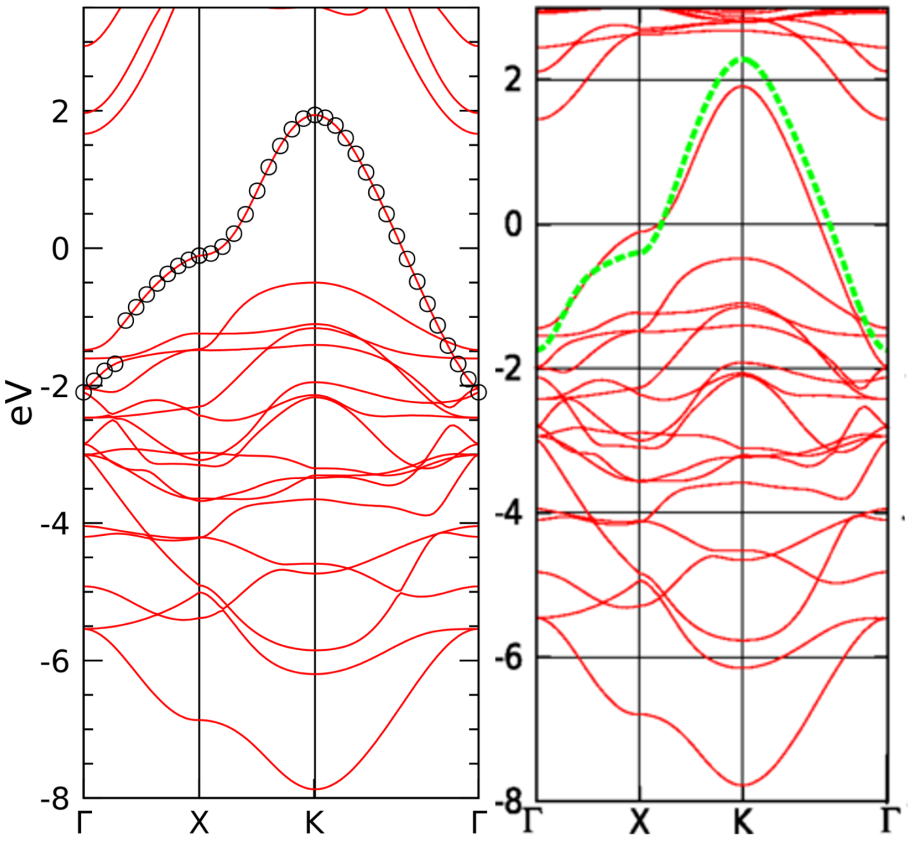

Figure 2.1: Disentanglement for La_2CuO_4. Left: Disentanglement procedure using our implementation for an antibonding orbital. Right: Disentanglement produced using procedure in reference [138]. Figure reproduced from reference [139]

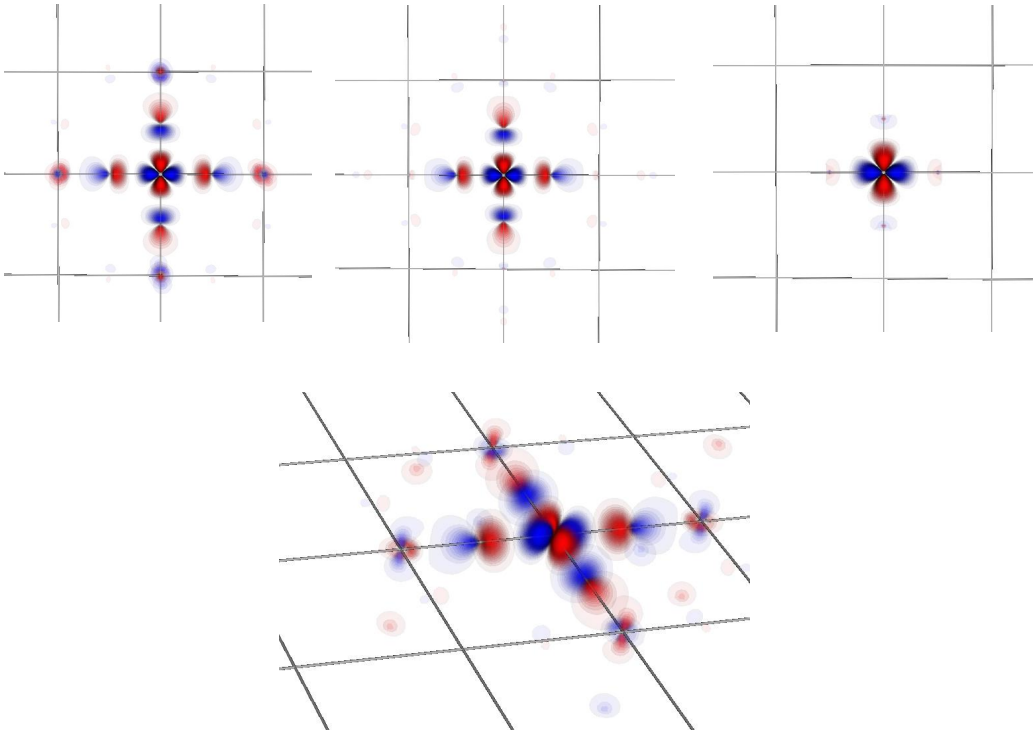

Figure 2.2: Wannier orbitals for La_2CuO_4. Top left: antibonding Wannier orbital in a Hilbert space of one orbital. Top middle: antibonding Wannier orbital in a Hilbert space of two e_g orbitals. Top right: antibonding Wannier orbital in a Hilbert space of seventeen orbitals including all the copper d and oxygen p orbitals. Bottom: Different view of antibonding Wannier orbital in a Hilbert space of one orbital.

wave vectors in the first Brillouin zone. Next, for *each* orbital we choose the band index, which we refer to as the locus for $j_{max}(\vec{k})$, that maximizes the overlap $|\tilde{a}_{nj\sigma}(\vec{k})|$. This allows us to *define* a band associated with a given orbital. From there, we include all of the loci of $j_{max}(\vec{k})$ to be included in the projection. If there is a *degeneracy* associated with two or more orbitals having the same $j_{max}(\vec{k})$, then we choose the second largest $j_{max}(\vec{k})$ to define the loci. Once all the loci of $j_{max}(\vec{k})$ are chosen, then we put them into the Löwdin orthonormalization procedure to produce our exactly entangled Wannier orbitals. As a success case, I have shown the corresponding band associated with the locus of $j_{max}(\vec{k})$ for an antibonding Wannier orbital for La_2CuO_4 in the left panel of figure 2.1. I showed the corresponding contour plots for this orbital in figure 2.2. I also showed contour plots in figure 2.2 of how this orbital is modified when it is part of a larger Hilbert space.

It is important to note that this development can cause difficulties with a tight-binding parameterization of the band structure due to a discontinuity in energy space from choosing the locus of $j_{max}(\vec{k})$ as seen going from the Γ to X path in the left panel of figure 2.1. This results in spurious oscillations in the band dispersion for wave vectors that were not in the $\vec{k}$-grid used in the definition of the Wannier orbitals from equation 2.40. However, this oscillation effect is reduced when the number of unit cells in the calculation are increased which increases the density of the grid in the first Brillouin zone. Therefore, we can conclude that our method is not one intended for *interpolating* band structure, however that is not the purpose of our method. Our method is built out of the *necessity* to *exactly* partition the Hilbert space into two disjoint subspaces to be used in downfolding time-dependent density functional theory which is introduced in section 2.2.3. This method could further adapted to fix this problem by using a measure to choose $j_{max}(\vec{k})$ to also consider smoothness in energy space as one of the criteria while strictly enforcing unitarity. Using this criteria may also give insight into which orbitals need to be added to the Hilbert space if the low-energy Hilbert space is not large enough to capture all the desired spectra.

2.2 Time-Dependent Density Functional Theory (TDDFT)

The hallmark theory for the ground state, density functional theory, is one of the most widely used theories in condensed matter physics to this date. However, there is an experimental dilemma that it is *impossible* to measure the ground state of a quantum mechanical system. The ground state of the material is often *inferred* through measuring energy differences from the excited states, and then compare with its agreement with a theoretical calculation. Therefore, an extension to DFT where a *time-dependent* potential is needed so the excited state spectrum can be inferred through the linear response function by using the Lehmann representation, which has resonances at the excited energies measured from the ground state. Time-dependent density functional theory (TDDFT) has its origin in the work by E.K.U gross and Erich Runge [14] twenty years after the original ground state theorems were proposed. The theory relies on the use of the Runge-Gross theorem and requires a more elegant theorem since the notion of a Hamiltonian giving a ground state energy is no longer valid with time-dependence and one must work in the Lagrangian formalism.

2.2.1 Runge-Gross Theorem

Runge-Gross Theorem: There is a one-to-one correspondence between the time-dependent potential[13] $V^{ext}(\vec{x},t)$ with the time-dependent electron density $n(\vec{x},t)$, *given* that the system was initially in a state $|\psi_0\rangle$.

The proof of this theorem is given in appendix D. It should be pointed out that the theorem requires the knowledge of the initial state $|\psi_0\rangle$ since there are cases where two different time dependent potentials $V^{ext,1}(\vec{x},t)$ and $V^{ext,2}(\vec{x},t)$ yield the same

[13] It is important to note that the uniqueness of the external potentials must differ by more than just a time dependent factor.

time-dependent density $n(\vec{x},t)$ given two different initial ground states. Throughout my thesis, I restrict the work within the linear response formalism of TDDFT.

2.2.2 Linear Response theory of TDDFT

In the presence of a time-dependent external potential $V^{ext}(\vec{x},t)$, the *exact* time-dependent charge density can be expanded in a Taylor series in powers of the potential

$$n(\vec{x},t) = n_0(\vec{x}) + \int_{-\infty}^{\infty} dt' \int d^3x' \chi_{nn}(\vec{x},\vec{x}';t-t')V^{ext}(\vec{x}',t')$$

$$+ \int_{-\infty}^{\infty} dt_1 \int_{-\infty}^{\infty} dt_2 \int d^3x_1 \int d^3x_2 \chi^{(2)}(\vec{x},\vec{x}_1,\vec{x}_2;t,t_1,t_2)V^{ext}(\vec{x}_1,t_1)V^{ext}(\vec{x}_2,t_2) + \ldots \tag{2.69}$$

in which the linear response function χ_{nn} is given through a functional differentiation of the external potential

$$\chi_{nn}(\vec{x},\vec{x}';t-t') = \left.\frac{\delta n(\vec{x},t)}{\delta V^{ext}(\vec{x}',t')}\right|_{n(\vec{x},t)=n_0(\vec{x})}. \tag{2.70}$$

It is important to note that the linear response function is *entirely* a quantity that has properties acquired *only* from the material properties and does not involve changes due to the external potential.

This formalism is especially convenient when the external potential weakly couples to the electron density which allows for linear response to be a good approximation of the *induced* electron density $\delta n(\vec{x},t) \equiv n(\vec{x},t) - n_0(\vec{x})$. This gives us the usual linear response equation[14]

$$\delta n(\vec{x},t) = \int_{-\infty}^{\infty} dt' \int d^3x' \chi_{nn}(\vec{x},\vec{x}';t-t')\delta V^{ext}[n](\vec{x}',t'). \tag{2.71}$$

[14] I use $\delta V^{ext}(\vec{x}',t')$ instead of $V^{ext}(\vec{x}',t')$ to indicate that the potential is weakly coupled to the system.

Invoking the Runge-Gross theorem, I can *equivalently* write equation 2.71 in terms of the so-called Kohn-Sham density response function[15] denoted as χ_0, and the *time-dependent* Kohn-Sham potential $\delta V^{KS}[n](\vec{x}', t')$ as

$$\delta n(\vec{x}, t) = \int_{-\infty}^{\infty} dt' \int d^3x' \chi_0(\vec{x}, \vec{x}'; t - t') \delta V^{KS}[n](\vec{x}', t'). \tag{2.72}$$

The response χ_0 is *not* a true response function and will *not* have poles at the true excitation energies of the system, but rather it will have excitations determined by the Kohn-Sham band structure—*which has no physical meaning.* Similarly, $\delta V^{KS}[n](\vec{x}, t)$ is not the external potential that the electrons respond to, but is the *total* potential that the Kohn-Sham electrons will respond to. The time-dependent Kohn Sham potential will thus be a sum of contributions from the time-dependent external potential, Hartree potential, and exchange-correlation potential, $\delta V^{KS}[n](\vec{x}, t) = \delta V^{ext}[n](\vec{x}, t) + \delta V^{H}[n](\vec{x}, t) + \delta V^{xc}(\vec{x}, t)$. It is important to note here that since the Hartree and exchange-correlation potentials are functionals of the electron density, they obtain a time-dependence because the electron density acquires time-dependence, which is similar to the case for mean field response[16]. By invoking the Runge-Gross theorem again, we can differentiate with respect to the electron density, so

$$\begin{aligned}\delta V^{KS}[n](\vec{x}, t) = \delta V^{ext}[n](\vec{x}, t) + \int_{-\infty}^{\infty} dt' \int d^3x' \frac{\delta V^{H}[n](\vec{x}, t)}{\delta n(\vec{x}', t')} \delta n(\vec{x}', t') \\ + \int_{-\infty}^{\infty} dt' \int d^3x' \frac{\delta V^{xc}[n](\vec{x}, t)}{\delta n(\vec{x}', t')} \delta n(\vec{x}', t').\end{aligned} \tag{2.73}$$

[15] It is very important that χ_0 to not be confused with the irreducible polarization function from many-body theory.

[16] It is important to make a distinguish something here. Despite the TDDFT equation taking the form of a mean field response, this analogy is completely wrong. Mean field response is an approximation of the true response, while the treatment in TDDFT is an *exact* method for calculating the *true* density response of the system

Upon performing the functional differentiation, the induced Kohn-Sham potential becomes

$$\delta V^{KS}[n](\vec{x},t) = \delta V^{ext}[n](\vec{x},t) + \int_{-\infty}^{\infty} dt' \int d^3x' \frac{e^2}{|\vec{x}-\vec{x}'|}\delta(t-t')\delta n(\vec{x}',t')$$

$$+ \int_{-\infty}^{\infty} dt' \int d^3x' f^{xc}(\vec{x},\vec{x}';t-t')\delta n(\vec{x}',t'). \tag{2.74}$$

Here, I have introduced here the exchange-correlation kernel, $f^{xc}(\vec{x},\vec{x}';t-t') \equiv \delta V^{xc}[n](\vec{x},t)/\delta n(\vec{x}',t')$, which includes information about the 'memory' of the system that will arise due to the time-dependence of this potential[17]. Using equation 2.71, this can be expanded in terms of the density response function

$$\delta V^{KS}[n](\vec{x},t) = \delta V^{ext}[n](\vec{x},t)$$

$$+ \int_{-\infty}^{\infty} dt' \int d^3x' \int d^3x'' \frac{e^2}{|\vec{x}-\vec{x}'|}\chi_{nn}(\vec{x}',\vec{x}'';t-t')\delta V^{ext}[n](\vec{x}'',t')$$

$$+ \int_{-\infty}^{\infty} dt' \int_{-\infty}^{\infty} dt'' \int d^3x' \int d^3x'' f^{xc}(\vec{x},\vec{x}';t-t')\chi_{nn}(\vec{x}',\vec{x}'';t'-t'')\delta V^{ext}[n](\vec{x}'',t''). \tag{2.75}$$

Now we have expressed the induced time-dependent Kohn Sham potential in terms of the external potential, so we can put this result into equation 2.72 to obtain the result from reference [110]

$$\chi_{nn}(\vec{x},\vec{x}';t-t') = \chi_0(\vec{x},\vec{x}';t-t') + \int_{-\infty}^{\infty} dt_1 \int_{-\infty}^{\infty} dt_2 \int d^3x_1 \int d^3x_2$$

$$\times \chi_0(\vec{x},\vec{x}_1;t-t_1)\left[\frac{e^2}{|\vec{x}_1-\vec{x}_2|}\delta(t_1-t_2) + f_{xc}(\vec{x}_1,\vec{x}_2;t_2-t')\right]\chi(\vec{x}_2,\vec{x}';t_2-t'), \tag{2.76}$$

To compare with spectroscopy, it is convenient to work by taking the double Fourier transform over the spatial degrees of freedom and a Fourier transform over the time difference $t-t'$. Then equation 2.75, which is derived in appendix E, takes

[17] This is a many-body effect and is absent in time-dependent Hartree or Hartree-Fock equation of motion techniques for the density-density response function.

the form of a matrix equation

$$\chi_{\vec{G}\vec{G}'}(\vec{q},\omega) = (\chi_0)_{\vec{G}\vec{G}'}(\vec{q},\omega)$$

$$+ \sum_{\vec{G}_1\vec{G}_2} (\chi_0)_{\vec{G}\vec{G}_1}(\vec{q},\omega)[v(\vec{q}) + f^{xc}(\vec{q},\omega)]_{\vec{G}_1\vec{G}_2}\chi_{\vec{G}_2\vec{G}'}(\vec{q},\omega), \tag{2.77}$$

or by summing the geometric series to infinite order,

$$\chi_{\vec{G}\vec{G}'}(\vec{q},\omega) = \sum_{\vec{G}_1} (\chi_0)_{\vec{G}\vec{G}_1}(\vec{q},\omega)[1 - [v(\vec{q}) + f^{xc}(\vec{q},\omega)]\,\chi_0(\vec{q},\omega)]^{-1}_{\vec{G}_1\vec{G}'}. \tag{2.78}$$

Here $v_{\vec{G}\vec{G}'}(\vec{q})$ is the Fourier transform of the Coulomb interaction

$$v_{\vec{G}\vec{G}'}(\vec{q}) = \frac{4\pi e^2}{|\vec{q}+\vec{G}|^2}\delta_{\vec{G}\vec{G}'}. \tag{2.79}$$

The Kohn-Sham density response function has the explicit form

$$(\chi_0)_{\vec{G}\vec{G}'}(\vec{q},\omega) = \sum_{\sigma}\sum_{\vec{k}}^{1BZ}\sum_{jj'} \langle \vec{k}j\sigma|\, e^{-i(\vec{q}+\vec{G})\cdot\hat{\mathbf{x}}}\, |\vec{k}+\vec{q}j'\sigma\rangle$$

$$\times \frac{f_{\vec{k}+\vec{q}j'\sigma} - f_{\vec{k}j\sigma}}{\varepsilon_{\vec{k}+\vec{q}j'\sigma} - \varepsilon_{\vec{k}j\sigma} + \hbar(\omega + i\eta^+)} \langle \vec{k}+\vec{q}j'\sigma|\, e^{i(\vec{q}+\vec{G}')\cdot\hat{\mathbf{x}}}\, |\vec{k}j\sigma\rangle\,, \tag{2.80}$$

which is derived in appendix appendix E. Here, the charge fluctuation matrix elements $\langle \vec{k}j\sigma|\, e^{-i(\vec{q}+\vec{G})\cdot\hat{\mathbf{x}}}\, |\vec{k}+\vec{q}j'\sigma\rangle$ are given by integrals over the macrocrystal

$$\langle \vec{k}j\sigma|\, e^{-i(\vec{q}+\vec{G})\cdot\hat{\mathbf{x}}}\, |\vec{k}+\vec{q}j'\sigma\rangle = \int d^3x \psi^*_{\vec{k}j\sigma}(\vec{x})\psi_{\vec{k}+\vec{q}j\sigma}(\vec{x})e^{-i(\vec{q}+\vec{G})\cdot\vec{x}}. \tag{2.81}$$

Spin-resolved Density Response function

We know that the functionals depend on the electron density per spin projection $n^\sigma(\vec{x})$ as opposed to the total electron density from the spin-polarized extension to DFT. It is therefore more meaningful to formulate TDDFT in this manner. By doing

so equation 2.71 has a more fundamental building block [22, 140] which is

$$\delta n^{\sigma}(\vec{x},\omega) = \sum_{\sigma'} \int d^3x' \chi^{\sigma\sigma'}(\vec{x},\vec{x}';\omega)\delta V^{ext,\sigma'}(\vec{x}',\omega). \tag{2.82}$$

In this context the Hartree and exchange-correlation kernels that enter the TDDFT linear response equation needs to be modified as

$$\frac{\delta V^{H}[n](\vec{x},t)}{\delta n(\vec{x}',t')} \rightarrow \frac{\delta V^{H,\sigma}[n_{\uparrow},n_{\downarrow}](\vec{x},t)}{\delta n^{\sigma'}(\vec{x}',t')} = \frac{e^2}{|\vec{x}-\vec{x}'|}\delta(t-t') \tag{2.83}$$

and

$$f^{xc}[n](\vec{x}_1,\vec{x}_2;t-t') \rightarrow f^{xc,\sigma\sigma'}[n_{\uparrow},n_{\downarrow}](\vec{x}_1,\vec{x}_2;t-t') \equiv \frac{\delta V^{xc,\sigma}[n](\vec{x},t)}{\delta n^{\sigma'}(\vec{x}',t')} \tag{2.84}$$

respectively. There are a few novelties that arise from this formalism. First, the Coulomb interaction $e^2/|\vec{x}-\vec{x}'|$ can explicitely be seen that it couples the Kohn-Sham band structure of opposite spin projections. The second, and more subtle, is the ability to define both the density-density response function χ_{nn} and the *longitudinal* spin-density response $\chi_{S_zS_z}$ respectively as

$$\chi_{nn}(\vec{x},\vec{x}';t-t') = \sum_{\sigma\sigma'} \chi^{\sigma\sigma'}(\vec{x},\vec{x}';t-t') \tag{2.85}$$

and

$$\chi_{S_zS_z}(\vec{x},\vec{x}';t-t') = \sum_{\sigma\sigma'} \sigma\sigma' \chi^{\sigma\sigma'}(\vec{x},\vec{x}';t-t'), \tag{2.86}$$

where $\sigma = +1$ for $\sigma =\uparrow$ and $\sigma = -1$ for $\sigma =\downarrow$ in the summation in equation 2.86. The consequences of both of these novelties will be relevant in chapter 3.

2.2.3 Downfolding TDDFT

Time-dependent density functional theory, in its form introduced in previous sections, has been used for computing several spectroscopic quantities since its

inception. However, in its presented form, it is a black box that does not offer insight into the microscopic origins of the spectra that it produces. This is because the *entire* Kohn-Sham band structure enters the calculation, both occupied and unoccupied states, to obtain the spectra, and the insight is at best done by 'drawing arrows' in the band structure to guess at the origins of the excitations. The main work I have done in my thesis is to get inside this black box to obtain the microscopic physics behind these response functions. This work is based on a formalism introduced in the 1970's by Werner Hanke, Liu Sham, and Giancarlo Strinati [141–147]. They however did not correctly downfold the full density response χ_{nn}, but rather the non-interacting response χ_0. In particular, my advisor and myself aspired to develop a form of TDDFT for the Wannier orbitals that are related to the Bloch states via a unitary transformation that was introduced in section 2.1.4.

However, the Wannier basis does not form a *complete* basis which is a requirement for a rigorous treatment of TDDFT to compare with physical spectra. We therefore had to recast the linear response functions for a basis of Wannier functions to rectify this problem.

In what follows, I will use a symbolic form of the matrix equation 2.78, $\chi = \chi_0[1 - V\chi_0]^{-1}$, where $V = v + f_{xc}$. Since χ_0 is a *sum* over intraband and interband 'transitions' we can separate $\chi_0 = \chi_0^t + \chi_0^r$ where the t is referred to as the target space associated with the Wannier orbitals and r is what is referred to as the 'rest' space. Then equation 2.78 is equivalent to

$$\chi = (\chi_0^t + \chi_0^r)[1 - V(\chi_0^t + \chi_0^r)]^{-1} \tag{2.87}$$

$$= (\chi_0^t + \chi_0^r)\big\{[1 - V\chi_0^r][(1 - V\chi_0^r)^{-1}V\chi_0^t]\big\}^{-1}. \tag{2.88}$$

Here, it is convenient to introduce the *dynamically screened* interaction

$$\tilde{V} \equiv (1 - V\chi_0^r)^{-1}V. \tag{2.89}$$

Then

$$\chi = (\chi_0^t + \chi_0^r)\Big\{[1 - V\chi_0^r][1 - \tilde{V}\chi_0^t]\Big\}^{-1} \tag{2.90}$$

$$= (\chi_0^t + \chi_0^r)\Big[1 - \tilde{V}\chi_0^t\Big]^{-1}[1 - V\chi_0^r]^{-1} \tag{2.91}$$

$$= \chi^t[1 - V\chi_0^r]^{-1} + \chi_0^r\Big[1 - \tilde{V}\chi_0^t\Big]^{-1}[1 - V\chi_0^r]^{-1}, \tag{2.92}$$

where I have introduced the *definition* of the response in the target space

$$\chi^t \equiv \chi_0^t\Big[1 - \tilde{V}\chi_0^t\Big]^{-1}. \tag{2.93}$$

Using the equality of

$$\Big[1 - \tilde{V}\chi_0^t\Big]^{-1} = 1 + \tilde{V}\chi^t, \tag{2.94}$$

it follows that

$$\chi = \chi^t[1 - V\chi_0^r]^{-1} + \chi_0^r\tilde{V}\chi^t[1 - V\chi_0^r]^{-1} + \chi_0^r[1 - V\chi_0^r]^{-1} \tag{2.95}$$

$$= \Big[1 + \chi_0^r\tilde{V}\Big]\chi^t[1 - V\chi_0^r]^{-1} + \chi_0^r[1 - V\chi_0^r]^{-1}. \tag{2.96}$$

The prefactor on the first term in equation 2.96 can be manipulated as

$$\Big[1 + \chi_0^r\tilde{V}\Big] = \big[1 + \chi_0^r(1 - V\chi_0^r)^{-1}V\big] = [1 - \chi_0^r V]^{-1}, \tag{2.97}$$

which allows us to rewrite the exact TDDFT linear response equation as

$$\chi = [1 - \chi_0^r V]^{-1}\chi^t[1 - V\chi_0^r]^{-1} + \chi_0^r[1 - V\chi_0^r]^{-1}. \tag{2.98}$$

At this point, I have made no approximation to the linear response formula but rather recasting it in an equivalent form. I have also not mentioned any implementation of

f_{xc} and its impact on the spectra. The easiest approximation to f_{xc} is setting it to zero which is referred to as the random phase approximation (RPA) of TDDFT[18].

The exchange-correlation kernel f_{xc} is often computed within the adiabatic LDA or GGA [110] based on functional differentiation of the exchange-correlation potentials evaluated from the ground state DFT calculation. Additionally, there are other proposed kernels such as the bootstrap kernel [148] or the Bethe-Salpeter based kernel referred to as the nanoquanta [149]. However, our formalism allows us to develop *models* for the kernel that act only in the target space. This can be understood if we partition our two disjoint subspaces in matrix form. Then the product $V\chi_0$ will become

$$V\chi_0 = \begin{pmatrix} v + f_{xc} & v \\ v & v \end{pmatrix} \begin{pmatrix} \chi_0^t & 0 \\ 0 & \chi_0^r \end{pmatrix} = \begin{pmatrix} (v + f_{xc})\chi_0^t & v\chi_0^r \\ v\chi_0^t & v\chi_0^r \end{pmatrix}. \tag{2.99}$$

Upon iterating this to infinite order, it allows equation 2.98 to become

$$\chi = [1 - \chi_0^r v]^{-1}\chi^t[1 - v\chi_0^r]^{-1} + \chi_0^r[1 - v\chi_0^r]^{-1}, \tag{2.100}$$

where it is convenient to define the response in the 'rest' space within the random-phase approximation as

$$\chi^r \equiv \chi_0^r[1 - v\chi_0^r]^{-1}. \tag{2.101}$$

It should be stressed that we have introduced an *approximation* in equation 2.99 to the TDDFT linear response function. However, as the target space size is increased to include more Wannier orbitals, this expression is expected to reproduce the exact result making our method a rigorous method to downfold TDDFT. It is important to mention here that the main purpose of this downfolding procedure is to understand the microscopic physics inside χ^t. In the Wannier basis, $\chi^t{}_{\vec{G}\vec{G}'}(\vec{q}, \omega)$ takes the form of

[18]It is important to note that this is not the same RPA that David Pines introduced for the plasmon of the electron gas [51]

a (four-point) particle-hole 'propagator' in which the external lines have been closed to obtain a response (two-point) function which is shown in appendix F.

We also want to understand dynamical screening within the target space to gain insight into the physics. This can be done through the inverse dielectric function. We put the result obtained in equation 2.100 into the result for the inverse dielectric function $\varepsilon^{-1} = 1 + v\chi$. It follows that

$$\varepsilon^{-1} = 1 + v\chi \tag{2.102}$$

$$= 1 + v\left([1 - \chi_0^r v]^{-1}\chi^t[1 - v\chi_0^r]^{-1} + \chi_0^r[1 - v\chi_0^r]^{-1}\right) \tag{2.103}$$

$$= 1 + v\left([1 - \chi_0^r v]^{-1}\chi^t + \chi_0^r\right)[1 - v\chi_0^r]^{-1}. \tag{2.104}$$

I then rewrite the identity matrix 1 as

$$1 = [1 - v\chi_0^r][1 - v\chi_0^r]^{-1}. \tag{2.105}$$

Then equation 2.102 becomes

$$\varepsilon^{-1} = \left[1 - v\chi_0^r + v[1 - \chi_0^r v]^{-1}\chi^t + v\chi_0^r\right][1 - v\chi_0^r]^{-1} \tag{2.106}$$

$$= \left[1 + \tilde{v}\chi^t\right][1 - v\chi_0^r]^{-1} \tag{2.107}$$

$$= \left[1 + \tilde{v}\chi^t\right][1 + v\chi^r]. \tag{2.108}$$

We then can *define* the inverse dielectric function for the target space as

$$\left(\varepsilon^t\right)^{-1} \equiv \left[1 + \tilde{v}\chi^t\right] \tag{2.109}$$

and the inverse dielectric function of the rest space as

$$\left(\varepsilon^r\right)^{-1} \equiv [1 + v\chi^r] \tag{2.110}$$

which allows a rewriting of the exact inverse dielectric function that will be measured in spectroscopy as

$$\varepsilon^{-1} = \left(\varepsilon^{t}\right)^{-1}(\varepsilon^{r})^{-1}. \tag{2.111}$$

This result takes a similar for as in chapter 25 of [5] where in that case the target space corresponds to the ions in the material and the rest space corresponds to the electrons. Since I have an inverse dielectric function, I can *define* a dielectric function for the target as

$$\varepsilon^{t} \equiv \frac{1}{(\varepsilon^{t})^{-1}} = \frac{1}{[1+\tilde{v}\chi^{t}]}, \tag{2.112}$$

and through this relation we can define a conductivity for the target space

$$\sigma^{t} = \frac{i\omega}{4\pi}\varepsilon^{t}. \tag{2.113}$$

2.2.4 Constucting *Ab initio* Hamiltonians using the Down-folded Random-Phase Approximation

To understand the entire energy spectrum by diagonalizing the electronic Hamiltonian is computationally impossible. As mentioned in 1, an effective Hamiltonian can be introduced. I will give a brief introduction in how this can be understood. We are trying to calculate the spectrum of the exact Hamiltonian given through the equation

$$\hat{H}_{el}\left|\psi\right\rangle_{el} = E\left|\psi\right\rangle_{el}. \tag{2.114}$$

We can define projection operators that act on the target and rest space given by $\hat{P}_t$ and $\hat{P}_t$ respectively which satisfy $\hat{P}_t + \hat{P}_r = \hat{I}$. We can therefore recast equation 2.114 in the form

$$\begin{pmatrix} \hat{P}_t\hat{H}_{el}\hat{P}_t & \hat{P}_t\hat{H}_{el}\hat{P}_r \\ \hat{P}_r\hat{H}_{el}\hat{P}_t & \hat{P}_r\hat{H}_{el}\hat{P}_r \end{pmatrix} \begin{pmatrix} |\psi_t\rangle \\ |\psi_r\rangle \end{pmatrix} = E \begin{pmatrix} |\psi_t\rangle \\ |\psi_r\rangle \end{pmatrix}, \tag{2.115}$$

where I have defined $|\psi_t\rangle \equiv \hat{P}_t\left|\psi\right\rangle_{el}$ and $|\psi_r\rangle \equiv \hat{P}_r\left|\psi\right\rangle_{el}$. It is important to note here that when taking the inner product of $\begin{pmatrix}\langle\psi_t| & \langle\psi_r|\end{pmatrix}$ with equation 2.115 reduces to

the usual eigenvalue equation for the entire Hilbert space. Now, I have redefined the eigenvalue equation in terms of two coupled equations. If we take the equation

$$\hat{P}_r\hat{H}_{el}\hat{P}_t\left|\psi_t\right\rangle + \hat{P}_r\hat{H}_{el}\hat{P}_r\left|\psi_r\right\rangle = E\left|\psi_r\right\rangle \tag{2.116}$$

and solve for $|\psi_r\rangle$, we obtain the relation

$$\left|\psi_r\right\rangle = \left(E\hat{I} - \hat{P}_r\hat{H}_{el}\hat{P}_r\right)^{-1}\hat{P}_r\hat{H}_{el}\hat{P}_t\left|\psi_t\right\rangle. \tag{2.117}$$

Putting this result into the other equation

$$\hat{P}_t\hat{H}_{el}\hat{P}_t\left|\psi_t\right\rangle + \hat{P}_t\hat{H}_{el}\hat{P}_r\left|\psi_r\right\rangle = E\left|\psi_t\right\rangle, \tag{2.118}$$

we obtain the result

$$\left[\hat{P}_t\hat{H}_{el}\hat{P}_t + \hat{P}_t\hat{H}_{el}\hat{P}_r(E\hat{I} - \hat{P}_r\hat{H}_{el}\hat{P}_r)^{-1}\hat{P}_r\hat{H}_{el}\hat{P}_t\right]\left|\psi_t\right\rangle = E\left|\psi_t\right\rangle, \tag{2.119}$$

which gives the result

$$\hat{H}_{eff}(E)\left|\psi_t\right\rangle = E\left|\psi_t\right\rangle, \tag{2.120}$$

where I have defined the effective Hamiltonian that acts on the target space

$$\hat{H}_{eff}(E) \equiv \left[\hat{P}_t\hat{H}_{el}\hat{P}_t + \hat{P}_t\hat{H}_{el}\hat{P}_r(E\hat{I} - \hat{P}_r\hat{H}_{el}\hat{P}_r)^{-1}\hat{P}_r\hat{H}_{el}\hat{P}_t\right]. \tag{2.121}$$

This is just manipulating the eigenvalue problem to a problem projected on the target Hilbert space. However, its spectrum is not independent since the effective Hamiltonian depend on it through the energy dependence of the effective Hamiltonian. To solve this equation would involve making approximations on the effective Hamiltonian which is the spirit of P.W. Anderson's theory of the low energy super-exchange spin Hamiltonian of the half-filled Hubbard model or the $t-J$ model away from half-filling. It can also be seen that by solving this Hamiltonian synthesis

approach will yield terms that pair higher number of particles than two due to the projection technique as shown in equation 1.12.

In our research group, we have a different procedure for computing $\hat{H}_{eff}$ using the random-phase approximation of TDDFT. This method follows that in reference [150]. To do so, we split the Hamiltonian into a single particle part $\hat{H}_0$ and an interaction piece $\hat{H}_{int}$. The single particle aspect of the Hamiltonian is obtained via a tight-binding parameterization of the Kohn-Sham band structure

$$\hat{H}_0 = \sum_{\sigma} \sum_{\vec{R}\vec{R}'} \sum_{nm} h^{\sigma}_{nm}(\vec{R} - \vec{R}') d^{\dagger}_{n\vec{R}\sigma} d_{m\vec{R}'\sigma}, \tag{2.122}$$

where the matrix element $h^{\sigma}_{nm}(\vec{R} - \vec{R}')$ is given by

$$h^{\sigma}_{nm}(\vec{R} - \vec{R}') = \langle W_{n\sigma}(\vec{R})| \hat{H}_{KS} |W_{m\sigma}(\vec{R}')\rangle = \int d^3x w^*_{n\sigma}(\vec{x} - \vec{R}) h_{KS}(\vec{x}) w_{m\sigma}(\vec{x} - \vec{R}'), \tag{2.123}$$

and it should be noted that this quantity is just a function of the *difference* of lattice vectors $\vec{R} - \vec{R}'$ due to the translational symmetry of the underlying crystal structure.

The interacting part of the Hamiltonian $\hat{H}_{int}$ is given by

$$\hat{H}_{int} = \frac{1}{2} \sum_{\sigma\sigma'} \sum_{\vec{R}_1\vec{R}_2\vec{R}_3\vec{R}_4} \sum_{nmn'm'} V^{\sigma\sigma'}_{nmn'm'}(\vec{R}_1, \vec{R}_2, \vec{R}_3, \vec{R}_4; \omega = 0^+) d^{\dagger}_{n\vec{R}_1\sigma} d^{\dagger}_{m\vec{R}_2\sigma'} d_{m'\vec{R}_3\sigma'} d_{n'\vec{R}_4\sigma}, \tag{2.124}$$

where the interaction matrices are given by

$$V^{\sigma\sigma'}_{nmn'm'}(\vec{R}_1, \vec{R}_2, \vec{R}_3, \vec{R}_4; \omega = 0^+)$$

$$= \langle W_{n\sigma}(\vec{R}_1)| \langle W_{m\sigma'}(\vec{R}_2)| \hat{W}^r(\omega = 0^+) |W_{n'\sigma}(\vec{R}_3)\rangle |W_{m'\sigma'}(\vec{R}_4)\rangle$$

$$= \int d^3x \int d^3x' w^*_{n\sigma}(\vec{x} - \vec{R}_1) w^*_{m\sigma'}(\vec{x}' - \vec{R}_2) w^r(\vec{x}, \vec{x}'; \omega = 0^+) w_{m'\sigma'}(\vec{x}' - \vec{R}_3) w_{n'\sigma}(\vec{x} - \vec{R}_4). \tag{2.125}$$

Here, the quantity used to compute the matrix elements for the effective interaction is *screened* by the degrees of freedom that are in the rest space which gives the equation for the screened interaction as

$$w^r(\vec{x},\vec{x}';\omega=0^+) = v(\vec{x}-\vec{x}') + \int d^3x_1 \int d^3x_2 v(\vec{x}-\vec{x}_1)\chi^r(\vec{x}_1,\vec{x}_2;\omega=0^+)v(\vec{x}_2-\vec{x}') \tag{2.126}$$

where $v(\vec{x}-\vec{x}') = e^2/|\vec{x}-\vec{x}'|$ is the bare Coulomb interaction and $\chi^r(\vec{x}_1,\vec{x}_2;\omega=0^+)$ is the static limit of equation 2.101. Using this formalism, we have constructed a *static* Hamiltonian where we have ignored the frequency dependence of the interaction in the downfolded target space. In principle, this should be included in the interaction and has been shown to play an important role for La_2CuO_4 in reference [139].

We have used this RPA downfolding procedure to construct a multi-orbital extended Hubbard model in chapter 4 for α-$RuCl_3$ which was published in an article in Physical review B [40].

Chapter 3

Collective Excitations in 'One-Dimensional' Mott Insulating Cuprates

One-dimensional cuprates are materials with a crystalline anisotropy along one direction formed by copper-oxygen chains. The chemistry of these chains plays a crucial role in the material properties witnessed via spectroscopy [2, 3, 17, 23, 26, 27, 31, 33]. One-dimensional cuprates are distinguished between the corner-sharing compounds such as (Ca)Sr_2CuO_3 and $SrCuO_2$ seen figure 3.1, where the copper atoms are bridged with an oxygen atom, from the edge-sharing compounds $CuGeO_3$ and $LiCuO_2$. In this dissertation, I focus solely on the corner-sharing compounds which are the epitome of being ideal realization of one dimensional Heisenberg chains.

In section 1.3, I had summarized the 'fractionalization' paradigm of these materials which has been used to interpret several experiments [3, 30, 33, 151–156]. In this chapter, I introduce and propose a brand new *ab initio* course of action for understanding the Mott-gapped charge-neutral particle-hole excitations in these materials through a rigorously downfolded implementation of time-dependent density functional theory (TDDFT) introduced in section 2.2.3.

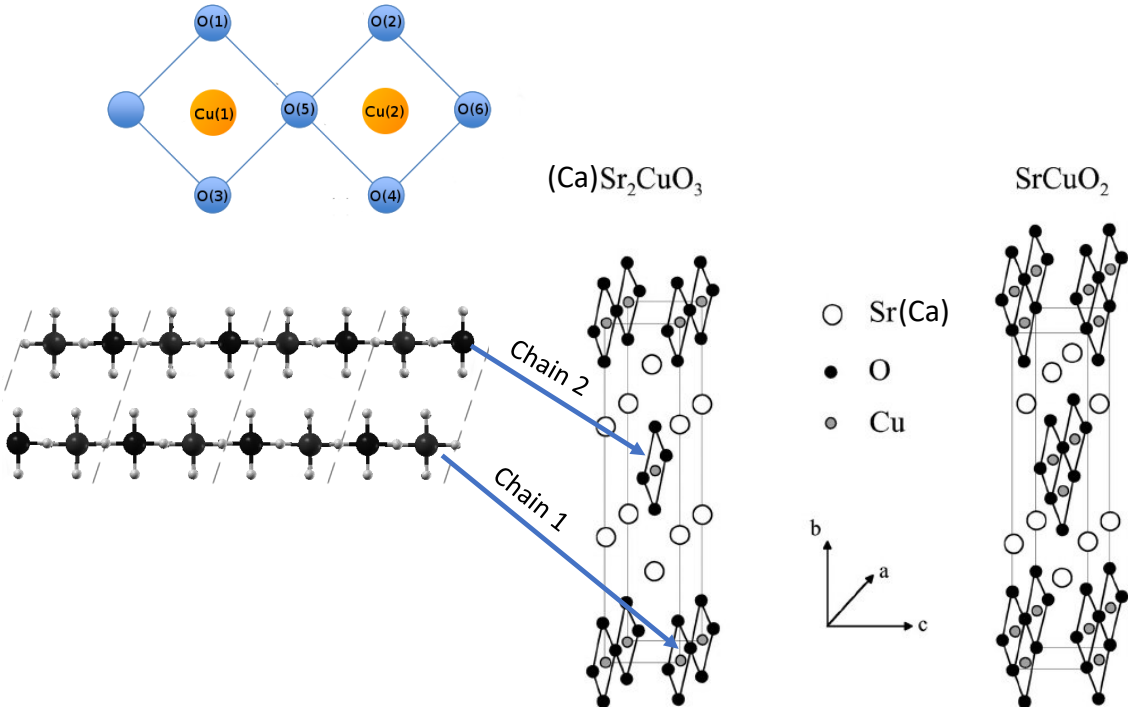

Figure 3.1: The crystal structure of $(Ca)Sr_2CuO_3$ and $SrCuO_2$. $Sr(Ca)_2CuO_3$ has a crystal structure is made up of separated corner-sharing CuO_3 chains. $SrCuO_2$'s crystal structure consists of two *magnetically decoupled chains* that form a zig-zag structure. Despite differences in the crystal structure, experiments find several similarities between these materials. Here, I have shown the two equivalent CuO_3 chains for $(Ca)Sr_2CuO_3$ that comprise the unit cell which I will use as a visual aid throughout this chapter. The dashed lines in the figure distinguish between unit cells. This figure was adapted from reference [157].

3.1 *Ab initio* Theory for 'One Dimensional' Cuprates

The main focus of my research has been to construct an *ab initio* description of the experimentally observed spectra. By doing so, I introduce a *parameter-free* explanation for the Mott-gapped particle-hole charge and (longitudinal) spin excitations in these materials by downfolding TDDFT to a low-energy space of *exactly disentangled* Wannier orbitals for the 'one-dimensional' cuprates. It follows that the active ingredients needed to describe these excitations are *dynamical long-ranged screening* and the *chemistry* inherit to the solid state. Before introducing these innermost constituents of the spectra I produced, I show the results for the *physical* spectra which are compared with experimental measurements and some predictions I make for potential future experiments to be performed.

3.1.1 *Ab initio* Spectra for (Ca)Sr_2CuO_3 and $SrCuO_2$

In the optical limit, my *ab initio* calculations agree *extremely* well quantitatively in the 'peak position' and intensity[1] with the current published data for $SrCuO_2$ and Sr_2CuO_3 as seen in figure 3.2. This figure is very pertinent to our proposed theory because it introduces the notion of a *pole*, seen as a crossing of the real part of the dielectric function in the optical limit, as the main arbiter for the charge excitations seen in these materials as opposed to a continuum of pairs of collective charged bosons [33, 34]. There have been no measurements that show the real part of the dielectric function for Sr_2CuO_3 or Ca_2CuO_3, so in its stead I have shown the optical conductivity for Sr_2CuO_3 [31] which is proportional to the imaginary part of the dielectric function. It is also noteworthy that although we agree extremely well with the dielectric function for $SrCuO_2$, small differences in the crossing of the dielectric function can manifest itself in noticeable differences in its inverse.

[1]The data published for EELS was done in arbitrary units, so an absolute comparison was not able to be done. My intention is for this work to motivate future experiments to be performed to produce the results with the correct intensities.

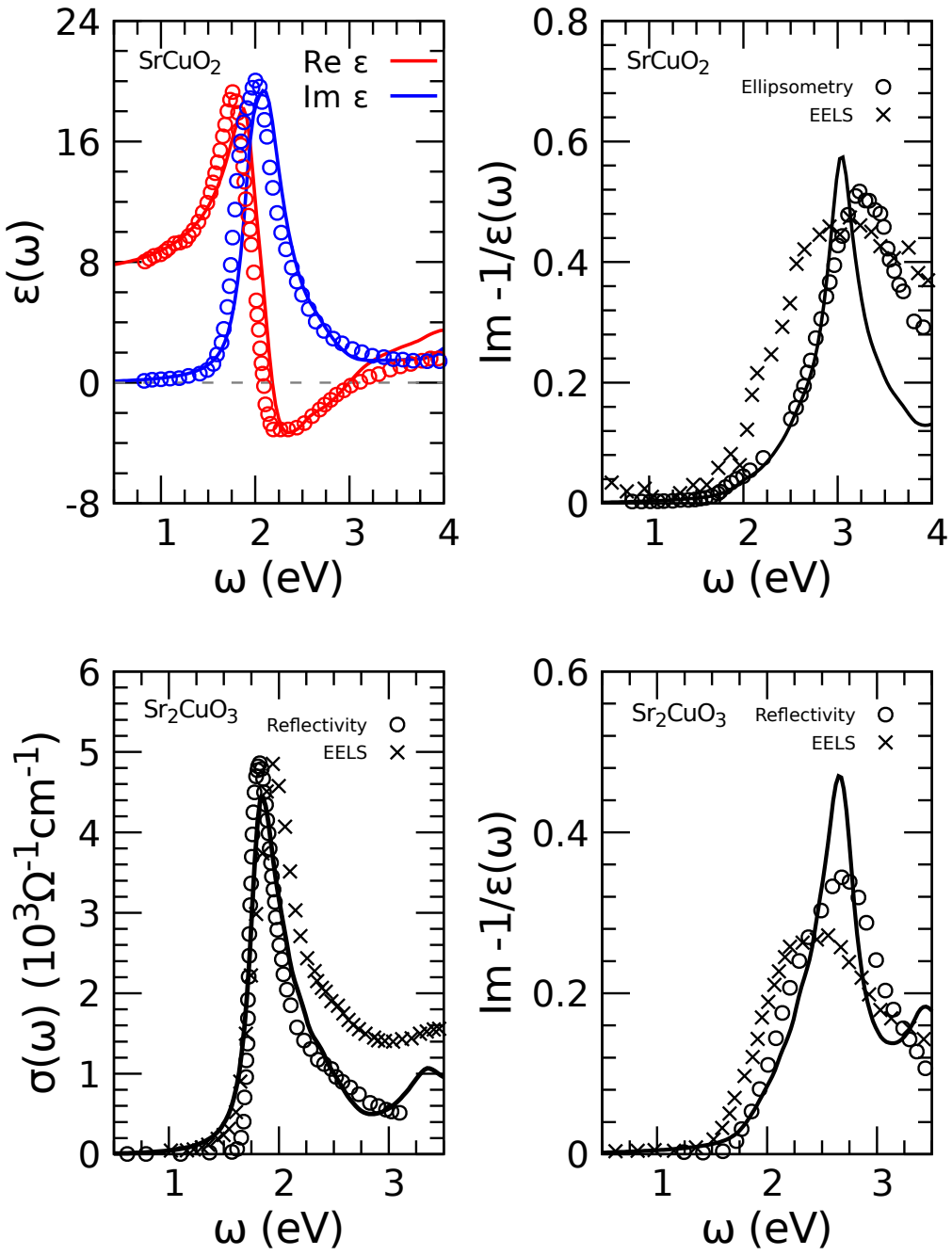

Figure 3.2: Dielectric response for one-dimensional cuprates. Top left: Ellipsometry measurements from [158] (open circles) and TDDFT calculations (solid lines) for real and imaginary parts of the dielectric function for $SrCuO_2$. Top right: Loss function from ellipsometry (open circles), EELS [87] (crosses), and TDDFT (solid line) for $SrCuO_2$. Bottom left: Optical conductivity from reflectivity [32] (open circles), from EELS (crosses), and TDDFT (solid line) for Sr_2CuO_3. Bottom right: Loss function from reflectivity (open circles), EELS [33] (crosses), and TDDFT (solid line) for Sr_2CuO_3.

In addition to the optical limit, we agree very well with finite momentum transfer *parallel* to the one dimensional chain from EELS measurements [33] which can be seen in figures 3.3 and 3.4. In figure 3.3, I have also plotted the dispersion with open shapes on the scale of reference [33] to show why this discontiunity was overlooked. I would like to draw attention to the behavior of the dispersion relation in the vicinity of the *antiferromagnetic* zone boundary at $q = 0.4$ Å^{-1}. It can be seen in the left panel of figures 3.3 and 3.4 there is a 'discontinuity' which was overlooked in the published work from references [33, 87]. In the right panel of figures 3.3 and 3.4, I use theory to fill in the dispersion relation which introduces a sharp change in the slope of the dispersion which would appear as a discontinuity with resolutions below $\Delta q = 0.025$ Å^{-1}.

I attribute this discontinuity to the sudden change in the line shape for the calculated dielectric function shown in figure 3.6. It can be seen that as the wave vector is increased, the imaginary part of $\varepsilon(\vec{q}, \omega)$ becomes much less sharp which through the Kramers-Kronig relation will not allow the real part of $\varepsilon(\vec{q}, \omega)$ to dip down as much as it did in the optical limit. As mentioned in section 1.3.3, there was a narrowing of the line shape for the loss function for wave vectors approaching $\vec{q} = 0.4$ Å^{-1} and then the line shape starts to broaden until the zone boundary at $\vec{q} = 0.8$ Å^{-1}.

This property is captured in the theoretical calculation which is shown in figure 3.5 which shows the width of the line shape fit with Gaussians for both the theoretical calculations and experimental measurements. The trend was consistent if I used one, two, or three Gaussians. The broadening of the line shape after the antiferromagnetic zone boundary is caused by the microscopic physics, i.e. electron-hole propogation. Beyond $\vec{q} = 0.4$ Å^{-1}, electron-hole propogation is equivalent to that less than $\vec{q} = 0.4$ Å^{-1} since they are related via a reciprocal lattice vector, hence the narrowing is a result of the microscopic physics. However, the propagation to spectroscopy is different due to the differences in the behavior of charge fluctuation matrix elements for different momentum transfer.

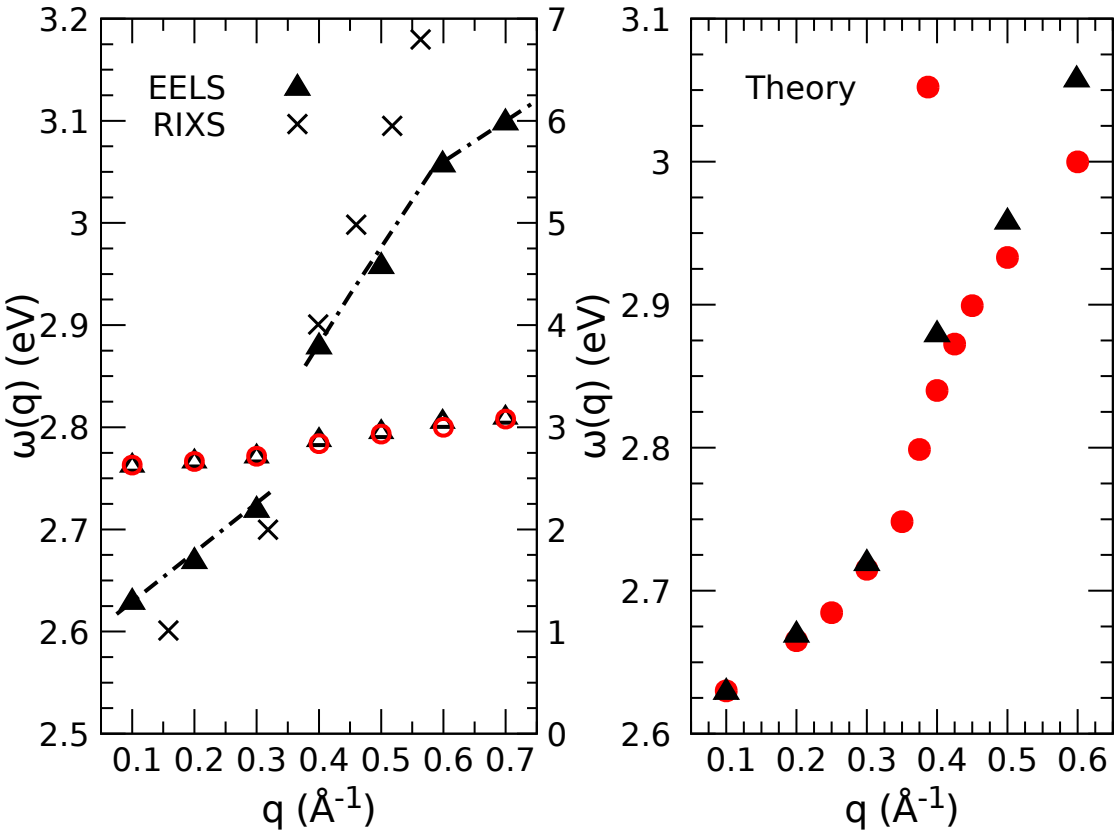

Figure 3.3: Dispersion relation for Sr_2CuO_3. Left: EELS dispersion obtained from reference [33] (filled black triangles) and RIXS dispersion obtained from reference [35] (black crosses). Theory (open red circles) and EELS (open black circles) correspond to the y-axis on the right side of this graph. The dashed black lines are guides to the eye to show the discontinuity in the dispersion relation. Right: TDDFT dispersion (filled red circles) to show our explanation our interpretation of the dispersion relation for wave vectors not measured and EELS measurements.

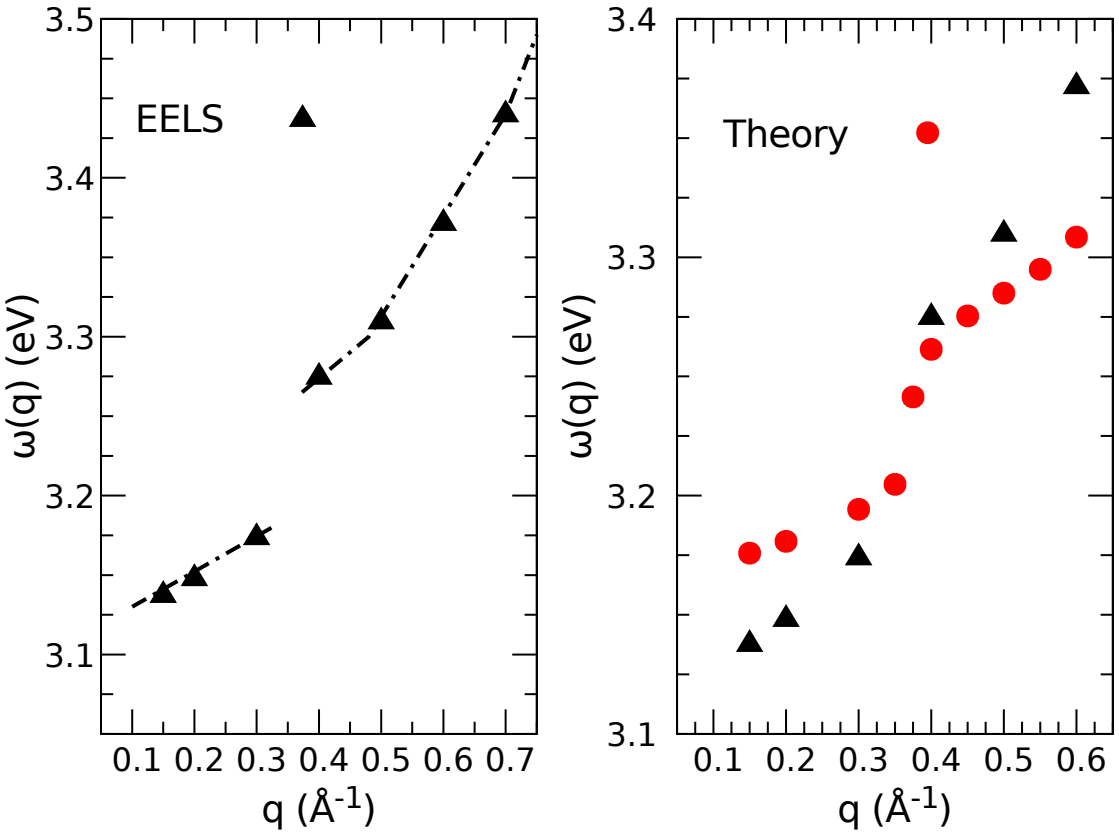

Figure 3.4: Dispersion relation for $SrCuO_2$. Left: EELS dispersion obtained from reference from Gaussian fits to the data [87] (filled black triangles). Dashed black lines are guides to the eye to emphasize the discontinuity in the dispersion relation. Right: TDDFT dispersion (filled red circles) to show our interpretation of the dispersion relation for wave vectors not measured and EELS measurements. Theory dispersion was shifted up by 0.1 eV.

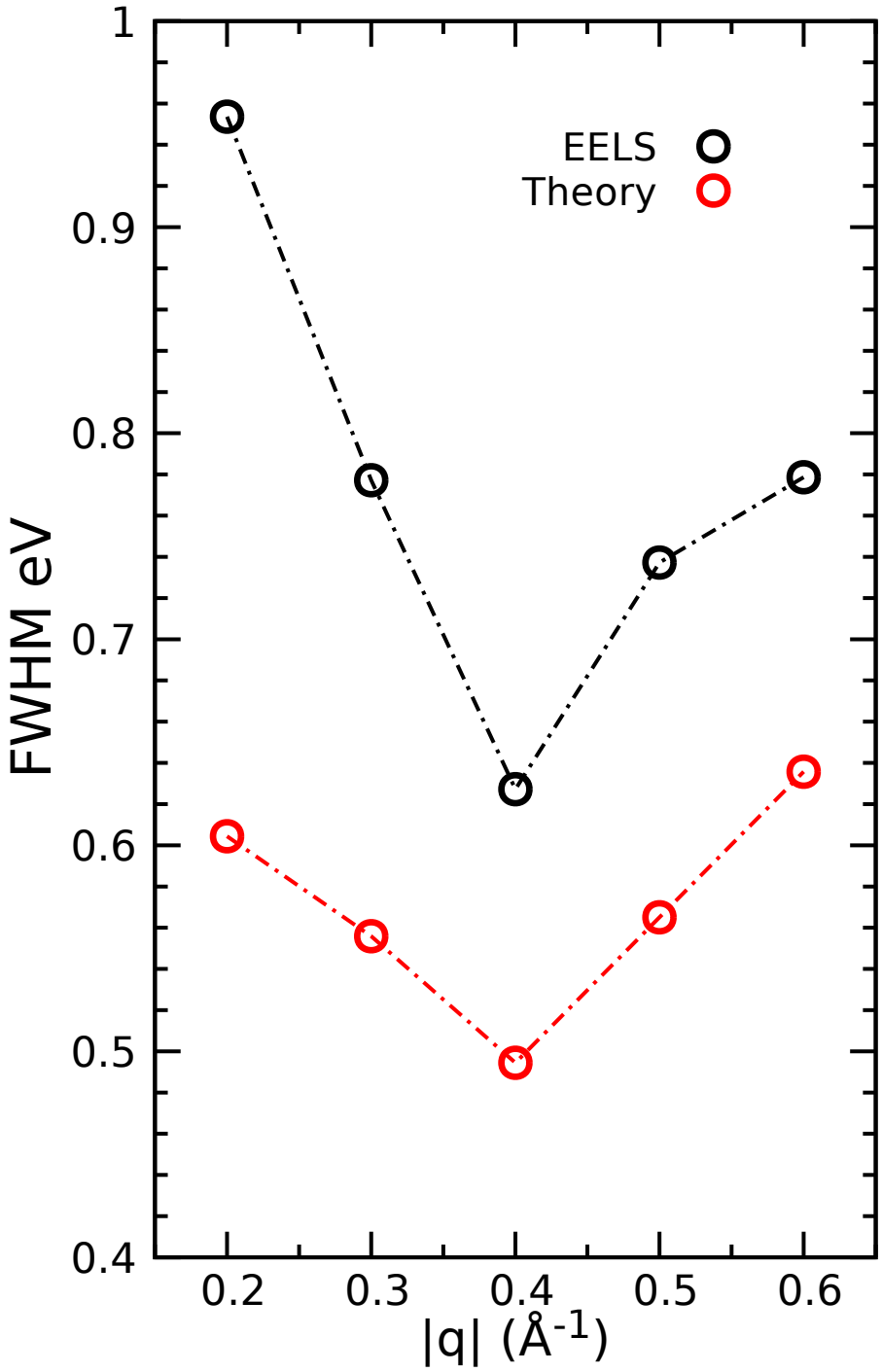

Figure 3.5: Linewidth for peak in Sr_2CuO_3. EELS linewidth (open black circles) obtained from full width at half maximum (FWHM) obtained from Gaussian fit of EELS measurements compared with FWHM of Gaussian fits for TDDFT calculations.

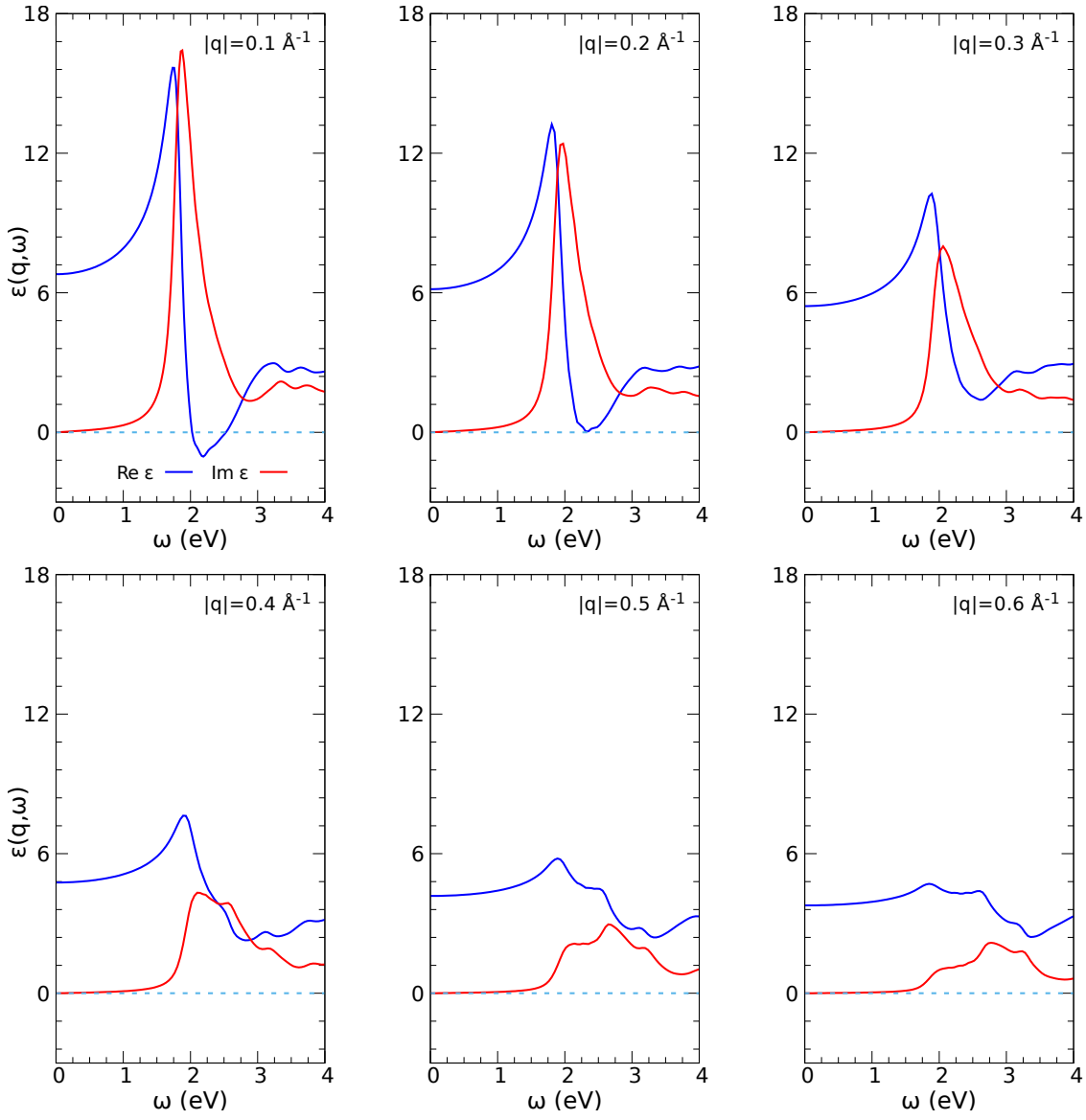

Figure 3.6: Dielectric function $\varepsilon(\vec{q},\omega)$ for Sr_2CuO_3 for wave vectors from $|\vec{q}| = 0.1 - 0.6$ Å^{-1}. It can be seen in the bottom left panel that the imaginary part of the dielectric function suddenly has a sudden change in the line shape which causes a drastic change in the behavior of the real part of the dielectric function through the Kramers-Kronig relation. This can be attributed to the discontinuity in the dispersion relation of the pole seen at $\vec{q} = 0.4$ Å^{-1}.

Although EELS data seems to suggest the collective mode is damped out at $q \sim 0.8$ Å^{-1} seen in figure 1.3, this is an artifact from the $1/|\vec{q}|^2$ prefactor that is present in the loss function, and the signal will appear even weaker for larger momentum transfer measurements due to the additional $1/|\vec{q}|^2$ prefactor of the DDCS. However, this peak still exists in the imaginary part of the density-density response function $\chi_{nn}(\vec{q},\omega)$, or equivalently the dynamical charge structure factor $S_{nn}(\vec{q},\omega)$.

As seen in figure 3.7, the peak in $S_{nn}(\vec{q},\omega)$, re-emerges in higher Brillouin zones which is similar to the case of MgB_2 [159]. Furthermore, this re-emergence is ubiquitous across all corner-sharing 'one dimensional' Mott-insulating cuprates, and can be validated by *non-resonant* inelastic X-ray (NIXS) measurements[2] since the cross section is directly proportional to $S_{nn}(\vec{q},\omega)$ in contrast to the $q^{-4}S_{nn}(\vec{q},\omega)$ dependence on the EELS cross section. I would advocate for a measurement of Ca_2CuO_3 as opposed to Sr_2CuO_3 since the proton number for calcium is $Z = 20$ while the proton number for strontium is $Z = 38$. This would give $\sim 13\times$ the count rate due to the photoabsorption of the NIXS measurement. Specifically, the DDCS for NIXS [48] is

$$\frac{d^2\sigma}{d\Omega d\hbar\omega} = r_0^2(\vec{e}_1 \cdot \vec{e}_2)^2 \left(\frac{\omega_1}{\omega_2}\right) S_{nn}(\vec{q},\omega). \tag{3.1}$$

As seen in figure 3.7, an ideal area in phase space to see the re-emergence would be in the vicinity $q \sim 2$ Å^{-1}. A measurement of this nature would further validate our theory and more generally would advocate for NIXS measurements as a more direct probe for excitations for quantum materials. It also would be quite interesting to perform a measurement taking the Fourier transform of $S_{nn}(\vec{q},\omega)$ over all wave vectors to examine the *real space* dynamics of the collective mode. Work has already been made on this front in reference [160] where they were able to directly measure the shape of the symmetry of the associated orbitals pertaining to the dynamics.

[2]For previous generation X-ray sources, the presence of strontium in some of these compounds made measurements difficult because of the Z^4 behavior for the absorption of X-rays and would require long allocations of beam time to get a discernable signal. However, with the introduction of the fourth generation of synchrotron sources, these measurements may be more feasible.

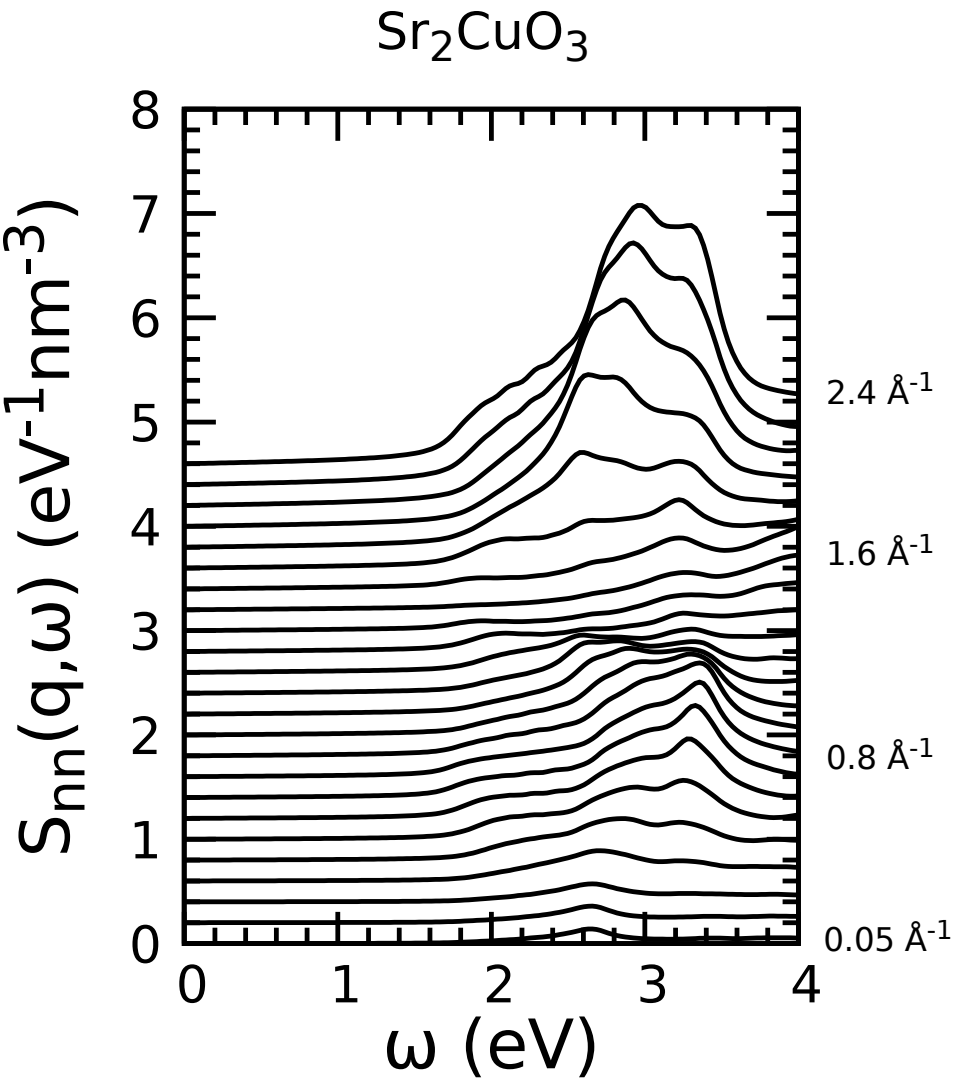

Figure 3.7: $S_{nn}(\vec{q},\omega)$ calculated for Sr_2CuO_3 for wave vectors of the first six Brillouin zones for the antiferromagnetic unit cells. It can be seen that between $|\vec{q}| = 1.2 - 1.8$ $Å^{-1}$ the collective mode would be difficult to discern, but at wave vectors $|\vec{q}| = 2.0 - 2.4$ $Å^{-1}$, the collective mode is predicted to be much more noticeable.

The more striking aspect of the *ab initio* theory is the *prediction* of a collective Mott-gapped *longitudinal* spin excitation seen in figure 3.8 that has the same 'periodicity' as the upper bound of the two-spinon continuum., and the peak position for all three cuprates are shown in figure 3.9. These excitations result from treating the charge and spin dynamics on the same footing by calculating the *spin-resolved* density response function and could be verified experimentally with INS measurements. This excitation is above the energy scale usually measured but within capabilities of state-of-the art facilities such as the spallation neutron source (SNS) at Oak Ridge National Lab. It is also noteworthy the energy region of this *magnetic* excitation overlaps in energy space with the xy 'orbiton' seen in the copper L_3 edge of the RIXS experiment [3], however, RIXS measurements do not directly measure correlation functions so this assignment cannot be definitively made. Furthermore, this excitation was seen in the energy region of the copper K edge of the RIXS experiment for $SrCuO_2$ [161] and was attributed to a shift in the single-spinon dispersion relation by 1.9 eV.

The reason this excitation is inherently gapped is because the *longitudinal* magnetic response, for a system which includes the effects of *electron dynamics*, is mediated via the direct Coulomb interaction in time-dependent density functional theory while the *transverse* magnetic response have their origin solely in the exchange and correlation aspect of the Coulomb interaction[3]. It is usually the case that the spin excitations are modeled using low energy spin models such as the Heisenberg model at half-filling or the $t-J$ model when away from half-filling, so these excitations are well beyond the energy scales these models were intended for. Furthermore, if you consider these spin models to be a fundamental Hamiltonian for the material, the ground state is a macroscopic $SU(2)$ spin singlet [68] with no long range magnetic order, so the longitudidal and transverse magnetic excitations are *equivalent* [74]. Therefore, the only magnetic excitations shown in the literature are the gapless excitations of continua comprised of even integer multiples of spinons.

[3]The longitudinal response also has a contribution from exchange and correlation, but I worked solely within the RPA, so these effects were absent in my calculation. Also, the direct interaction has much stronger of an effect.

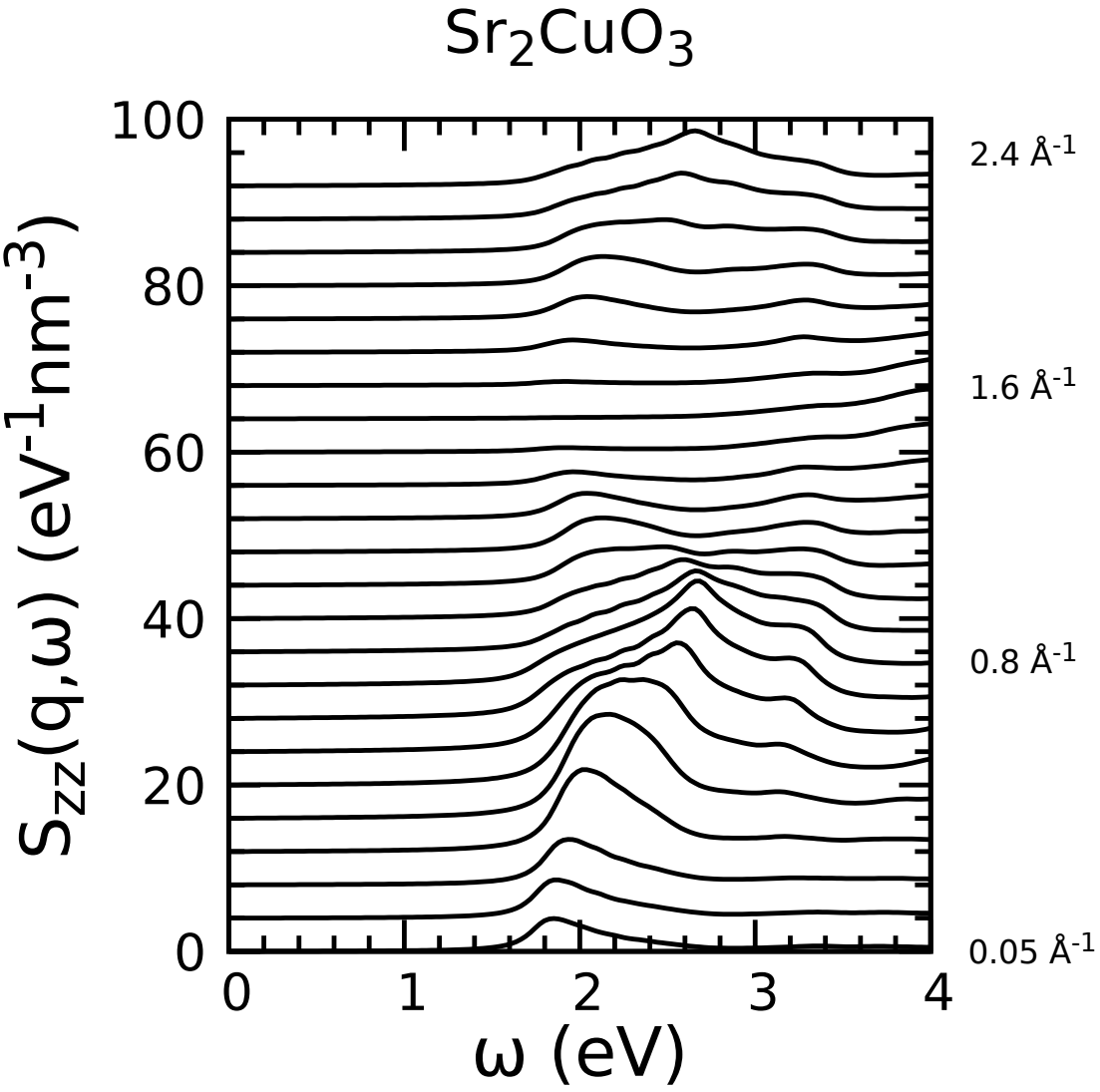

Figure 3.8: $S_{zz}(\vec{q},\omega)$ calculated for Sr_2CuO_3 for wave vectors of the first six Brillouin zones for the antiferromagnetic unit cells. The excitation has an energy of ~ 1.8 eV and has a rather large dispersion ~ 0.8 eV which is consistent with the dispersion of the upper bound of the two-spinon continuum. Here, there is no gapless excitation seen in this spectrum, so for our theory to agree with experiment, there should be a gapless excitation seen in the transverse dynamical spin structure factor $S_{+-}(\vec{q},\omega)$

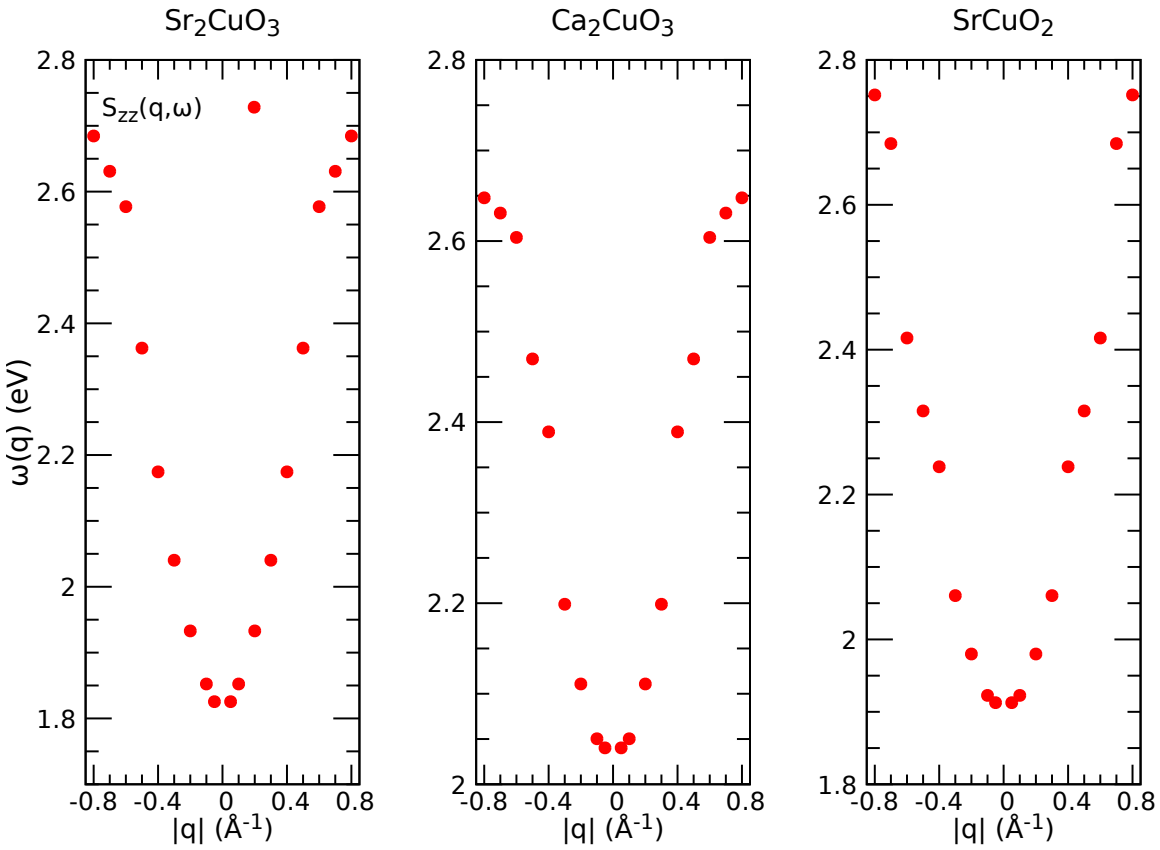

(a) Sr_2CuO_3 **(b)** Ca_2CuO_3 **(c)** $SrCuO_2$

Figure 3.9: Peak position for the longitudinal spin dynamical structure factor $S_{zz}(\vec{q},\omega)$ for a) Sr_2CuO_3, b) Ca_2CuO_3, and c) $SrCuO_2$. I propose INS measurements on the energy scale shown in these figures to validate our proposed theory. It should be noted that the discontinuity and line shape at the antiferromagnetic zone boundary is not present in this calculation.

3.1.2 The Ground State

Now that I have introduced the calculated spectra, it is necessary for me to cover the details of the calculations that gave rise to these results and provide microscopic insight into the physics underlying them. For the ground state density functional theory calculation, I used the orthorhombic unit cell and the (*Immm*) space group for Sr_2CuO_3 and Ca_2CuO_3. The lattice constants I used as inputs are $a = 3.906$ Å, $b = 3.496$ Å, and $c = 12.684$ Å for Sr_2CuO_3 [162] and $a = 3.7870$ Å, $b = 3.2781$ Å, and $c = 12.277$ Å for Ca_2CuO_3 [163]. For $SrCuO_2$, I used the orthorhombic unit cell and (*Cmcm*) space group with lattice constants $a = 3.577$ Å, $b = 3.9182$ Å and $c = 16.342$ Å from reference [164]. The crystal structure used includes two equivalent corner-sharing CuO_3 chains which can be visualized in figure 3.1. To capture the insulating nature of these materials, I have doubled the unit cell along the chain axis generating two sublattices which yields four formula units in each unit cell. Additionally, I imposed these sublattices to be antiferromagnetically ordered.

The calculations were performed using a 16x16x4 unit cell macrocrystal in which the Born van Karmen boundary conditions were imposed. To check convergence, I doubled the macrocrystal and the electronic structure and spectroscopic calculations were unchanged. One hundred and fifty empty states were included above the condition of charge neutrality which corresponds to a Hilbert space that extends to ~ 25 eV to be used in the TDDFT linear response equation for polarization processes. For the exchange-correlation functional, I used the generalized gradient approximation (GGA) parameterized by John Perdew, Kieron Burke, and Matthias Ernzerhof [119] and an additional Hubbard U and the Hunds coupling J_H [165] on the $l = 2$ orbital content which further opened the band gap, and the fully-localized limit (FLL) [122] to account for double counting in the exchange-correlation potential.

While the Hubbard U in the ground state DFT calculation is often used as an *adjustable* parameter to fit an experimental measured quantity, such as optical band gap or magnetic moment, I estimated the value of the Hubbard U and Hund's J_H

using the random phase approximation of TDDFT. Since the Hubbard U and Hund's J_H act on a particular orbital character of the LAPW basis functions, here I projected five d orbitals on the copper sites for the RPA estimate. For Ca_2CuO_3 and Sr_2CuO_3, this corresponded to a value of U=4.7 eV and J_H=0.9 eV and U=4.8 eV and J_H=0.9 eV[4] for $SrCuO_2$. Due to the expensive nature to calculating the Hubbard U due to the large number of reciprocal lattice vectors needed; the largest number used in the calculation used was $\sim$ 3200. From there, a fit of the data was extrapolated to obtain the values that were used in the calculation. The convergence of the Hubbard U and ground state electronic structure for the antiferromagnetic ground state for all three materials are shown in figure 3.10.

Figure 3.11 shows the band structure along high symmetry points in the first Brillouin zone and the density of states for Sr_2CuO_3 where the content derived from the oxygen p and copper d overlap in energy space which generates a manifold of *entangled* valence states from ~ -7 to 2 eV. This degeneracy of content must do with the strong *covalency* in this material. Figure 3.12 and 3.13 show the orbitally decomposed density of states from the copper d and oxygen p content for the l-decomposed content in figure 3.11.

This hybridization makes it very difficult to construct Wannier orbitals. I show the construction and disentanglement of these Wannier orbitals in section 3.1.3 using the method that was introduced in section 2.1.4 of this thesis and showed the paramagnetic phase of La_2CuO_4 as an example. Here, I can to disentangle a Hilbert space spanned by *two* Wannier orbitals for each spin projection and for each chain in the unit cell. These two orbitals will be shown to describe well the microscopic origin of the spectra seen in figure 3.2, however, I need to add an additional *four* oxygen-centered Wannier orbitals to the Hilbert space to capture the dispersion seen in figure 3.3 and 3.4 which will be introduced in section 3.1.5.

[4]It is noteworthy that for the cuprates J_H does not really affect the electronic structure, but for iron-based materials it has much more prominent role in determining the ground state density

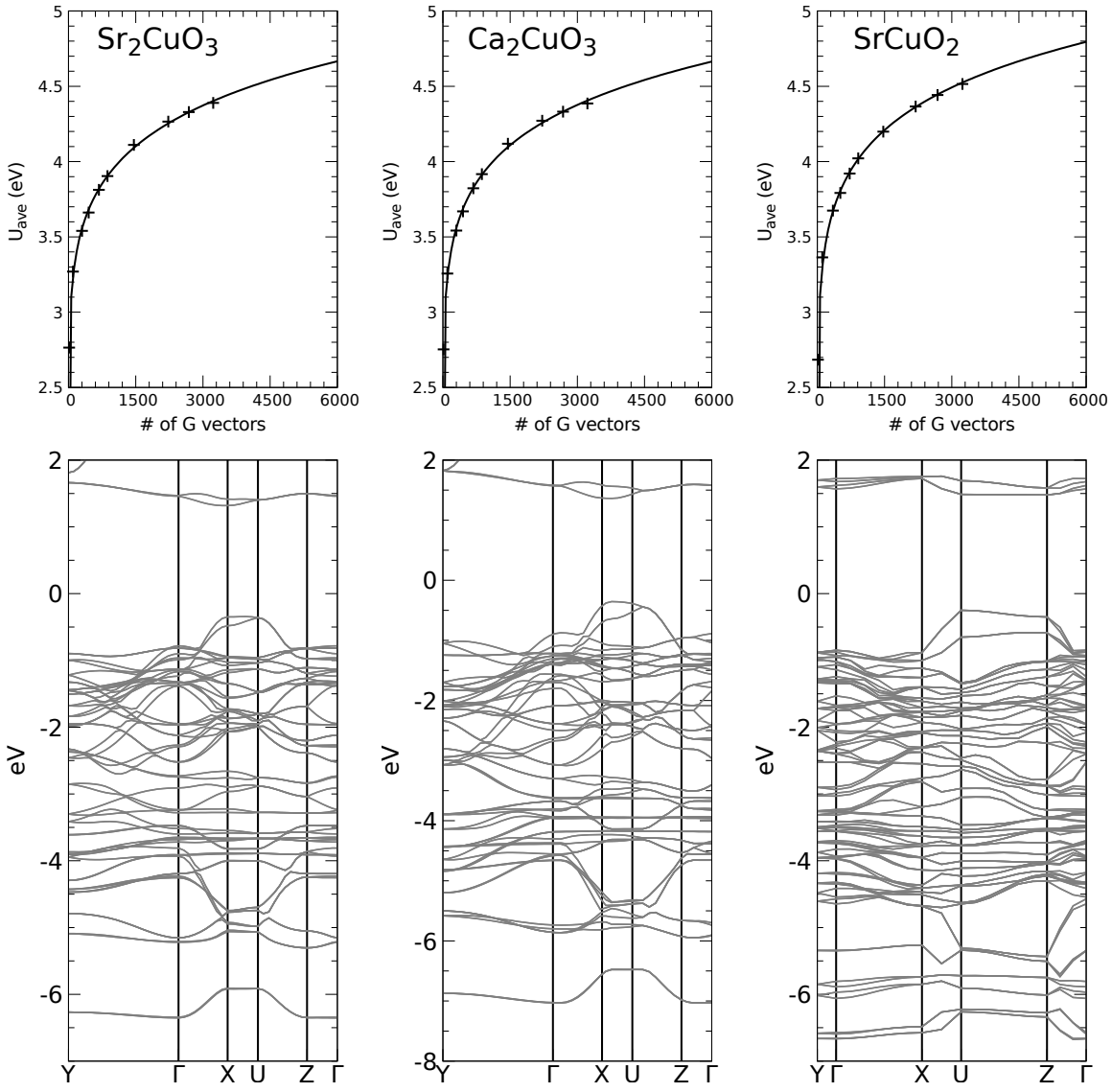

(a) Sr_2CuO_3 **(b)** Ca_2CuO_3 **(c)** Sr_2CuO_3

Figure 3.10: Band structure and convergence of RPA estimate for Hubbard U for ground state calculation. a) Band structure along high symmetry points for Sr_2CuO_3 and showing convergence of Hubbard U for a Hilbert space consisting of all five d Wannier orbitals. b) Band structure along high symmetry points for Ca_2CuO_3 and showing convergence of Hubbard U for a Hilbert space consisting of all five d Wannier orbitals. c) Band structure along high symmetry points for $SrCuO_2$ and showing convergence of Hubbard U for a Hilbert space consisting of all five d Wannier orbitals which is what orbitals the Hubbard U acts upon.

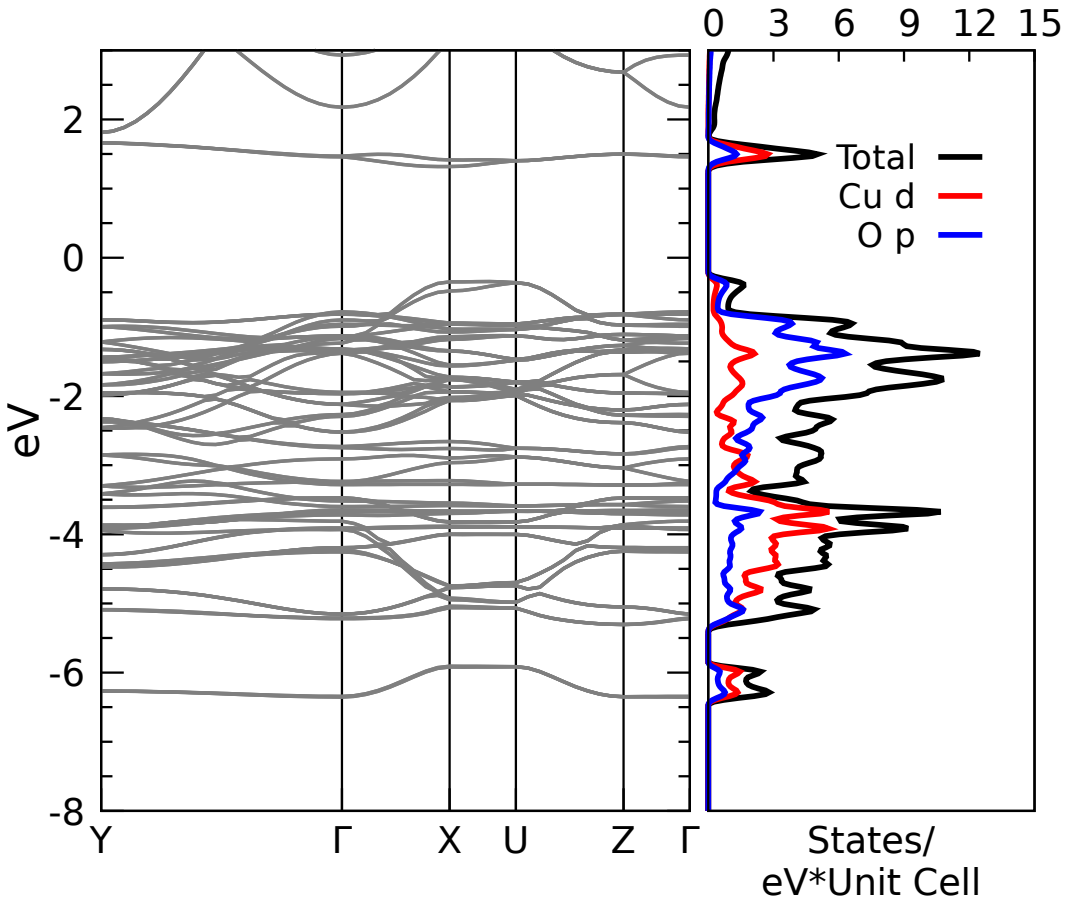

Figure 3.11: Band structre and (l-decomposed) partial density of states (pDOS) for the coppper d and oxygen p content for Sr_2CuO_3. using the GGA+U functional. In this calculation $U = 4.7$ eV and $J_H = 0.9$ eV. It can be seen that the l content for both the copper d and oxygen p are degenerate in energy space which corresponds to a strong hybridization in real space.

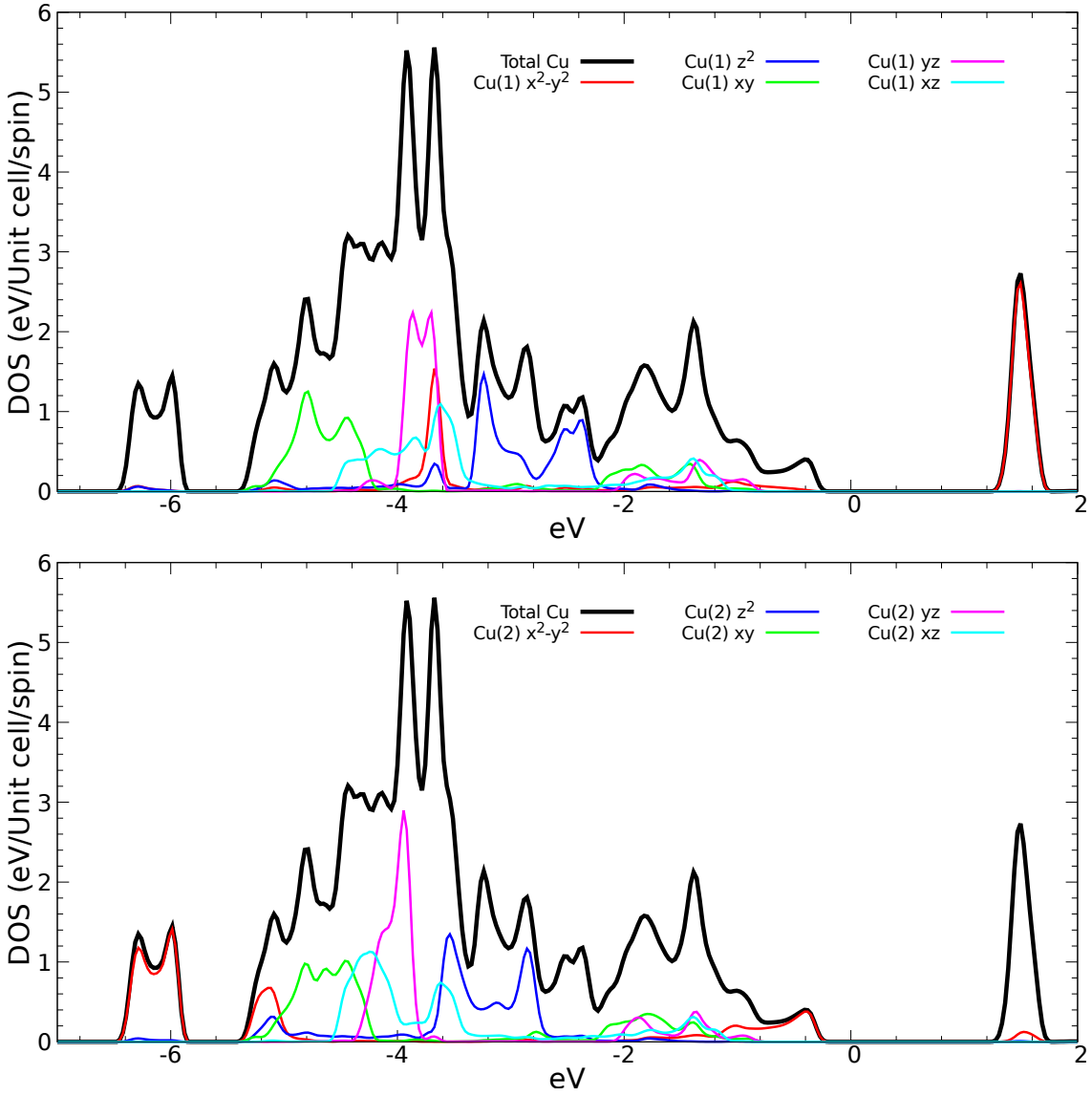

Figure 3.12: Partial density of states for the copper d content decomposed into their orbital content. Top: pDOS for copper 1. Bottom: pDOS for coppper 2. The other two copper atoms give identical density of states.

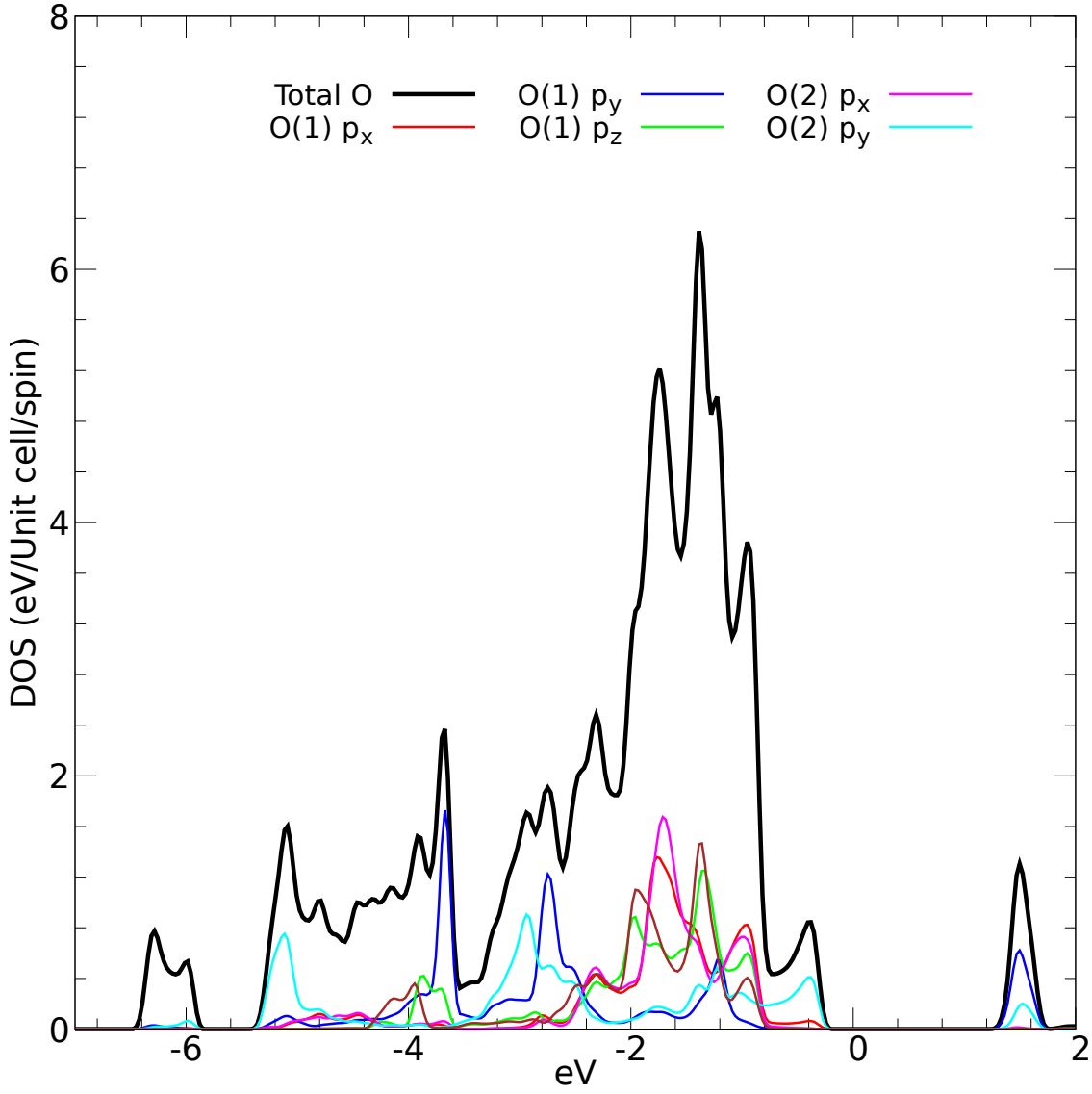

Figure 3.13: Partial density of states for the oxygen p content decomposed into their orbital content. All other oxygen atoms in the unit cell will give the pDOS of either of these two oxygen atoms.

3.1.3 Low-Energy Hilbert Space

To gain insight into the microscopic physics of the spectroscopy shown in the spectra shown at the beginning of this section, I needed to construct an exactly disentangled basis of Wannier orbitals. Without loss of generality, I will show the details for Sr_2CuO_3 for the rest of this chapter to avoid redundancies. To do so, I needed to enforce unitarity and I desired for my projection to be energy window independent. The one-dimensional cuprates have a very entangled band structure, as seen by the overlapping copper d and oxygen p l-decomposed density of states in figure 3.11, so I needed to invoke our disentanglement procedure introduced in section 2.1.4 to accomplish this.

Since I am computing dynamics, the minimal size Hilbert space required is one occupied and one unoccupied Wannier function per formula unit and spin projection. Looking at the density of states (DOS) plot in figure 3.12, it appears that the unoccupied flat band $\sim$ 1 eV has strong copper $d_{x^2-y^2}$ on the copper 1 site. Upon projecting a local orbital of this character over the entire Hilbert space, this indeed is the case. Figure 3.14 shows the corresponding locus for $j_{max}(\vec{k})$ of this Wannier orbital and the corresponding contour plot. These unoccupied bands are quite isolated from the rest, so the disentanglement procedure is not as difficult as it will be for the occupied band structure.

For the occupied states, the hybridization between the copper d and oxygen p states is very strong as seen in figure 3.11. I ultimately desire a Wannier orbital that will be near the top of the occupied states to capture the low energy charge dynamics seen in figure 3.2. Since the one dimensional cuprates are considered to be Mott insulators, as a first attempt, I will try and project a copper d orbital. Looking at the DOS in figure 3.12, it appears that a copper $d_{x^2-y^2}$ on the copper 2 site seems most appropriate and is consistent with most modeling based on the one-band Hubbard model and the crystal field splitting of square planar geometry inherit to the corner-sharing one-dimensional cuprates.

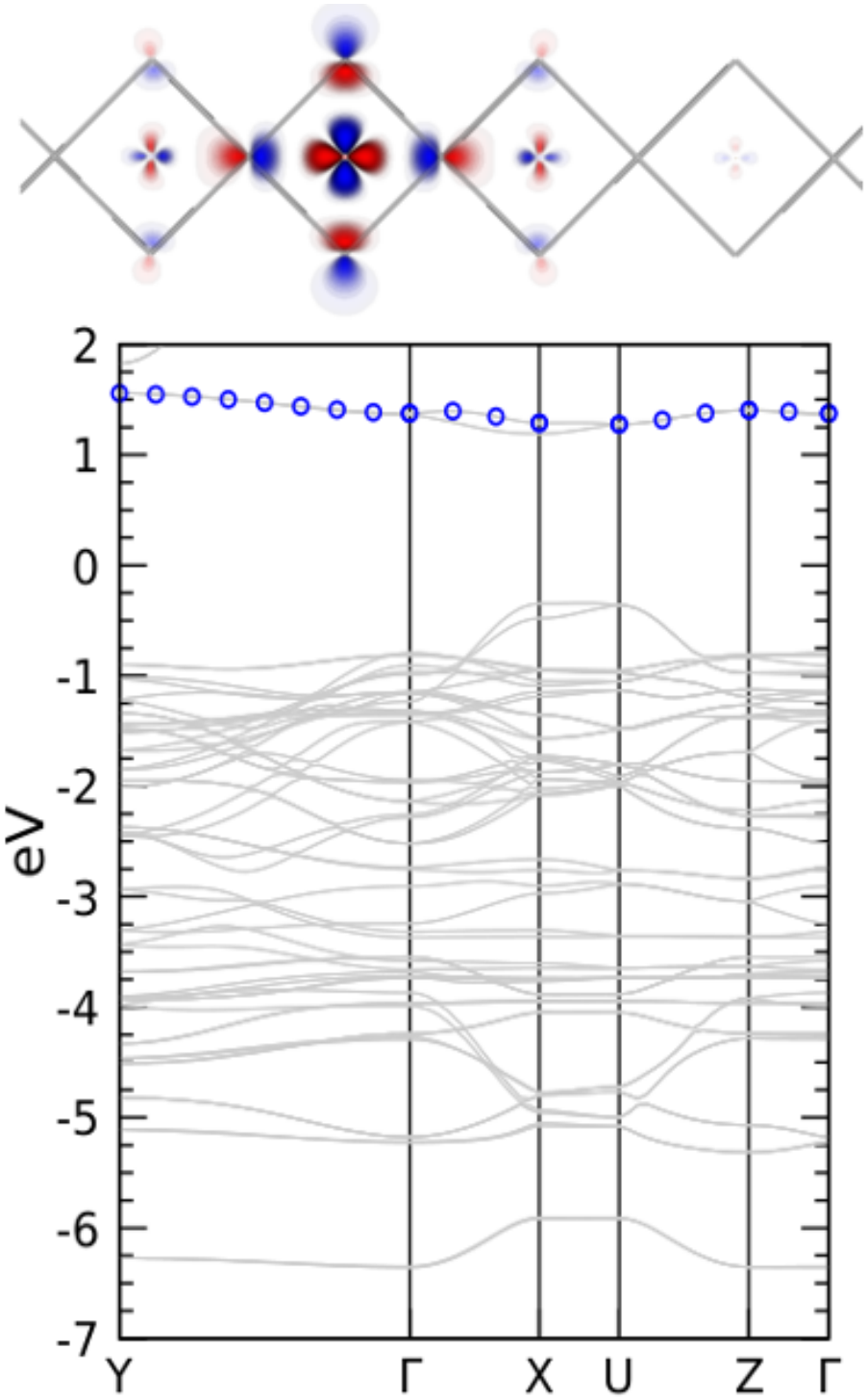

Figure 3.14: Unoccupied orbital contour plot and locus for $j_{max}(\vec{k})$ from $d_{x^2-y^2}$ Wannier orbital centered on the copper 1 site.. It is noteworthy that this orbital has strong *hybridization tails on the oxygen atoms within the plaquette and on the neighboring copper 2 sites.*

Two-Orbital Hilbert Space: d→d Picture

Using an *energy independent* window for projecting the local orbital of copper $d_{x^2-y^2}$ symmetry on the copper 2 site, the orbital surprisingly has its locus for $j_{max}(\vec{k})$ at the bottom of the valence bands at ∼-7 eV which can be seen in the left panel of figure 3.15. The orbital associated with this projection shows a *bonding* configuration with the copper $d_{x^2-y^2}$ orbital and the neighboring oxygen p content of its hybridization tails. This plot shows several different contours where areas with stronger opacity correspond to a larger contour value.

Considering I need an orbital that is located higher in energy to describe the low energy dynamics, I relax the imposition to have an energy independent window. Therefore, I *impose* an energy dependent window that cuts off to only include bands above ∼-5 eV. By doing so, the locus for $j_{max}(\vec{k})$ now resides at the top of the occupied states seen in the right panel of figure 3.15 as desired. It can be seen through the contour plot that this orbital has an *anti-bonding* configuration with its hybridization tails on the surrounding oxygen atoms within the plaquette.

It is also worth mentioning that this orbital has strong hybridization tails on the *neighboring* copper atoms which form a bonding configuration seen in the right panel of figure 3.15 while the unoccupied state has an anti-bonding configuration with its neighboring copper atoms seen in figure 3.14. This will play a crucial role in the dynamics. One striking result is the main energy separation in the electronic structure between these orbitals and more generally the cuprates due to the chemistry.

By doing this projection, I have chosen a *bias* in which I assume a *Mott-insulating* ground state meaning the excitations across the gap are controlled by $d \rightarrow d$ processes. However, it could be argued that these materials fall under a *charge-transfer* insulating ground state. Therefore, I will now try to see if the charge transfer picture can be realized through the projection of a Wannier orbital that has oxygen p character. In addition, the success of this projection could be measured through its reliance on the energy window.

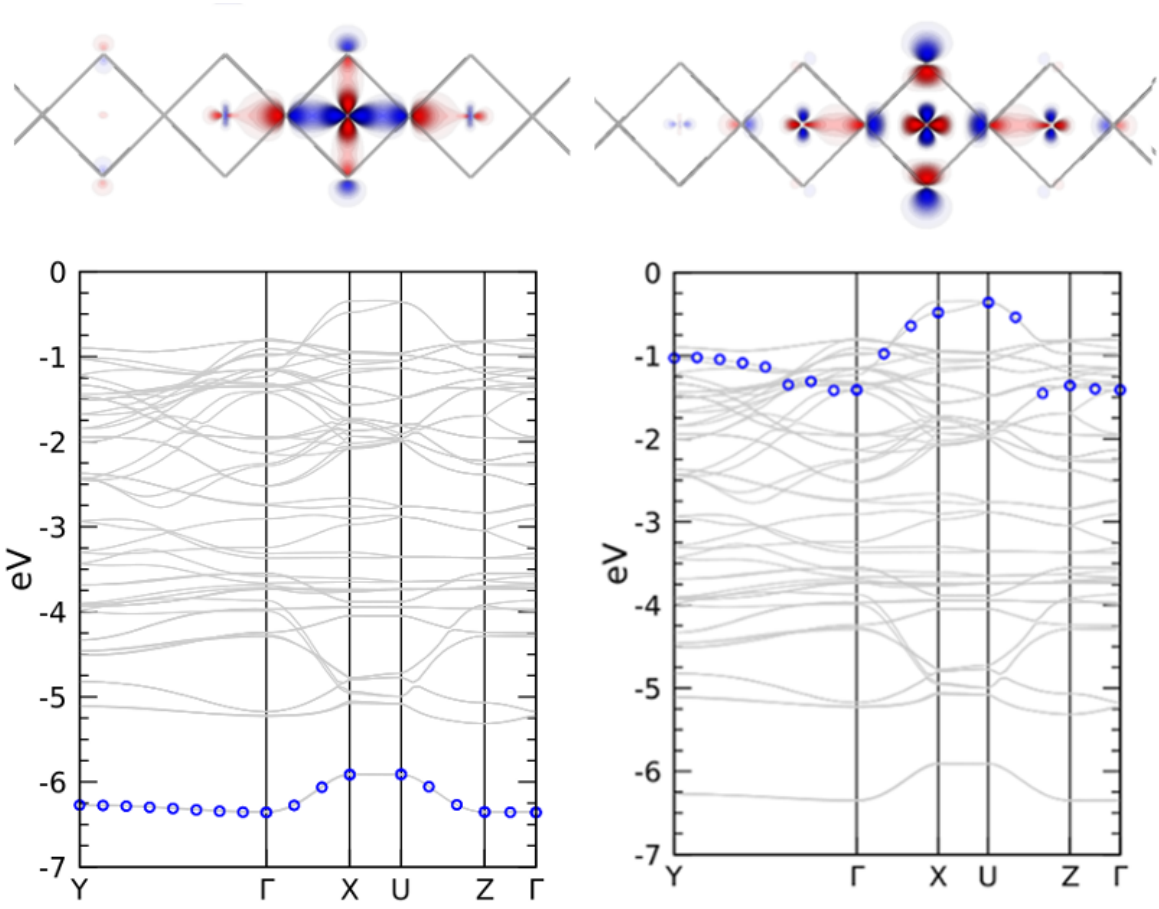

Figure 3.15: Occupied orbital contour plot and locus for $j_{max}(\vec{k})$ from $d_{x^2-y^2}$ Wannier orbital centered on the copper 2 site. The left panel corresponds to projecting the Wannier orbital using no energy window constraints and the corresponding plot of contours associated with this orbital. It can be seen through the contour plot that this orbital has a *bonding* configuration with its surrounding oxygen atoms within the plaquette. The right panel corresponds to projecting the Wannier orbital using an energy window that extends down to about $\sim$ -5 eV and the corresponding plot of contours associated with this orbital. It can be seen through the contour plot that this orbital has a *anti-bonding* configuration with its surrounding oxygen atoms within the plaquette.

Two-Orbital Hilbert Space: p→d Picture

Since I want these orbitals to be energy window independent, I cannot declare complete success with the previous projection of the $d_{x^2-y^2}$ Wannier orbital projected on the copper 2 site. Re-examimining the l-decomposed density of states in figure 3.13, it is seen that there is strong oxygen p content near the top of the occupied bands. Additionally, the oxygen p content manifests itself through strong hybridization tails around the copper $d_{x^2-y^2}$ Wannier orbital seen in the right panel of 3.15.

Therefore, I chose to try to project an oxygen p orbital which is more consistent with a 'charge-transfer' [166] insulator, where the neutral charge excitations *across* the band gap are determined by transitions from $p \rightarrow d$ as opposed to transitions from $d \rightarrow d$ excitations from the Mott-insulating paradigm by using the copper $d_{x^2-y^2}$ Wannier orbitals. Examining the copper $d_{x^2-y^2}$ derived Wannier orbital in the right panel of figure 3.15, I chose a linear combination of local orbitals respecting this configuration. Therefore, I use a linear combination of p orbitals specifically given by

$$|p\rangle = \frac{1}{2}\left(|O(2), p_y\rangle - |O(4), p_y\rangle + |O(5), p_x\rangle - |O(6), p_x\rangle\right), \tag{3.2}$$

where the enumeration of atoms is given in figure 3.1.

By using this projection, the energy window independence is *almost* satisfied except a few points corresponding to a much smaller measure in the first Brillouin zone than the copper $d_{x^2-y^2}$ Wannier orbital as seen in figure 3.16. Here, the outlying points are shown by magenta circles. By imposing an energy window down to $\sim$ -6eV, which is about $\sim$ 1 eV lower in energy space than the copper $d_{x^2-y^2}$ Wannier orbital for energy window independence, the orbital is entirely at the top of the valence band seen in figure 3.16 by the blue circles and is very similar in energy space and visually to the copper $d_{x^2-y^2}$ derived Wannier orbital. In figure 3.16, for clarity, I have shown both an energy dependent and energy independent window in the same plot. The blue circles track $j_{max}(\vec{k})$ with an energy dependent window down to $\sim$ -6 eV and the magenta circles show $j_{max}(\vec{k})$ for an energy independent window.

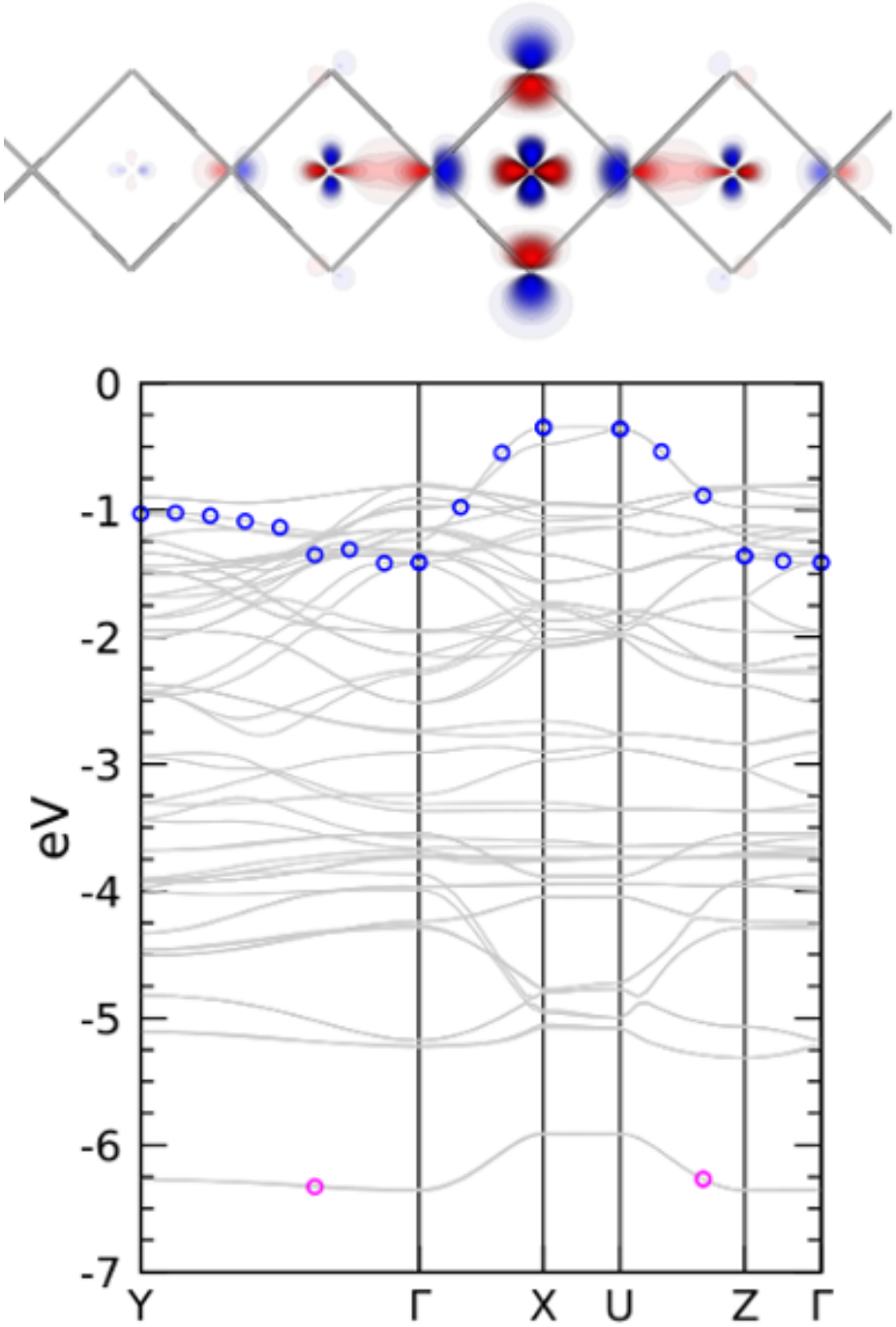

Figure 3.16: Occupied orbital contour plot and locus for $j_{max}(\vec{k})$ for the linear combination of p orbitals. The linear combination used is $|p\rangle = \frac{1}{2}\left(|O(2), p_y\rangle - |O(4), p_y\rangle + |O(5), p_x\rangle - |O(6), p_x\rangle\right)$. The blue circles track the associated band when an energy window that extends down to $\sim$ -6 eV and the magenta circles show the outlying points when no energy window is used.

Two-Orbital Hilbert Space: 'Antibonding'→d Picture

While the $d \rightarrow d$ and $p \rightarrow d$ Hilbert spaces could be considered satisfactory as far as unitarity and almost energy window independence is concerned, I still felt that these projections could be improved for a few reasons. The first being the ability to develop a completely energy independent window so this method could be extended to any material where a Wannier orbital projection is desirable. The second is I do not want to impose personal preference on which type of orbital should be used.

This caused me to reconsider what figure 3.15 was trying to tell me. When I did not impose an energy window on the projection, the Wannier orbital seems to be in a bonding configuration between the copper $d_{x^2-y^2}$ and oxygen p and inside the copper 2 plaquette. However, when I chose an energy dependent window, the Wannier orbital appears as an anti-bonding orbital inside the plaquette. I then thought it would be best to think about the band structure in terms of the chemistry between both the oxygen p and copper d derived content. It followed that I chose a *molecular* orbital picture defined via a local orbital of character

$$|MO:\pm\rangle = \frac{1}{\sqrt{5}}\left(|O(2),p_y\rangle - |O(4),p_y\rangle + |O(5),p_x\rangle - |O(6),p_x\rangle \pm |Cu(2),x^2-y^2\rangle\right), \tag{3.3}$$

where the +(-) refers to the bonding(antibonding) orbital. It can be seen in figure 3.17, that this picture is completely energy window independent and gives much more insight than my previous two projections. It is often the case in the literature [31, 167] that in the schematic view of the DOS, the orbital that I refer to as the bonding orbital is referred to, in the hole language, as the upper Hubbard band, and the antibonding orbital is referred to as the Zhang-Rice singlet for these one dimensional corner-sharing cuprates. When comparing the occupied orbital, either the d, p or the anti-bonding molecular orbital interpretation, the locus for $j_{max}(\vec{k})$ are almost identical which justifies that this orbital appears quite robust and truly wants to be in its location in energy space, which can be seen in figure 3.18.

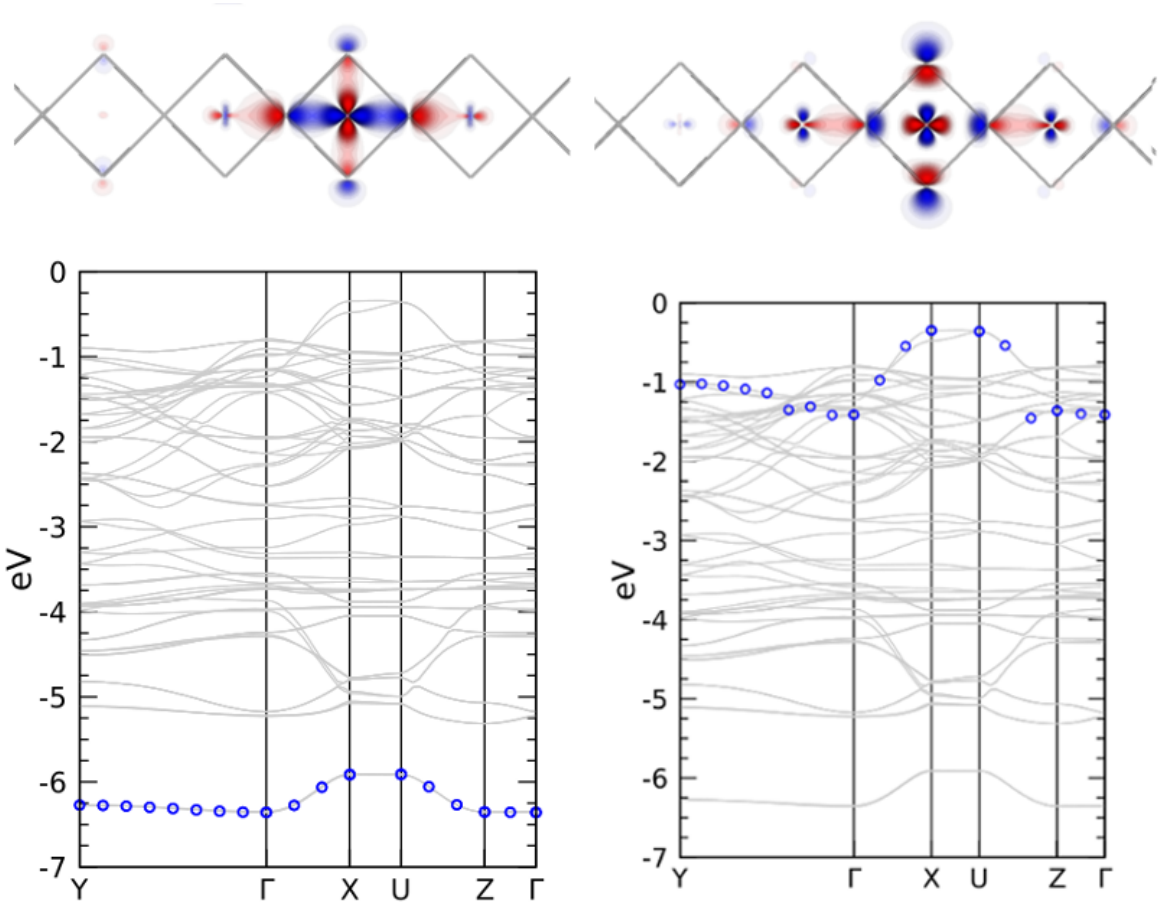

Figure 3.17: Occupied orbital contour plot and locus for $j_{max}(\vec{k})$ for the bonding and anti-bonding molecular orbital. The left panel shows the molecular bonding orbital given by the configuration for the local orbitals as $|MO:+\rangle = \frac{1}{\sqrt{5}}(|O(2),p_y\rangle - |O(4),p_y\rangle + |O(5),p_x\rangle - |O(6),p_x\rangle + |Cu(2),x^2-y^2\rangle)$. The right panel shows the molecular anti-bonding orbital given by the configuration for the local orbitals as $|MO:-\rangle = \frac{1}{\sqrt{5}}(|O(2),p_y\rangle - |O(4),p_y\rangle + |O(5),p_x\rangle - |O(6),p_x\rangle - |Cu(2),x^2-y^2\rangle)$. Both projections are completely energy window independent satisfying our desired criterium for Wannier orbital projection.

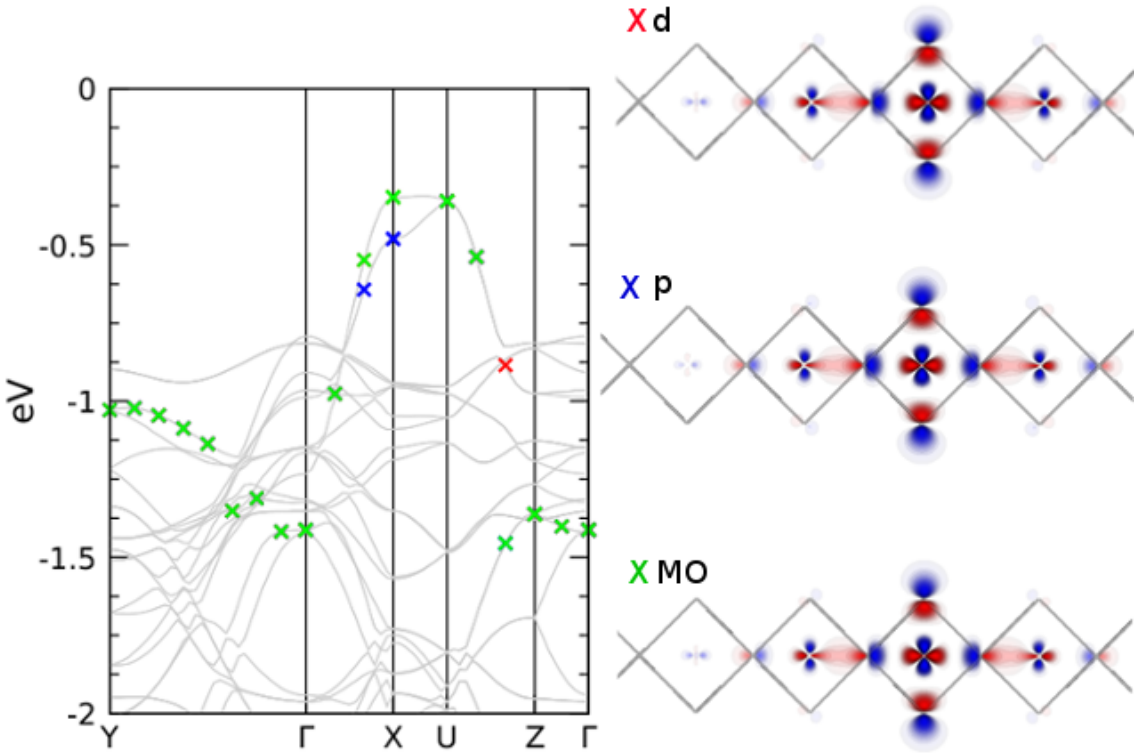

Figure 3.18: Comparing the contour plots and locus for $j_{max}(\vec{k})$ for d, p, and anti-bonding molecular orbital. It can be seen that the orbitals are almost identical in energy space and the contour plots look visually very similar.

3.1.4 Dynamics from Low-Energy Space

Now that I have defined a low energy Hilbert space of exactly disentangled Wannier orbitals which is both *unitary* and *energy window independent*, I can now examine their ability to capture the relevant physics for the dynamics. This entails calculating $(\chi^t)_{\vec{G}_{\vec{q}}\vec{G}_{\vec{q}}}$ from the Wannier basis to compare with various spectroscopic quantities. From the Wannier basis, as derived in appendix F, the target space response is given

$$\left(\chi^t\right)_{\vec{G}\vec{G}'}(\vec{q},\omega) = \sum_{\sigma\sigma'}\sum_{\bar{1}\bar{2}\bar{3}\bar{4}} A^{\sigma}_{\bar{1}\bar{2}}(\vec{q}+\vec{G})\left(\chi^t\right)^{\sigma\sigma'}_{\bar{1}\bar{2}\bar{3}\bar{4}}(\vec{q},\omega)A^{\sigma'*}_{\bar{3}\bar{4}}(\vec{q}+\vec{G}'), \tag{3.4}$$

where each of the numbers in the subscript represent the type of character and the unit cell location for an electron or hole from a Wannier orbital, i.e. $1 \equiv \{n_1\vec{R}_1\}$, and the bars over the numbers correspond that they are summed over. $(\chi^t)^{\sigma\sigma'}_{1234}(\vec{q},\omega)$ has the structure of an electron-hole propagator[5] taking the form

$$\left(\chi^t\right)^{\sigma\sigma'}_{1234}(\vec{q},\omega) = \left(\chi^t_0\right)^{\sigma\sigma'}_{1234}(\vec{q},\omega)$$

$$+\sum_{\sigma_1\sigma_2}\sum_{\bar{1}\bar{2}\bar{3}\bar{4}}\left(\chi^t_0\right)^{\sigma\sigma_1}_{12\bar{3}\bar{4}}(\vec{q},\omega)\left[\tilde{v}(\vec{q},\omega)+f^{xc}(\vec{q},\omega)\right]^{\sigma_1\sigma_2}_{\bar{1}\bar{2}\bar{3}\bar{4}}\left(\chi^t\right)^{\sigma_2\sigma'}_{\bar{1}\bar{2}34}(\vec{q},\omega). \tag{3.5}$$

The charge fluctuation matrix elements $A_{\bar{1}\bar{2}}(\vec{q}+\vec{G})$ are integrals over the macrocrystal

$$A^{\sigma}_{\bar{1}\bar{2}}(\vec{q}+\vec{G}) = \int d^3x w^*_{n_1\sigma}(\vec{x}-\vec{R}_1)e^{-i(\vec{q}+\vec{G})\cdot\vec{x}}w_{n_2\sigma}(\vec{x}-\vec{R}_2) \tag{3.6}$$

For this project, I work within the random-phase approximation (RPA) of TDDFT, so I set $f^{xc,\sigma\sigma'}_{1234} = 0$. Since I am using a two orbital Hilbert space for the optical limit, the four orbital configurations that enter $(\chi^t)^{\sigma\sigma'}_{1234}(\vec{q},\omega)$ can be visualized in figure 3.19 where I have shown *an* example of one of these configuration. Each of the opaque atoms represent the plaquette in which the Wannier orbital resides.

[5] It is important to note that this is not an actual electron-hole propagator that arises from Green function theory.

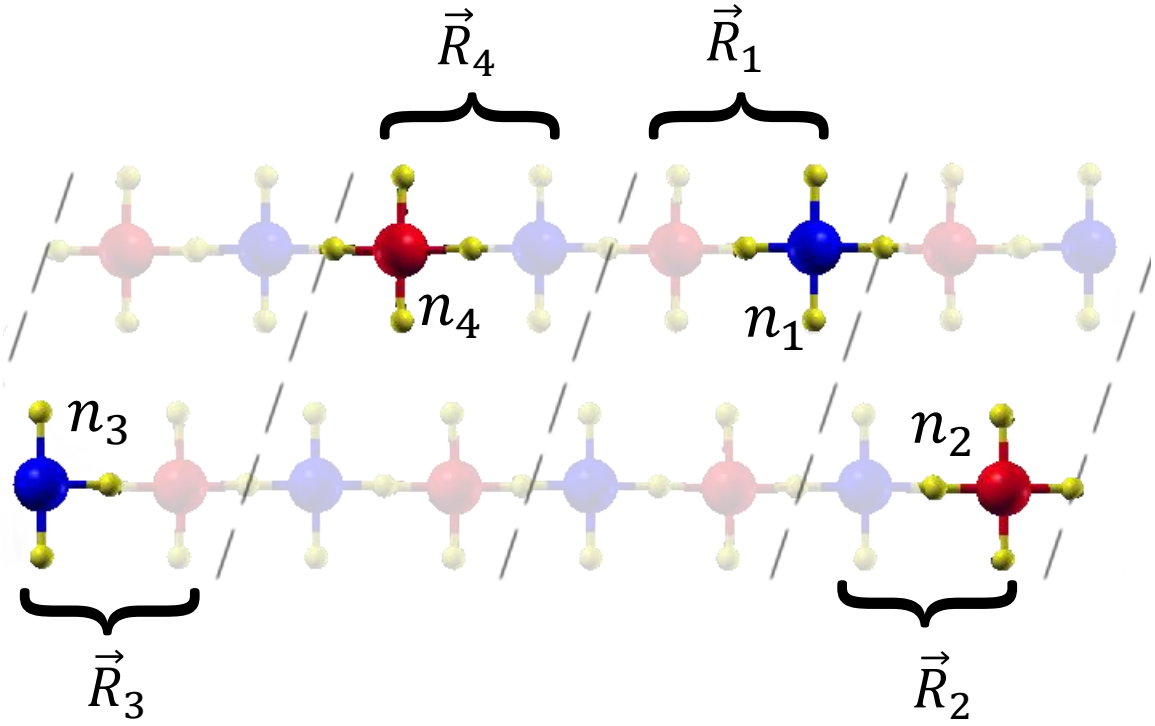

Figure 3.19: A general four orbital configuration for $(\chi_0^t)_{1234}$ and χ_{1234}^t for the two orbital Hilbert space of Wannier orbitals. The red and blue colors for the atoms are to distinguish between each of the sublattices in the antiferromagnetic unit cell for the ground state configuration. The dashed lines are put there to show the boundary of the unit cells. There are two chains in each unit cell, so they are depicted slightly offset from each other. For a full rendering of how these chains are in the unit cell, refer to figure 3.1.

The Optical Limit

First, I want to compare the result of the response in the target space $\chi^t_{\vec{G}_{\vec{q}}\vec{G}_{\vec{q}}}(\vec{q},\omega)$ with the full *physical* density response $\chi_{\vec{G}_{\vec{q}}\vec{G}_{\vec{q}}}(\vec{q},\omega)$. If the target space is chosen wisely, then the spectra produced from the target space should look very similar to the spectra in the entire Hilbert space other than the intensity of both calculations being different. Here, I will show that the collective mode is comprised of primarily nearest neighbor charge fluctuations that *span* the entire macrocrystal. Additionally, I will show the role of the spin degree of freedom and the three dimensional nature of the 'one-dimensional' cuprates. This is key because it strongly suggests that the fractionalization paradigm fails to be compatible with the *ab initio* interpretation for the Mott-gapped particle-hole excitations.

Next, I will unveil the microscopic physics by getting inside the black box calculation by showing the physics behind the electron-hole 'propagator' $(\chi^t)^{\sigma\sigma'}_{1234}(\omega)$. Here, I will show extensive details in the optical limit, i.e. $\vec{q}\to\vec{0}$ and $\vec{G}_{\vec{q}}=\vec{0}$, where the collective mode is well-defined. Due to the divergence in the Coulomb interaction in momentum space for $\vec{q}\to\vec{0}$, I show the calculation performed for the smallest wave vector in my $\vec{k}$-grid which is 0.05 Å^{-1}.

I present the spectra that is produced in the target space and compare with the calculations which include the rest of the Hilbert space computed through equation 2.98 to the get the *true* response functions in figure 3.20. In the left panel, I show the quantity $[\chi^t(\omega)][1-v\chi^r_0(\omega)]^{-2}$, which is equivalent to $\chi(\omega)-\chi^r(\omega)$, compared with $\chi(\omega)$ where the agreement is quite well for energies up to ~ 3 eV. In the right panel, I scale χ^t down by a factor of twenty-five and the agreement is very good between the calculations! This agreement can further be rationalized through the *pole* existing in both the calculations which can be seen through the dielectric function calculations plotted in figure 3.21. It is crucial the *pole* still exists since it is key to the interpretation of the loss which is outside the bosonized interpretation of the collective excitations being comprised of pairs of collective bosons.

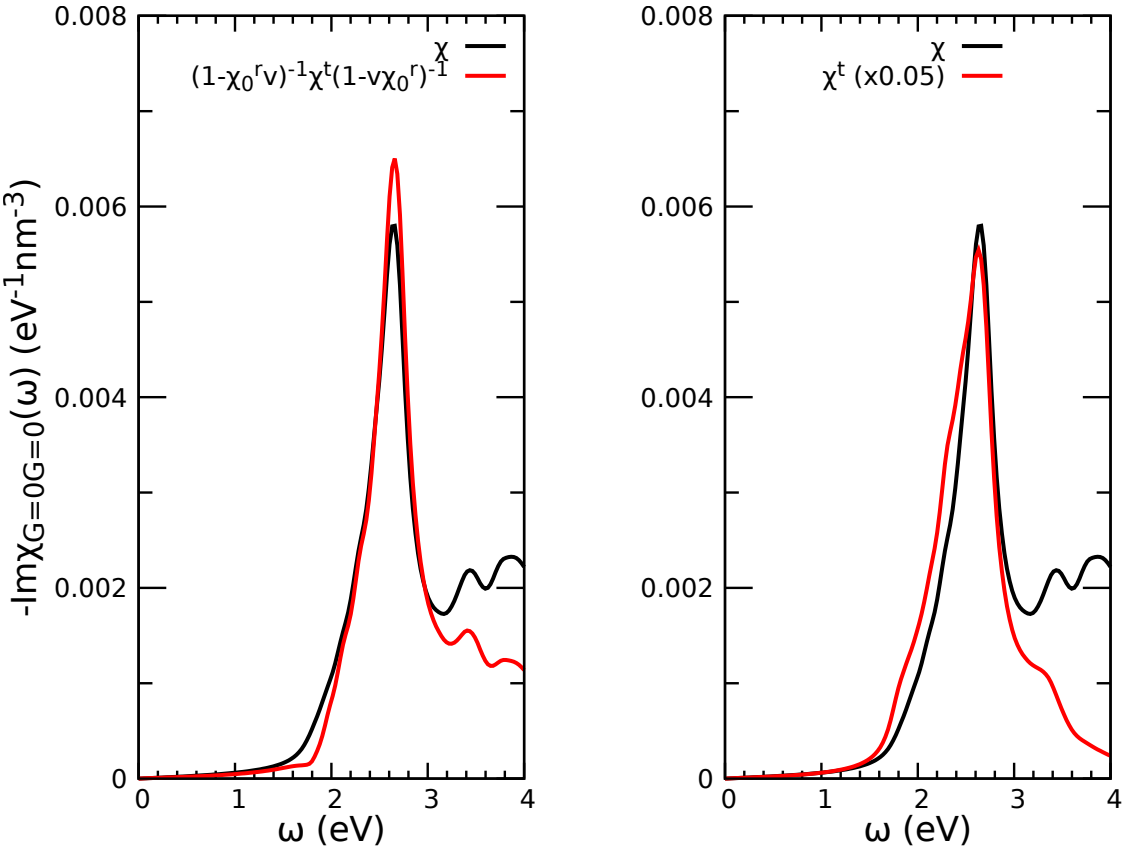

Figure 3.20: $\chi^t(\omega)$ for the two orbital Hilbert space. Left: $[\chi^t(\omega)]1 - \tilde{v}\chi_0^r(\omega)^{-2}$ (red) and $\chi(\omega)$ (black) plotted in *absolute* units. Right: $\chi^t(\omega)$ (red) and $\chi(\omega)$ (black) where the target response has been scaled down by a factor of 25. It can be seen in both figures that the response from these two orbitals captures the physics of the collective mode seen at $\omega \sim 2.6$ eV.

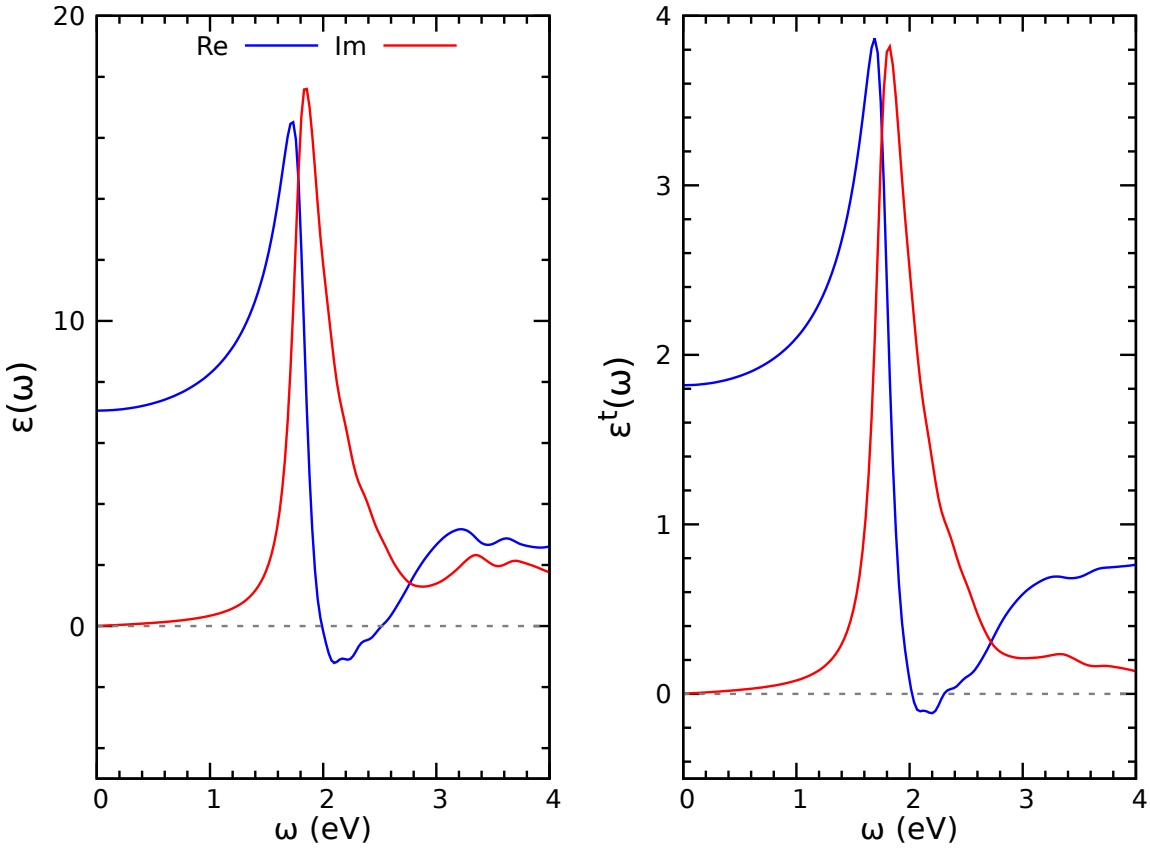

Figure 3.21: $\varepsilon(\omega)$ and $\varepsilon^t(\omega)$. Left: The dielectric function obtained using the inverse of the relation $\varepsilon^{-1} = (\varepsilon^t)^{-1}(\varepsilon^r)^{-1}$ from equation 2.111. Right: $\varepsilon^t(\omega)$ calculated from the two orbital Hilbert space using equation 2.112. It can be seen that the line shapes are very similar and both capture the pole, but the target space dielectric function is about $5\times$ smaller than the calculation which includes the degrees of freedom from the rest space.

Now that I have shown that we can reproduce the collective mode within the target Hilbert space of two orbitals, I will unveil some of the physics that gives rise to the spectra. First, I want to understand the 'size' of the collective mode. In the electron gas paradigm for simple metals, the plasmon can be interpreted as a collective oscillation of the *entire* gas of electrons. Within the random-phase approximation [168–170], the plasma frequency is given by a L'Hospital interplay between the long wave length limit of the Lindhard function, which is proportional to q^2, with that from the divergent $1/q^2$ behavior of the Coulomb interaction and is *entirely* controlled by the *homogeneous* electron density n, i.e. $\omega_p = \sqrt{4\pi n e^2/m}$. However, the one dimensional cuprates' physics are quite different since they are not metals nor is the electron density homogeneous, so this interpretation cannot be assumed to be the case for this excitation.

To gain insight into the 'size', I have restricted the sum over lattice vectors by the number of unit cells included in the target space response calculation. In figure 3.22, I show that this collective mode is indeed an excitation which consists of electron-hole pairs which span the entire macrocrystal by plotting $\chi^t_{\uparrow\uparrow}(\omega)$, $\chi^t_{\uparrow\downarrow}(\omega)$, $\chi^t_{nn}(\omega)$, and $\chi^t_{S_z S_z}(\omega)$ in terms of unit cells included in the calculation. For a small portion of the macrocrystal, the agreement with the entire macrocrystal is quite poor.

In a similar spirit, I also examine the role of size and the effective interaction on the calculation for the optical conductivity. It can be seen in the top right panel of figure 3.23, that if the calculation includes the effective interaction, the optical conductivity appears to be just a scale factor between the calculations of different size. However, if the interaction is ignored, the calculation is degraded which is shown in the top left panel of figure 3.23. For a calculation of about $\sim$ three unit cells (bottom left panel of figure 3.23), these calculations are almost identical which is a consequence of the Coulomb interaction not having enough space to act. I also show that the optical conductivity of the target space does not agree in *intensity* with that of the true physical conductivity, seen in the bottom right panel of figure 3.23.

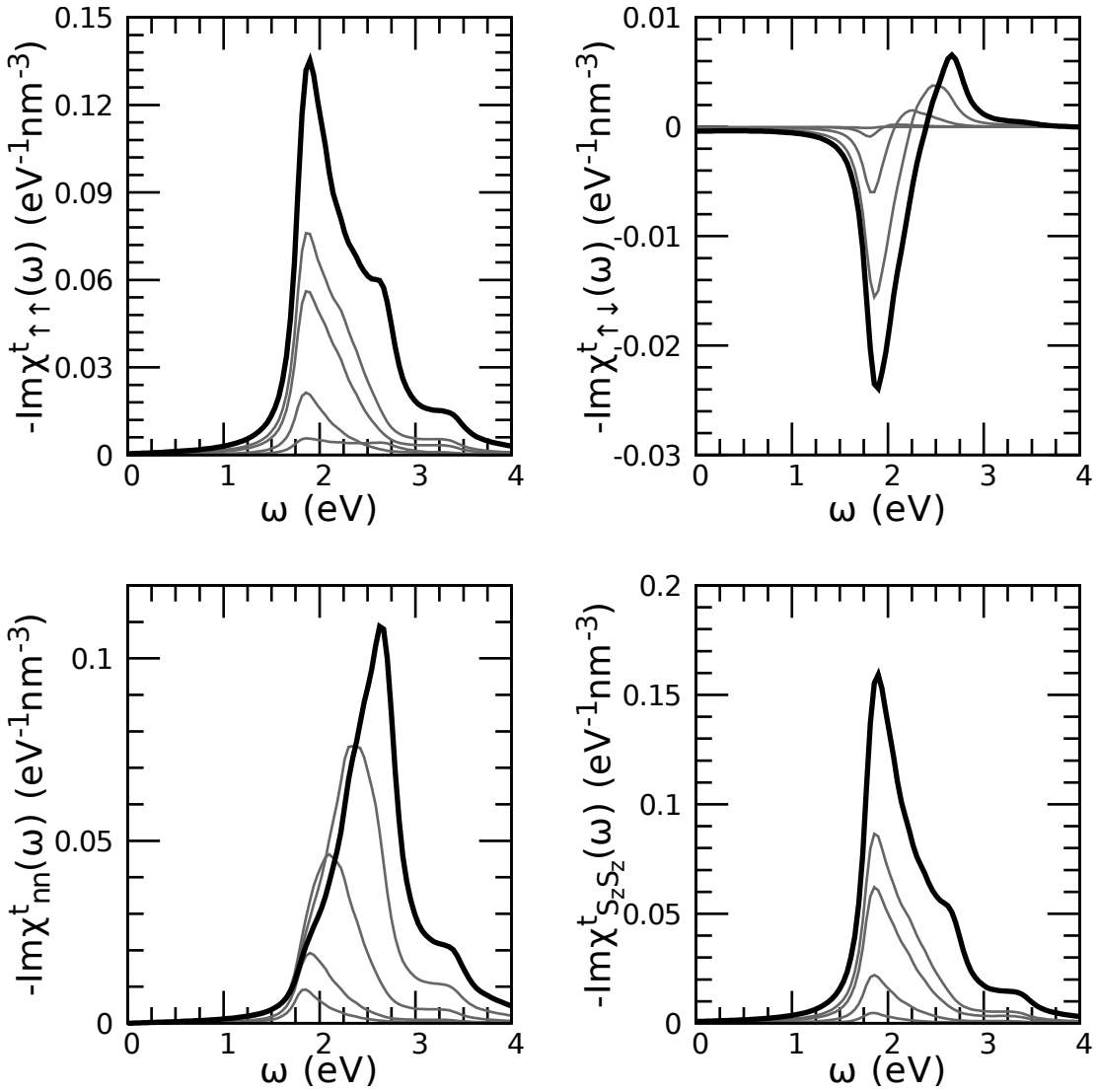

Figure 3.22: Size of collective mode for Sr_2CuO_3. Top left: $\chi^t_{\uparrow\uparrow}(\omega)$. Top right: $\chi^t_{\uparrow\downarrow}(\omega)$. Bottom left: $\chi^t_{nn}(\omega)$. Bottom right: $\chi^t_{S_zS_z}(\omega)$. All calculations shown are for one, five, nine, thirteen unit cells (thin grey curves) and the entire macrocrystal (thick black curve).

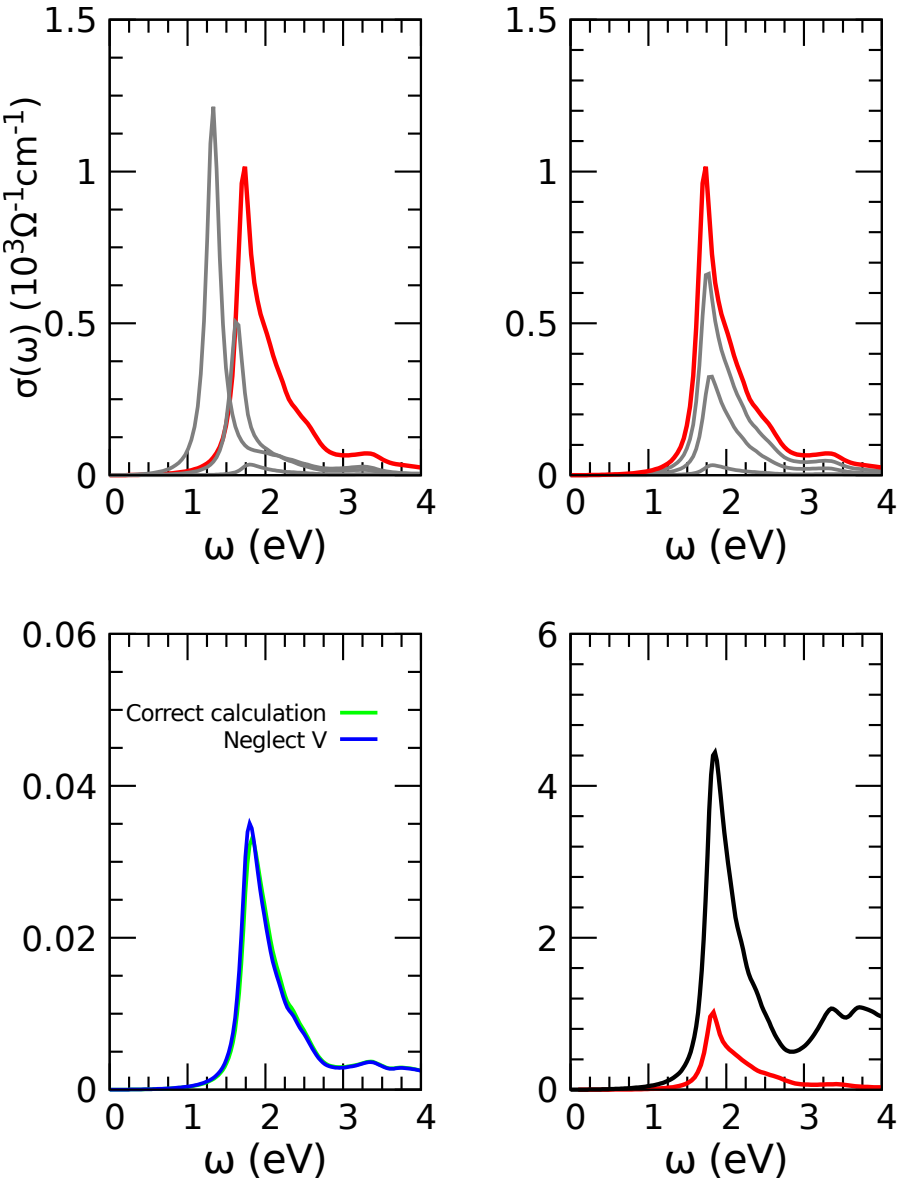

Figure 3.23: Lattice vector dependence of optical conductivity. Top left: computation where effective interaction is completely ignored and summing over different number of lattice vectors. Top right: computation including effective interaction and summing over different number of lattice vectors. Bottom left: Comparing the calculation with and without effective interaction summing over three unit cells. Bottom right: comparing optical conductivity of target (red curve) with the optical conductivity of entire Hilbert space.

Since electron-hole propagation occuring over the *entire* macrocrystal has been established, I will now discuss the role of the *spin* and *orbital* degree of freedom. This calculation is very pertinent to the relevance of *spin-charge* separation since the interpretation of these Mott-gapped excitations have been in terms of a spin-independent background consisting of holon-doublon particle hole pairs for EELS [33] and a *continuum* of holon-antiholon pairs for the RIXS measurements [161].

Here, I performed three different calculations where I impose errors by suppressing terms in $\tilde{v}^{\sigma\sigma'}_{1234}(\omega)$ to compare with the correct calculation within the target space. In the first calculation, I suppress spin-reversal terms in the effective interaction $\tilde{v}^{\sigma\sigma'}_{1234}(\omega)$ meaning I set $\tilde{v}^{\uparrow\downarrow}_{1234}(\omega) = 0$ and $\tilde{v}^{\downarrow\uparrow}_{1234}(\omega) = 0$. The resulting dielectric and loss function are in the second column of figure 3.24. This is to be compared with the first column which shows the *correct* calculation in the absence of errors imposed within the target space. In the second calculation, I suppressed the coupling between charge fluctuations, triggered by $\tilde{v}^{\sigma\sigma'}_{1234}(\omega)$, *across* the two chains throughout the macroscrystal and the resulting spectra are shown in the third column of figure 3.24. In the third calculation I ignored the charge fluctuations that involved spin-reversal *and* across both chains which is shown the fourth column of figure 3.24.

Each of these approximations *ruins* the integrity of the *pole*, hence destroys the collective mode. Furthermore, it can be seen in appendix A that a requirement to bosonize the Hamiltonian, one must neglect the backscattering spin-reversal terms in the Hamiltonian. Therefore, our calculation shows that the spin-reversal terms are *necessary* and cannot simply be ignored to describe the dynamics properly. This calculation strongly suggests that the fractionalization paradigm *appears* to break down for the Mott-gapped particle-hole excitations. Furthermore, when we restrict the electron-hole fluctuations to one CuO_3 chain, the pole is also compromised suggesting that the excitation is three dimensional in nature. It is also noteworthy that in one dimension, the Coulomb interaction cannot behave like $1/|\vec{q}|^2$ due to dimensional analysis. Also, the calculation where both approximations result in an even worse degradation of the pole.

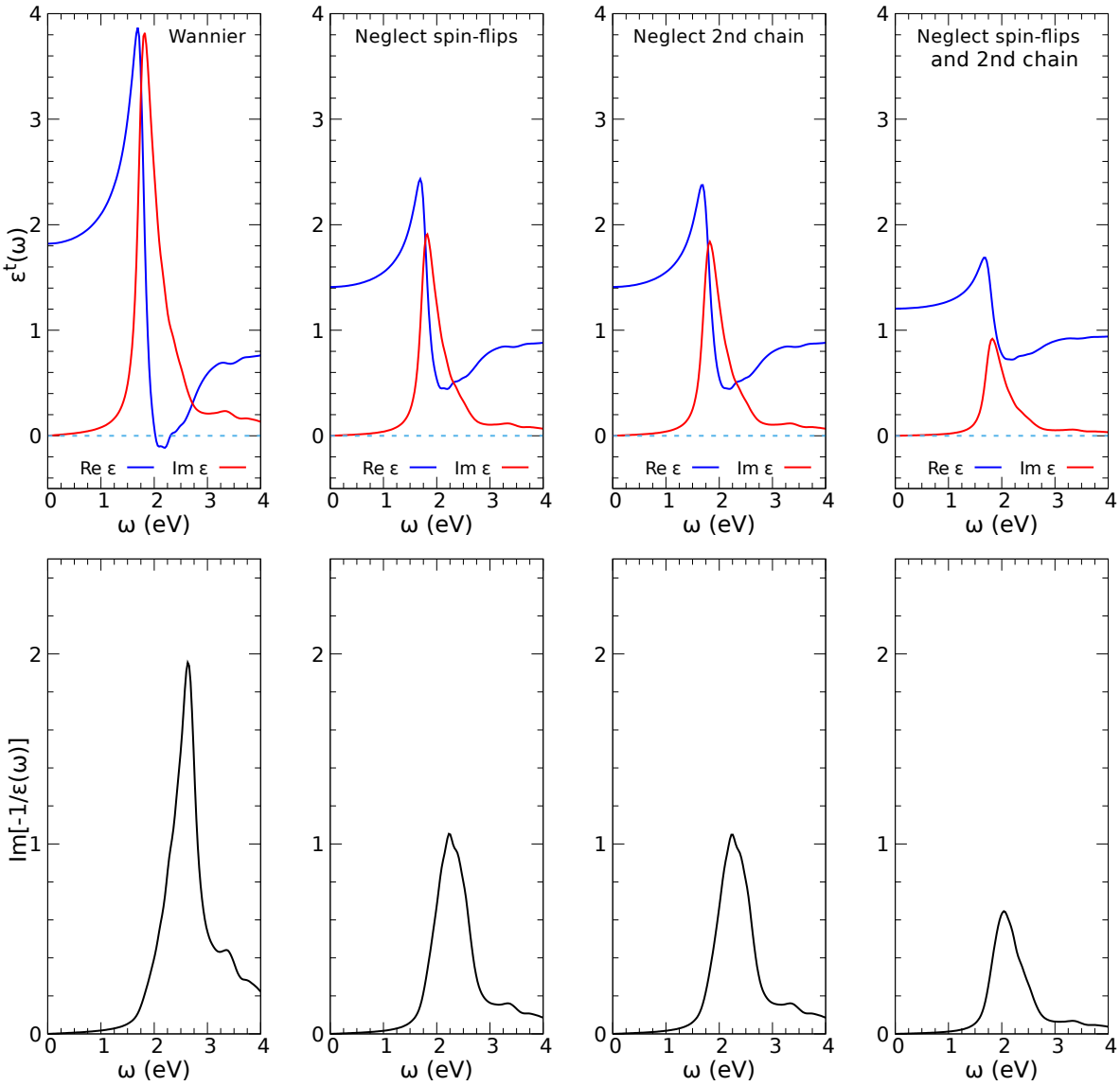

Figure 3.24: Impact on $\varepsilon^t(\omega)$ and $\mathrm{Im}(-1/\varepsilon^t(\vec{q},\omega))$ when spin-reversal and three dimensional coupling in the effective interaction are suppressed. First column: No approximations in target space. Second column: calculation where spin-reversal terms in $\tilde{v}^{\sigma\sigma'}_{1234}(\omega)$ are suppressed. Third column: calculation where $\tilde{v}^{\sigma\sigma'}_{1234}(\omega)$ between both chains in unit cell are suppressed. Fourth column: calculation where $\tilde{v}^{\sigma\sigma'}_{1234}(\omega)$ that involve spin reversal and interchain terms are suppressed.

Zeroth Order Dynamics: Definition of Classes

Although I have given a hint of some of the ingredients that comprise the collective mode, what I have shown is still very much a black box. To get inside the black box, I must show the microscopic physics behind $(\chi^t)^{\sigma\sigma'}_{1234}(\omega)$. As a first approximation, I am going to *completely ignore* the role that the effective interaction $\tilde{v}^{\sigma\sigma'}_{1234}(\omega)$ between pairs of the Kohn-Sham electron-hole pairs. This amounts to understanding $(\chi^t_0)^{\sigma\sigma'}_{1234}(\omega)$ and its propagation to the spectra it produces $(\chi^t_0)_{\vec{G}_{\vec{q}}=\vec{0}\vec{G}_{\vec{q}}=\vec{0}}$. As derived in appendix F, $(\chi^t_0)_{1234}(\vec{q},\omega)$ in the Wannier basis takes the form

$$\left(\chi^t_0\right)_{1234}(\vec{q},\omega) \equiv \left(\chi^t_0\right)^{\sigma' n_3 \vec{R}_3, \sigma' n_4 \vec{R}_4}_{\sigma n_1 \vec{R}_1, \sigma n_2 \vec{R}_2}(\vec{q},\omega)$$

$$= \delta_{\sigma\sigma'} \frac{1}{(N_{BvK})^2} \frac{1}{V_{BvK}} e^{-i\vec{q}\cdot(\vec{R}_4-\vec{R}_2)} \sum_{\vec{k}}^{1BZ} e^{i\vec{k}\cdot(\vec{R}_2-\vec{R}_1)} e^{-i\vec{k}\cdot(\vec{R}_4-\vec{R}_3)} \sum_{jj'} c^*_{jn_1\sigma}(\vec{k}) c_{j'n_2\sigma}(\vec{k}+\vec{q})$$

$$\times \frac{f_{\vec{k}+\vec{q}j'\sigma} - f_{\vec{k}j\sigma}}{\varepsilon_{\vec{k}+\vec{q}j'\sigma} - \varepsilon_{\vec{k}j\sigma} + \hbar(\omega + i\eta^+)} c^*_{j'n_4\sigma}(\vec{k}+\vec{q}) c_{jn_3\sigma}(\vec{k}), \tag{3.7}$$

where the c's correspond to the expansion coefficients from the Bloch to the Wannier basis, the f's are the occupancies with respect to the Kohn-Sham band structure and the ε's are the Kohn-Sham eigenvalues. For an insulating band structure in the optical limit ($\vec{q} \to \vec{0}$), this expression simplifies to

$$\left(\chi^t_0\right)^{\sigma\sigma'}_{1234}(\omega) = \delta_{\sigma\sigma'} \frac{1}{(N_{BvK})^2} \frac{1}{V_{BvK}} \sum_{\vec{k}}^{1BZ} e^{i\vec{k}\cdot\left[(\vec{R}_2-\vec{R}_1)-(\vec{R}_4-\vec{R}_3)\right]} \sum_{jj'} c^*_{jn_1\sigma}(\vec{k}) c_{j'n_2\sigma}(\vec{k})$$

$$\times \frac{f_{\vec{k}j'\sigma} - f_{\vec{k}j\sigma}}{\varepsilon_{\vec{k}j'\sigma} - \varepsilon_{\vec{k}j\sigma} + \hbar(\omega + i\eta^+)} c^*_{j'n_4\sigma}(\vec{k}) c_{jn_3\sigma}(\vec{k}). \tag{3.8}$$

As evident in equation 3.8, the Kohn-Sham 'propagators' are controlled by the distance $\vec{R}-\vec{R}'$ where $\vec{R} \equiv \vec{R}_2 - \vec{R}_1$ and $\vec{R}' \equiv \vec{R}_4 - \vec{R}_3$. This allows for the *definition* of classes defined by pairs of Kohn-Sham electron-hole pairs which have the same value of $\vec{R}-\vec{R}'$. This greatly simplifies the amount of topologically distinct charge

fluctuations that need to be considered in the calculation[6]. It will turn out there are only two classes needed to describe the dynamics which are shown in figure 3.25. I will refer to these classes as class a and class b. Class a is where $\vec{R} - \vec{R}' = 0\vec{a}$ where $\vec{a}$ is the lattice vector along the chain direction. This class involves an electron in the copper one plaquette fills the hole in the copper two plaquette creating an electron-hole pair with a distance[7] $\vec{R}$. Then the electron-hole pair will propagate to another electron-hole pair which are separated by the same distance as the original created electron-hole pair. Class b is defined where $\vec{R} - \vec{R}' = \pm 1\vec{a}$.

Most of the spectrum comes from the top left and top right panels of figure 3.25 which are subsets from classes a and b. In the left panel of figure 3.26, summing over these two subsets gives the red curve, and longer range class b configurations, such as that shown in the bottom left panel of 3.25, gives the remaining $\sim 20\%$ of the spectrum. The black curve shows the contribution from *all* classes. In panel b of figure 3.26, I separated the contribution from the top left and top right panels from classes a and b of figure 3.25. It can be seen that each of these classes have a two peak structure, however they cancel in a manner in which the *total* spectrum has only one peak.

To my knowledge, a figure of this nature has not been produced in any literature published and gives valuable insight into the nature of an excitation. Usually, in an experiment, we see several peaks with different intensities, and we attribute them to *separate* excitations. Here, by getting inside the black box of the calculation, the origin of several peaks seen in experiments most likely have their origin in the interference of several complicated line shapes and probably should not be interpreted as *separate* excitations. This message will be important in describing features seen for larger wave vectors where a shoulder appears in the spectrum from the interference.

[6]To avoid redundancies, I only show the result for one spin projection which I choose to be $\sigma = \uparrow$. Since I am using an antiferromagnetic ground state, the $\sigma = \downarrow$ projection is exactly identical but interchanging copper 1 and copper 2.

[7]I would like to mention that $\vec{R}$ does not give the distance between orbitals, but the difference in unit cells in which they are located at. To find the distance, one must additionally have to know which orbital in the unit cell the electron and hole are referring to.

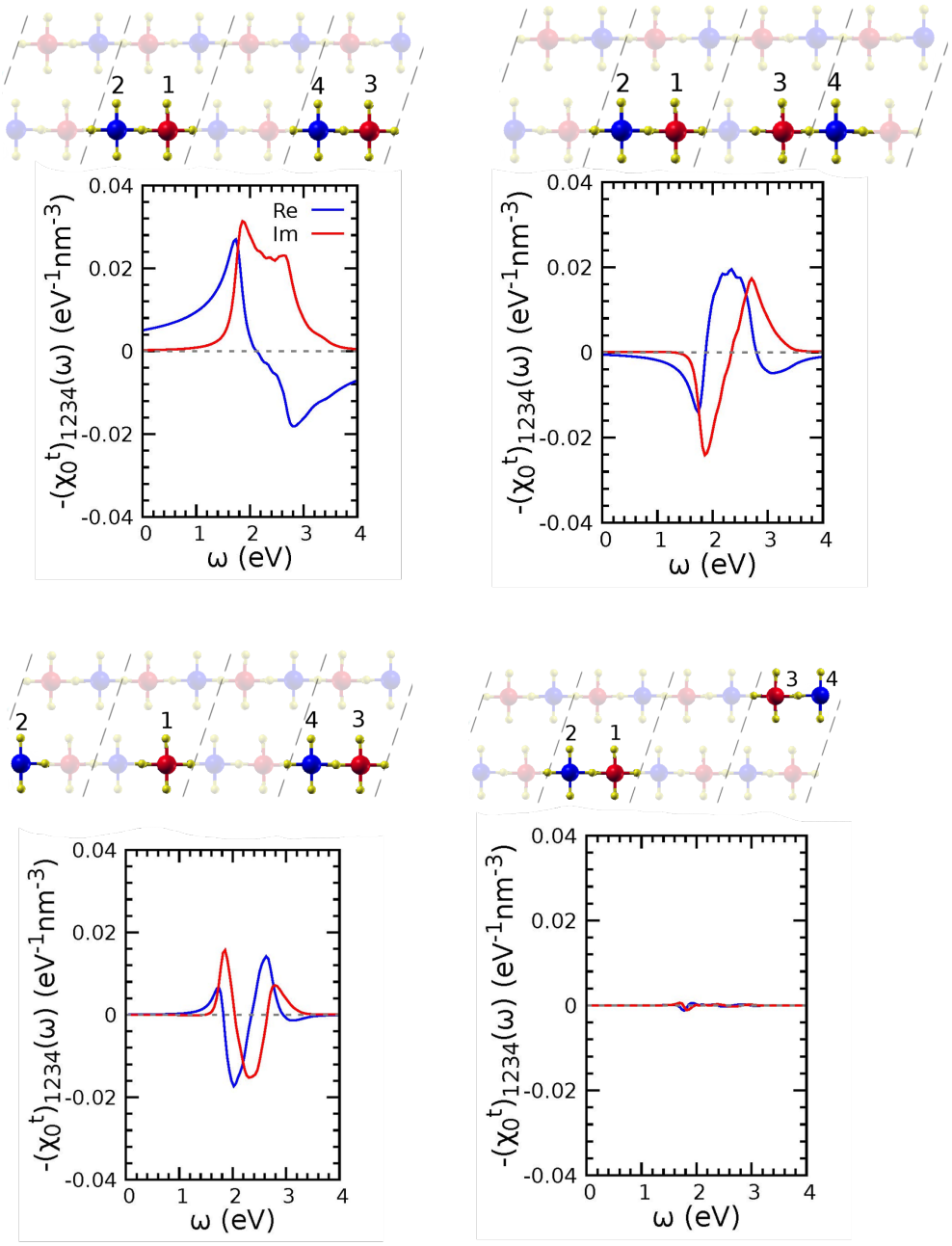

Figure 3.25: Examples of classes for $(\chi_0^t)_{1234}(\omega)$. Top left: Class a fluctuations where $\vec{R} - \vec{R}' = \vec{0}$ involving both pairs of Kohn-Sham electron-hole pairs in one chain. Top right: Class b fluctuations where $\vec{R} - \vec{R}' = \pm\vec{1}a$ involving both pairs of Kohn-Sham electron-hole pairs in one chain. Bottom left: Class b (long) fluctuations where one of the Kohn-Sham electron-hole pairs are the third nearest neighbor apart. Bottom right: Class a fluctuations where $\vec{R} - \vec{R}' = \vec{0}a$ involving both pairs of Kohn-Sham electron-hole pairs residing in two chains.

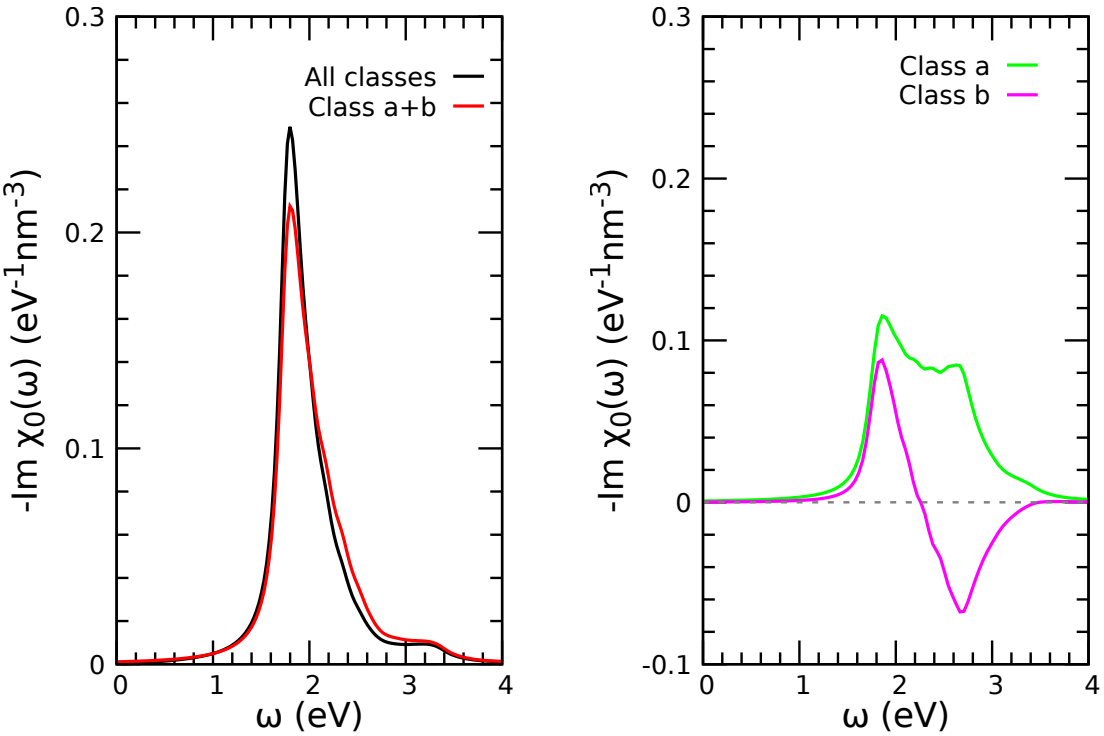

Figure 3.26: Spectrum produced from $(\chi_0^t)_{1234}(\omega)$. Left: $\chi_0(\omega)$ produced from all classes (black curve) and from class a and b (red curve) from the top left and top right panels of figure 3.25. Right: Separate contribution to $\chi_0(\omega)$ from class a and b from the top left and top right panels of figure 3.25.

First Order Dynamics: Effects of the Effective Interaction

Since the response is well understood in the absence of the effective interaction between Kohn-Sham electron hole pairs as shown in the previous section, we want to understand the role of the interaction and its propagation to spectroscopy. As derived in appendix F, the effective interaction between pairs of electron-hole pairs is given by the equation

$$v^{\sigma\sigma'}_{1234}(\vec{q},\omega) = \sum_{\vec{G}\vec{G}'} A^{\sigma *}_{12}(\vec{q}+\vec{G})\tilde{v}_{\vec{G}\vec{G}'}(\vec{q},\omega)A^{\sigma}_{34}(\vec{q}+\vec{G}'), \tag{3.9}$$

where $\tilde{v}_{\vec{G}\vec{G}'}(\vec{q},\omega)$ is the *dynamically* screened Coulomb interaction in which the screening is due to electron-hole polarization processes which are outside the target Hilbert space[8], i.e.

$$\tilde{v}_{\vec{G}\vec{G}'}(\vec{q},\omega) = \frac{4\pi e^2}{|\vec{q}+\vec{G}|^2}(\varepsilon^r)^{-1}_{\vec{G}\vec{G}'}(\vec{q},\omega). \tag{3.10}$$

In figure 3.27, I have shown the real and imaginary[9] part of the effective interaction for configurations of class a. One novelty that emerges is the coupling of electron-hole pairs of one spin projection with that of the opposite spin projection[10]. Additionally, there is a coupling of electron-hole pairs in one of the chains in the unit cell with that of the other which will inhibit electron-hole processes from one chain to propagate into the other. This process is *negligible* in the absence of the effective interaction seen in the bottom right panel of figure 3.25. It is also noteworthy that some of these interactions are *attractive* in nature shown second and third panels of figure 3.27.

In the optical limit, the interaction in equation 3.9 can be conveniently cast as

$$v^{\sigma\sigma'}_{1234}(\omega) = \lim_{\vec{q}\to\vec{0}} A^{\sigma *}_{12}(\vec{q})\tilde{v}_{\vec{0}\vec{0}}(\vec{q},\omega)A^{\sigma}_{34}(\vec{q}) + \lim_{\vec{q}\to\vec{0}} \sum_{\vec{G}\vec{G}'\neq\vec{0}} A^{\sigma *}_{12}(\vec{q}+\vec{G})\tilde{v}_{\vec{G}\vec{G}'}(\omega)A^{\sigma}_{34}(\vec{q}+\vec{G}'), \tag{3.11}$$

[8] There are processes in which an electron(hole) within the target space can fill a hole(electron) outside the target space. These polarization processes also screen the interaction.

[9] The imaginary part comes from processes that are not included in the target space but are within the energy range of interest.

[10] Each of the electron-hole pairs has the *same* spin projection.

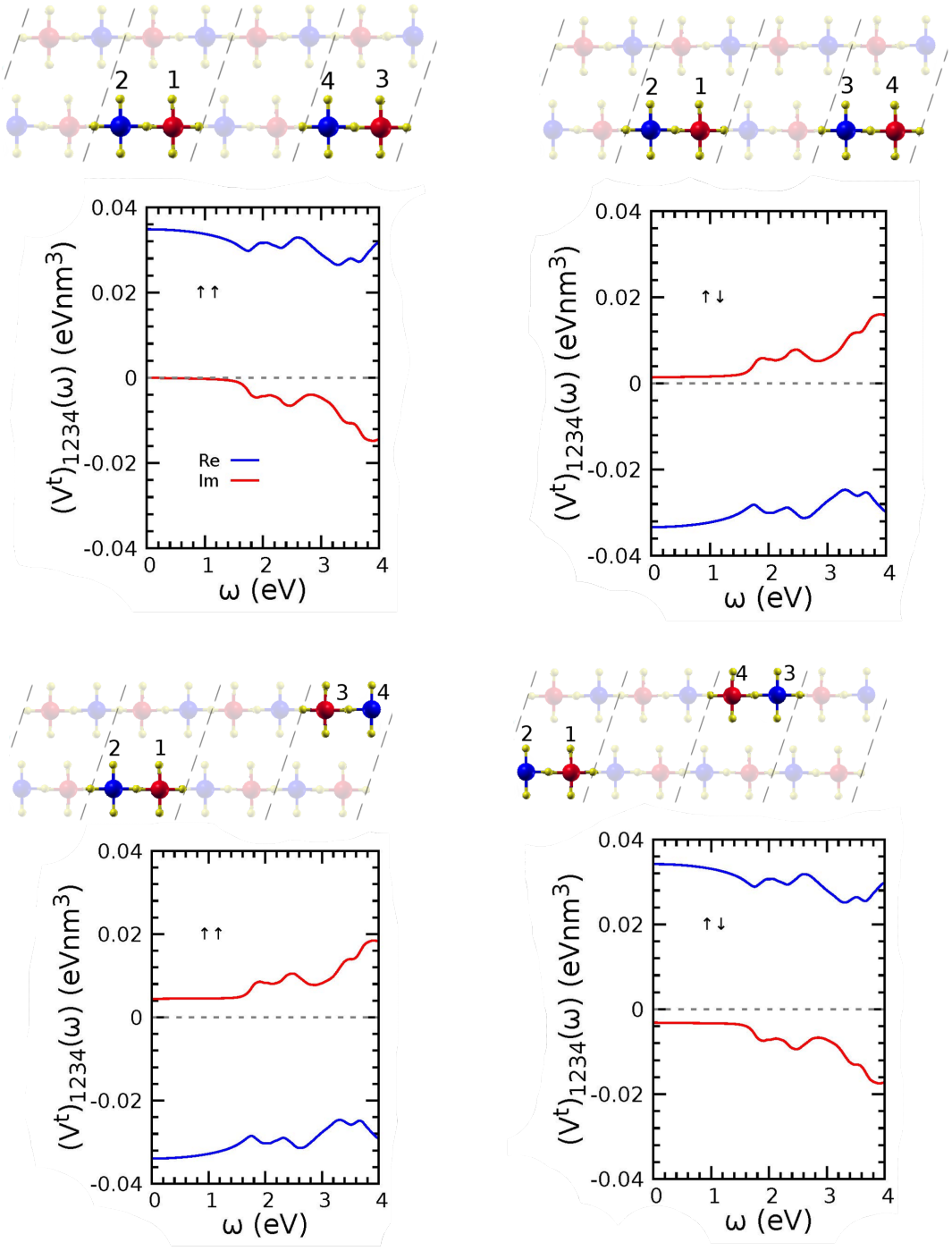

Figure 3.27: $\tilde{v}_{1234}(\omega)$ for all class a configurations. Top left: all four Wannier orbitals in one chain with the same spin projection. Top right: all four Wannier orbitals in one chain where each electron-hole pair has the opposite spin projection as the other (spin-reversal). Top right: one electron-hole pair in one chain and the other pair is in the other chain with the same spin projection. Bottom left: one electron-hole pair in one chain and the other pair is in the other chain with the opposite spin projection.

where we have *isolated* the $\vec{G} = \vec{G}' = \vec{0}$ term in the summation. In the optical limit, we expand the charge fluctuation matrix element $A_{12}^{\sigma*}(\vec{q})$ as

$$A_{12}^{\sigma*}(\vec{q}) = \int d^3x w_{n_2\sigma}^*(\vec{x} - \vec{R}_2) e^{i\vec{q}\cdot\vec{x}} w_{n_1\sigma}(\vec{x} - \vec{R}_1)$$

$$= \int d^3x w_{n_2\sigma}^*(\vec{x}-\vec{R}_2) w_{n_1\sigma}(\vec{x}-\vec{R}_1) + i\vec{q}\cdot \int d^3x w_{n_2\sigma}^*(\vec{x}-\vec{R}_2)\vec{x} w_{n_1\sigma}(\vec{x}-\vec{R}_1) + \dots \quad (3.12)$$

The first term in this is zero since the Wannier orbitals are orthonormal. Therefore, by keeping the first non-zero contribution, the charge fluctuation matrix element can be approximated as

$$A_{12}^{\sigma*}(\vec{q}) \approx i\vec{q}\cdot \int d^3x w_{n_2\sigma}^*(\vec{x} - \vec{R}_2)\vec{x} w_{n_1\sigma}(\vec{x} - \vec{R}_1). \quad (3.13)$$

For $\vec{G} = \vec{G}' = \vec{0}$, the dynamically screened interaction is

$$\tilde{v}_{\vec{0}\vec{0}}(\vec{q},\omega) = \frac{4\pi e^2}{|\vec{q}|^2} (\varepsilon^r)^{-1}_{\vec{0}\vec{0}}(\omega), \quad (3.14)$$

Using the above approximations, equation 3.11 can be approximated by the first term as

$$\lim_{\vec{q}\to\vec{0}} A_{12}^{\sigma*}(\vec{q}) \tilde{v}_{\vec{0}\vec{0}}(\vec{q},\omega) A_{34}^{\sigma'}(\vec{q}) \approx 4\pi e^2 (\varepsilon^r)^{-1}_{\vec{0}\vec{0}}(\omega) \lim_{\vec{q}\to\vec{0}} \frac{1}{|\vec{q}|^2} \left[\vec{q}\cdot \int d^3x w_{n_2\sigma}(\vec{x} - \vec{R}_2)\vec{x} w_{n_1\sigma}^*(\vec{x} - \vec{R}_1) \right.$$

$$\left. \times \vec{q}\cdot \int d^3x' w_{n_4\sigma}^*(\vec{x}' - \vec{R}_4)\vec{x}' w_{n_3\sigma}(\vec{x}' - \vec{R}_3) \right]. \quad (3.15)$$

At this point, it is convenient to define the *electric* dipole moment between Wannier orbitals

$$\vec{d}_{12}^{\sigma} \equiv \sqrt{4\pi e^2} \int d^3x w_{n_1\sigma}(\vec{x} - \vec{R}_1)\vec{x} w_{n_2\sigma}^*(\vec{x} - \vec{R}_2), \quad (3.16)$$

and its projection along the direction of $\vec{q}$

$$d_{12}^{\sigma}(\hat{q}) \equiv \frac{\vec{q}}{|\vec{q}|}\cdot \vec{d}_{12}. \quad (3.17)$$

Using the above manipulations, the effective interaction in the Wannier basis can be approximated in a form which has a physical interpretation

$$v^{\sigma\sigma'}_{1234}(\omega) \approx d^{\sigma *}_{12}(\hat{q}) d^{\sigma}_{34}(\hat{q}) (\varepsilon^{r})^{-1}_{\vec{0}\vec{0}}(\omega) \tag{3.18}$$

in terms of solid state chemistry and dynamical screening. I will refer to the terms that are not included in this approximation as crystal local field effects (CLFE). In the optical limit, equation 3.18 is a very good approximation which can be seen in figure 3.28 where the dashed lines show the interaction within this approximation, and the solid lines are the calculation of the effective interaction by summing over all reciprocal lattice vectors.

Now we have a physically motivated approximation to the Coulomb interaction, and we can understand the mediators of electron-hole propagation in terms the product of *electric dipole moments* and *dynamical screening* triggering the collective mode. We can now inspect the impact this has on the first order term in the geometric series for $(\chi^{t})^{\sigma\sigma'}_{1234}(\omega)$, so we are considering the quantity

$$\sum_{\sigma_1\sigma_2} \sum_{\bar{1}\bar{2}\bar{3}\bar{4}} \left(\chi^{t}_{0}\right)^{\sigma\sigma_1}_{12\bar{1}\bar{2}}(\omega) \tilde{v}^{\sigma_1\sigma_2}_{\bar{1}\bar{2}\bar{3}\bar{4}}(\omega) \left(\chi^{t}_{0}\right)^{\sigma_2\sigma'}_{\bar{3}\bar{4}34}(\omega). \tag{3.19}$$

I have shown the contributions from the most important subset of class a configurations in figure 3.29.

In the absence of the effective interaction, the top right and bottom left panels of figure 3.29 were identically zero due to $(\chi^{t}_{0})^{\sigma\sigma'}_{1234}(\omega)$ being diagonal with respect to the spin index. Also, the bottom right panel in figure 3.25 was extremely small and played no role in the spectra produced but now must be considered due to the coupling of the chains by the effective interaction. By looking at the first order term in the series, we can now start to see the role of the effective interaction. In figure 3.30, I have shown the sum of the zeroth and first order terms for the terms that had a finite contribution in $(\chi^{t}_{0})_{\vec{G}_{\vec{q}}=\vec{0}\vec{G}_{\vec{q}}=\vec{0}}(\omega)$.

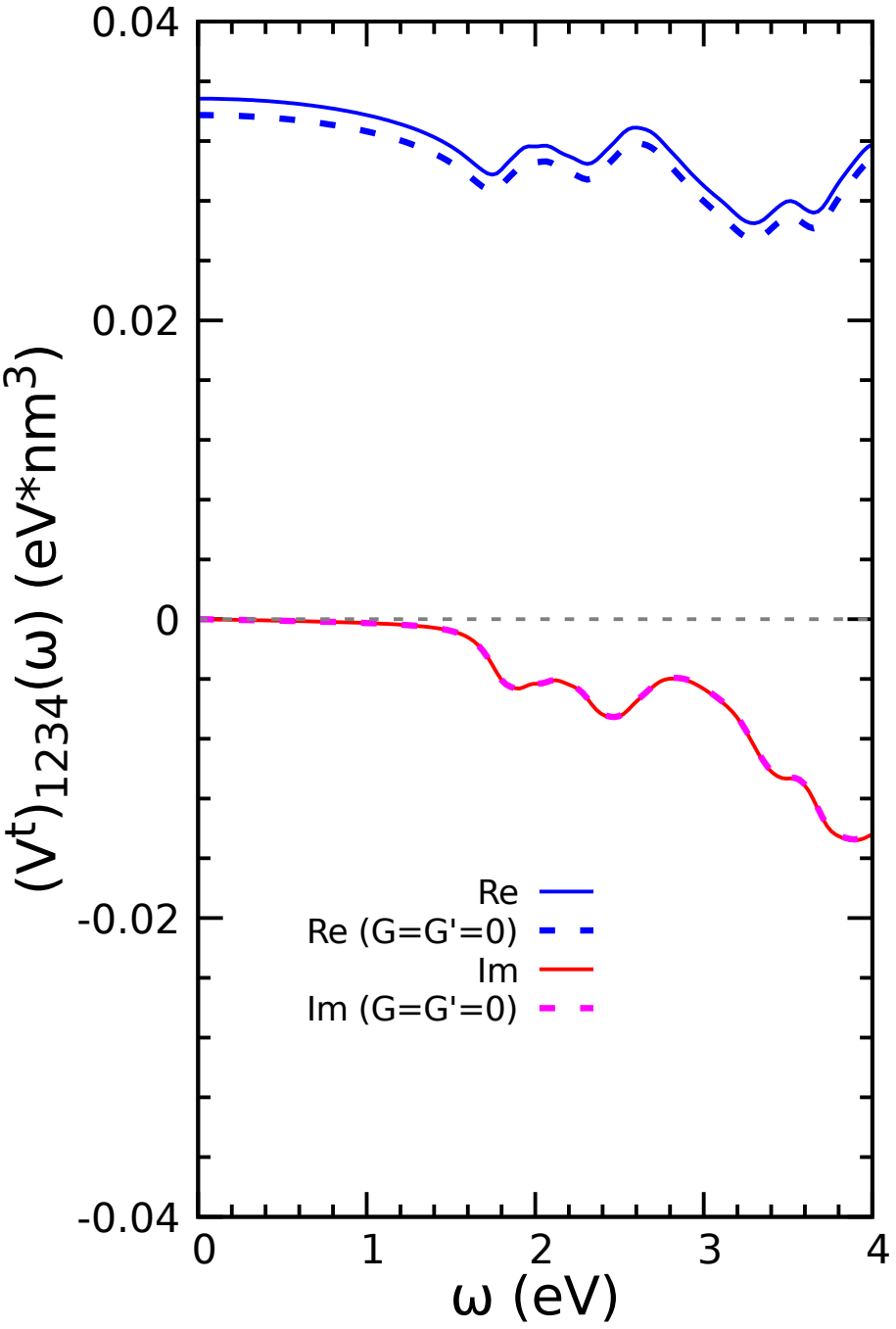

Figure 3.28: Effect of crystal local field effects on the effective interaction in the Wannier basis. The dashed lines represent the effective interaction by only considering the $\vec{G} = \vec{G}' = \vec{0}$ term in the summation.

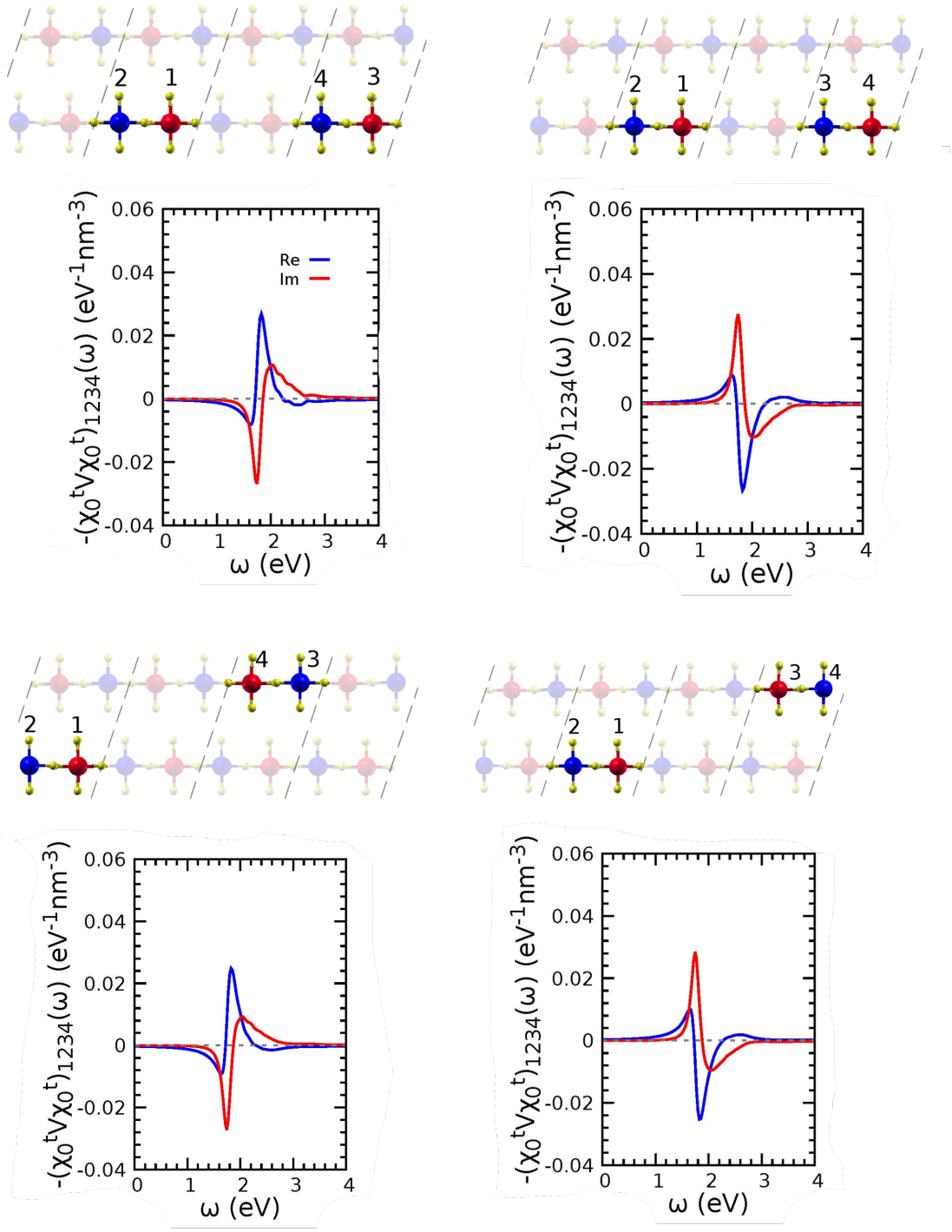

Figure 3.29: $(\chi_0^t \tilde{v} \chi_0^t)_{1234}(\omega)$ for class a configurations. Top left: all four Wannier orbitals in one chain with the same spin projection. Top right: all four Wannier orbitals in one chain where each electron-hole pair has the opposite spin projection as the other (spin-reversal). Top right: one electron-hole pair in one chain and the other pair is in the other chain with the same spin projection. Bottom left: one electron-hole pair in one chain and the other pair is in the other chain with the opposite spin projection.

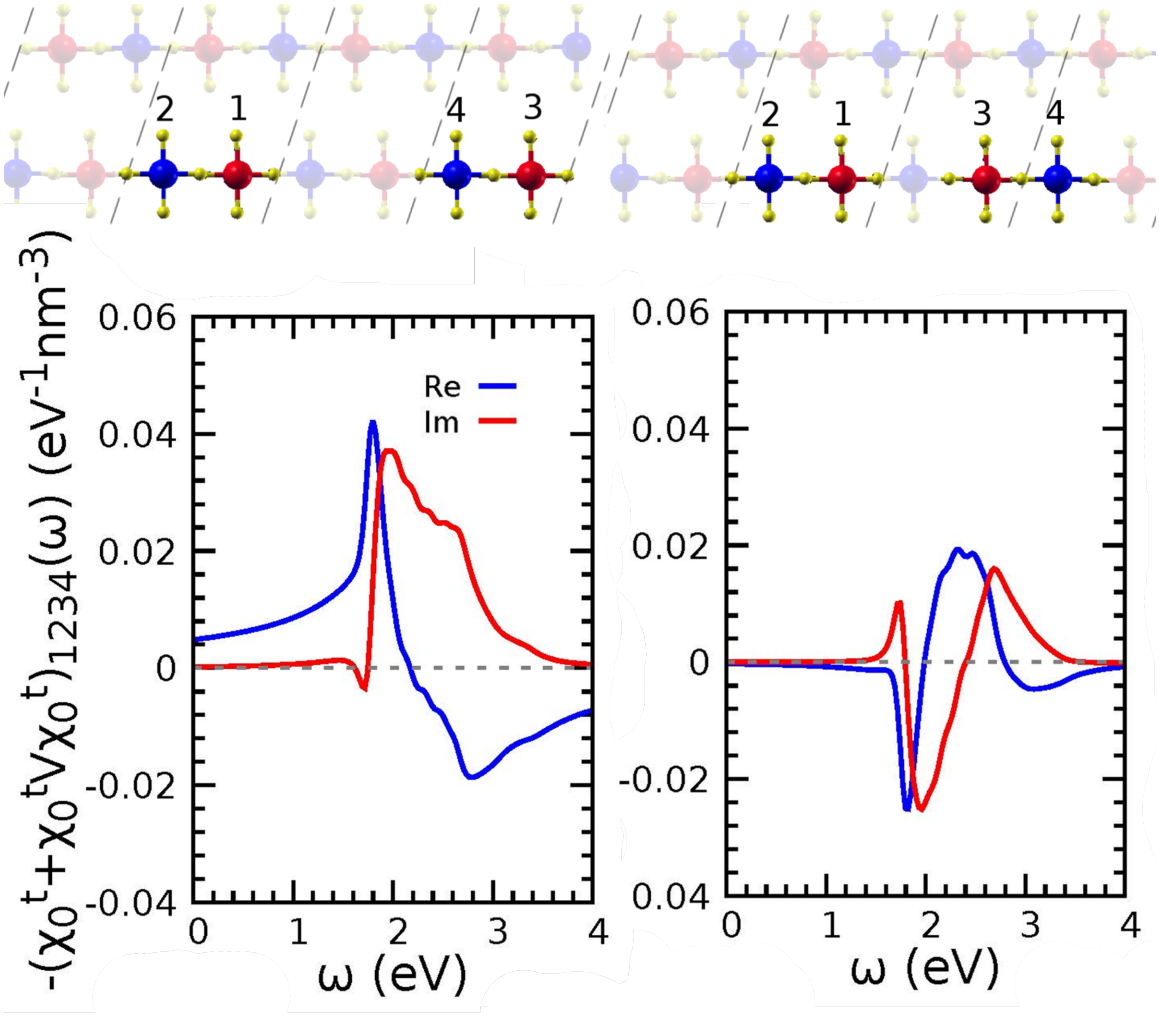

Figure 3.30: $(\chi_0^t + \chi_0^t \tilde{v} \chi_0^t)^{\sigma\sigma}_{1234}(\omega)$. Left: An example of the largest contribution from class a. Right: An example of the largest contribution from class b.

It can be seen in figure 3.31, that the quantity

$$\lim_{\vec{q}\to\vec{0}} \sum_{\sigma\sigma'} \sum_{\bar{1}\bar{2}\bar{3}\bar{4}} A^{\sigma}_{\bar{1}\bar{2}}(\vec{q}) \left[(\chi_0)^t(\omega) + (\chi_0)^t(\omega)\tilde{v}(\omega)(\chi_0)^t(\omega) \right]^{\sigma\sigma'}_{\bar{1}\bar{2}\bar{3}\bar{4}} A^{\sigma'*}_{\bar{3}\bar{4}}(\vec{q}), \tag{3.20}$$

which is the density response function calulated up to first order in the effective interaction does not yield anything closely resembling the spectrum shown in figure 3.20. Moreover, summing up to the first order term does not even yield a *physical* response since the response has to be positive definite within the framework of linear response.

Additionally, by adding the second order term in $\tilde{v}$, third order term, etc. (not shown) does not converge or resemble anything close to the response shown in 3.20. Hence the *pole* exists through a summation to *all* orders in the effective interation in the geometric series to obtain $(\chi^t)^{\sigma\sigma'}_{1234}(\omega)$. This is indicative of the *existence* of the pole by definition. This physics should manifest itself in the electron-hole propagators computed to infinite order in the effective interaction.

In the next section, I will introduce the physics obtained from considering the entire geometric series of the four point functions that generate $(\chi^t)^{\sigma\sigma'}_{1234}(\omega)$. There, I will introduce the notion of a diagnostic tool which will act as somewhat of a dielectric function for the Kohn-Sham electron-hole propagators. It will turn out that this diagnostic tool will look almost identical to the effective dielectric function for the target space from equation 2.112 thereby showing the *pole* in the thermodynamic limit is a consequence of the microscopic physics that can be realized entirely within the target space. It will also be shown, similar to the case in the absence of the effective interaction for $(\chi^t_0)^{\sigma\sigma'}_{1234}(\omega)$, the target response will be a superposition of two-peak electron-hole propagators interfering to give one peak at the frequency of the zero of the dielectric function. It will be shown in the following section that this rich physics in the optical limit resulting from the two orbital Hilbert space is not enough to capture the dynamics for finite wave vectors outside the 'dipolar' regime.

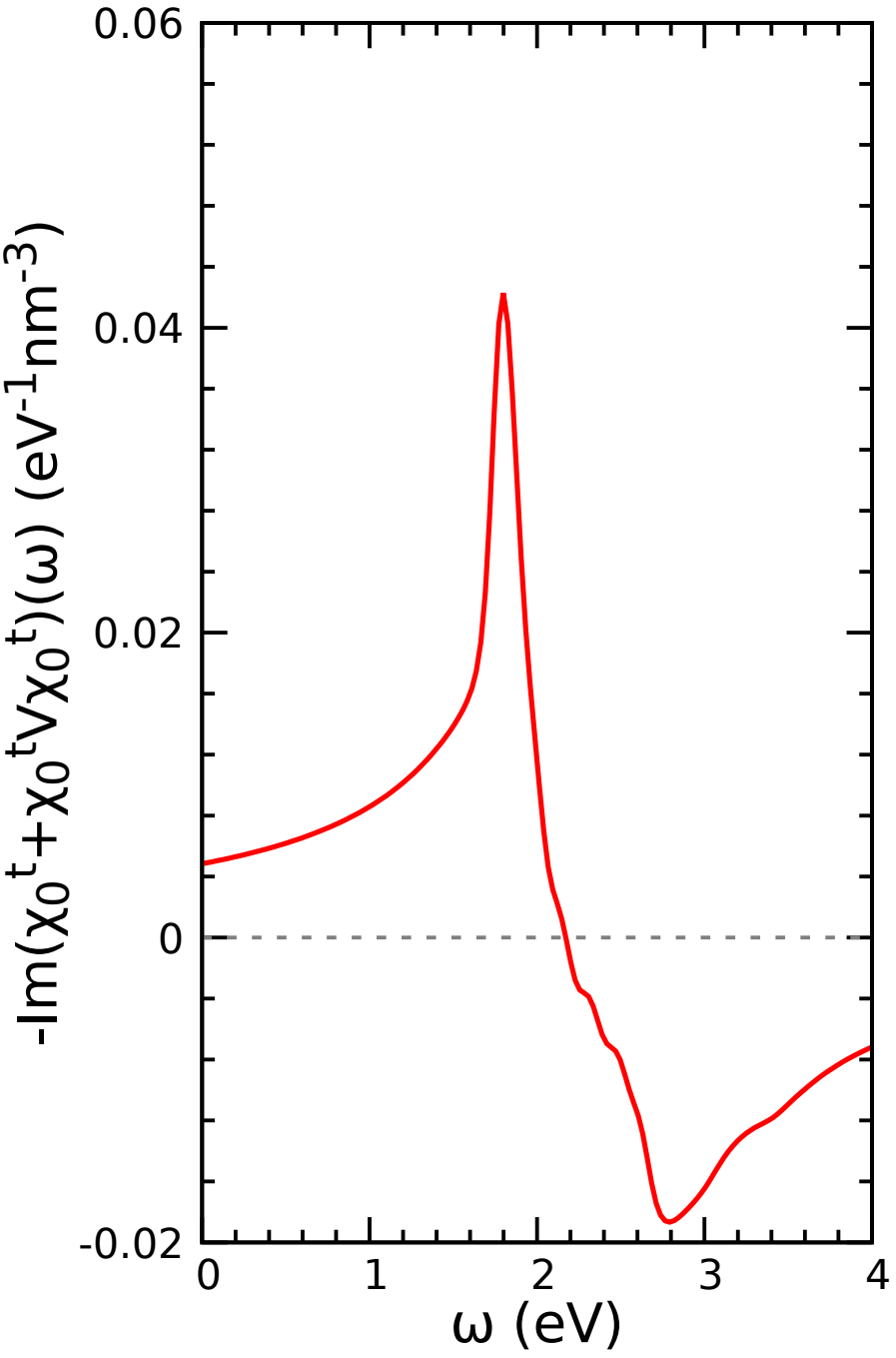

Figure 3.31: Spectroscopy calculated up to first order in $\tilde{V}^{\sigma\sigma'}_{1234}(\omega)$. Evaluating the expression $\lim_{\vec{q}\to\vec{0}} \sum_{\sigma\sigma'} \sum_{\bar{1}\bar{2}\bar{3}\bar{4}} A^{\sigma}_{\bar{1}\bar{2}}(\vec{q}) \left[(\chi_0)^t(\omega) + (\chi_0)^t(\omega)\tilde{v}(\omega)(\chi_0)^t(\omega)\right]_{\bar{1}\bar{2}\bar{3}\bar{4}} A^{\sigma'*}_{\bar{3}\bar{4}}(\vec{q})$. It can be seen that the spectrum does not resemble that shown in figure 3.20.

Emergence of Pole in the Target Space

As mentioned in the previous section, the origin of the *pole* involves summing over *all* the terms in the geometric series for χ^t. It was also shown in section 3.1.4, in the absence of interactions the spectrum produced was due to an interference of complicated line shapes. Therefore, we cannot isolate only one contribution to show the emergence of the pole in Wannier space. Moreover, $(\chi^t)^{\sigma\sigma'}_{1234}(\omega)$ is a *four-point* function as opposed to the *two point* function that are used in dielectric spectroscopy for examining the pole.

Therefore, it is worthwhile to introduce a quantity as a *diagnostic tool* for understanding the existence of the *pole* in the density response function. Symbolically, the interacting electron-hole 'propagator' is $\chi^t = (\chi^t_0)[1 - \tilde{v}(\chi^t_0)]^{-1}$, and the quantity $[1 - \tilde{v}(\chi^t_0)]$ *looks* similar to a dielectric function. Since the inverse of a matrix is proportional to the inverse of the determinant of the matrix, I will take the determinant to be the diagnostic tool I will use. Using the approximation in equation 3.18, the quantity $[1 - \tilde{v}(\chi^t_0)]^{\sigma\sigma'}_{1234}$ is given by

$$\delta_{12,34}\delta_{\sigma\sigma'} - \tilde{v}^{\sigma\sigma'}_{12\bar{1}\bar{2}}(\omega)(\chi_0^{t,\sigma\sigma'})_{\bar{1}\bar{2}34}(\omega) \approx \delta_{12,34}\delta_{\sigma\sigma'} - d^{\sigma *}_{12}(\hat{q})d^{\bar{\sigma}}_{\bar{1}\bar{2}}(\hat{q})(\chi_0^{t,\bar{\sigma}\sigma'})_{\bar{1}\bar{2}34}(\omega)(\varepsilon^r)^{-1}_{\vec{0}\vec{0}}(\omega), \tag{3.21}$$

where indices with a bar over them are summed over. It can be seen in figure 3.32 where I have plotted the determinant and the imaginary part of the negative of the inverse, which act as an 'effective' dielectric and loss function respectively. It can be seen that the determinant acts as an excellent diagnostic tool by its striking resemblance with the right panel of figure 3.21 which shows the dielectric function defined in the target space.

This figure is of the utmost importance because it shows the most direct microscopic description of the origin of the pole in terms of *physical* quantities. The dipole moment can be visualized in figure 3.33 where I have shown both the occupied and unoccupied orbital along with their product. The dipole is *across* neighboring

plaquettes due to the 'hybridization tails' of the Wannier orbitals, and the dipole moment is obtained by multiplying the product by x and performing an integral. Since this formula involves the sum over these dipoles over the macrocrystal, the dipole moment *triggers* the collective mode. Dynamically screening also enters this equation through $(\varepsilon^r)^{-1}_{\vec{0}\vec{0}}(\omega)$. It can be seen in figure 3.34, if screening is neglected, the pole is shifted to higher energies and the loss function becomes completely spurious. Not only is the dielectric function on the wrong scale in absolute units for the target space, but the pole has been shifted to $\sim$ 4 eV which is beyond the scale in which the dynamics of the target space are meant to capture.

This pole manifests itself in $\chi^{t,\sigma\sigma'}_{1234}(\omega)$. This can be seen in figure 3.5 where I have shown four examples of class a 'propogators'. Here, the line shape of these propagators is vastly different from the zeroth and first order terms. Up to a negative sign, the 'propogators' involving charge fluctuations across the two chains and the ones involving spin-reversals look identical. This similarity manifests their propagation to spectroscopy as equivalent contributions which can be seen in the top four panels of figure 3.36. Similar to the case in the absence of interactions, the resulting line shape that appears in the target response will be an *interference* of line shapes with two natural frequencies, one at $\sim$ 1.8 eV and one at $\sim$ 2.6 eV. In the case without interactions, class a contributions resulted in a two peak structure, but with interactions all the contributions interfere in a manner where there appears to be one peak at $\sim$ 2.6 eV—the location of the *pole*. This can be seen in the red curve of the left panel of figure 3.37.

The case for the larger contributions that come from class b have a different effect than they did in the absence of interactions. In the case without interactions, there was a two peak anti-nodal structure which interfered with the class a contributions to give one frequency at $\sim$ 1.8 eV. Here, the dominant terms in this class primarily cancel each other which can be seen as the sum of the four green curves in figure 3.36 that sum together to give the green curve in figure 3.37.

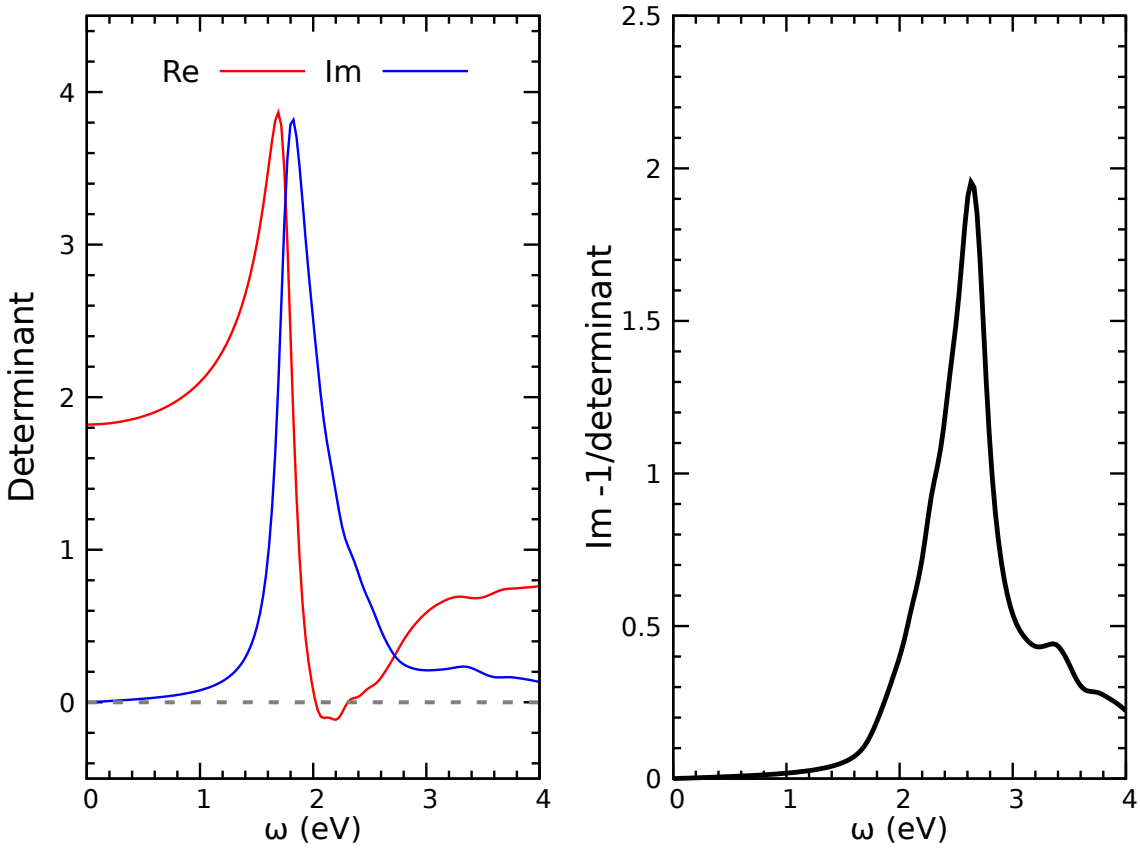

Figure 3.32: Pole realized through Determinant. Left: determinant of $\delta_{12,34} - \tilde{v}_{12\bar{1}\bar{2}}(\omega)(\chi_0^t)_{\bar{1}\bar{2}34}(\omega)$. Right: Imaginary part of -1/determinant. The determinant acts as an effective dielectric function in the target space to determine the energy of the pole while the imaginary part of -1/determinant shows an effective loss realized in the Wannier space.

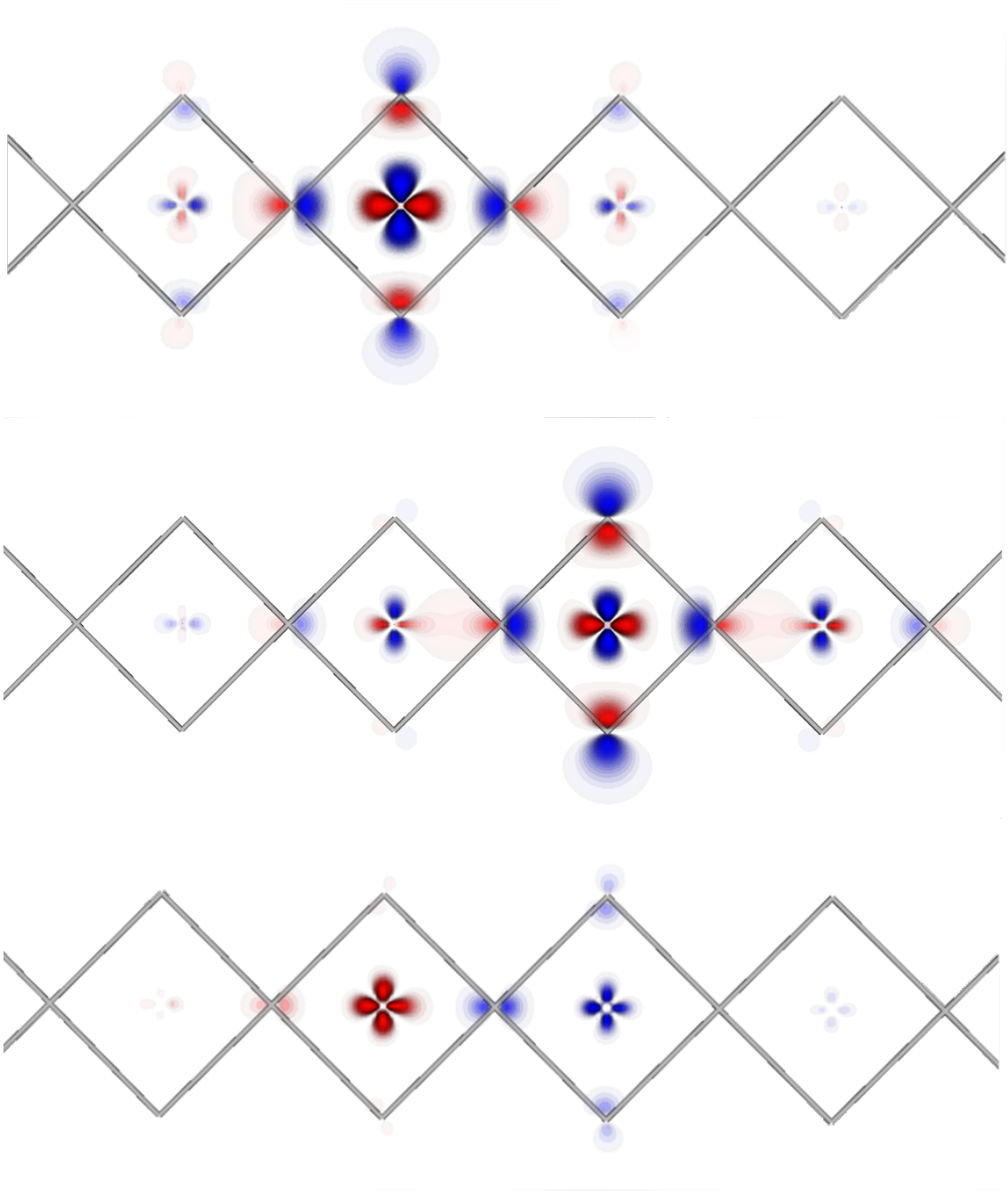

Figure 3.33: Dipole moment between Wannier orbitals. The top panel shows the $d_{x^2-y^2}$ Wannier orbital centered on the copper 1 site. The middle panel shows the anti-bonding molecular Wannier orbital projected in the copper 2 plaquette. The bottom panel shows the product of the two above orbitals. If you multiply this product by x and integrate, this will yield a finite dipole moment.

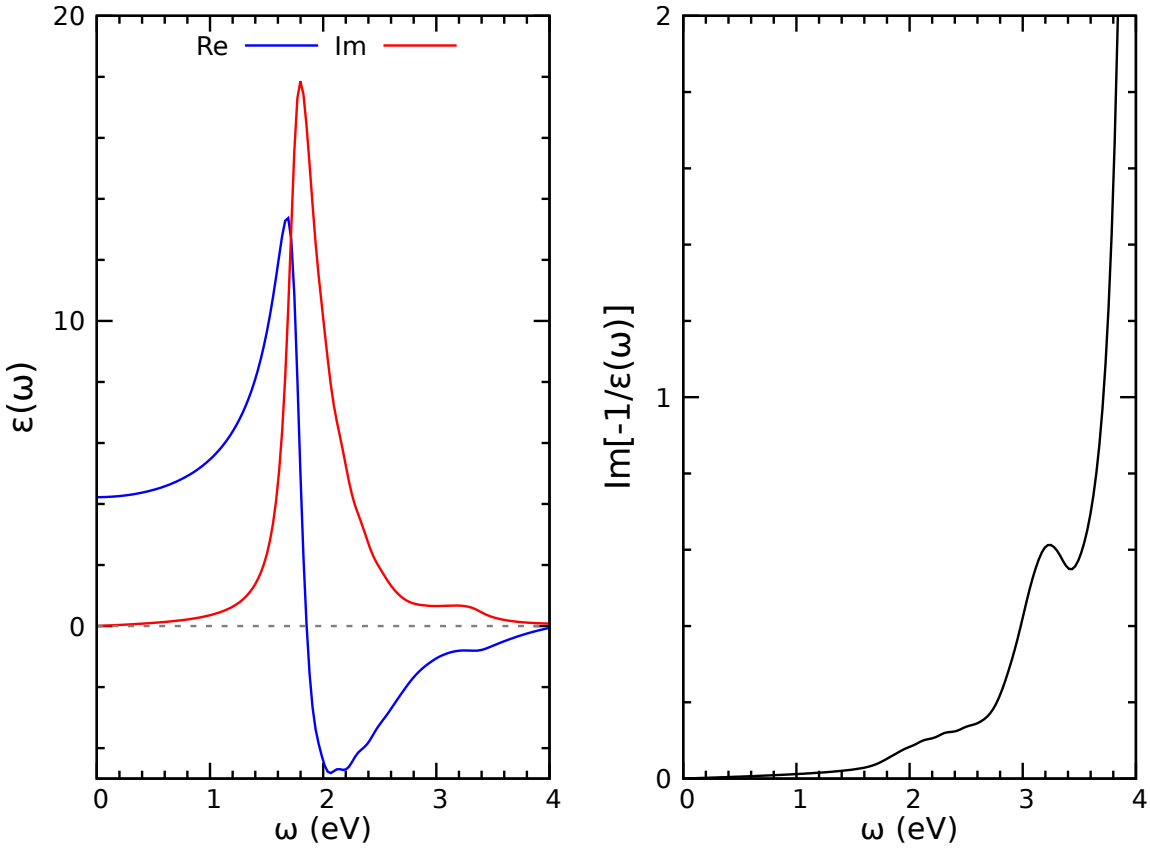

Figure 3.34: Target dielectric function and target loss function without screening. It can be seen that the figure does not agree in an absolute scale with the target dielectric function seen in figure 3.21. The pole has also been shifted to an energy scale in which the target space is not able to capture, so the pole is completely spurious.

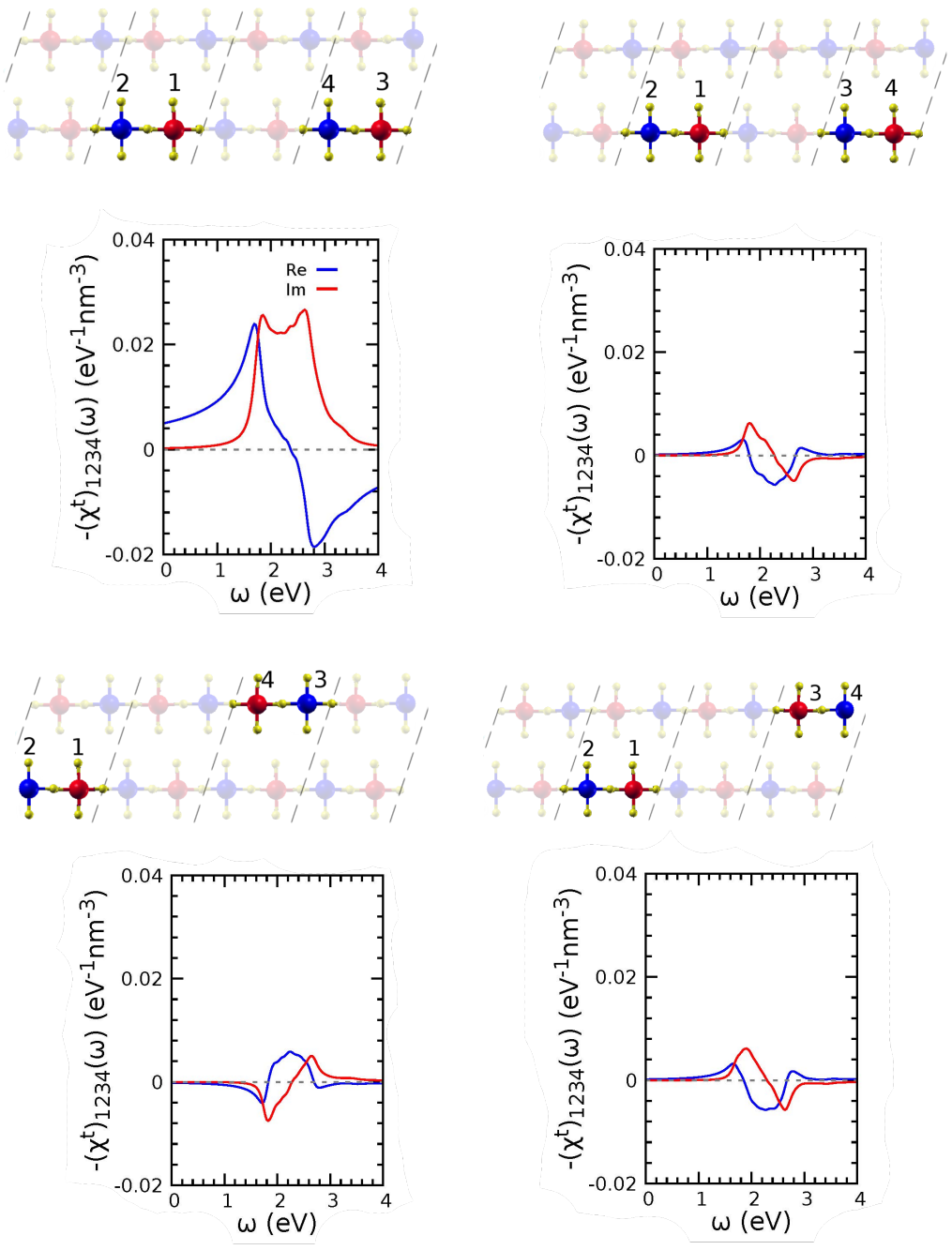

Figure 3.35: $\chi^{t,\sigma\sigma'}_{1234}(\omega)$ for class a configurations. Top two panels correspond to the main class a configurations where all four orbitals are in one chain. Bottom two panels correspond to the main class a configurations where all four orbitals are across both chains.

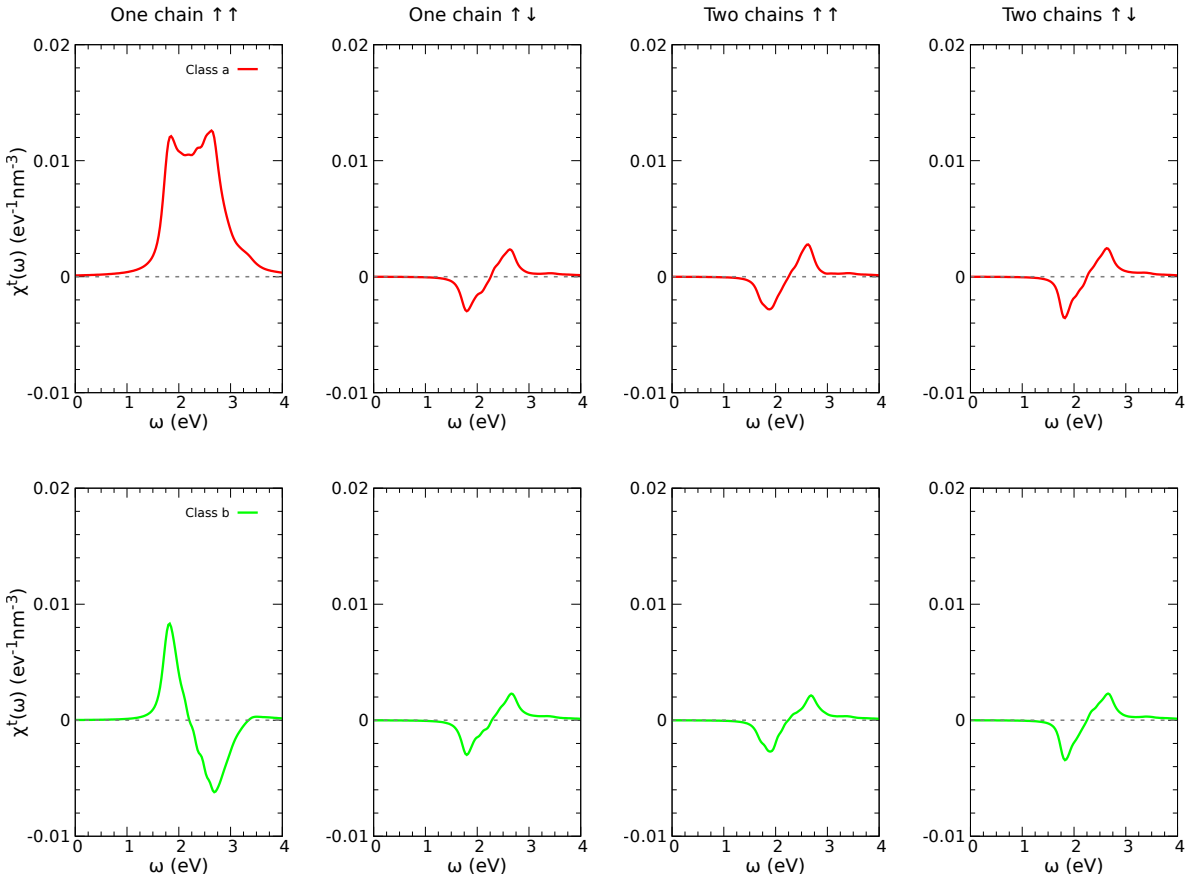

Figure 3.36: $\chi^t_{\vec{G}=\vec{0}\vec{G}=\vec{0}}(\omega)$ from class a and b configurations. The top row shows the four subsets of class a that contribute to spectroscopy. Like the case of $(\chi^t_0)_{\vec{G}=\vec{0}\vec{G}=\vec{0}}(\omega)$, these are two frequencies that interfere to give spectroscopy. The second row shows the four subsets of class a that contribute to spectroscopy. It can be seen that class a will constructively interfere to give one peak while class b will deconstructively interfere.

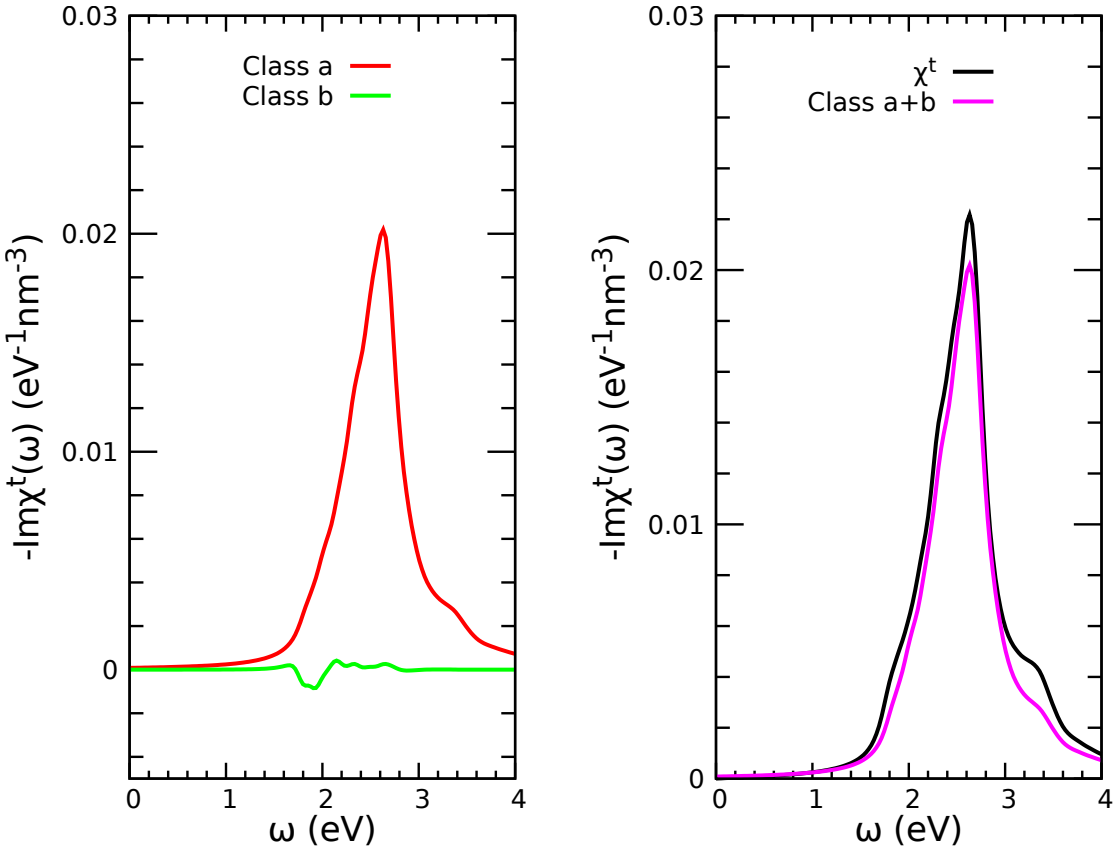

Figure 3.37: $\chi^t_{\vec{G}=\vec{0}\vec{G}=\vec{0}}(\omega)$ from class a and b configurations. Left panel: the sum over the four panels shown in 3.36 where the red shows the constructive interference of the two peak line shapes of class a while the green shows the deconstructive interference of the two peak line shapes of class b. Right panel: the purple curve shows the sum of the red and the green curves from the dominant contributions from class a and b and the black curve shows the sum over all classes.

3.1.5 Finite Wave Vectors

While two Wannier orbitals were enough to capture the collective mode in the optical limit, it does not possess the physics needed to describe the *dispersion* of the pole for arbitrary wave vector. This can be seen where I have plotted the dispersion of the pole from the two Wannier orbital Hilbert space in the blue circles in figure 3.39 which do not capture the position of the pole away from the optical limit. To obtain the correct dispersion, I needed to augment the Hilbert space by adding an additional four Wannier orbitals per spin projection for each chain. These orbitals are of atomic p_x content and are centered on the atoms above and below the copper atoms which correspond to the oxygen 1,2,3 and 4 atoms shown in figure 3.1. The contour plots for the six orbitals in the Hilbert space are shown in figure 3.38. These orbitals are in a π-bonding configuration with the d_{xy} hybridization tails on the copper atoms. These orbitals are also similar to those introduced for the one-center exciton configurations mentioned in reference [171].

The reason that these orbitals play an active role for the dynamics for larger wave vector is due to the product between the occupied copper $d_{x^2-y^2}$ orbital and them yield a *quadrupole* moment within one plaquette and a very small overall dipole moment. The quadrupole moment is due to the d_{xy} hybridization tails from the p_x Wannier orbitals and the $d_{x^2-y^2}$ content from the occupied Wannier orbital. The consequence of this chemistry can be seen in figure 3.40 where in the optical limit (top left panel), the loss function from the two and six orbital Hilbert spaces are almost identical due to the small dipole moment contribution from the p_x Wannier orbitals in the dipolar excitation. However, for larger wave vectors this quadrupole moment yields larger spectral weight and captures the correct dispersion due to the leading q^2 behavior of the charge fluctuation matrix elements which become more pronounced and result in noticeable differences to spectroscopy.

The dispersion of the six Wannier orbitals is given by the red circles and can be compared to the dispersion from two Wannier orbitals in figure 3.39. It can be seen

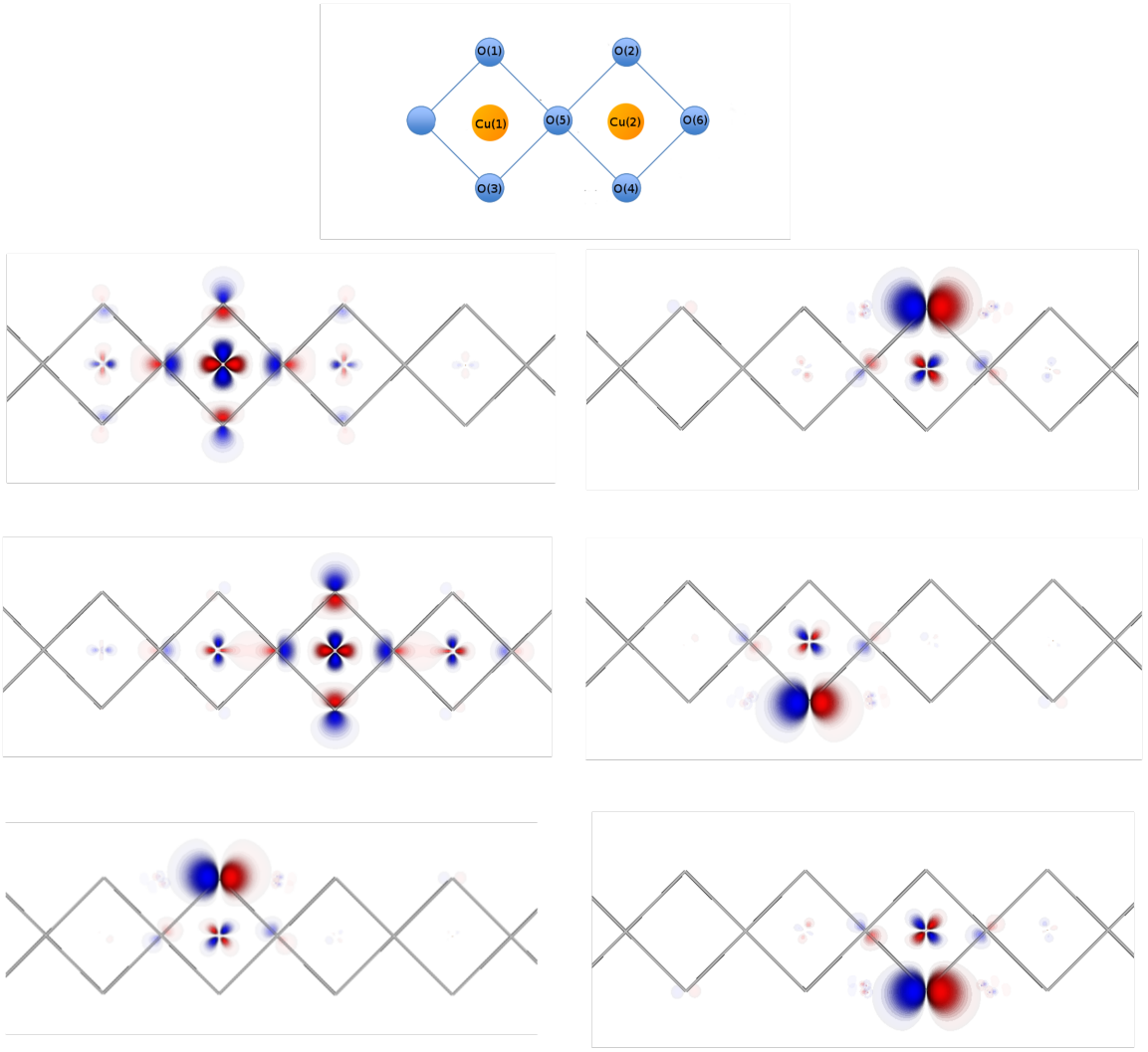

Figure 3.38: Contour plots of six orbital Hilbert Space. In addition to the two orbitals that were adequate to describe dynamics in the optical limit, an additional four p_x Wannier orbitals are shown that are needed to properly describe dynamics for arbitrary wave vector.

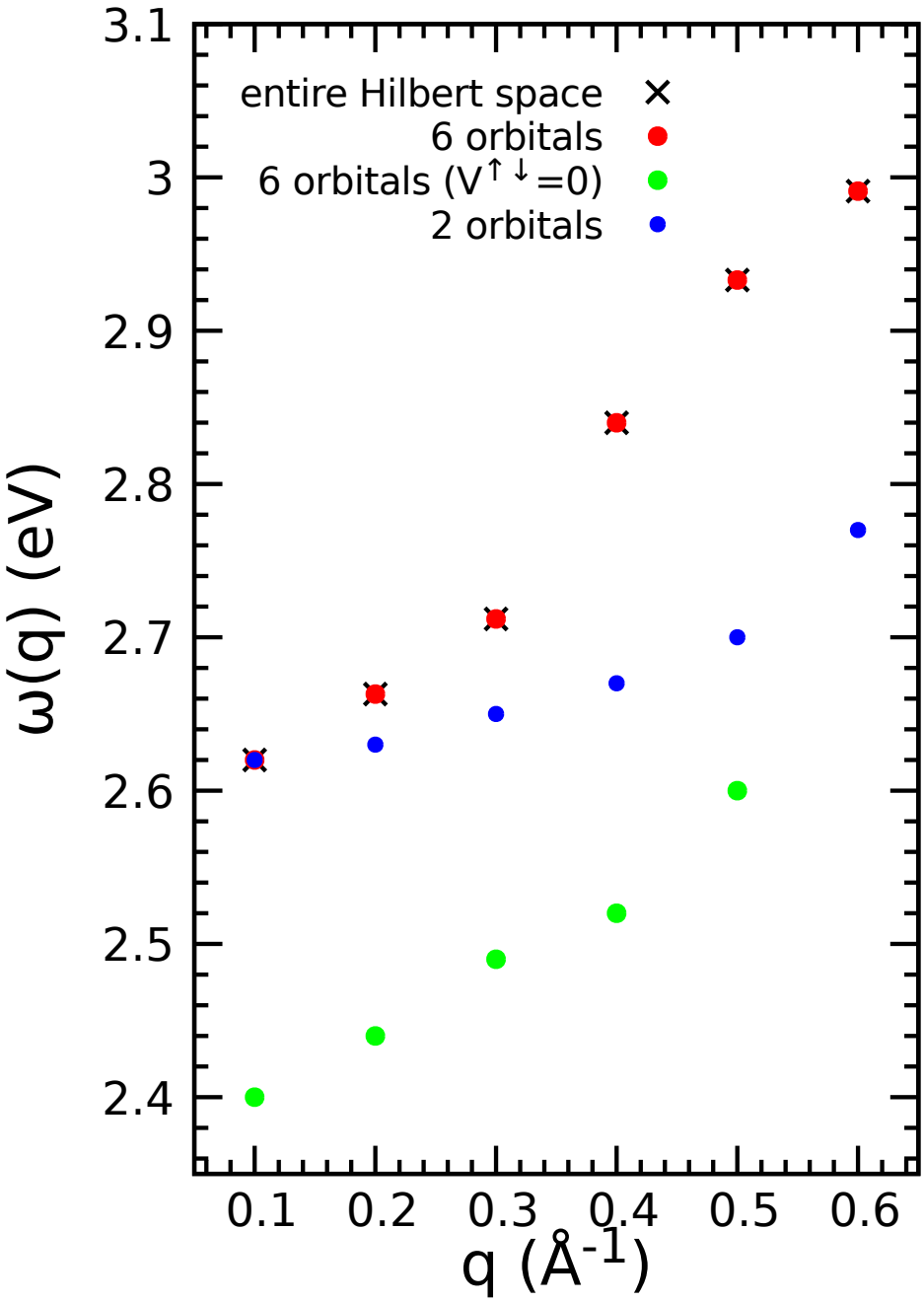

Figure 3.39: Dispersion of charge collective mode in the target space. The black crosses show the dispersion obtained from the exact calculation which should be used to compare with spectroscopy. The red circles represent the dispersion obtained from the six orbitals within the target space. The green circles show the dispersion obtained from the six orbital Hilbert space, but neglect spin-reversal terms in the interaction $\tilde{v}^{\uparrow\downarrow}(\omega)$. The blue circles show the dispersion obtained from the two orbital Hilbert space.

that by using only two orbitals, the dispersion is bad, and moreover does not capture the 'discontinuity' at $|\vec{q}| = 0.4$ Å^{-1} while the Hilbert space with six orbitals does capture this. Also, when the spin-reversal terms are neglected for the six Wannier orbital Hilbert space, the dispersion is also destroyed. This is another example, along with the optical limit, that the fractionalization paradigm is incompatible with the physics of the Mott-gapped particle-hole excitations shown in my calculations for the one-dimensional cuprates.

The corresponding loss and dielectric functions for the target space are shown in figures 3.40 and 3.41 respectively. It can be seen in both of these figures that as we depart away from the optical limit, the loss and dielectric function between both the Hilbert spaces disagree with each other. These figures are also extremely important because it shows, as was the case in the optical limit, that I am tracking a *pole* within the target space to describe the loss which is realized as a local minimum in the dielectric function for finite wave vectors.

I would also like to draw attention to the shoulder that appears in the loss function for larger wave vectors in 3.40. As mentioned previously, this is due to the *interference* of line shapes from the superposition of quantities from $\left(\chi^t\right), {\sigma\sigma'}_{1234}$ which are shown in figure 3.42 for momentum transfer $\vec{q} = 0.4$ Å^{-1}. In the left panel of this figure, I showed a class a configuration from both the six Wannier orbital Hilbert space (solid curves) along with the same element of the class from the two Wannier orbital Hilbert space (dashed curves). It can be seen that the propagators in the left panel of 3.42 have slightly different line shapes which is due to the augmented Hilbert space they span and the modification of the orbital and the electronic structure that ensues. In the right panel I show an electron-hole propagator which consists of an electron-hole pair $p_x \rightarrow x^2 - y^2$ going to another $p_x \rightarrow x^2 - y^2$ in the same chain. Therefore, to accurately describe the dispersion for arbitrary wave vector, the interpretation is due to a *superposition* of electron-hole fluctuations involving intertwined charge, spin, and orbital degrees of freedom.

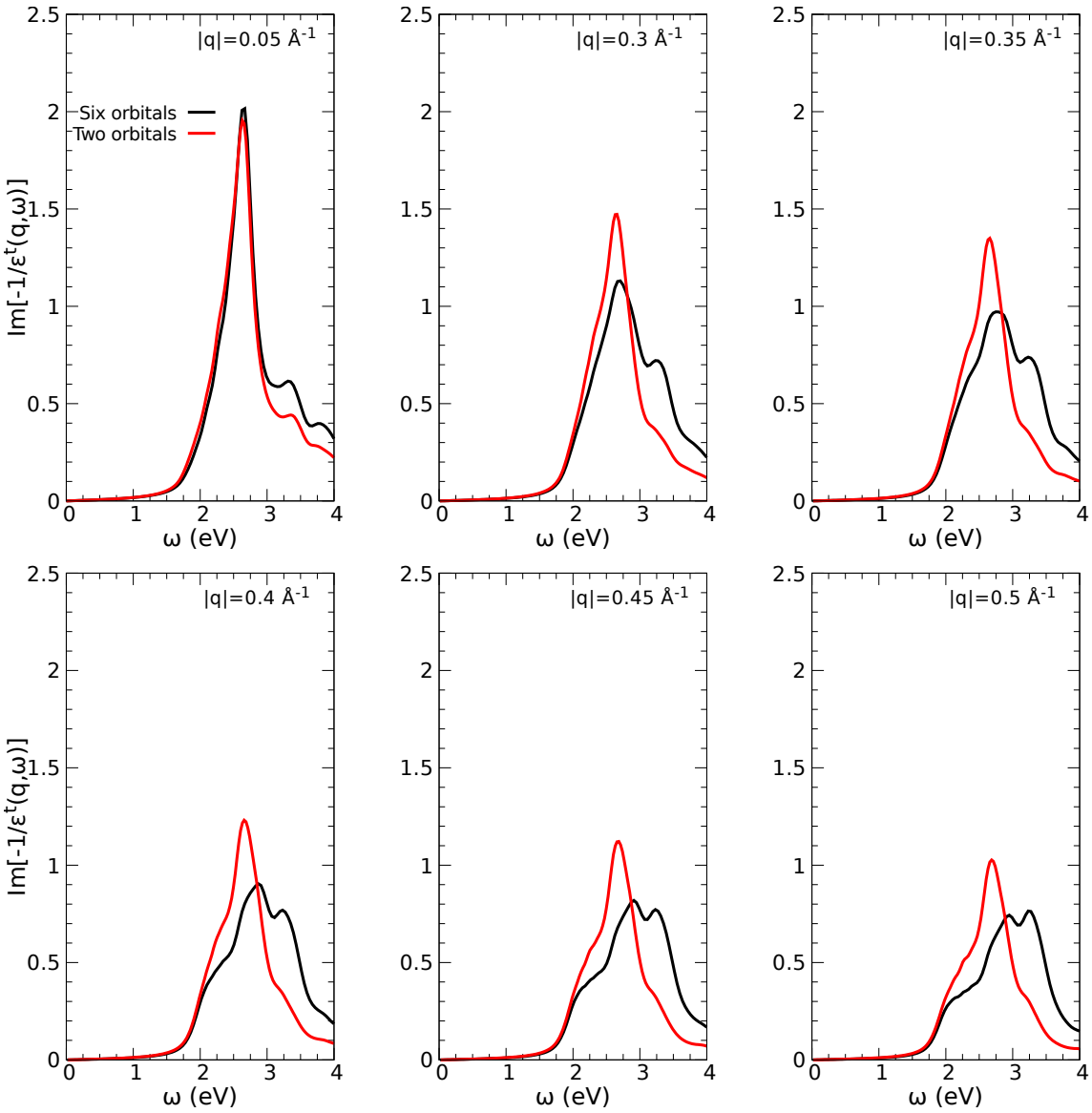

Figure 3.40: Target loss function $\mathrm{Im}(\varepsilon^t)^{-1}(\vec{q},\omega)$ for two and six orbital Hilbert spaces. The black curves and red curves are for the six and two orbital Hilbert space respectively. It can be seen in the optical limit (top-left panel), the loss functions of both Hilbert spaces capture the pole, while for finite wave vector (other five panels), there is disagreement.

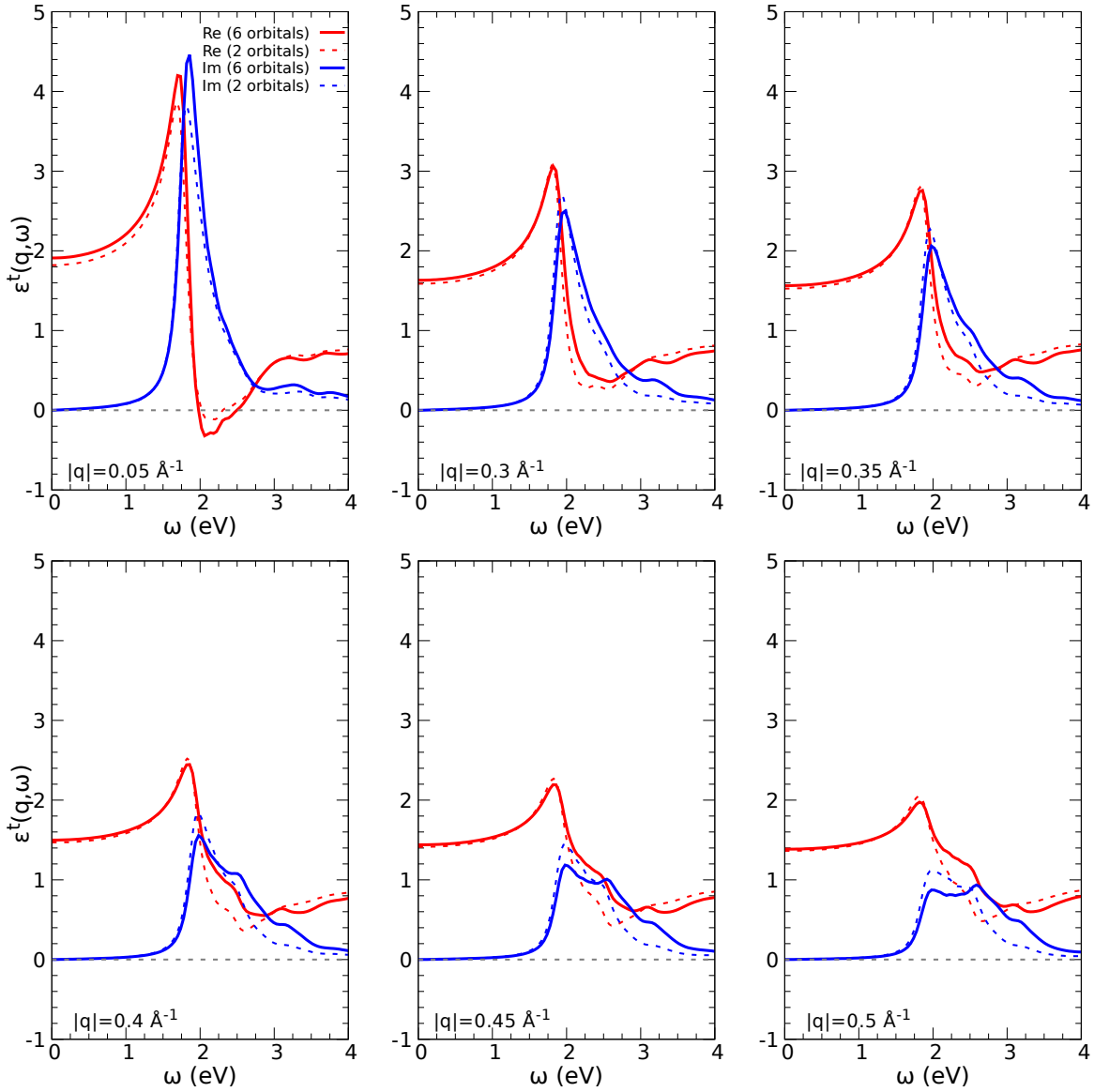

Figure 3.41: Target dielectric function $\varepsilon^t(\vec{q},\omega)$ for two and six orbital Hilbert spaces. The solid lines are for the six orbital Hilbert space and the dashed lines are for the two orbital Hilbert space. It can be seen in the optical limit (top-left panel), the dielectric functions of both Hilbert spaces capture the pole, while for finite wave vector (other five panels), there is disagreement.

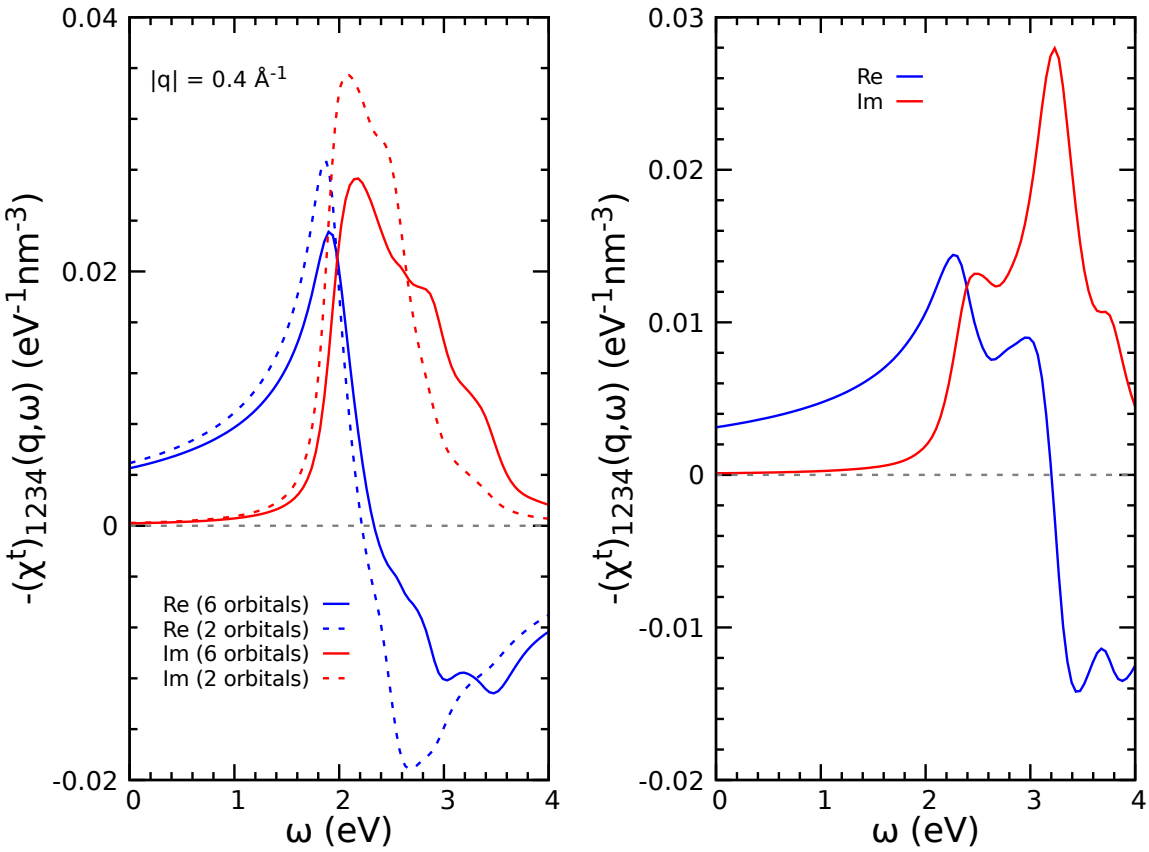

Figure 3.42: $(\chi^t)^{\sigma\sigma}_{1234}(\vec{q} = 0.4\mathring{A}^{-1}, \omega)$. In the left panel, I show the dominant contribution to spectroscopy from the class a configuration where all four orbitals are in one chain and are of the same spin projection. I ploted the same configuration for the six orbital Hilbert space (solid line) and the two orbital Hilbert space (dashed line). In the right panel I show the new contribution which arises from the newly added p_x Wannier orbtal. The configuration I am showing is $p_x \rightarrow x^2 - y^2$ where all four orbitals are in one chain and of the same spin projection.

3.2 Concluding Remarks

In summary, I have rigorously downfolded time-dependent density functional theory to a low energy space of *exactly-disentangled* Wannier orbitals. In the optical limit, I was able to understand the Mott-gapped spectrum for the particle-hole probes of optical conductivity, dielectric function, and loss function with a Hilbert space size of two Wannier orbitals where the Mott gap was determined by Wannier orbitals projected in neighboring plaquettes. Through this Hilbert space, I was able to realize the dielectric function and loss function through a collective superposition of electron-hole fluctuations spanning the entire macrocrystal consisting of dipolar nearest-neighbor charge fluctuations. The line shapes observed are due to an interference of two-peak line shapes seen in the electron-hole propagators of TDDFT. The interpretation introduces a *pole* from a zero in the real part of the dielectric function manifesting itself as a pole in the loss function. In addition, if spin-reversal terms in the dynamically screened Coulomb interaction in the TDDFT linear response equation are ignored, this severely degrades the pole. This suggests that the fractionalization paradigm is not compatible with the underlying physics behind the pole due to the necessity of removing spin-reversal back-scattering interaction for the bosonization procedure for the one-dimensional Hubbard model or electron gas.

To capture the physics of the dispersion of the pole, I had to augment the Hilbert space size by adding an additional four out-of-chain oxygen p_x orbitals. By using this Hilbert space, I captured the narrowing of the line shape at $\vec{q} = 0.4$ Å^{-1} and observed an overlooked discontinuity about this wave vector also seen in experiment. Moreover, by ignoring spin-reversal terms in the TDDFT linear response equation, the dispersion was compromised further suggesting the fractionalization paradigm *appears* absent in my calculation. Additionally, the calculations have a prediction of a Mott-gapped longitudinal spin excitation that can be validated with an INS measurement and a re-emergence of the pole in higher Brillouin zones which can be verified through NIXS measurements which would further validate this *ab initio* interpretation.

It is also noteworthy that I imposed an *antiferromagnetic* insulating ground state for the calculations. It has been accepted experimentally [28, 29] that this material has no long range order above their Neél temperature and is interpretted via a macroscopic $SU(2)$ singlet ground state [68]. However, I would make the argument that the calculations I put forth cannot be deemed incompatible with realistic simulations of the one dimensional Mott-insulating cuprates since no spectroscopic experiments have been performed below the Neél temperature, to show that the spectra is drastically different from the three dimensional ordered phase.

Another comment worthwhile making is that I am specifically arguing that the particle-hole Mott-gapped excitations seen in experiment appear incompatible with the fractionalization paradigm with the interpretation through my calculations. This claim is a consequence of a) the *existence* of a *pole* witnessed through the loss function from the experiment of reference [33] and b) the importance of spin-reversal interactions' impact on the pole for arbitrary wave vector along the chain direction. While DFT nor TDDFT are not 'bosonizable', the numerical fact that these interactions play a prominent role in the dynamics strongly suggests a new interpretation of these materials deserve reinvestigation.

I cannot make arguements about the ARPES and INS experiments and their current interpetation. I can attest that the claim that the former are 'outside' that of band theory of solid is dubious since the claims from the LDA band structure [25] are without a doubt ill-founded. A realistic method to compute the spectral function in a realistic manner would either prove or disprove my claim that the ARPES data could be described within the band theory of solid. Furthermore, it would be beneficial for an experimental measurements for the one-dimensional cuprates below the Neél temperature as compulsory to verify if the observed measurements are drastically different than above T_N. The INS spectrum urges further calculations based upon a formalism similar to that used in my dissertation to compute the *transverse* magnetic response to see if the gapless excitations could be obtained via other methods.

Chapter 4

Ab initio Approach to Quantum Spin Liquid Candidate α-$RuCl_3$

In this chapter, I summarize the work that was published in physical review B [40] on constructing a multi-orbital extended Hubbard model for t_{2g} Wannier orbitals. This project involved a collaboration with Dr. Tom Berlijn, Dr. Pontus Laurell, Dr. Satoshi Okamoto, Dr. Yi Zhang, and my advisor Dr. Adolfo Eguiluz. The work I did in this project was to synthesize the Hubbard model used in this calculation. Using exact diagonalization and strong coupling perturbation theory, Dr. Tom Berlijn, Dr. Pontus Laurell, Dr. Satoshi Okamoto and Dr. Yi Zhang were able to generate an effective two-dimensional Kitaev-Heisenberg spin model for $\alpha-RuCl_3$ in using the C2/m space group. I will also discuss some of the work that was done using the spin model produced in this paper which was published in npj [106] by Dr. Satoshi Okamoto and Dr. Pontus Laurell examining thermal and spectroscopic properties from the magnetic excitations of this material.

This project motivated a follow up project where the out-of-plane interactions in which we use both the C2/m and R$\bar{3}$ space groups to understand the role of how the three dimensional interactions and the stacking of the hexagonal planes effect the properties of the material. In addition, we have examined other potential quantum

spin liquid candidates such as $Na_3Co_2SbO_6$ to syntehsize effective Hamiltonians to gain a fully *ab initio*-based understanding of these classes of materials.

4.1 Introduction

In Alexei Kitaev's paper [172], he presented an exact solution of the Kitaev model and found it to host a quantum spin-liquid ground state with fractionalized Majorana fermion and gauge flux excitations. This exotic state of matter is not only interesting from a fundamental scientific point of view but also has been proposed to have potential applications in topological quantum computing [9, 10]. Further progress was made by the idea that the Kitaev quantum spin liquid ground state can possibly be realized in the honeycomb iridates A_2IrO_3 with A=Na,Li [173].

Assuming that in A_2IrO_3 the electrons are in the strong coupling limit in which the interactions dominate over the kinetic energy and taking into account the spin-orbit coupling, oxidation state and crystal field splitting in the iridium atoms, it was concluded that this compound contains strong Kitaev interactions in addition to the usual Heisenberg exchange couplings. Depending on the material parameters, it was found that the system can be pushed from an antiferromagnetic (AFM) stripy state into the desired quantum spin liquid state. However, based on combined theoretical and experimental findings, it was deduced that A_2IrO_3 displays AFM zigzag order instead of the AFM stripy order or the quantum spin liquid ground state [174].

This was later confirmed by multiple experiments [175, 176]. To account for the experimentally observed zigzag state it was clear that an accurate description of A_2IrO_3 needed to involve extension beyond the Heisenberg-Kitaev model. To that end it was proposed that second and third nearest neighbor Heisenberg exchange couplings can stabilize the experimentally observed AFM zigzag configuration [177]. Alternatively, first principles simulations have shown that A_2IrO_3 contains strong nearest neighbor magnetic anisotropic interactions that favor the AFM zigzag state [178]. In a third interpretation, it is proposed that A_2IrO_3 is not in the strong

coupling limit, but the strong oxygen assisted hopping between the Ir atoms causes the electrons to delocalize into molecular orbitals [179]. This is similar to the case for the one dimensional Mott-insulating cuprates covered in detail in chapter 3 of this thesis.

Another closely related Kitaev spin-liquid candidate material is α-$RuCl_3$. In this compound, the chemically active ruthenium transition metal atoms form a honeycomb lattice and have a valence of four d electrons with strong spin-orbit coupling and electron-electron interactions. Additionally, there is a strong octahedral crystal field induced by the the chlorine anions splitting the t_{2g} and e_g ruthenium derived content. Therefore, just like in A_2IrO_3, the materials specifications of α-$RuCl_3$ appear to fulfill the conditions required laid out in reference [173] for the emergence of Kitaev interactions [180, 181].

Inelastic neutron scattering experiments [182] on α-$RuCl_3$ displayed, in addition to AFM zig-zag order [182–185], a broad continuum in the magnetic excitation spectrum that is interpreted within the framework of fractionalized excitations. This led to the conclusion that α-$RuCl_3$ is proximate to being in the desired quantum spin-liquid phase [182]. More recent neutron scattering experiments have shown that the AFM zig-zag order can be suppressed by applying an $8\ T$ magnetic field yielding a magnetic excitation spectrum consistent with a quantum spin liquid phase [186]. Further evidence for the quantum spin liquid phase has been provided by the observation of the thermal quantum Hall effect in α-$RuCl_3$ at similar magnetic field strengths [187].

To understand the properties of α-$RuCl_3$ and to investigate how this material can be manipulated towards potential applications in topological quantum computing, a microscopic understanding is instrumental. For that purpose, there has been a large effort to map out the magnetic exchange couplings of α-$RuCl_3$ both via experimental and theoretical techniques [188–195].

On the experimental side, models have been derived by fitting a generalized spin model to various experiments such as inelastic neutron scattering [188, 196], THz

spectroscopy [189], and anisotropic susceptibility measurements [190]. The derived magnetic interaction via these fits however display a large variations depending on the experiments. In some of the theoretical approaches the magnetic interactions are derived by computing the hopping parameters of the ruthenium t_{2g} electrons from *ab initio* electronic structure while their interaction parameters are taken to fit experimental data [181, 191, 195–197]. In another approach the first neighboring magnetic interactions are derived from first principles via quantum chemistry techniques, while the second and third neighboring magnetic exchange couplings are modeled phenomenologically [192]. However, there was not an attempt to derive the low energy effective spin model of α-$RuCl_3$ fully from first principles.

For this project, we derived the spin model of α-$RuCl_3$ entirely from *ab initio* based methods using the random phase approximation method introduced in chapter 2.2.4. First, I calculated all the parameters that enter the multi-orbital extended Hubbard model for the Ru-t_{2g} Wannier orbitals. In the second stage, Dr. Satoshi Okamoto applied second order perturbation theory in the strong coupling limit to obtain a model where the charge fluctuations are 'frozen', and we are left with an effective Hamiltonian with only spin degrees of freedom.

We found that in the Hubbard model the inter-atomic Coulomb repulsions and spin-orbit coupling effects are non-negligible when compared to their intra-atomic counterparts. The effect of the inter-atomic interactions is found to strongly enhance the nearest neighboring magnetic couplings by a factor $3-7\times$. The effects of the inter-atomic 'spin-orbit' effects is mainly to enhance the Kitaev coupling by 15%. The magnetic interactions in our first-principles spin model deviate significantly from the values obtained by fitting experiments. Our findings allow for a better understanding of the mangetic properties of α-$RuCl_3$ and quantum spin liquid materials in general from first principles.

4.2 Methods

To derive the spin-model for $RuCl_3$ from first principles, I will briefly review the methodology used. The first step is to perform density functional theory calculations of α-$RuCl_3$ to obtain the Kohn-Sham eigenvalues and eigenfunctions. The DFT calculations were performed within the generalized gradient approximation [119] for the exchange-correlation potential. The space group C2/m and the structural parameters of α-$RuCl_3$ are taken from X-ray diffraction measurements [184]. Two ground state DFT calculation were performed, one with and one without spin-orbit coupling. All calculations are performed on a $6 \times 6 \times 4$ unit cell macrocrystal in which the Born Van Karmen periodic boundary conditions are imposed. To compute the interaction matrices which are given in equation 4.9 and 4.10 we use 701 LAPW basis functions and 60 empty Kohn-Sham eigenfunctions for the onsite, and 545 LAPW basis functions and 100 empty Kohn-Sham eigenfunctions for the offsite interactions.

The second step is to derive the effective electron-electron interactions using the random-phase approximation discussed in section 2.2.4. To that end the Hilbert space is divided into two subspaces, the target space t consisting of the bands close to the Fermi level bands and the "rest" space r consisting of all the other bands.

The third step is to apply a transformation of the Kohn Sham eigenfunctions to obtain the multi-orbital Hubbard model in the basis of Wannier functions. [198] Specifically a projected Wannier function transformation using the the Löwdin orthonormalization procedure [137] which ensures the Wannier functions are orthonormal. In our study the projected local orbitals $|\phi_n\rangle$ which are taken to be the ruthenium t_{2g} orbitals yz, xz, xy expressed in the local basis defined in figure 4.1 such that the local coordinates (x, y, z) are approximately along the Ru-Cl bonds and the Ru-t_{2g} satisfy the symmetry properties in reference [195]. In the calculations with spin-orbit coupling the spins are rotated into the local coordinate system with the quantization axis along the local z axes. From here we derive the multi-orbital Hubbard model. First, we define the on-site energy and hopping parameters obtained

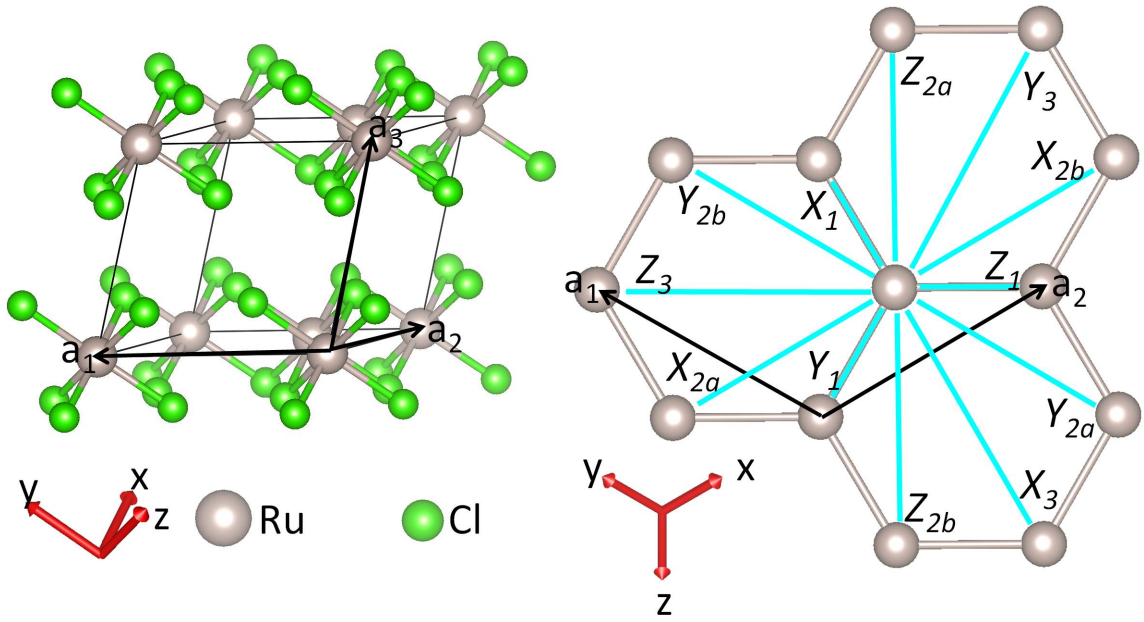

Figure 4.1: Crystal structure of α-$RuCl_3$. (color online) Definition of the first (X_1, Y_1, Z_1), second $(X_{2a}, X_{2b}, Y_{2a}, Y_{2b}, Z_{2a}, Z_{2b})$ and third (X_3, Y_3, Z_3) nearest neighboring Ru-Ru bonds (cyan lines) and the local coordinates x, y, z (red arrows) relative to the primitive lattice vectors a_1, a_2, a_3 (black arrows) of the $C2/m$ unit cell of $RuCl_3$.

from the calculation in the absence of spin-orbit coupling using the Kohn-Sham band structure

$$\varepsilon^{\sigma}_{n_1 n_2}(\vec{0}) = \langle W_{n_1\sigma}(\vec{0})|\, \hat{H}_{KS}\, |W_{n_1\sigma}(\vec{0})\rangle \tag{4.1}$$

$$t^{\sigma}_{n_1 n_2}(\vec{R}_1 - \vec{R}_2) = \langle W_{n_1\sigma}(\vec{R}_1)|\, \hat{H}_{KS}\, |W_{n_1\sigma}(\vec{R}_2)\rangle \tag{4.2}$$

where $\vec{R}_1 \neq \vec{R}_2$. Similarly we compute the on-site energy and hopping parameters from the DFT calculations in which the spin-orbit coupling is included in the second variational treatment [134]

$$\varepsilon^{SOC,\sigma_1\sigma_2}_{n_1 n_2}(\vec{0}) = \langle W_{n_1\sigma_1}(\vec{0})|\, \hat{H}^{SOC}_{KS}\, |W_{n_1\sigma_2}(\vec{0})\rangle \tag{4.3}$$

$$t^{SOC,\sigma_1\sigma_2}_{n_1 n_2}(\vec{R}_1 - \vec{R}_2) = \langle W_{n_1\sigma_1}(\vec{R}_1)|\, \hat{H}^{SOC}_{KS}\, |W_{n_1\sigma_2}(\vec{R}_2)\rangle\,. \tag{4.4}$$

From here we define the 'crystal-field' Hamiltonian

$$H_{cf} = \sum_{\vec{R}} \sum_{n_1,n_2} \sum_{\sigma} \varepsilon_{n_1 n_2} c^{\dagger}_{n_1\vec{R}\sigma} c_{n_2\vec{R}\sigma} + h.c., \tag{4.5}$$

the hopping Hamiltonian

$$H_{hop} = \sum_{\vec{R}_1 \neq \vec{R}_2} \sum_{n_1,n_2} \sum_{\sigma} t_{n_1 n_2}(\vec{R}_1 - \vec{R}_2) c^{\dagger}_{n_1\vec{R}_1\sigma} c_{n_2\vec{R}_2\sigma} + h.c. + h.c., \tag{4.6}$$

the local spin-orbit coupling Hamiltonian

$$\begin{aligned} H^{loc}_{soc} = & \sum_{\vec{R}} \sum_{n_1,n_2} \sum_{\sigma_1,\sigma_2} \left(\varepsilon^{SOC,\sigma_1\sigma_2}_{n_1 n_2}(\vec{0}) - \varepsilon^{\sigma_1}_{n_1 n_2}(\vec{0})\delta_{\sigma_1\sigma_2}\right) \\ & \left(c^{\dagger}_{n_1\vec{R}\sigma_1} c_{n_2\vec{R}\sigma_2} + h.c.\right), \end{aligned} \tag{4.7}$$

and the non-local spin-orbit coupling Hamiltonian

$$H_{soc}^{nloc} = \sum_{\vec{R}_1 \neq \vec{R}_2} \sum_{n_1,n_2} \sum_{\sigma_1,\sigma_2} \left(t_{n_1 n_2}^{SOC,\sigma_1\sigma_2}(\vec{R}_1 - \vec{R}_2) - t_{n_1 n_2}^{\sigma_1}(\vec{R}_1 - \vec{R}_2)\delta_{\sigma_1\sigma_2} \right) \left(c^{\dagger}_{n_1\vec{R}_1\sigma_1} c_{n_2\vec{R}_2\sigma_2} + h.c. \right). \tag{4.8}$$

We restrict the interactions to the local ($\vec{R}_1 = \vec{R}_2$) and non-local ($\vec{R}_1 \neq \vec{R}_2$)[1] Hubbard matrices

$$U(\vec{R}_1 - \vec{R}_2, n_1, n_2) = \int d^3x \int d^3x' |w_{n_1\sigma}(\vec{x} - \vec{R}_1)|^2 W^r(x, x', \omega = 0^+) |w_{n_2\sigma}(\vec{x}' - \vec{R}_1)|^2 \tag{4.9}$$

and the local exchange matrix

$$J(n_1, n_2) = \int d^3x \int d^3x' w^*_{n_1\sigma}(\vec{x} - \vec{R}) w_{n_2\sigma}(\vec{x} - \vec{R}) W^r(x, x', \omega = 0^+) w^*_{n_2\sigma}(\vec{x} - \vec{R}) w_{n_1\sigma}(\vec{x} - \vec{R}). \tag{4.10}$$

From here we obtain the local interacting Hamiltonian

$$\begin{aligned} H_{int}^{loc} &= U \sum_{\vec{R}n} n_{n\vec{R}\uparrow} n_{n\vec{R}\downarrow} + U' \sum_{\vec{R}, n \neq n'} n_{n\vec{R}\uparrow} n_{n'\vec{R}\downarrow} \\ &+ J_H \sum_{\vec{R}, n \neq n'} \left(c^{\dagger}_{n\vec{R}\uparrow} c^{\dagger}_{n\vec{R}\downarrow} c_{n'\vec{R}\downarrow} c_{n'\vec{R}\uparrow} - c^{\dagger}_{n\vec{R}\uparrow} c_{n\vec{R}\downarrow} c^{\dagger}_{n'\vec{R}\downarrow} c_{n'\vec{R}\uparrow} \right) \\ &+ (U' - J) \sum_{\vec{R}, n < n', \sigma} n_{n\vec{R}\sigma} n_{n'\vec{R}\sigma} \end{aligned} \tag{4.11}$$

[1] It should be mentioned that there are two ruthenium atoms in the unit cell, so there is a further implicit assumption that the onsite refers to where all the Wannier orbitals are on the same ruthenium atom. Here, the Bravais lattice vectors $\vec{R}$, can be thought to have a basis dependent label τ for the two ruthenium atoms in the unit cell so $\vec{R} \to \vec{R}_{\vec{\tau}}$.

with U and U' the intra- and inter-orbital Coulomb repulsion and J_H the Hund's coupling. The non-local interacting Hamiltonian is given by

$$H_{int}^{nloc} = \sum_{m=1}^{3} \sum_{\langle \vec{R}, \vec{R}' \rangle^m} \sum_{n,n'} \sum_{\sigma,\sigma'} V^m n_{n\vec{R}\sigma} n_{n'\vec{R}\sigma'} \tag{4.12}$$

with $\langle \vec{R}, \vec{R}' \rangle^m$ denoting $\vec{R}$ and $\vec{R}'$ being m-th nearest in-plane neighbors and V^m the in-plane m-th nearest neighboring Coulomb repulsion. The U, U', J_H and V^m parameters are obtained from orbital averaging the Hubbard and exchange matrices in equations 4.9 and 4.10. After this, the multi-orbital Hubbard model is assembled

$$H_{hub} = H_{cf} + H_{hop} + H_{soc}^{loc} + H_{soc}^{nloc} + H_{int}^{loc} + H_{int}^{nloc} \tag{4.13}$$

In the last step perturbation theory in the strong coupling limit is performed. To this end the multi-orbital Hubbard model is split in two pieces: the unperturbed part $H_0 = H_{cf} + H_{soc}^{loc} + H_{int}^{loc} + H_{int}^{nloc}$ and the perturbation $V = H_{hop} + H_{soc}^{nloc}$. Then H_0 is diagonalized exactly and V is treated with second order perturbation theory in the strong coupling limit:

$$\langle l | H_{spin} | l' \rangle = \langle l | V \sum_{h} \frac{|h\rangle\langle h|}{E_h - E_l} V | l' \rangle \tag{4.14}$$

where $|l\rangle$ and E_l are the degenerate low-energy eigenstates and energies of H_0 that contain 1 hole in each ruthenium atom and $|h\rangle$ and E_h are all the high-energy eigenstates and energies of H_0 that contain different distributions of the holes. To simplify the analysis the states $|l\rangle$ are restricted to the lowest energy Kramers doublet states that for zero crystal field reduce to the so-called $j_{\text{eff}} = 1/2$ doublet. [195] To fix the gauge of these doublet states we define up and down in the Kramers doublet as being the states that diagonalize $L_z - S_z$. As a final step the spin Hamiltonian is

compactly rewritten in terms of spin-operators

$$H_{spin} = \sum_{m=1}^{3} \sum_{\langle \vec{R}\vec{R}' \rangle^m} \mathbf{S}_{\vec{R}} \cdot \mathbf{J}_{\vec{R}\vec{R}'} \cdot \mathbf{S}_{\vec{R}'} \tag{4.15}$$

with $\langle \vec{R}, \vec{R}' \rangle^m$ denoting $\vec{R}$ and $\vec{R}'$ being m-th nearest in-plane neighbors. To compare with the available experimental studies, we consider the following reduced model

$$\begin{aligned} H^{red}_{spin} \quad = \quad & \sum_{\langle \vec{R}\vec{R}' \rangle^1} \left(J_1 \mathbf{S}_{\vec{R}} \cdot \mathbf{S}_{\vec{R}'} + K_1 S^{\gamma}_{\vec{R}} S^{\gamma}_{\vec{R}'} + \Gamma_1 S^{\alpha}_{\vec{R}} S^{\beta}_{\vec{R}'} \right) \\ & + J_3 \sum_{\langle \vec{R}\vec{R}' \rangle^3} \left(\mathbf{S}_{\vec{R}} \cdot \mathbf{S}_{\vec{R}'} \right) \end{aligned} \tag{4.16}$$

in which $\{\alpha, \beta, \gamma\}$ is equal to $\{y, z, x\}$, $\{z, x, y\}$ and $\{x, y, z\}$ for the X_1, Y_1 and Z_1 bonds defined in figure 4.1 and in which the first neighbor Kitaev, Heisenberg and anisotropy terms K_1, J_1 and Γ are obtained from bond averaging the results in equation 4.15 and the rest of the parameters are set to zero.

4.3 Results

In figure 4.2 and table 4.1 we present results corresponding to the non-interacting part of the Hubbard Hamiltonian without spin-orbit coupling, i.e. H_{cf} and H_{hop} defined in equation 4.5 and 4.6 respectively. Figure 4.2(a) shows a comparison of the band structure obtained from scalar relativistic DFT calculation against the one obtained from the non-interacting scalar-relativistic part of the Hubbard Hamiltonian $H_{cf}+H_{hop}$. Fig 4.2(b) shows one of the corresponding Wannier functions that displays a t_{2g} character at the center of the Ru atom and strong Cl-p hybridization tails in the nearest neighboring Cl atoms. In table 4.1 the on-site matrix corresponds to H_{cf} obtained from one of the two identical ruthenium atoms. The hopping matrices corresponding to hopping along the Z_1 and Z_3 bonds defined in figure 4.1. The

Table 4.1: Parameters calculated from multi-orbital Hubbard model. Top row: On-site energy and hopping parameters in meV from the non-interacting scalar-relativistic part of the Ru-t_{2g} Wannier orbital based Hubbard model: $H_{cf} + H_{hop}$. Second row: Elements of the local and non-local Hubbard U matrices and local exchange matrix in meV. Bottom two rows: Spin-orbit coupling parameters in meV. Local (third row right) and non-local (third row left) parameters derived via first principles Wannier functions compared to (fourth row) atomic-orbital form of the spin-orbit coupling $\frac{\lambda}{2} L \cdot S$ with spin-orbit coupling constant λ fitted to the local part of the spin-orbit coupling derived from first principles.

	local			Z_1 bond			Z_3 bond		
	yz	xz	xy	yz	xz	xy	yz	xz	xy
yz	-362	-7	-10	52	159	-21	-9	-7	12
xz	-7	-362	-10	159	52	-21	-7	-9	12
xy	-10	-10	-375	-21	-21	-150	12	12	-40

	U local			U Z_1 bond			J local		
	yz	xz	xy	yz	xz	xy	yz	xz	xy
yz	2578	1896	1901	833	898	928		286	288
xz	1896	2578	1901	898	832	928	286		288
xy	1901	1901	2589	929	928	1020	288	288	

	atomic-orbital fit $\frac{\lambda}{2} L \cdot S$						local					
	$yz\uparrow$	$xz\uparrow$	$xy\uparrow$	$yz\downarrow$	$xz\downarrow$	$xy\downarrow$	$yz\uparrow$	$xz\uparrow$	$xy\uparrow$	$yz\downarrow$	$xz\downarrow$	$xy\downarrow$
$yz\uparrow$		59i	0	0	0	-59		58i	i	0	-1-i	-59+i
$xz\uparrow$	-59i		0	0	0	59i	-58i		-i	1+i	0	-1+59i
$xy\uparrow$	0	0		59	-59i	0	-i	i		59-i	1-59i	0
$yz\downarrow$	0	0	59		-59i	0	0	1-i	59+i		-58i	-i
$xz\downarrow$	0	0	59i	59i		0	-1+i	0	1+59i	58i		i
$xy\downarrow$	-59	-59i	0	0	0		-59-i	-1+59i	0	i	-i	

Z_1 bond

	$yz\uparrow$	$xz\uparrow$	$xy\uparrow$	$yz\downarrow$	$xz\downarrow$	$xy\downarrow$
$yz\uparrow$	0	1+2i	0	0	1+i	2+12i
$xz\uparrow$	1-2i	0	0	-1-i	0	-12+2i
$xy\uparrow$	0	0	2	-2-12i	12+2i	0
$yz\downarrow$	0	-1-i	-2+12i	0	1-2i	0
$xz\downarrow$	2-i	0	12-2i	1+2i	0	0
$xy\downarrow$	2-12i	-12-2i	0	0	0	2

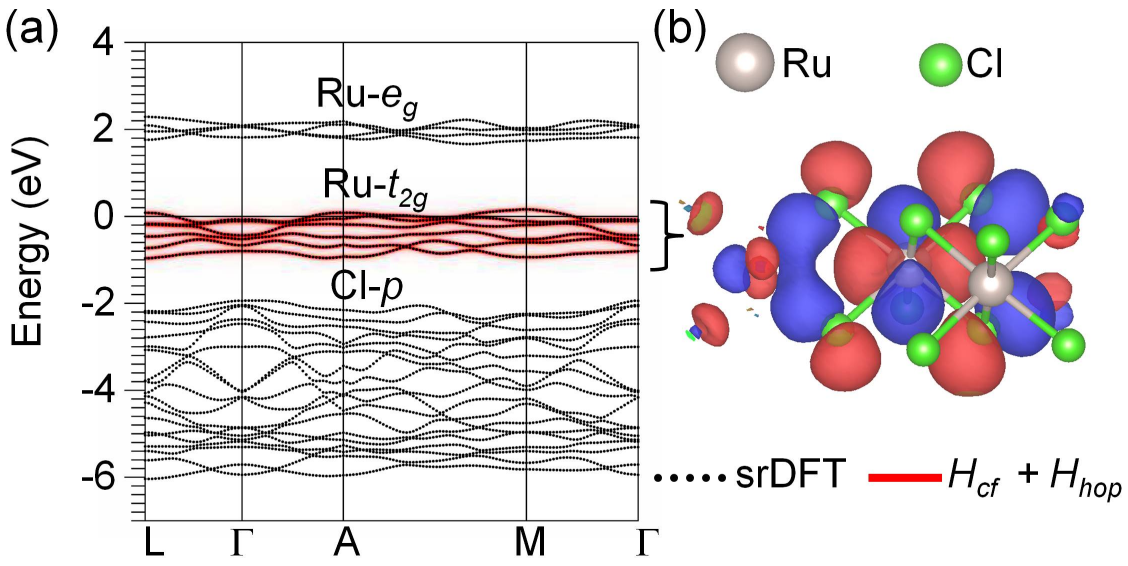

Figure 4.2: Density functional theory band structure and contour plot of Wannier orbital for α-$RuCl_3$. (color online) Left: comparison of the band structure from scalar-relativistic Density Functional Theory (srDFT) and the non-interacting scalar-relativistic part of the Wannier function based Hubbard model: $H_{cf} + H_{hop}$. Right: one of the corresponding Ru-t_{2g} Wannier functions.

crystal field and hopping parameters shown in table 4.1 obey the symmetry properties detailed in Ref. [195] and their numerical values agree within 1 meV.

Table 4.1 shows part of the Hubbard and exchange matrices defined in equation 4.9 and 4.10. The orbital dependence is relatively weak. Variations are on the order of 10 meV. The orbitally averaged values of the interaction parameters defined in equation 4.11 are given by the intra- and inter-orbital Coulomb repulsions $U = 2.6$ eV and $U' = 1.9$ eV and the Hund's coupling $J_H = 0.288$ eV. The first, second and third nearest neighbor repulsions defined in equation 4.12 are given by $V_1 = 0.9$ eV, $V_2 = 0.54$ eV and $V_3 = 0.44$ eV respectively. Our interaction parameters derived for $RuCl_3$ closely resemble the values $U = 2.7$ eV $J_H = 0.28$ eV and $V_1 = 1.1$ eV obtained from cRPA calculations for another Ru based compound $SrRu_2O_6$ [199]. It should be noted that in general large non-local Coulomb repulsions are expected in realistic models of materials because of the slow decay of the bare Coulomb potential. For example Hubbard models derived from the RPA for Fe pnictides and chalcogenides [200], $SrRu_2O_6$ [199] and Na_2IrO_3 [178] all display significant non-local Coulomb repulsions relative to their intra-atomic Coulomb repulsions. While the non-local Coulomb repulsions have been ignored in some of the previous derivations of the spin-models for α-$RuCl_3$ [191, 195] they have a significant effect on the magnetic interactions as discussed below.

Table 4.1 presents the spin-orbit coupling parameters. Specifically, the on-site spin-orbit coupling matrix corresponds to H_{soc}^{loc} defined in equation 4.7. The Z_1 spin-orbit coupling matrix is part of H_{soc}^{nloc} defined in equation 4.8. It should be noted that in previous derivations of the spin Hamiltonian for α-$RuCl_3$ [191, 195], a form of the spin-orbit coupling based on atomic orbitals is assumed.

Here we investigate how well that assumption compares with the spin-orbit coupling derived with first principles Wannier functions. The form of the spin-orbit coupling based on atomic t_{2g} orbitals is worked out for example in reference [201] and is denoted $\frac{\lambda}{2} L \cdot S$ in table 4.1. By fitting this form to H_{soc}^{nloc} derived from first

principles we find the value of the spin-orbit coupling strength $\lambda = 118$ meV which agrees well with for example the value used in reference [195].

By comparing the on-site spin-orbit coupling matrix and the atomic orbital fit in table 4.1 we see that the atomic orbital approximation is nearly perfect for the local part of the spin-orbit coupling. However, it should also be noted that there are significant values of the non-local spin-orbit coupling that are absent in the atomic orbital approximation for the spin-orbit coupling. Specifically, there are large non-local spin-orbit couplings between Ru1-xz/yz and Ru2-xy orbitals on the order of 12 meV with Ru1 and Ru2 along the nearest neighboring Z_1 bond. Similar sized values of the spin-orbit coupling are found along the X_1 and Y_1 bonds. Along the second and third nearest neighboring bonds the non-local spin-orbit coupling parameters are negligible. The values of the first neighboring non-local spin-orbit coupling parameters of 12 meV are sizable relative $\frac{\lambda}{2} = 59$ meV given that for each local spin-orbit coupling there are three nearest neighboring non-local spin-orbit couplings on the honeycomb Ru lattice.

We note that also in reference [178] for the closely related compound Na_2IrO_3 a similar structure of the non-local spin-orbit coupling is reported where the elements between Ir1-xz/yz and Ir2-xy orbitals with Ir1 and Ir2 along the Z_1 bond are significant relative to $\frac{\lambda}{2}$ in that system. The origin of the non-local spin-orbit couplings in α-$RuCl_3$ and Na_2IrO_3 and in general any transition metal halide, pnictide or chalcogenide is the strong hybridization between the transition metal d orbitals and the anion p orbitals exemplified by the Wannier function in figure 4.2(b). An interesting question is what the influence of such non-local spin-orbit coupling parameters will be on the magnetic exchanges in α-$RuCl_3$.

Having obtained the first principles multi-orbital Hubbard model, Dr. Satoshi Okamoto performed strong coupling perturbation theory detailed in equation 4.14 and 4.15 to derive the magnetic interactions. Just as in reference [195] we found that the parameters display sizable variations on the order of 50% depending on the bond directions which illustrates the complex dependence of the magnetic interactions

Table 4.2: Bond averaged magnetic interaction parameters in meV derived for three different cases compared to experimental reports [188–190, 196] with $C = 3J_1 + K_1$

	J_1	K_1	Γ_1	J_3	C
This study case 1 full	-2.7	-15.3	12.6	1.0	-23.4
This study case 2 w/o H_{int}^{nloc}	-0.6	-4.8	3.8	0.7	-6.6
This study case 3 w/o H_{soc}^{nloc}	-2.8	-12.8	11.5	1.0	-21.2
Inelastic Neutron Scattering [188]	-0.5	-5	2.5	0.5	-6.5
Inelastic Neutron Scattering [196]	n.a.	-6.8	9.5	n.a.	n.a.
THz Spectroscopy [189]	-0.35	-2.8	2.4	0.34	-3.9
Anisotropic Susceptibility [190]	n.a.	n.a.	29.2	n.a.	14.3
Mag. specific heat [193, 202, 203]	-1.5	-24.4	5.3	0	-29.0

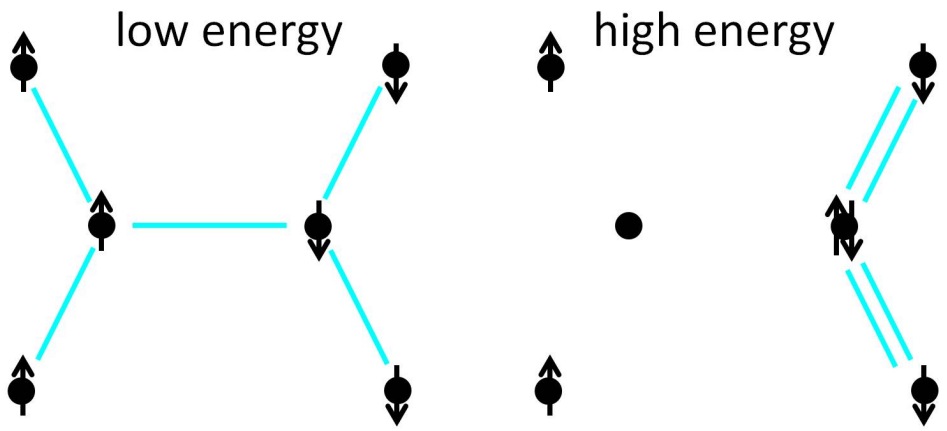

Figure 4.3: (color online) Comparison of low and high energy state in simplified model with 1 orbital per site. Arrows indicate spin-up and spin-down holes and cyan lines indicate nearest neighboring holes.

on the details of the crystal structure and the need for their derivation from first principles. Nonetheless, we proceed by deriving the parameters of the simplified bond-averaged model defined in equation 4.16 to be able to compare to the available experimental studies. The results are listed in table 4.2. Specifically, we consider three cases.

Case 1 corresponds to the full first principles model. Case 2 and 3 correspond to the first principles model in which the non local interactions and spin-orbit coupling are omitted respectively. When we compare case 1 with case 2 we note that the effect of the non-local interactions is to significantly increase the magnetic interactions roughly by a factor 3. To understand this, we consider in figure 4.3 a low and a high energy state in a simple model consisting of 6 sites with 1 orbital per site, nearest neighbor hopping t and local and non-local Coulomb repulsions U and V respectively. By counting nearest neighboring holes in both cases (indicated with cyan lines in figure 4.3 we see that the corresponding energies are $E_l = 5V$ for the low energy state and $E_h = U + 4V$ for the high energy state. When we plugged those values into equation 4.14 we see that the magnetic interactions go as $t^2/(U - V)$ instead of the usual t^2/U. In other words, the effect of the non-local repulsions will be to enhance the magnetic interactions. These enhancements are quite strong given that for example the nearest neighbor non-local interactions $V_1 = 0.9$ eV are quite strong compared to the intra-atomic repulsions $U = 2.6$ eV. From comparing case 1 and 3 we note that the effect of the non-local spin-orbit coupling is not as dramatic as that of the non-local interactions. Still the influence of these coupling is non-negligible, especially for the Kitaev interactions.

4.4 Conclusion

We have derived the magnetic exchange couplings of α-$RuCl_3$ via first principles techniques. To this end we utilized the Random Phase Approximation (RPA) to derive the ruthenium t_{2g} Wannier orbital based Hubbard Hamiltonian to which we

applied second order perturbation theory in the limit of the hopping parameters being small compared to the interactions. We have found that the first, second and third nearest neighboring Coulomb repulsions are significant compared to on-site ones. Furthermore, we found sizable elements in the spin-orbit coupling between orbitals on nearest neighboring Ru atoms that are usually ignored in model treatments of the spin-orbit coupling based on atomic orbitals instead of realistic first principles Wannier functions. We have investigated the effect of both the non-local interactions and the non-local spin-orbit coupling on the magnetic exchange couplings. The non-local spin-orbit couplings overall have a less dramatic effect although it still has a sizable influence on the Kitaev interaction strength. Our full model that includes the influence of both local and non-local interactions and spin-orbit coupling has too large magnetic exchanges couplings compared to the available experiments. Highlighting the importance of non-local electron-electron interaction and spin-orbit coupling effects and laying out the problem of the combined RPA and perturbation theory approach in our study contributes to the understanding and virtual engineering of quantum spin liquid candidate materials via first principles calculations.

4.5 Magnetic Specific Heat and INS cross section

The work in this chapter that I contributed to myself, I have completely shown. For completeness, I would like to briefly discuss some of the results from reference [106] performed by Dr. Satoshi Okamoto and Dr. Pontus Laurell where the used Lanczos exact diagonalization [204] on 24 site clusters to compute the INS cross section and thermal pure quantum state methods [205] to compute the magnetic specific heat from various spin model Hamiltonians including our own from reference [40]. In this work, they came to the numerical-based conclusion that models estimated using *ab initio* methods fail to get the INS spectrum at the Brillouin zone center. On the other hand, models based on the fitting from the INS data fail to reproduce the features seen in the magnetic specific heat. To mitigate this problem, they proposed a 'modified'

ab initio model in which they tweaked some of our parameters [40] that can describe both experimental measurenebts. Although there are a plethora of proposed models out there, they only considered six of the models with ferromagnetic Kitaev couplings $K_1 < 0$ [40, 188, 189, 191, 192, 195].

In figure 4.4, they show the INS spectrum from the six models that were used. In figure 4.5, the specific heat from experiment and the six models were shown along with the specific heat from each of the terms in the $J-K-\Gamma$ spin model Hamiltonian. In this study, in addition to the Hamiltonian given in equation 4.16, an off-diagonal Γ_1' interaction was used which adds a term to the the Hamiltonian 4.16

$$\hat{H}_{\Gamma_1'} = \Gamma_1' \sum_{<i,j>} \sum_{\alpha \neq \gamma} \left[S^{\gamma}_{\vec{R}_i} S^{\alpha}_{\vec{R}_j} + S^{\alpha}_{\vec{R}_i} S^{\gamma}_{\vec{R}_j} \right]. \tag{4.17}$$

This term originates in the trigonal distortion [206, 207]. In figure 4.6 a modified Hamiltonian from our derived spin model [40] was taken in which they reduced the Γ_1' factor by $20\times$ to compute the INS spectrum and magnetic specific heat.

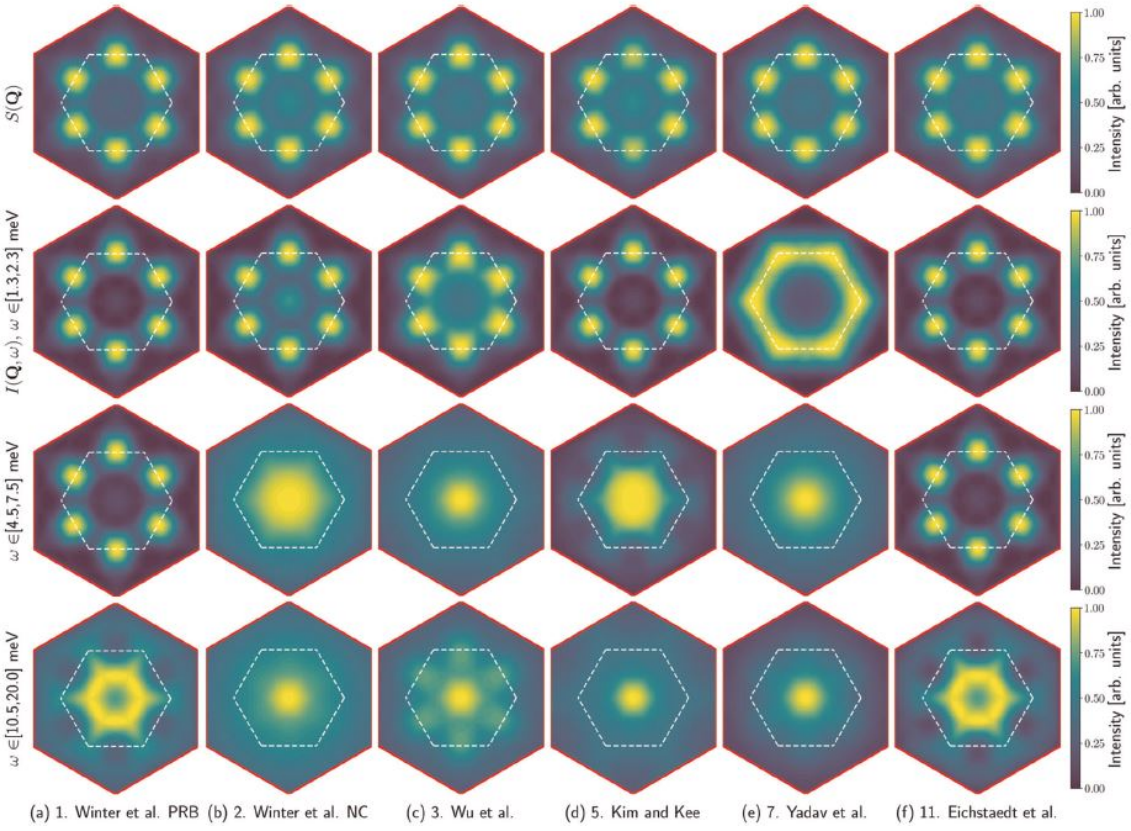

Figure 4.4: INS spectrum computed using Lanczos exact diagonalization for six different spin model Hamiltonians. The first column comes from [195]. The second column comes from [189]. The third column comes from [188]. The fourth column comes from [191]. The fifth column comes from [192]. The sixth column comes from [40]. The first row corresponds to the calculated static spin structure factor. The second-fourth rows are various energy ranges which were integrated over. Figure reproduced from reference [106].

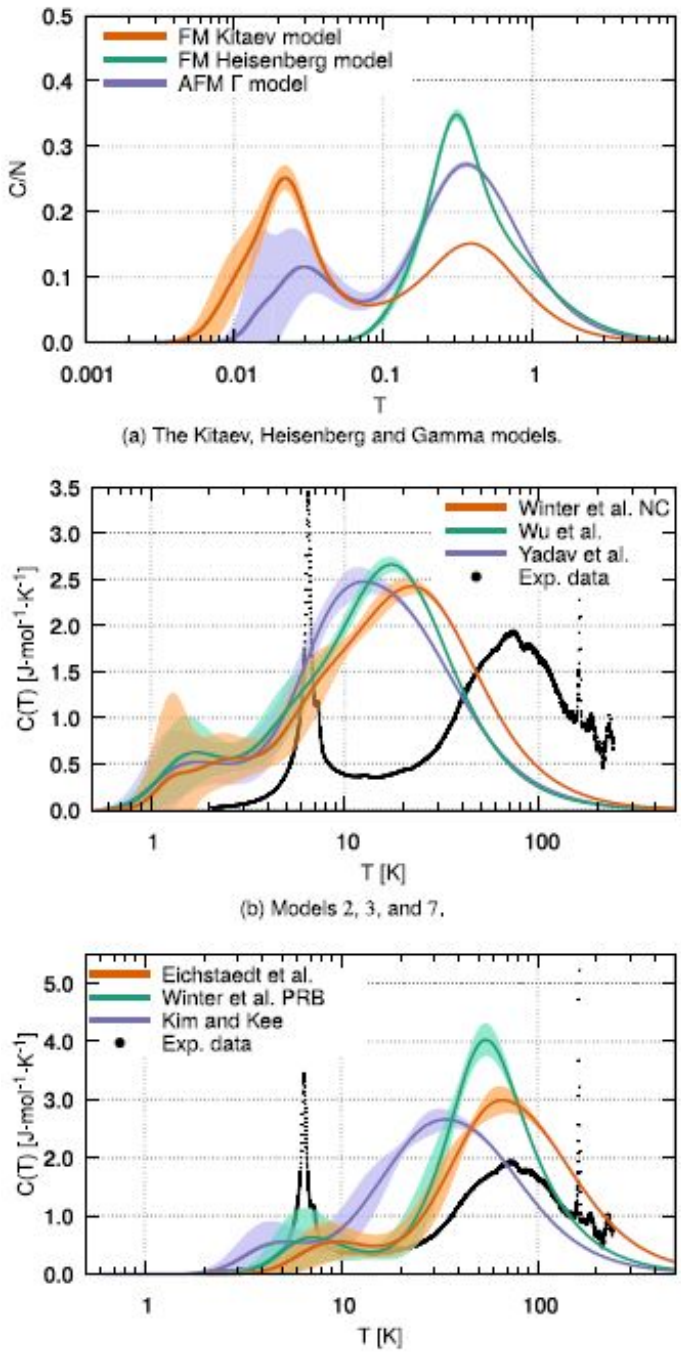

Figure 4.5: Experimental and computed specific heat using the thermal pure quantum state method. Top panel: The calculated specific heat contribution from each of the terms in the $J - K - \Gamma$ spin model Hamiltonian. Middle panel: Experimental and calculated specific heat contribution from references [188, 189, 192]. Bottom panel: Experimental and calculated specific heat contribution from references [40, 191, 195]. Figure reproduced from reference [106].

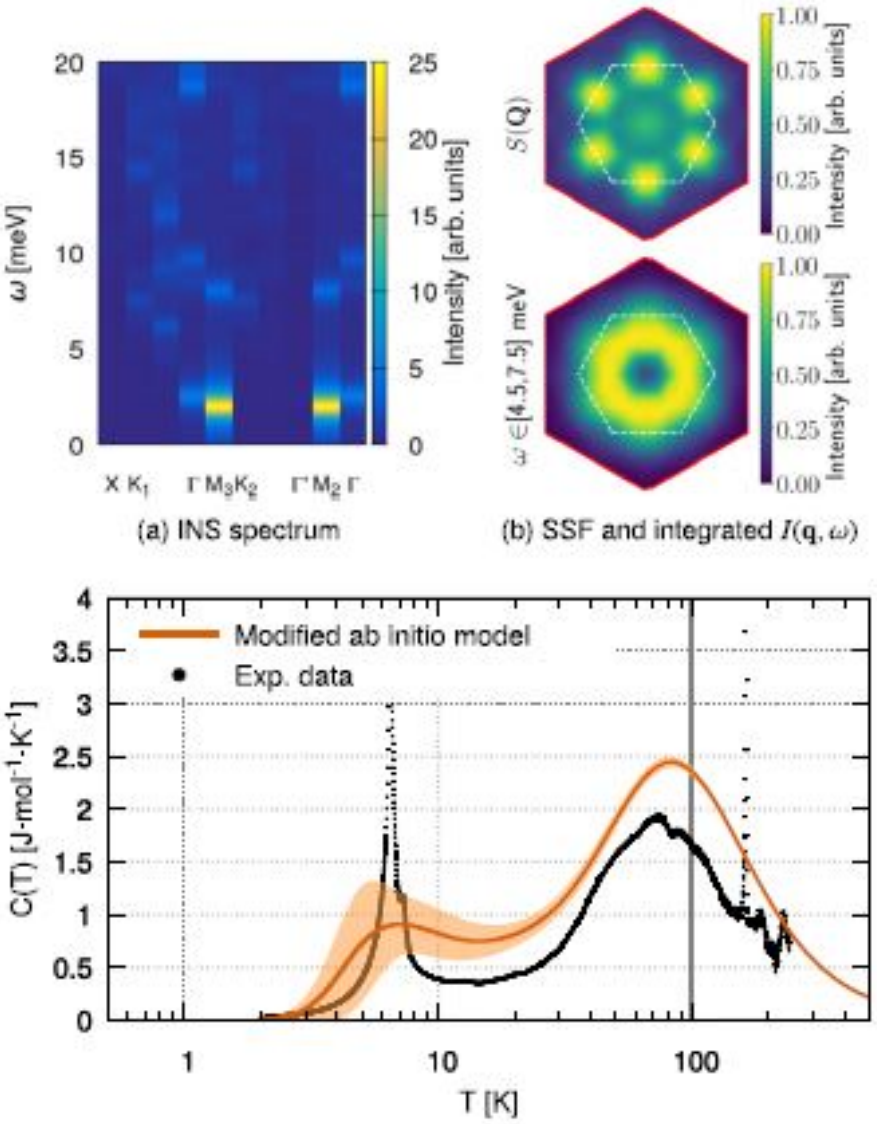

Figure 4.6: Experimental and calculated specific heat from 'modified' *ab initio* Hamiltonian. Figure reproduced from reference [106].

Conclusion

In conclusion, I have used *ab initio* techniques to examine the charge and spin dynamics for particle-hole charge neutral excitations for quantum materials. Specifically, I have shown as an example of the methods developed within our research group that we can describe qualitatively and quantitatively the measured loss function, dielectric function, and optical conductivity for the 'one dimensional' cuprates. Additionally, I was able to perform calculations for a *longitudinal* dynamical spin structure factor in which I predict there should be a *Mott-gapped* spin excitation which can be measured with magnetic inelastic neutron scattering, and I have calculated the dynamical charge structure factor for several Brillouin zones in which I make a prediction that the collective mode seen in the EELS spectrum re-emerges in higher Brillouin zones which can be measured with *non-resonant* inelastic X-ray scattering.

The main focus of my research was to get inside the black box of the time-dependent density functional theory calculations to understand the microscopic origin of the physical spectra which was unveiled in chapter 3. To do so required developing a method to exactly disentangle Wannier orbitals which is a requirement to rigorously downfold time-dependent density functional theory to a low energy space of Wannier orbitals. It was required to use this technique for the one-dimensional Mott-insulating cuprates due to the strong degeneracy in energy space of the copper d and oxygen p derived content in the band structure. By doing so, I was able to get inside the black box of the spectra of the cuprates I studied and show that to accurately

describe the spectra, the key ingredients were dynamical long-range screening and the solid state chemistry which manifests itself as hybridization tails of the Wannier orbitals. Moreover, the neglection of spin-reversal terms in the Coulomb interaction for the response from the Wannier orbitals severely affected the calculated dielectric function, loss function, and optical conductivity which strongly suggests that the 'fractionalization' paradigm is not compatible with our proposed interpretation of the experimental data that we compared with our calculations. Hopefully this work will motivate further investigation of spectra that I did not consider in this thesis such as calculations of the *transverse* dynamical structure factor and a realistic calculation of the spectral function inspired by the techniques I introduced to compare with angle-resolved photoemission data.

In chapter 4, I synthesized an *effective* multi-orbital extended Hubbard model for the t_{2g} Wannier orbitals using the random phase approximation method for time-dependent density functional theory for quantum material α-$RuCl_3$, a potential host for a quantum spin liquid ground state. Through collaboration with researchers at Oak Ridge National Lab, they were able to use this effective Hamiltonian to construct an effective Kitaev-Heisenberg-Gamma spin model using strong coupling perturbation theory which was the first *fully ab initio* derived model to examine the magnetic properties of these materials. This project motivated study of further calculations of the Hubbard model parameters for different stacking structures of these materials and to investigate other potential quantum spin liquid ground state candidates.

Bibliography

[1] Walters, A. C. *et al.* Effect of covalent bonding on magnetism and the missing neutron intensity in copper oxide compounds. *Nature Physics* **5**, 867–872 (2009). URL https://doi.org/10.1038/nphys1405. xii, 3, 15, 19, 20

[2] Kim, B. J. *et al.* Distinct spinon and holon dispersions in photoemission spectral functions from one-dimensional $SrCuo_2$. *Nature Physics* **2**, 397 (2006). URL https://doi.org/10.1038/nphys316. xii, 3, 15, 24, 25, 78

[3] Schlappa, J. *et al.* Spin-orbital separation in the quasi-one-dimensional Mott insulator Sr_2CuO_3. *Nature* **485**, 82–85 (2012). xii, 3, 15, 34, 36, 78, 89

[4] Cava, R., de Leon, N. & Xie, W. Introduction: Quantum materials. *Chem. Rev.* **121**, 2777–2779 (2021). URL https://pubs.acs.org/doi/10.1021/acs.chemrev.0c01322. 1

[5] Ashcroft, N. & Mermin, N. D. *Solid State Physics* (Cengage, 1976). 1, 15, 31, 50, 74

[6] Kittel, C. *Introduction to Solid State Physics* (Wiley, 2004), 8th edn. 1, 50

[7] Malozemoff, A. 1 - the power grid and the impact ofhigh-temperature superconductor technology: Anoverview. In Rey, C. (ed.) *Superconductors in the Power Grid*, Woodhead Publishing Series in Energy, 3–28 (Woodhead Publishing, 2015). URL https://www.sciencedirect.com/science/article/pii/B9781782420293000017. 1

[8] Castelvecci, D. The Race to Save the Internet from quantum hackers. *Nature* **602**, 198–201 (2002). 1

[9] Kitaev, A. Fault-tolerant quantum computation by anyons. *Annals of Physics* **303**, 2 – 30 (2003). URL http://www.sciencedirect.com/science/article/pii/S0003491602000180. 148

[10] Nayak, C., Simon, S. H., Stern, A., Freedman, M. & Das Sarma, S. Non-abelian anyons and topological quantum computation. *Rev. Mod. Phys.* **80**, 1083–1159 (2008). URL https://link.aps.org/doi/10.1103/RevModPhys.80.1083. 1, 148

[11] Hubbard, J. Electron correlations in narrow energy bands. *Proc. R. Soc. Lond.* **276**, 238–257 (1963). URL http://doi.org/10.1098/rspa.1963.0204. 1, 201

[12] Hohenberg, P. & Kohn, W. Inhomogeneous Electron Gas. *Phys. Rev.* **136**, B864–B871 (1964). 2, 7, 40, 41, 42, 226

[13] Kohn, W. & Sham, L. J. Self-consistent equations including exchange and correlation effects. *Phys. Rev.* **140**, A1133–A1138 (1965). URL https://link.aps.org/doi/10.1103/PhysRev.140.A1133. 2, 7, 45

[14] Runge, E. & Gross, E. K. U. Density-functional theory for time-dependent systems. *Phys. Rev. Lett.* **52**, 997–1000 (1984). URL https://link.aps.org/doi/10.1103/PhysRevLett.52.997. 2, 40, 64

[15] Bednorz, J. & Muller, K. Possible high Tc superconductivity in the Ba-La-Cu-O system. *Z. Phys. B* **64**, 189–193 (1986). 2

[16] Zou, Z. & Anderson, P. W. Neutral fermion, charge-e boson excitations in the resonating-valence-bond state and superconductivity in la_2cuo_4-based compounds. *Phys. Rev. B* **37**, 627–630 (1988). URL https://link.aps.org/doi/10.1103/PhysRevB.37.627. 2

[17] Kishida, H. *et al.* Large third-order optical nonlinearity of cu-o chains investigated by third-harmonic generation spectroscopy. *Phys. Rev. Lett.* **87**,

177401 (2001). URL https://link.aps.org/doi/10.1103/PhysRevLett.87.177401. 2, 30, 78

[18] Ono, M. *et al.* Linear and nonlinear optical properties of one-dimensional mott insulators consisting of Ni-halogen chain and CuO-chain compounds. *Phys. Rev. B* **70**, 085101 (2004). URL https://link.aps.org/doi/10.1103/PhysRevB.70.085101.

[19] Kishida, H. *et al.* Gigantic optical nonlinearity in one-dimensional motthubbard insulators. *Nature* **405**, 929 (2000). URL https://doi.org/10.1038/35016036.

[20] Kidd, T. E. *et al.* Doping of a one-dimensional mott insulator: Photoemission and optical studies of $sr_2Cuo_{3+\delta}$. *Phys. Rev. B* **77**, 054503 (2008). URL https://link.aps.org/doi/10.1103/PhysRevB.77.054503. 2, 30

[21] Giamarchi, T. & Press, O. U. *Quantum Physics in One Dimension*. International Series of Monographs on Physics (Clarendon Press, 2004). URL https://books.google.com/books?id=1MwTDAAAQBAJ. 2, 15, 204, 205

[22] Giuliani, G. & Vignale, G. *Quantum Theory of the Electron Liquid* (Cambridge, 2005). 2, 15, 69, 203, 204, 205, 226

[23] Kim, C. *et al.* Observation of spin-charge separation in one-dimensional $srcuo_2$. *Phys. Rev. Lett.* **77**, 4054–4057 (1996). URL https://link.aps.org/doi/10.1103/PhysRevLett.77.4054. 3, 15, 22, 23, 78

[24] Kim, C. *et al.* Separation of spin and charge excitations in one-dimensional $srcuo_2$. *Phys. Rev. B* **56**, 15589–15595 (1997). URL https://link.aps.org/doi/10.1103/PhysRevB.56.15589. 22

[25] Fujisawa, H. *et al.* Angle-resolved photoemission spectroscopy of srcuo2: spin-charge separation? *Journal of Electron Spectroscopy and Related Phenomena*

88-91, 461–465 (1998). URL https://www.sciencedirect.com/science/article/pii/S0368204897001722. Proceedings of the Seventh International Conference on Electron Spectroscopy. 23, 146

[26] Fujisawa, H. *et al.* Spin-charge separation in single-chain compound sr2cuo3 studied by angle-resolved photoemission. *Solid State Communications* **106**, 543–547 (1998). URL https://www.sciencedirect.com/science/article/pii/S0038109898000994. 23, 78

[27] Suga, S. *et al.* High-energy angle-resolved photoemission spectroscopy probing bulk correlated electronic states in quasi-one-dimensional v_6o_{13} and $SrCuo_2$. *Phys. Rev. B* **70**, 155106 (2004). URL https://link.aps.org/doi/10.1103/PhysRevB.70.155106. 3, 15, 23, 78

[28] Ami, T. *et al.* Magnetic susceptibility and low-temperature structure of the linear chain cuprate sr_2cuo_3. *Phys. Rev. B* **51**, 5994–6001 (1995). URL https://link.aps.org/doi/10.1103/PhysRevB.51.5994. 3, 15, 17, 146

[29] Motoyama, N., Eisaki, H. & Uchida, S. Magnetic susceptibility of ideal spin 1 /2 heisenberg antiferromagnetic chain systems, sr_2cuo_3 and $srcuo_2$. *Phys. Rev. Lett.* **76**, 3212–3215 (1996). URL https://link.aps.org/doi/10.1103/PhysRevLett.76.3212. 17, 146

[30] Zaliznyak, I. A. *et al.* Spinons in the strongly correlated copper oxide chains in $srcuo_2$. *Phys. Rev. Lett.* **93**, 087202 (2004). URL https://link.aps.org/doi/10.1103/PhysRevLett.93.087202. 3, 15, 19, 78

[31] Kim, K. W. & Gu, G. D. Optical excitations in sr_2cuo_3. *Phys. Rev. B* **79**, 085121 (2009). URL https://link.aps.org/doi/10.1103/PhysRevB.79.085121. 3, 15, 31, 78, 80, 104

[32] Kim, K. W., Gu, G. D., Homes, C. C. & Noh, T. W. Bound excitons in sr_2cuo_3. *Phys. Rev. Lett.* **101**, 177404 (2008). URL https://link.aps.org/doi/10.1103/PhysRevLett.101.177404. 3, 15, 30, 81

[33] Neudert, R. *et al.* Manifestation of spin-charge separation in the dynamic dielectric response of one-dimensional sr_2CuO_3. *Phys. Rev. Lett.* **81**, 657–660 (1998). URL https://link.aps.org/doi/10.1103/PhysRevLett.81.657. 3, 15, 26, 28, 29, 30, 34, 78, 80, 81, 82, 83, 115, 146

[34] Kim, Y.-J. *et al.* Resonant inelastic x-ray scattering of the holon-antiholon continuum in $srcuo_2$. *Phys. Rev. Lett.* **92**, 137402 (2004). URL https://link.aps.org/doi/10.1103/PhysRevLett.92.137402. 3, 34, 80

[35] Hasan, M. Z. *et al.* Momentum-resolved charge excitations in a prototype one-dimensional mott insulator. *Phys. Rev. Lett.* **88**, 177403 (2002). URL https://link.aps.org/doi/10.1103/PhysRevLett.88.177403. 3, 31, 34, 83

[36] Bube, R. *Photovoltaic Materials.* Series on properties of semiconductor materials (Imperial College Press, 1998). URL https://books.google.com/books?id=fIgTBAIza34C. 4

[37] W., B. K. *Survey of Semiconductor Physics, Electronic Transport in Semiconductors (Volume 2)* (Wiley, 2002). 4

[38] Born, M. & Oppenheimer, R. Zur quantentheorie der molekeln. *Annalen der Physik* **389**, 457–484 (1927). URL https://onlinelibrary.wiley.com/doi/abs/10.1002/andp.19273892002. https://onlinelibrary.wiley.com/doi/pdf/10.1002/andp.19273892002. 5

[39] Aryasetiawan, F., Karlsson, K., Jepsen, O. & Schönberger, U. Calculations of hubbard u from first-principles. *Phys. Rev. B* **74**, 125106 (2006). URL https://link.aps.org/doi/10.1103/PhysRevB.74.125106. 8, 40

[40] Eichstaedt, C. *et al.* Deriving models for the kitaev spin-liquid candidate material $\alpha-\mathrm{rucl}_3$ from first principles. *Phys. Rev. B* **100**, 075110 (2019). URL https://link.aps.org/doi/10.1103/PhysRevB.100.075110. 8, 39, 77, 147, 164, 165, 166, 167

[41] Zheng, H., Changlani, H. J., Williams, K. T., Busemeyer, B. & Wagner, L. K. From real materials to model hamiltonians with density matrix downfolding. *Frontiers in Physics* **6** (2018). URL https://www.frontiersin.org/article/10.3389/fphy.2018.00043. 8

[42] Wilson, K. G. Renormalization group and critical phenomena. i. renormalization group and the kadanoff scaling picture. *Phys. Rev. B* **4**, 3174–3183 (1971). URL https://link.aps.org/doi/10.1103/PhysRevB.4.3174.

[43] White, S. R. Numerical canonical transformation approach to quantum many-body problems. *The Journal of Chemical Physics* **117**, 7472–7482 (2002). URL https://doi.org/10.1063/1.1508370. https://doi.org/10.1063/1.1508370.

[44] Shankar, R. Renormalization-group approach to interacting fermions. *Rev. Mod. Phys.* **66**, 129–192 (1994). URL https://link.aps.org/doi/10.1103/RevModPhys.66.129. 8

[45] Callen, H. B. & Welton, T. A. Irreversibility and generalized noise. *Phys. Rev.* **83**, 34–40 (1951). URL https://link.aps.org/doi/10.1103/PhysRev.83.34. 9, 12, 220

[46] Sakurai, J. & Napolitano, J. *Modern Quantum Mechanics*. Œı (ł) (Addison-Wesley, 2011). URL https://books.google.com/books?id=N4I-AQAACAAJ. 11

[47] Taylor, J. *Scattering Theory: The Quantum Theory of Nonrelativistic Collisions*. Dover Books on Engineering (Dover Publications, 2012). URL https://books.google.com/books?id=OIaXvuwZMLQC. 11

[48] Schuelke, W. *Electron Dynamics by Inelastic X-Ray Scattering*. Oxford Series on Synchrotron Radiation (OUP Oxford, 2007). URL https://books.google.com/books?id=vwlREAAAQBAJ. 11, 12, 87

[49] Van Hove, L. Correlations in space and time and born approximation scattering in systems of interacting particles. *Phys. Rev.* **95**, 249–262 (1954). URL https://link.aps.org/doi/10.1103/PhysRev.95.249. 12, 16, 26

[50] Neudert, R. *et al.* Manifestation of spin-charge separation in the dynamic dielectric response of one-dimensional sr_2CuO_3. *Phys. Rev. Lett.* **81**, 657–660 (1998). URL https://link.aps.org/doi/10.1103/PhysRevLett.81.657. 12

[51] Pines, D. *Elementary Excitations In Solids*. Advanced Books Classics (Avalon Publishing, 1999). URL https://books.google.com/books?id=RVyXngEACAAJ. 15, 72

[52] Essler, F., Frahm, H., Göhmann, F., Klümper, A. & Korepin, V. *The One-Dimensional Hubbard Model* (Cambridge University Press, 2005). URL https://books.google.com/books?id=wo0VPXtlK6oC. 15

[53] Richter, J., Waidacher, C. & Becker, K. W. Role of zhang-rice singletlike excitations in one-dimensional cuprates. *Phys. Rev. B* **61**, 9871–9874 (2000). URL https://link.aps.org/doi/10.1103/PhysRevB.61.9871. 15, 28

[54] Hübsch, A., Richter, J., Waidacher, C., Becker, K. W. & Linden, W. v. d. Realistic description of electron-energy-loss spectroscopy for one-dimensional sr_2cuo_3. *Phys. Rev. B* **63**, 205103 (2001). URL https://link.aps.org/doi/10.1103/PhysRevB.63.205103. 15, 28, 29

[55] Squires, G. *Introduction to the Theory of Thermal Neutron Scattering*. Dover books on physics (Dover Publications, 1996). URL https://books.google.com/books?id=Lx4xcz3v9IMC. 16, 19

[56] Affeck, I., Gelfand, M. P. & Singh, R. R. P. A plane of weakly coupled heisenberg chains: theoretical arguments and numerical calculations. *Journal of Physics A: Mathematical and General* **27**, 7313–7325 (1994). URL https://doi.org/10.1088/0305-4470/27/22/009. 17

[57] Satija, S. K., Axe, J. D., Shirane, G., Yoshizawa, H. & Hirakawa, K. Neutron scattering study of spin waves in one-dimensional antiferromagnet $kcuf_3$. *Phys. Rev. B* **21**, 2001–2007 (1980). URL https://link.aps.org/doi/10.1103/PhysRevB.21.2001. 17

[58] Nagler, S. E., Tennant, D. A., Cowley, R. A., Perring, T. G. & Satija, S. K. Spin dynamics in the quantum antiferromagnetic chain compound $kcuf_3$. *Phys. Rev. B* **44**, 12361–12368 (1991). URL https://link.aps.org/doi/10.1103/PhysRevB.44.12361. 17

[59] Tennant, D. A., Perring, T. G., Cowley, R. A. & Nagler, S. E. Unbound spinons in the s=1/2 antiferromagnetic chain $kcuf_3$. *Phys. Rev. Lett.* **70**, 4003–4006 (1993). URL https://link.aps.org/doi/10.1103/PhysRevLett.70.4003. 17

[60] Tennant, D. A., Cowley, R. A., Nagler, S. E. & Tsvelik, A. M. Measurement of the spin-excitation continuum in one-dimensional $kcuf_3$ using neutron scattering. *Phys. Rev. B* **52**, 13368–13380 (1995). URL https://link.aps.org/doi/10.1103/PhysRevB.52.13368. 17

[61] Keren, A. *et al.* Muon-spin-rotation measurements in infinite-layer and infinite-chain cuprate antiferromagnets: $ca_{0.86}sr_{0.14}cuo_2$ and sr_2cuo_3. *Phys. Rev. B* **48**,

12926–12935 (1993). URL https://link.aps.org/doi/10.1103/PhysRevB.48.12926. 17

[62] Kojima, K. M. *et al.* Reduction of ordered moment and néel temperature of quasi-one-dimensional antiferromagnets sr_2cuo_3 and ca_2cuo_3. *Phys. Rev. Lett.* **78**, 1787–1790 (1997). URL https://link.aps.org/doi/10.1103/PhysRevLett.78.1787. 17

[63] Suzuura, H., Yasuhara, H., Furusaki, A., Nagaosa, N. & Tokura, Y. Singularities in optical spectra of quantum spin chains. *Phys. Rev. Lett.* **76**, 2579–2582 (1996). URL https://link.aps.org/doi/10.1103/PhysRevLett.76.2579. 17

[64] Zaliznyak, I. A., Broholm, C., Kibune, M., Nohara, M. & Takagi, H. Anisotropic spin freezing in the $S = 1/2$ zigzag chain compound $srcuo_2$. *Phys. Rev. Lett.* **83**, 5370–5373 (1999). URL https://link.aps.org/doi/10.1103/PhysRevLett.83.5370. 17

[65] Rosner, H., Eschrig, H., Hayn, R., Drechsler, S.-L. & Málek, J. Electronic structure and magnetic properties of the linear chain cuprates $sr_2cuo_3$and ca_2cuo_3. *Phys. Rev. B* **56**, 3402–3412 (1997). URL https://link.aps.org/doi/10.1103/PhysRevB.56.3402. 17

[66] Mermin, N. D. & Wagner, H. Absence of ferromagnetism or antiferromagnetism in one- or two-dimensional isotropic heisenberg models. *Phys. Rev. Lett.* **17**, 1133–1136 (1966). URL https://link.aps.org/doi/10.1103/PhysRevLett.17.1133. 17

[67] Anderson, P. W. Antiferromagnetism. theory of superexchange interaction. *Phys. Rev.* **79**, 350–356 (1950). URL https://link.aps.org/doi/10.1103/PhysRev.79.350. 18

[68] Bethe, H. Zur theorie der metalle. *Zeitschrift fr Physik* **71**, 205–226 (1931). URL https://doi.org/10.1007/BF01341708. 18, 89, 146

[69] Lieb, E. H. & Wu, F. Y. Absence of mott transition in an exact solution of the short-range, one-band model in one dimension. *Phys. Rev. Lett.* **20**, 1445–1448 (1968). URL https://link.aps.org/doi/10.1103/PhysRevLett.20.1445. 18, 204

[70] Hughes, H. & Starnberg, H. *Electron Spectroscopies Applied to Low-dimensional Structures*. Physics and Chemistry of Materials with Low-Dimensional Structures (Springer Netherlands, 2001). URL https://books.google.com/books?id=OLWm9YnPSqcC. 18

[71] Müller, G., Thomas, H., Beck, H. & Bonner, J. C. Quantum spin dynamics of the antiferromagnetic linear chain in zero and nonzero magnetic field. *Phys. Rev. B* **24**, 1429–1467 (1981). URL https://link.aps.org/doi/10.1103/PhysRevB.24.1429. 18, 19

[72] des Cloizeaux, J. & Pearson, J. J. Spin-wave spectrum of the antiferromagnetic linear chain. *Phys. Rev.* **128**, 2131–2135 (1962). URL https://link.aps.org/doi/10.1103/PhysRev.128.2131. 18

[73] Yamada, T. Fermi-Liquid Theory of Linear Antiferromagnetic Chains. *Progress of Theoretical Physics* **41**, 880–890 (1969). URL https://doi.org/10.1143/PTP.41.880. https://academic.oup.com/ptp/article-pdf/41/4/880/5337110/41-4-880.pdf. 18

[74] Walters, A. C. *Using X-ray and neutron scattering to study the dynamics of low-dimensional systems*. Ph.D. thesis (2009). 18, 19, 89

[75] Caux, J.-S. & Hagemans, R. The four-spinon dynamical structure factor of the heisenberg chain. *Journal of Statistical Mechanics: Theory and Experiment*

2006, P12013–P12013 (2006). URL https://doi.org/10.1088/1742-5468/2006/12/p12013. 19

[76] Mourigal, M. *et al.* Fractional spinon excitations in the quantum heisenberg antiferromagnetic chain. *Communications Physics* **4**, 435 (2013). URL https://doi.org/10.1038/nphys2652. 19

[77] Benthien, H., Gebhard, F. & Jeckelmann, E. Spectral function of the one-dimensional hubbard model away from half filling. *Phys. Rev. Lett.* **92**, 256401 (2004). URL https://link.aps.org/doi/10.1103/PhysRevLett.92.256401. 19

[78] Lorenzana, J., Seibold, G. & Coldea, R. Sum rules and missing spectral weight in magnetic neutron scattering in the cuprates. *Phys. Rev. B* **72**, 224511 (2005). URL https://link.aps.org/doi/10.1103/PhysRevB.72.224511. 19

[79] Tohyama, T. & Maekawa, S. Approximate decoupling of spin and charge excitations in the two-dimensional t- j model. *Journal of the Physical Society of Japan* **65**, 1902–1905 (1996). URL https://doi.org/10.1143/JPSJ.65.1902. https://doi.org/10.1143/JPSJ.65.1902. 22

[80] Nagasako, N. *et al.* Electronic band structure of srcuo2. *Journal of the Physical Society of Japan* **66**, 1756–1761 (1997). URL https://doi.org/10.1143/JPSJ.66.1756. https://doi.org/10.1143/JPSJ.66.1756. 23

[81] Li, S., Nocera, A., Kumar, U. & Johnston, S. Particle-hole asymmetry in the dynamical spin and charge responses of corner-shared 1d cuprates. *Communications Physics* **4**, 217 (2021). URL https://doi.org/10.1038/s42005-021-00718-w. 19, 24

[82] Baym, G. & Kadanoff, L. P. Conservation laws and correlation functions. *Phys. Rev.* **124**, 287–299 (1961). URL https://link.aps.org/doi/10.1103/PhysRev.124.287. 24

[83] Lundqvist, B. I. Single-particle spectrum of the degenerate electron gas. *Physik der kondensierten Materie* **6**, 193–205 (1967). URL https://doi.org/10.1007/BF02422716. 24

[84] Ley, L. & Cardona, M. *Photoemission in Solids II: Case Studies*. Topics in Applied Physics (Springer Berlin Heidelberg, 1979). URL https://books.google.com/books?id=n-hAAQAAIAAJ.

[85] Gatti, M., Panaccione, G. & Reining, L. Effects of low-energy excitations on spectral properties at higher binding energy: The metal-insulator transition of vo_2. *Phys. Rev. Lett.* **114**, 116402 (2015). URL https://link.aps.org/doi/10.1103/PhysRevLett.114.116402. 24

[86] Roth, F., Knig, A., Fink, J., Bchner, B. & Knupfer, M. Electron energy-loss spectroscopy: A versatile tool for the investigations of plasmonic excitations. *Journal of Electron Spectroscopy and Related Phenomena* **195**, 85–95 (2014). URL https://www.sciencedirect.com/science/article/pii/S0368204814001169. 26

[87] Fink, J., Knupfer, M., Atzkern, S. & Golden, M. Electronic correlations in solids, studied using electron energy-loss spectroscopy. *Journal of Electron Spectroscopy and Related Phenomena* **117-118**, 287–309 (2001). URL https://www.sciencedirect.com/science/article/pii/S0368204801002547. Strongly correlated systems. 26, 81, 82, 84

[88] Zhang, F. C. & Rice, T. M. Effective hamiltonian for the superconducting cu oxides. *Phys. Rev. B* **37**, 3759–3761 (1988). URL https://link.aps.org/doi/10.1103/PhysRevB.37.3759. 28

[89] Moskvin, A. S. *et al.* Evidence for two types of low-energy charge transfer excitations in sr_2cuo_3. *Phys. Rev. Lett.* **91**, 037001 (2003). URL https://link.aps.org/doi/10.1103/PhysRevLett.91.037001. 28

[90] Benthien, H. & Jeckelmann, E. Spin and charge dynamics of the one-dimensional extended hubbard model. *Phys. Rev. B* **75**, 205128 (2007). URL https://link.aps.org/doi/10.1103/PhysRevB.75.205128. 30, 31

[91] Essler, F. H. L., Gebhard, F. & Jeckelmann, E. Excitons in one-dimensional mott insulators. *Phys. Rev. B* **64**, 125119 (2001). URL https://link.aps.org/doi/10.1103/PhysRevB.64.125119. 30

[92] Jeckelmann, E. Optical excitations in a one-dimensional mott insulator. *Phys. Rev. B* **67**, 075106 (2003). URL https://link.aps.org/doi/10.1103/PhysRevB.67.075106. 31

[93] Ament, L. J. P., van Veenendaal, M., Devereaux, T. P., Hill, J. P. & van den Brink, J. Resonant inelastic x-ray scattering studies of elementary excitations. *Rev. Mod. Phys.* **83**, 705–767 (2011). URL https://link.aps.org/doi/10.1103/RevModPhys.83.705. 33

[94] Kramers, H. A. & Heisenberg, W. Über die Streuung von Strahlung durch Atome. *Zeitschrift fur Physik* **31**, 681–708 (1925). 33

[95] Kim, J. *et al.* Comparison of resonant inelastic x-ray scattering spectra and dielectric loss functions in copper oxides. *Phys. Rev. B* **79**, 094525 (2009). URL https://link.aps.org/doi/10.1103/PhysRevB.79.094525. 34

[96] Jia, C., Wohlfeld, K., Wang, Y., Moritz, B. & Devereaux, T. P. Using rixs to uncover elementary charge and spin excitations. *Phys. Rev. X* **6**, 021020 (2016). URL https://link.aps.org/doi/10.1103/PhysRevX.6.021020. 34

[97] Tsutsui, K., Tohyama, T. & Maekawa, S. Resonant inelastic x-ray scattering in one-dimensional copper oxides. *Phys. Rev. B* **61**, 7180–7182 (2000). URL https://link.aps.org/doi/10.1103/PhysRevB.61.7180. 34

[98] Stephan, W. & Penc, K. Dynamical density-density correlations in one-dimensional mott insulators. *Phys. Rev. B* **54**, R17269–R17272 (1996). URL https://link.aps.org/doi/10.1103/PhysRevB.54.R17269.

[99] Penc, K. & Stephan, W. Dynamical correlations in one-dimensional charge-transfer insulators. *Phys. Rev. B* **62**, 12707–12714 (2000). URL https://link.aps.org/doi/10.1103/PhysRevB.62.12707. 34

[100] Hasan, M. Z. *et al.* Electronic structure of mott insulators studied by inelastic x-ray scattering. *Science* **288**, 1811–1814 (2000). URL https://www.science.org/doi/abs/10.1126/science.288.5472.1811. https://www.science.org/doi/pdf/10.1126/science.288.5472.1811. 34

[101] Kugel, K. I. & Khomskiĭ, D. I. The jahn-teller effect and magnetism: transition metal compounds. *Soviet Physics Uspekhi* **25**, 231–256 (1982). URL https://doi.org/10.1070/pu1982v025n04abeh004537. 35

[102] Wohlfeld, K., Nishimoto, S., Haverkort, M. W. & van den Brink, J. Microscopic origin of spin-orbital separation in sr_2cuo_3. *Phys. Rev. B* **88**, 195138 (2013). URL https://link.aps.org/doi/10.1103/PhysRevB.88.195138. 35

[103] http://elk.sourceforge.net. 37

[104] Kozhevnikov, A., Eguiluz, A. G. & Schulthess, T. C. Toward first principles electronic structure simulations of excited states and strong correlations in nano- and materials science. In *Proceedings of the 2010 ACM/IEEE International Conference for High Performance Computing, Networking, Storage and Analysis*, SC '10, 110 (IEEE Computer Society, USA, 2010). URL https://doi.org/10.1109/SC.2010.55. 37

[105] Phan, W. Y. *Accelerating Dynamical Density Response Code on Summit and Its Application for Computing the Density Response Function of Vanadium Sesquioxide*. Ph.D. thesis (2021). 37

[106] Laurell, P. & Okamoto, S. Dynamical and thermal magnetic properties of the kitaev spin liquid candidate α-rucl$_3$. *npj Quantum Materials* **5** (2020). URL https://doi.org/10.1038/s41535-019-0203-y. 39, 147, 164, 166, 167, 168

[107] Wannier, G. H. The structure of electronic excitation levels in insulating crystals. *Phys. Rev.* **52**, 191–197 (1937). URL https://link.aps.org/doi/10.1103/PhysRev.52.191. 40, 54

[108] Souza, I., Marzari, N. & Vanderbilt, D. Maximally localized wannier functions for entangled energy bands. *Phys. Rev. B* **65**, 035109 (2001). URL https://link.aps.org/doi/10.1103/PhysRevB.65.035109. 40

[109] Pizzi, G. *et al.* Wannier90 as a community code: new features and applications. *Journal of Physics: Condensed Matter* **32**, 165902 (2020). 40

[110] Petersilka, M., Gossmann, U. J. & Gross, E. K. U. Excitation energies from time-dependent density-functional theory. *Phys. Rev. Lett.* **76**, 1212–1215 (1996). URL https://link.aps.org/doi/10.1103/PhysRevLett.76.1212. 40, 67, 72

[111] Mermin, N. D. Thermal properties of the inhomogeneous electron gas. *Phys. Rev.* **137**, A1441–A1443 (1965). URL https://link.aps.org/doi/10.1103/PhysRev.137.A1441. 41

[112] Vignale, G. & Rasolt, M. Density-functional theory in strong magnetic fields. *Phys. Rev. Lett.* **59**, 2360–2363 (1987). URL https://link.aps.org/doi/10.1103/PhysRevLett.59.2360. 44

[113] von Barth, U. & Hedin, L. A local exchange-correlation potential for the spin polarized case. i. *Journal of Physics C: Solid State Physics* **5**, 1629–1642 (1972). URL https://doi.org/10.1088/0022-3719/5/13/012. 44

[114] Thomas, L. H. The calculation of atomic fields. *Mathematical Proceedings of the Cambridge Philosophical Society* **23**, 542548 (1927). 45

[115] Gunnarsson, O. & Lundqvist, B. I. Exchange and correlation in atoms, molecules, and solids by the spin-density-functional formalism. *Phys. Rev. B* **13**, 4274–4298 (1976). URL https://link.aps.org/doi/10.1103/PhysRevB.13.4274. 48

[116] Ceperley, D. M. & Alder, B. J. Ground state of the electron gas by a stochastic method. *Phys. Rev. Lett.* **45**, 566–569 (1980). URL https://link.aps.org/doi/10.1103/PhysRevLett.45.566. 49

[117] Perdew, J. P. & Zunger, A. Self-interaction correction to density-functional approximations for many-electron systems. *Phys. Rev. B* **23**, 5048–5079 (1981). URL https://link.aps.org/doi/10.1103/PhysRevB.23.5048. 49

[118] Perdew, J. P. & Wang, Y. Accurate and simple analytic representation of the electron-gas correlation energy. *Phys. Rev. B* **45**, 13244–13249 (1992). URL https://link.aps.org/doi/10.1103/PhysRevB.45.13244. 49

[119] Perdew, J. P., Burke, K. & Ernzerhof, M. Generalized gradient approximation made simple. *Phys. Rev. Lett.* **77**, 3865–3868 (1996). URL https://link.aps.org/doi/10.1103/PhysRevLett.77.3865. 49, 92, 151

[120] Petukhov, A. G., Mazin, I. I., Chioncel, L. & Lichtenstein, A. I. Correlated metals and the LDA + u method. *Phys. Rev. B* **67**, 153106 (2003). URL https://link.aps.org/doi/10.1103/PhysRevB.67.153106. 49

[121] Anisimov, V. I., Zaanen, J. & Andersen, O. K. Band theory and mott insulators: Hubbard u instead of stoner i. *Phys. Rev. B* **44**, 943–954 (1991). URL https://link.aps.org/doi/10.1103/PhysRevB.44.943. 49

[122] Czyżyk, M. T. & Sawatzky, G. A. Local-density functional and on-site correlations: The electronic structure of la_2cuo_4 and $lacuo_3$. *Phys. Rev. B* **49**, 14211–14228 (1994). URL https://link.aps.org/doi/10.1103/PhysRevB.49.14211. 50, 92

[123] Quinn, J. & Yi, K. *Solid State Physics: Principles and Modern Applications*. UNITEXT for Physics (Springer International Publishing, 2018). URL https://books.google.com/books?id=vJRNDwAAQBAJ. 50

[124] Phillips, J. C. & Kleinman, L. New method for calculating wave functions in crystals and molecules. *Phys. Rev.* **116**, 287–294 (1959). URL https://link.aps.org/doi/10.1103/PhysRev.116.287. 52

[125] Hamann, D. R., Schlüter, M. & Chiang, C. Norm-conserving pseudopotentials. *Phys. Rev. Lett.* **43**, 1494–1497 (1979). URL https://link.aps.org/doi/10.1103/PhysRevLett.43.1494.

[126] Bachelet, G. B., Hamann, D. R. & Schlüter, M. Pseudopotentials that work: From h to pu. *Phys. Rev. B* **26**, 4199–4228 (1982). URL https://link.aps.org/doi/10.1103/PhysRevB.26.4199.

[127] Kleinman, L. & Bylander, D. M. Efficacious form for model pseudopotentials. *Phys. Rev. Lett.* **48**, 1425–1428 (1982). URL https://link.aps.org/doi/10.1103/PhysRevLett.48.1425.

[128] Vanderbilt, D. Soft self-consistent pseudopotentials in a generalized eigenvalue formalism. *Phys. Rev. B* **41**, 7892–7895 (1990). URL https://link.aps.org/doi/10.1103/PhysRevB.41.7892.

[129] Pickett, W. E. Pseudopotential methods in condensed matter applications. *Computer Physics Reports* **9**, 115–197 (1989). URL https://www.sciencedirect.com/science/article/pii/0167797789900026. 52

[130] Methfessel, M., Rodriguez, C. O. & Andersen, O. K. Fast full-potential calculations with a converged basis of atom-centered linear muffin-tin orbitals: Structural and dynamic properties of silicon. *Phys. Rev. B* **40**, 2009–2012 (1989). URL https://link.aps.org/doi/10.1103/PhysRevB.40.2009. 53

[131] Methfessel, M. Elastic constants and phonon frequencies of si calculated by a fast full-potential linear-muffin-tin-orbital method. *Phys. Rev. B* **38**, 1537–1540 (1988). URL https://link.aps.org/doi/10.1103/PhysRevB.38.1537. 53

[132] Slater, J. C. & Koster, G. F. Simplified lcao method for the periodic potential problem. *Phys. Rev.* **94**, 1498–1524 (1954). URL https://link.aps.org/doi/10.1103/PhysRev.94.1498. 53

[133] Ku, W. & Eguiluz, A. G. Band-gap problem in semiconductors revisited: Effects of core states and many-body self-consistency. *Phys. Rev. Lett.* **89**, 126401 (2002). URL https://link.aps.org/doi/10.1103/PhysRevLett.89.126401. 53

[134] Singh, D. J. & Nordström, L. *Planewaves, Pseudopotentials, and the LAPW Method* (Springer, 2006), 2 edn. 53, 153

[135] Marzari, N. & Vanderbilt, D. Maximally localized generalized wannier functions for composite energy bands. *Phys. Rev. B* **56**, 12847–12865 (1997). URL https://link.aps.org/doi/10.1103/PhysRevB.56.12847. 54

[136] Ku, W., Rosner, H., Pickett, W. E. & Scalettar, R. T. Insulating ferromagnetism in $la_4ba_2cu_2o_{10}$: An ab initio wannier function analysis. *Phys. Rev. Lett.* **89**, 167204 (2002). URL https://link.aps.org/doi/10.1103/PhysRevLett.89.167204. 57

[137] Mayer, I. On lwdin's method of symmetric orthogonalization*. *International Journal of Quantum Chemistry* **90**, 63–65 (2002). URL https://onlinelibrary.wiley.com/doi/abs/10.1002/qua.981. https://onlinelibrary.wiley.com/doi/pdf/10.1002/qua.981. 58, 151

[138] Souza, I., Marzari, N. & Vanderbilt, D. Maximally localized wannier functions for entangled energy bands. *Phys. Rev. B* **65**, 035109 (2001). URL https://link.aps.org/doi/10.1103/PhysRevB.65.035109. 60, 61

[139] Werner, P., Sakuma, R., Nilsson, F. & Aryasetiawan, F. Dynamical screening in la_2cuo_4. *Phys. Rev. B* **91**, 125142 (2015). URL https://link.aps.org/doi/10.1103/PhysRevB.91.125142. 61, 77

[140] Marques, M., Maitra, N., Nogueira, F., Gross, E. & Rubio, A. *Fundamentals of Time-Dependent Density Functional Theory*. Lecture Notes in Physics (Springer Berlin Heidelberg, 2012). URL https://books.google.com/books?id=bvRZhGR3BnwC. 69

[141] Strinati, G., Mattausch, H. J. & Hanke, W. Dynamical aspects of correlation corrections in a covalent crystal. *Phys. Rev. B* **25**, 2867–2888 (1982). URL https://link.aps.org/doi/10.1103/PhysRevB.25.2867. 70

[142] Strinati, G., Mattausch, H. J. & Hanke, W. Dynamical correlation effects on the quasiparticle bloch states of a covalent crystal. *Phys. Rev. Lett.* **45**, 290–294 (1980). URL https://link.aps.org/doi/10.1103/PhysRevLett.45.290.

[143] Hanke, W. *The role of electron-hole interaction in the optical spectra of semiconductors and insulators*, 43–75 (Springer Berlin Heidelberg, Berlin, Heidelberg, 1979). URL https://doi.org/10.1007/BFb0108325.

[144] Hanke, W. & Sham, L. J. Many-particle effects in the optical spectrum of a semiconductor. *Phys. Rev. B* **21**, 4656–4673 (1980). URL https://link.aps.org/doi/10.1103/PhysRevB.21.4656.

[145] Hanke, W. & Sham, L. J. Local-field and excitonic effects in the optical spectrum of a covalent crystal. *Phys. Rev. B* **12**, 4501–4511 (1975). URL https://link.aps.org/doi/10.1103/PhysRevB.12.4501.

[146] Hanke, W. & Sham, L. J. Many-particle effects in the optical excitations of a semiconductor. *Phys. Rev. Lett.* **43**, 387–390 (1979). URL https://link.aps.org/doi/10.1103/PhysRevLett.43.387.

[147] Hanke, W. & Sham, L. J. Dielectric response in the wannier representation: Application to the optical spectrum of diamond. *Phys. Rev. Lett.* **33**, 582–585 (1974). URL https://link.aps.org/doi/10.1103/PhysRevLett.33.582. 70

[148] Sharma, S., Dewhurst, J. K., Sanna, A. & Gross, E. K. U. Bootstrap approximation for the exchange-correlation kernel of time-dependent density-functional theory. *Phys. Rev. Lett.* **107**, 186401 (2011). URL https://link.aps.org/doi/10.1103/PhysRevLett.107.186401. 72

[149] Sottile, F., Olevano, V. & Reining, L. Parameter-free calculation of response functions in time-dependent density-functional theory. *Phys. Rev. Lett.* **91**, 056402 (2003). URL https://link.aps.org/doi/10.1103/PhysRevLett.91.056402. 72

[150] Aryasetiawan, F., Miyake, T. & Sakuma, R. The constrained rpa method for calculating the hubbard u from first-principles. In Pavarini, E., Koch, E., Vollhardt, D. & Lichtenstein, A. (eds.) *The LDA+DMFT approach to strongly correlated materials*, chap. 7 (Forschungszentrum Jülich GmbH Institute for Advanced Simulations, Jülich, 2004). 76

[151] Kim, C. *et al.* Observation of spin-charge separation in one-dimensional $srcuo_2$. *Phys. Rev. Lett.* **77**, 4054–4057 (1996). URL https://link.aps.org/doi/10.1103/PhysRevLett.77.4054. 78

[152] Kim, C. *et al.* Separation of spin and charge excitations in one-dimensional $srcuo_2$. *Phys. Rev. B* **56**, 15589–15595 (1997). URL https://link.aps.org/doi/10.1103/PhysRevB.56.15589.

[153] Fujisawa, H. *et al.* Angle-resolved photoemission spectroscopy of srcuo2: spin-charge separation? *Journal of Electron Spectroscopy and Related Phenomena* **88-91**, 461–465 (1998). URL https://www.sciencedirect.com/science/

article/pii/S0368204897001722. Proceedings of the Seventh International Conference on Electron Spectroscopy.

[154] Koitzsch, A. *et al.* Current spinon-holon description of the one-dimensional charge-transfer insulator $SrCuo_2$: Angle-resolved photoemission measurements. *Phys. Rev. B* **73**, 201101 (2006). URL https://link.aps.org/doi/10.1103/PhysRevB.73.201101.

[155] Kim, B. J. *et al.* Distinct spinon and holon dispersions in photoemission spectral functions from one-dimensional $SrCuo_2$. *Nature Physics* **2**, 397–401 (2006). URL https://doi.org/10.1038/nphys316.

[156] Fujisawa, H. *et al.* Spin-charge separation in single-chain compound sr2cuo3 studied by angle-resolved photoemission. *Solid State Communications* **106**, 543–547 (1998). URL https://www.sciencedirect.com/science/article/pii/S0038109898000994. 78

[157] Neudert, R. *et al.* Four-band extended hubbard hamiltonian for the one-dimensional cuprate sr_2cuo_3 : distribution of oxygen holes and its relation to strong intersite coulomb interaction. *Phys. Rev. B* **62**, 10752–10765 (2000). URL https://link.aps.org/doi/10.1103/PhysRevB.62.10752. 79

[158] Hilgers, C. *The electronic structure of spin ladders and spin chains studied by ellipsometry*. Ph.D. thesis (2009). 81

[159] Cai, Y. Q. *et al.* Low-energy charge-density excitations in mgb_2: Striking interplay between single-particle and collective behavior for large momenta. *Phys. Rev. Lett.* **97**, 176402 (2006). URL https://link.aps.org/doi/10.1103/PhysRevLett.97.176402. 87

[160] Yava, H. *et al.* Evidence for two types of low-energy charge transfer excitations in sr_2cuo_3. *Nature Physics* **15**, 559 (2019). URL https://doi.org/10.1038/s41567-019-0471-2. 87

[161] Kim, Y.-J. *et al.* Resonant inelastic x-ray scattering of the holon-antiholon continuum in srcuo$_2$. *Phys. Rev. Lett.* **92**, 137402 (2004). URL https://link.aps.org/doi/10.1103/PhysRevLett.92.137402. 89, 115

[162] Teske, C. L. & Mller-Buschbaum, H. ber erdalkalimetalloxocuprate. ii. zur kenntnis von sr$_2$CuO$_3$. *Zeitschrift fr anorganische und allgemeine Chemie* **371**, 325–332 (1969). URL https://onlinelibrary.wiley.com/doi/abs/10.1002/zaac.19693710515. https://onlinelibrary.wiley.com/doi/pdf/10.1002/zaac.19693710515. 92

[163] Hjorth, M. & Hyldtoft, J. Crystal structure of dicalcium cuprate, ca$_2$CuO$_3$. *Acta Chem. Scand.* **44**, 516–518. 92

[164] Matsushita, Y., Oyama, Y., Hasegawa, M. & Takei, H. Growth and structural refinement of orthorhombic srcuo2 crystals. *Journal of Solid State Chemistry* **114**, 289–293 (1995). URL https://www.sciencedirect.com/science/article/pii/S0022459685710432. 92

[165] Liechtenstein, A. I., Anisimov, V. I. & Zaanen, J. Density-functional theory and strong interactions: Orbital ordering in mott-hubbard insulators. *Phys. Rev. B* **52**, R5467–R5470 (1995). URL https://link.aps.org/doi/10.1103/PhysRevB.52.R5467. 92

[166] Zaanen, J., Sawatzky, G. A. & Allen, J. W. Band gaps and electronic structure of transition-metal compounds. *Phys. Rev. Lett.* **55**, 418–421 (1985). URL https://link.aps.org/doi/10.1103/PhysRevLett.55.418. 102

[167] Fulde, P. *Correlated Electrons in Quantum Matter* (WORLD SCIENTIFIC, 2012). URL https://www.worldscientific.com/doi/abs/10.1142/8419. https://www.worldscientific.com/doi/pdf/10.1142/8419. 104

[168] Bohm, D. & Pines, D. A collective description of electron interactions. i. magnetic interactions. *Phys. Rev.* **82**, 625–634 (1951). URL https://link.aps.org/doi/10.1103/PhysRev.82.625. 112

[169] Pines, D. & Bohm, D. A collective description of electron interactions: Ii. collective vs individual particle aspects of the interactions. *Phys. Rev.* **85**, 338–353 (1952). URL https://link.aps.org/doi/10.1103/PhysRev.85.338.

[170] Bohm, D. & Pines, D. A collective description of electron interactions: Iii. coulomb interactions in a degenerate electron gas. *Phys. Rev.* **92**, 609–625 (1953). URL https://link.aps.org/doi/10.1103/PhysRev.92.609. 112

[171] Moskvin, A. S. *et al.* Evidence for Two Types of Low-Energy Charge Transfer Excitations in Sr_2CuO_3. *Phys. Rev. Lett.* **91**, 037001 (2003). 138

[172] Kitaev, A. Anyons in an exactly solved model and beyond. *Annals of Physics* **321**, 2 – 111 (2006). URL http://www.sciencedirect.com/science/article/pii/S0003491605002381. January Special Issue. 148

[173] Chaloupka, J. c. v., Jackeli, G. & Khaliullin, G. Kitaev-heisenberg model on a honeycomb lattice: Possible exotic phases in iridium oxides A_2iro_3. *Phys. Rev. Lett.* **105**, 027204 (2010). URL https://link.aps.org/doi/10.1103/PhysRevLett.105.027204. 148, 149

[174] Liu, X. *et al.* Long-range magnetic ordering in na_2iro_3. *Phys. Rev. B* **83**, 220403 (2011). URL https://link.aps.org/doi/10.1103/PhysRevB.83.220403. 148

[175] Choi, S. K. *et al.* Spin waves and revised crystal structure of honeycomb iridate na_2iro_3. *Phys. Rev. Lett.* **108**, 127204 (2012). URL https://link.aps.org/doi/10.1103/PhysRevLett.108.127204. 148

[176] Ye, F. *et al.* Direct evidence of a zigzag spin-chain structure in the honeycomb lattice: A neutron and x-ray diffraction investigation of single-crystal na_2iro_3.

Phys. Rev. B **85**, 180403 (2012). URL https://link.aps.org/doi/10.1103/PhysRevB.85.180403. 148

[177] Kimchi, I. & You, Y.-Z. Kitaev-heisenberg-J_2-J_3 model for the iridates $A_2\mathrm{iro}_3$. *Phys. Rev. B* **84**, 180407 (2011). URL https://link.aps.org/doi/10.1103/PhysRevB.84.180407. 148

[178] Yamaji, Y., Nomura, Y., Kurita, M., Arita, R. & Imada, M. First-principles study of the honeycomb-lattice iridates $\mathrm{na}_2\mathrm{iro}_3$ in the presence of strong spin-orbit interaction and electron correlations. *Phys. Rev. Lett.* **113**, 107201 (2014). URL https://link.aps.org/doi/10.1103/PhysRevLett.113.107201. 148, 159, 160

[179] Mazin, I. I., Jeschke, H. O., Foyevtsova, K., Valentí, R. & Khomskii, D. I. $\mathrm{na}_2\mathrm{iro}_3$ as a molecular orbital crystal. *Phys. Rev. Lett.* **109**, 197201 (2012). URL https://link.aps.org/doi/10.1103/PhysRevLett.109.197201. 149

[180] Plumb, K. W. *et al.* $\alpha - \mathrm{rucl}_3$: A spin-orbit assisted mott insulator on a honeycomb lattice. *Phys. Rev. B* **90**, 041112 (2014). URL https://link.aps.org/doi/10.1103/PhysRevB.90.041112. 149

[181] Kim, H.-S., V., V. S., Catuneanu, A. & Kee, H.-Y. Kitaev magnetism in honeycomb rucl_3 with intermediate spin-orbit coupling. *Phys. Rev. B* **91**, 241110 (2015). URL https://link.aps.org/doi/10.1103/PhysRevB.91.241110. 149, 150

[182] Banerjee, A. *et al.* Proximate kitaev quantum spin liquid behaviour in a honeycomb magnet. *Nature Materials* **15**, 733 EP – (2016). URL https://doi.org/10.1038/nmat4604. Article. 149

[183] Sears, J. A. *et al.* Magnetic order in $\alpha - \mathrm{rucl}_3$: A honeycomb-lattice quantum magnet with strong spin-orbit coupling. *Phys. Rev. B* **91**, 144420 (2015). URL https://link.aps.org/doi/10.1103/PhysRevB.91.144420.

[184] Johnson, R. D. *et al.* Monoclinic crystal structure of $\alpha - \mathrm{rucl}_3$ and the zigzag antiferromagnetic ground state. *Phys. Rev. B* **92**, 235119 (2015). URL https://link.aps.org/doi/10.1103/PhysRevB.92.235119. 151

[185] Cao, H. B. *et al.* Low-temperature crystal and magnetic structure of $\alpha - \mathrm{rucl}_3$. *Phys. Rev. B* **93**, 134423 (2016). URL https://link.aps.org/doi/10.1103/PhysRevB.93.134423. 149

[186] Banerjee, A. *et al.* Excitations in the field-induced quantum spin liquid state of î-rucl3. *npj Quantum Materials* **3**, 8 (2018). URL https://doi.org/10.1038/s41535-018-0079-2. 149

[187] Kasahara, Y. *et al.* Majorana quantization and half-integer thermal quantum hall effect in a kitaev spin liquid. *Nature* **559**, 227–231 (2018). URL https://doi.org/10.1038/s41586-018-0274-0. 149

[188] Winter, S. M. *et al.* Breakdown of magnons in a strongly spin-orbital coupled magnet. *Nature Communications* **8**, 1152 (2017). URL https://doi.org/10.1038/s41467-017-01177-0. 149, 161, 165, 166, 167

[189] Wu, L. *et al.* Field evolution of magnons in $\alpha-\mathrm{rucl}_3$ by high-resolution polarized terahertz spectroscopy. *Phys. Rev. B* **98**, 094425 (2018). URL https://link.aps.org/doi/10.1103/PhysRevB.98.094425. 150, 161, 165, 166, 167

[190] Lampen-Kelley, P. *et al.* Anisotropic susceptibilities in the honeycomb kitaev system $\alpha - \mathrm{rucl}_3$. *Phys. Rev. B* **98**, 100403 (2018). URL https://link.aps.org/doi/10.1103/PhysRevB.98.100403. 150, 161

[191] Kim, H.-S. & Kee, H.-Y. Crystal structure and magnetism in $\alpha - \mathrm{rucl}_3$: An ab initio study. *Phys. Rev. B* **93**, 155143 (2016). URL https://link.aps.org/doi/10.1103/PhysRevB.93.155143. 150, 159, 165, 166, 167

[192] Yadav, R. *et al.* Kitaev exchange and field-induced quantum spin-liquid states in honeycomb î-rucl3. *Scientific Reports* **6**, 37925 (2016). URL https://doi.org/10.1038/srep37925. Article. 150, 165, 166, 167

[193] Suzuki, T. & Suga, S.-i. Effective model with strong kitaev interactions for $\alpha-rucl_3$. *Phys. Rev. B* **97**, 134424 (2018). URL https://link.aps.org/doi/10.1103/PhysRevB.97.134424. 161

[194] Winter, S. M. *et al.* Models and materials for generalized kitaev magnetism. *Journal of Physics: Condensed Matter* **29**, 493002 (2017).

[195] Winter, S. M., Li, Y., Jeschke, H. O. & Valentí, R. Challenges in design of kitaev materials: Magnetic interactions from competing energy scales. *Phys. Rev. B* **93**, 214431 (2016). URL https://link.aps.org/doi/10.1103/PhysRevB.93.214431. 149, 150, 151, 155, 159, 160, 165, 166, 167

[196] Ran, K. *et al.* Spin-wave excitations evidencing the kitaev interaction in single crystalline $\alpha-rucl_3$. *Phys. Rev. Lett.* **118**, 107203 (2017). URL https://link.aps.org/doi/10.1103/PhysRevLett.118.107203. 149, 161

[197] Hou, Y. S., Xiang, H. J. & Gong, X. G. Unveiling magnetic interactions of ruthenium trichloride via constraining direction of orbital moments: Potential routes to realize a quantum spin liquid. *Phys. Rev. B* **96**, 054410 (2017). URL https://link.aps.org/doi/10.1103/PhysRevB.96.054410. 150

[198] Marzari, N. & Vanderbilt, D. Maximally localized generalized wannier functions for composite energy bands. *Phys. Rev. B* **56**, 12847–12865 (1997). URL https://link.aps.org/doi/10.1103/PhysRevB.56.12847. 151

[199] Tian, W. *et al.* High antiferromagnetic transition temperature of the honeycomb compound $srru_2o_6$. *Phys. Rev. B* **92**, 100404 (2015). URL https://link.aps.org/doi/10.1103/PhysRevB.92.100404. 159

[200] Miyake, T., Nakamura, K., Arita, R. & Imada, M. Comparison of ab initio low-energy models for lafepo, lafeaso, bafe2as2, lifeas, fese, and fete: Electron correlation and covalency. *Journal of the Physical Society of Japan* **79**, 044705 (2010). URL https://journals.jps.jp/doi/abs/10.1143/JPSJ.79.044705. https://journals.jps.jp/doi/pdf/10.1143/JPSJ.79.044705. 159

[201] Jones, M. D. & Albers, R. C. Spin-orbit coupling in an f-electron tight-binding model: Electronic properties of th, u, and pu. *Phys. Rev. B* **79**, 045107 (2009). URL https://link.aps.org/doi/10.1103/PhysRevB.79.045107. 159

[202] Kubota, Y., Tanaka, H., Ono, T., Narumi, Y. & Kindo, K. Successive magnetic phase transitions in $\alpha - \mathrm{rucl}_3$: Xy-like frustrated magnet on the honeycomb lattice. *Phys. Rev. B* **91**, 094422 (2015). URL https://link.aps.org/doi/10.1103/PhysRevB.91.094422. 161

[203] Do, S.-H. *et al.* Majorana fermions in the kitaev quantum spin system $\alpha - \mathrm{rucl}_3$. *Nature Physics* **13**, 1079 (2017). URL https://doi.org/10.1038/nphys4264. 161

[204] Dagotto, E. Correlated electrons in high-temperature superconductors. *Rev. Mod. Phys.* **66**, 763–840 (1994). URL https://link.aps.org/doi/10.1103/RevModPhys.66.763. 164

[205] Sugiura, S. & Shimizu, A. Thermal pure quantum states at finite temperature. *Phys. Rev. Lett.* **108**, 240401 (2012). URL https://link.aps.org/doi/10.1103/PhysRevLett.108.240401. 164

[206] Rau, J. G., Lee, E. K.-H. & Kee, H.-Y. Generic spin model for the honeycomb iridates beyond the kitaev limit. *Phys. Rev. Lett.* **112**, 077204 (2014). URL https://link.aps.org/doi/10.1103/PhysRevLett.112.077204. 165

[207] Rau, J. G. & Kee, H.-Y. Trigonal distortion in the honeycomb iridates: Proximity of zigzag and spiral phases in na2iro3 (2014). URL https://arxiv.org/abs/1408.4811. 165

[208] Drude, P. Zur Elektronentheorie der Metalle. *Annalen der Physik* **306**, 566613 (1900). 200

[209] Sommerfeld, A. Zur Quantentheorie der Spektrallinien. *Annalen der Physik* **51**, 1–94 (1928). 200

[210] Landau, L. Theory of Fermi-Liquids. *Sov. Phys. JETP-USSR* **3**, 920–925 (1956). 201

[211] Mahan, G. *Many-Particle Physics* (Springer, 2000), 3rd edn. 202, 204, 205

[212] Taylor, P. L. & Heinonen, O. *A Quantum Approach to Condensed Matter Physics* (Cambridge, 2002). 202

[213] Bloch, F. Inkohärente röntgenstreuung und dichteschwankungen eines entarteten fermigases. *Helv. Phys. Acta* **7**, 385–405 (1934). 202

[214] Haldane, F. D. M. luttinger liquid theory of one-dimensional quantum fluids. i. properties of the luttinger model and their extension to the general 1d interacting spinless fermi gas. *Journal of Physics C: Solid State Physics* **14**, 2585–2609 (1981). URL https://doi.org/10.1088/0022-3719/14/19/010. 203, 204

[215] Tomonaga, S.-i. Remarks on Bloch's Method of Sound Waves applied to Many-Fermion Problems. *Progress of Theoretical Physics* **5**, 544–569 (1950). URL https://doi.org/10.1143/ptp/5.4.544. https://academic.oup.com/ptp/article-pdf/5/4/544/5430161/5-4-544.pdf. 203

[216] Luttinger, J. M. An exactly soluble model of a manyfermion system. *Journal of Mathematical Physics* **4**, 1154–1162 (1963). URL https://doi.org/10.1063/1.1704046. https://doi.org/10.1063/1.1704046. 203

[217] Mattis, D. C. & Lieb, E. H. Exact solution of a manyfermion system and its associated boson field. *Journal of Mathematical Physics* **6**, 304–312 (1965). URL https://doi.org/10.1063/1.1704281. https://doi.org/10.1063/1.1704281. 204, 206

[218] Schulz, H. J. Fermi liquids and non–fermi liquids (1995). URL https://arxiv.org/abs/cond-mat/9503150. 204

[219] Hughes, H. & Starnberg, H. *Electron Spectroscopies Applied to Low-Dimensional Materials* (Springer,Dordrecht, 2000). 204

[220] Phillips, P. *Advanced Solid State Physics* (Cambridge, 2012), 2nd edn. 204

[221] Sòlyom, J. *Fundamentals of the Physics of Solids Vol. 3* (Springer-Verlag, 2010), 1st edn. 205, 212

[222] van Leeuwen, R. Mapping from Densities to Potentials in Time-Dependent Density-Functional Theory. *Phys. Rev. Lett.* **82**, 3863–3866 (1999). 226, 227

[223] Ullrich, C. A. *Time-dependent density-functional theory: concepts and applications* (Oxford University Press, New York, 2012). 226

Appendix A

Luttinger Liquids

A Brief History: Electron Modeling in Three Dimensions

Modeling materials is an extremely difficult task due to the numerical complexity and the countless number of materials that have been synthesized with widely different properties. After James Clerk Maxwell solidified the equations that govern electromagnetism in the 19th century, it motivated industry and government to electrify our world. Since our electrical grid is dependent on transmission of electrical energy using materials that conduct electricity very well, it was of the utmost importance to understand how the material properties come to be. I will briefly highlight some of the most influential ideas that have led us to where we are today in our understanding of conducting materials which are used to this very day.

In 1900, shortly after the discovery of the electron, Paul Drude proposed a theory [208], based on the kinetic theory of gases, that was able to describe many properties, such as AC and DC electrical conductivity and the Hall effect, of Alkali metals surprisingly well with very few and simple assumptions. In 1928, Arnold Sommerfeld [209] expanded Drude's model by treating the electrons correctly as *quantum* particles with Fermionic statistics where the ground state is understood through the notion

of the filled 'Fermi sea'. Shortly thereafter, the modelling improved to include the interactions between electrons which is referred to as the *interacting* electron gas or *Jellium* model. In this model, the periodic nature of the underlying crystal lattice is replaced by a positive background which is chosen to neutralize the gas of electrons. The Jellium model Hamiltonian in second quantization in a box of volume V with periodic boundary conditions is[1]

$$\hat{H}_{Jellium} = \sum_{\sigma} \sum_{\vec{k}} \frac{\hbar^2 k^2}{2m} c^{\dagger}_{\vec{k}\sigma} c_{\vec{k}\sigma} + \frac{1}{2V} \sum_{\sigma\sigma'} {\sum_{\vec{k},\vec{p},\vec{q}}}' \frac{4\pi e^2}{|\vec{q}|^2} c^{\dagger}_{\vec{k}+\vec{q}\sigma} c^{\dagger}_{\vec{p}-\vec{q}\sigma'} c_{\vec{p}\sigma'} c_{\vec{k}\sigma}. \tag{A.1}$$

In 1956, Lev Landau rigorously justified the success of Sommerfeld's model by introducing the Fermi-liquid theory [210] which maps the interacting electron gas model to a 'renormalized' Fermi sea.

The Jellium model is often invoked when the material is comprised of atoms with one valence electron that will usually come from an atomic-like s or p derived character. This allowed the treatment of the relevant electrons as being 'free' works very well. In addition, this model accounts for the *long-range* Coulomb interaction which gives rise to the collective charge-neutral elementary excitations, the plasmons, in an accurate manner. To this date, the electron liquid paradigm and the physics it entails describes materials which are in a 'normal metallic' state.

This paradigm fails miserably in the case where the relevant electrons cannot ignore the effects of the underlying crystal lattice or treat it as a small perturbation. It was a great triumph in 1963 where John Hubbard introduced the 'narrow-band' Hamiltonian [11] to describe the Mott metal-to-insulator transition and spin wave properties of itinerant electron magnets; such as iron, nickel, and cobalt. The

[1] The prime on the summations means that we omit the summation for the long wavelength limit $\vec{q} = \vec{0}$. This is an exact cancellation of three terms; the electron-ion, ion-ion, and long wavelength limit of the electron-electron interaction

Hamiltonian is the simplest form of electrons on a lattice and has the form

$$\hat{H}_{Hubbard} = -t \sum_{\langle i,j \rangle \sigma} (c^{\dagger}_{i\sigma} c_j + h.c) + U \sum_i \hat{n}_{i\uparrow} \hat{n}_{i\downarrow}, \tag{A.2}$$

where t is the matrix element of an electron in a single particle Hamiltonian on neighboring sites

$$t = \int d^3x \phi^*(\vec{x} - \vec{R}_i) h_0(\vec{x}) \phi(\vec{x} - \vec{R}_j), \tag{A.3}$$

and U is the onsite statically screened interaction between electrons

$$U = 2 \int d^3x \int d^3x' |\phi(\vec{x} - \vec{R}_i)|^2 W(\vec{x}, \vec{x}') |\phi(\vec{x}' - \vec{R}_i)|^2 \tag{A.4}$$

Unlike the Jellium model, Hubbard's model incorporates the effect of the static external potential of the periodic lattice of ions.

These models are still used to this day as (or at the very least motivates) model Hamiltonians to study many material properties, albeit with exponentially more computational resources. By no means did I list all model Hamiltonians that are used to describe various phenomena, so for a more detailed discussion refer to [211, 212] for a more extensive list and their applications in describing material properties.

Electrons in One Dimension

The interest in electrons in one dimensional has been a widely studied area for quite some time. Its inception could probably be attributed to Felix Bloch [213] in 1934 where he was researching a *non-interacting* gas of electrons similar to Sommerfeld. The low energy electronic specific heat of this model for 'spinless' electrons is given, courtesy of Wolfgang Pauli, by

$$C^{1D}_{el}(T) = \frac{\pi}{3} \kappa_B \left(\frac{\kappa_B T}{\hbar v_F} \right). \tag{A.5}$$

This was striking because this had the exact same form that Debye calculated for a one dimensional Harmonic chain

$$C^{1D}_{lattice}(T) = \frac{\pi}{3}\kappa_B \left(\frac{\kappa_B T}{\hbar c_s}\right), \tag{A.6}$$

where the only difference is the replacement of the speed of sound c_s with the Fermi velocity v_F. He therefore inferred that the low energy excitations of a *one dimensional* electron gas were *collective* 'sound waves', which are *bosonic* in nature, that propagated through the electron gas. Since this time, it has been a high goal of condensed matter physics to study and find real material/systems that can be perceived as electrons in one dimension.

Here, I give a brief overview on the theory behind *interacting* electron systems in one dimension. Unlike the case in two and three dimensions that fall under the Landau-Fermi liquid theory, electrons in one dimension behave entirely different due to the very strong correlations between electrons which are *independent* of the strength of interaction [22]. This *extremely* correlated state of matter is expected to occur for all one-dimensional and systems [214] falls under the paradigm of the *Luttinger liquid* which was served as a replacement to Landau's Fermi liquid in higher dimensions.

The Luttinger Liquid

Sin-itiro Tomonaga first studied the *interacting* electron gas in one dimension in 1950 [215]. His model imposed linearizing the free electron dispersion about the Fermi level and terminated at wave vector $k = 0$. The model was only a model to describe the low-lying excited states because there was no well-defined ground state. To fix this, J. M. Luttinger [216] extended the linearized dispersion to encompass the *filled* Dirac sea of electrons, introducing a ground state to the spectrum. With a few approximations, his model, similar to Tomonaga's, was *exactly* solvable by 'Bosonizing' the Hamiltonian. This technique relied on the fact that the elementary

excitations were approximately bosonic in nature, so his triumph was to cast the excitations exactly as bosons [211]. Although Luttinger proposed an exact solution to the model, it obtained an inconsistency in the commutation relations imposed by the canonical transformation he proposed. To rectify this, Daniel Mattis and Elliot Lieb in 1965 [217] published the *correct* exact solution to Luttinger's model. In 1981, Nobel Laureate Duncan Haldane introduced the notion of the *Luttinger liquid* [214] to be taken as the one dimensional analogue of the Fermi liquid theory proposed by Landau, which stands to this day as the paradigm for interacting electrons confined to one dimension.

Here, I will briefly[2] introduce Luttinger's model and some of the basic steps needed to 'bosonize' the Hamiltonian. Luttinger's model was introduced by ignoring the spin degree of freedom, but we know that electrons are spin 1/2 particles. Upon making further approximations to the Hamiltonian, the spin degree of freedom can be introduced to create a decoupled Hamiltonian described by two sound wave-like Hamiltonians corresponding to the 'spin' and 'charge' degree of freedom. The velocity of these sound waves are theoretically different which introduces the notion of *'spin-charge separation'*. For the one dimensional cuprates, the behavior of the relevant electrons appear to be classified as being correlated, so a more realistic picture is realized by Hubbard's model in one dimension. Hubbard's model in one dimension also is one of the few models that has an exact solution [69] via an integral equation based on the Bethe-ansatz, however it is very difficult to compute correlation functions from this solution are a very difficult task [219]. Similar to the Luttinger model, the one dimensional Hubbard model can also be reformulated in a bosonized Hamiltonian [21, 220]. This bosonized Hamiltonian can be mapped onto the electron gas analog with renormalized parameters [21]. The main difference between the Luttinger liquid obtained from the Hubbard model and the electron gas in one dimension is the collective modes for the charge sector are gapped while the collective modes that carry $S = 1/2$ collective modes remains gapless.

[2]For more details on this procedure, please refer to [22, 211, 218]

Luttinger Model

For this section, I will go over the bosonization procedure for Luttinger's model. This procedure will follow closely that derived in reference [221], while other references such as [21, 22, 211] are also very nice references. Luttinger's model is very similar to Tomonaga's model except for the technique used linearization of the dispersion of the non-interacting dispersion of free electrons. In Tomonaga's model, he linearized the free electron dispersion about the Fermi wave vector k_F, but truncated the dispersion at $k = 0$. In Luttinger's model, he linearized the free electron dispersion indefinitely. Due to the similarities, this model is sometimes referred to as the Tomonaga-Luttinger model. While both Tomonaga and Luttinger ignored the role of the spin degree of freedom, I will include it since I desire to make connection with the concept of spin-charge separation.

The Hamiltonian for an electron gas in one dimension is given by

$$\hat{H}_{1D} = \sum_{\sigma} \sum_{k} \frac{\hbar^2 k^2}{2m} c^{\dagger}_{k\sigma} c_{k\sigma} + \sum_{\sigma\sigma'} \sum_{pkq} v(q) c^{\dagger}_{k+q\sigma} c^{\dagger}_{p-q\sigma'} c_{p\sigma'} c_{k\sigma}. \tag{A.7}$$

The heavy work actually is built into bosonizing the non-interacting part of the Hamiltonian, so that is what I present in greater detail. The work of Luttinger relied on linearizing the free electron dispersion around k_F and $-k_F$, so we can rewrite the quadratic dispersion of the free electrons as

$$\varepsilon(k) = \begin{cases} \hbar v_F (k - k_F) & k > 0 \\ -\hbar v_F (k + k_F) & k < 0 \end{cases}$$

.

which allows us to write the non-interacting part of the Hamiltonian $\hat{H}_0$ in terms of 'right moving' particles $k > 0$ and 'left moving' particles $k < 0$

$$\hat{H}_0 = \sum_{\sigma} \sum_{k>0} \hbar v_F (k - k_F) c^{\dagger}_{k\sigma} c_{k\sigma} - \sum_{\sigma} \sum_{k<0} \hbar v_F (k + k_F) d^{\dagger}_{k\sigma} d_{k\sigma}, \tag{A.9}$$

where I have associated the right(left) moving particles with the operator $c_{k\sigma}(d_{k\sigma})$. The linearized dispersion can be seen in figureA.1 However, by introducing the linearization of the dispersion indefinitely, Luttinger introduced a problem due to the infinite filled Dirac sea of electronic states, which will cause commutators between density operators that should be zero, using first quantization, to no longer be zero in a field theoretical framework. This problem was realized by Mattis and Lieb [217]. To rectify this issue, similar to that in the Dirac equation, the operators should be *normal ordered*, meaning

$$c^{\dagger}_{k\sigma} c_{k\sigma} \rightarrow : c^{\dagger}_{k\sigma} c_{k\sigma} := c^{\dagger}_{k\sigma} c_{k\sigma} - \langle c^{\dagger}_{k\sigma} c_{k\sigma} \rangle_0 \tag{A.10}$$

and

$$d^{\dagger}_{k\sigma} d_{k\sigma} \rightarrow : d^{\dagger}_{k\sigma} d_{k\sigma} := d^{\dagger}_{k\sigma} d_{k\sigma} - \langle d^{\dagger}_{k\sigma} d_{k\sigma} \rangle_0 \tag{A.11}$$

where the average value is computed with the filled Dirac sea

$$\langle c^{\dagger}_{k\sigma} c_{k\sigma} \rangle_0 = \theta(k_F - k) \qquad \langle d^{\dagger}_{k\sigma} d_{k\sigma} \rangle_0 = \theta(k + k_F). \tag{A.12}$$

Equivalently, the normal ordering becomes

$$: c^{\dagger}_{k\sigma} c_{k\sigma} := \begin{cases} c^{\dagger}_{k\sigma} c_{k\sigma} & k > k_F \\ -c_{k\sigma} c^{\dagger}_{k\sigma} & k < k_F \end{cases}$$

for the right movers and

$$: d^{\dagger}_{k\sigma} d_{k\sigma} := \begin{cases} d^{\dagger}_{k\sigma} d_{k\sigma} & k < -k_F \\ -d_{k\sigma} d^{\dagger}_{k\sigma} & k > -k_F \end{cases}$$

for the left movers.

As a way of circumventing the issue of the normal ordering, we can restrict ourselves to a region around the Fermi wave vector k_F[3], where we impose a cutoff k_Λ. Upon measuring the dispersion with respect to the Fermi wave vector, we can rewrite equation A.10 as

$$\hat{H}_0 = \sum_{\sigma} \sum_{k,|k|<k_\Lambda} \hbar v_F k \left(c^{\dagger}_{k_F+k\sigma} c_{k_F+k\sigma} - d^{\dagger}_{-k_F+k\sigma} d_{-k_F+k\sigma} \right) \tag{A.15}$$

where v_F is the Fermi velocity defined by

$$v_F \equiv \frac{\hbar k_F}{m}. \tag{A.16}$$

While this part of deriving the non-interacting part of the one-dimensional electron gas Hamiltonian was quite straight forward, what follows is the more difficult part. It is difficult because we must now cast the non-interacting part of the Hamiltonian involving pairs of creation and annihilation operators in terms of pairs of *bosonic* operators which themselves consisting of pairs of creation and annihilation operators. This seems counter-intuitivite because the interaction terms usually give the difficult aspect of the problem, however, if one knows which terms to neglect, the interaction terms just involve straight forward algebra to obtain the bosonized Hamiltonian.

[3]This is important to the Hubbard model where there is a finite band width.

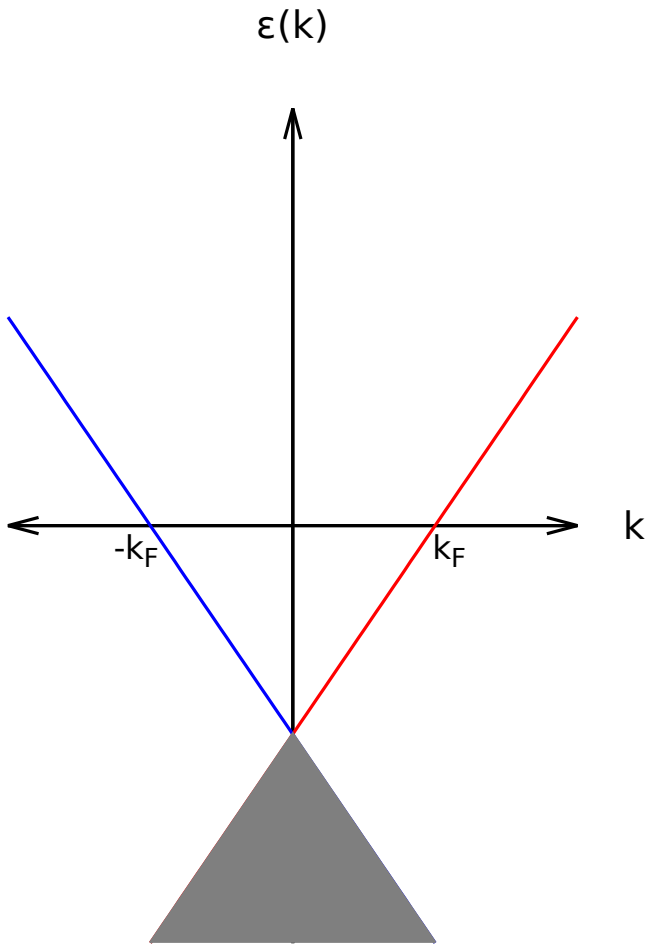

Figure A.1: Linear dispersion for the Luttinger model. The red curve represents the curve corresponding to the right moving electrons. The blue curve corresponds to the left moving electrons. The filled region represents the region in which Luttinger added to Tomonaga's model to give a ground state to the spectrum.

Now we can introduce the Fourier transform of the density operator for a given spin projection for the right and left moving electrons as

$$n_{R,\sigma}(q) = \sum_{k,|k|<k_\Lambda} c^\dagger_{k_F+k\sigma} c_{k_F+k+q\sigma} \tag{A.17}$$

and

$$n_{L,\sigma}(q) = \sum_{k,|k|<k_\Lambda} d^\dagger_{-k_F+k\sigma} d_{-k_F+k+q\sigma} \tag{A.18}$$

respectively. It is important to note that for without a cutoff k_Λ, the $q = 0$ would not be well defined due to the infinite filled Dirac sea. Now we want to consider the commutator[4]

$$[n_{R\sigma}(q), n_{R\sigma'}(q')]_- = \sum_{kk'} \left[c^\dagger_{k_F+k\sigma} c_{k_F+k+q\sigma}, c^\dagger_{k_F+k'\sigma} c_{k_F+k'+q'\sigma} \right]_- \tag{A.19}$$

$$= \delta_{\sigma\sigma'} \sum_k \left(c^\dagger_{k_F+k\sigma} c_{k_F+k+q+q'\sigma} - c^\dagger_{k_F+k-q'\sigma} c_{k_F+k+q\sigma} \right) \tag{A.20}$$

which can be realized through the commutator identity

$$\left[\hat{A}, \hat{B}\hat{C}\right]_- = \hat{B}\left[\hat{A}, \hat{C}\right]_- + \left[\hat{A}, \hat{B}\right]_- \hat{C} \tag{A.21}$$

and the commutator to anticommutator identity

$$\left[\hat{A}\hat{B}, \hat{C}\right]_- = -\hat{A}\left[\hat{B}, \hat{C}\right]_+ + \left[\hat{A}, \hat{C}\right]_+ \hat{B}. \tag{A.22}$$

It can be shown that the commutator in equation A.19 vanishes for q_Λ by shifting the dummy summation in the second term in equation A.20 by $k \to k + q'$, however this

[4]Here, I am neglecting the explicit notation that we are only summing over wave vectors less than the cutoff.

is not the case when $q' = -q$. In this case, we have

$$[n_{R\sigma}(q), n_{R\sigma'}(-q)]_- = \delta_{\sigma\sigma'} \sum_k \left(c^\dagger_{k_F+k\sigma} c_{k_F+k\sigma} - c^\dagger_{k_F+k+q\sigma} c_{k_F+k+q\sigma} \right). \tag{A.23}$$

Since the second term can only contribute for right movers if $k\, k_F$ for $q > 0$, so we are restricted to the summation over the region $-k_F < k < -k_F + q$, so we obtain the commutation relation

$$[n_{R\sigma}(q), n_{R\sigma'}(-q)]_- = \delta_{\sigma\sigma'} \sum_{-k_F<k<-k_F+q} c^\dagger_{k_F+k\sigma} c_{k_F+k\sigma} \qquad \text{for } q > 0. \tag{A.24}$$

Similarly, for $q < 0$ we are restricted to the range $-k_F < k < -k_F - q$ have the commutation relation

$$[n_{R\sigma}(q), n_{R\sigma'}(-q)]_- = -\delta_{\sigma\sigma'} \sum_{-k_F<k<-k_F-q} c^\dagger_{k_F+k\sigma} c_{k_F+k\sigma} \qquad \text{for } q < 0. \tag{A.25}$$

Our summation extends in a region where all these terms in the summation are well below the Fermi energy, so the number of states within a given width of q, assuming we impose periodic boundary conditions on a line of length L, is $qL/2\pi$, so

$$\delta_{\sigma\sigma'} \sum_{-k_F<k<-k_F+q} c^\dagger_{k_F+k\sigma} c_{k_F+k\sigma} = \delta_{\sigma\sigma'} \frac{qL}{2\pi} \qquad \text{for } q > 0 \tag{A.26}$$

and

$$-\delta_{\sigma\sigma'} \sum_{-k_F<k<-k_F-q} c^\dagger_{k_F+k\sigma} c_{k_F+k\sigma} = \delta_{\sigma\sigma'} \frac{qL}{2\pi} \qquad \text{for } q < 0. \tag{A.27}$$

We can therefore write the commutation relation for the density fluctuations for the right movers as

$$[n_{R\sigma}(q), n_{R\sigma'}(q')]_- = \delta_{\sigma\sigma'} \delta_{q-q'} \frac{qL}{2\pi}. \tag{A.28}$$

It can also be shown for the left movers that we obtain the commutation relation

$$[n_{L\sigma}(q), n_{L\sigma'}(q')]_- = -\delta_{\sigma\sigma'}\delta_{q-q'}\frac{qL}{2\pi}. \tag{A.29}$$

and obviously

$$[n_{R\sigma}(q), n_{L\sigma'}(q')]_- = 0. \tag{A.30}$$

Since $n_{\lambda\sigma}(q) = n^\dagger_{\lambda\sigma}(-q)$, we can write the generalized commutation relation

$$\left[n_{\lambda\sigma}(q), n^\dagger_{\lambda'\sigma'}(q')\right]_- = \lambda\delta_{\sigma\sigma'}\delta_{qq'}\delta_{\lambda\lambda'}\frac{qL}{2\pi} \tag{A.31}$$

where $\lambda = +1$ when $\lambda = R$ and $\lambda = -1$ when $\lambda = L$.

Now we can introduce the boson operators $b_{q\sigma}$

$$b_{q\sigma} \equiv \begin{cases} \sum_k \sqrt{\frac{2\pi}{qL}} c^\dagger_{k_F+k\sigma} c_{k_F+k+q\sigma} & q > 0 \\ \sum_k \sqrt{\frac{2\pi}{|q|L}} d^\dagger_{-k_F+k\sigma} d_{-k_F+k+q\sigma} & q < 0 \end{cases}$$

and the Hermitian conjugate is

$$b^\dagger_{q\sigma} \equiv \begin{cases} \sum_k \sqrt{\frac{2\pi}{qL}} c^\dagger_{k_F+k+q\sigma} c_{k_F+k\sigma} & q > 0 \\ \sum_k \sqrt{\frac{2\pi}{|q|L}} d^\dagger_{-k_F+k+q\sigma} d_{-k_F+k\sigma} & q < 0 \end{cases}$$

which obey the canonical commutation relation

$$\left[b_{q\sigma}, b^\dagger_{q'\sigma'}\right]_- = \delta_{\sigma\sigma'}\delta_{qq'}. \tag{A.34}$$

Introducing these bosonic operators, allows the rewriting of the non-interacting Hamiltonian[5] in A.15 as

$$\hat{H}_0 = \sum_{q\neq 0\sigma} \hbar v_F |q| b^\dagger_{q\sigma} b_{q\sigma}. \tag{A.35}$$

This is by no means obvious, but it can be realized by taking the commutation relation with the boson operator $b_{q\sigma}$ and the non-interacting Hamiltonian in equation A.15 that has in it the electron operators, i.e. calculating the equation of motion

$$\left[\hat{H}_0, b_{q\sigma}\right]_- = -\hbar v_F |q| b_{q\sigma} \tag{A.36}$$

and its Hermitian conjugate

$$\left[\hat{H}_0, b^\dagger_{q\sigma}\right]_- = \hbar v_F |q| b^\dagger_{q\sigma}. \tag{A.37}$$

Additionally, the boson operators annihilate the Dirac sea

$$b_{q\sigma} \left|\psi\right\rangle_{DS} = 0\hat{I}. \tag{A.38}$$

These bosonic operators represent *collective* excitations of particle-hole pairs. Since the interest is to understand the phenomenon of spin-charge separation, we introduce both the collective *charge* boson b_{qc} and the collective *spin* boson b_{qs} as

$$b_{qc} \equiv \frac{1}{\sqrt{2}} \left(b_{q\uparrow} + b_{q\downarrow}\right) \qquad b_{qs} \equiv \frac{1}{\sqrt{2}} \left(b_{q\uparrow} - b_{q\downarrow}\right) \tag{A.39}$$

and the Hermitian conjugate

$$b^\dagger_{qc} \equiv \frac{1}{\sqrt{2}} \left(b^\dagger_{q\uparrow} + b^\dagger_{q\downarrow}\right) \qquad b^\dagger_{qs} \equiv \frac{1}{\sqrt{2}} \left(b^\dagger_{q\uparrow} - b^\dagger_{q\downarrow}\right). \tag{A.40}$$

[5]Here, I am assuming that there are the same number of left movers as right movers. If this assumption is lifted, then there will be additional terms in the Hamiltonian associated with 'topological' charges and currents. Please see reference [221] for details on these terms. These 'topological' charges and currents are related to the fact that I have omitted the $q = 0$ in the summation over wave vectors.

This allows us to rewrite the non-interacting Hamiltonian from equation A.41 *separated* into two terms as

$$\hat{H}_0 = \sum_{q\neq 0\sigma} \hbar v_F |q| \left(b^\dagger_{qc} b_{qc} + b^\dagger_{qs} b_{qs} \right). \tag{A.41}$$

Now we must handle the interacting piece of the Hamiltonian. For now, I will assume a momentum independent Hamiltonian which will be replaced by coupling constant $g_{i\sigma\sigma'}$. Then the interaction in the Hamiltonian A.7 has the general form in terms of right and left moving electrons as

$$\begin{aligned}
\hat{H}_{int} = \frac{1}{2L} \sum_{\sigma\sigma'} \sum_{kk'q} g_{1\sigma\sigma'} \Big[& c^\dagger_{k_F+k+q\sigma} d^\dagger_{-k_F+k'-q\sigma'} c_{k_F+k'\sigma'} d_{-k_F+k\sigma} \\
& + d^\dagger_{-k_F+k+q\sigma} c^\dagger_{k_F+k'-q\sigma'} d_{-k_F+k'\sigma'} c_{k_F+k\sigma} \Big] \\
+ \frac{1}{2L} \sum_{\sigma\sigma'} \sum_{kk'q} g_{2\sigma\sigma'} \Big[& c^\dagger_{k_F+k+q\sigma} d^\dagger_{-k_F+k'-q\sigma'} d_{-k_F+k'\sigma'} c_{k_F+k\sigma} \\
& + d^\dagger_{-k_F+k+q\sigma} c^\dagger_{k_F+k'-q\sigma'} c_{k_F+k'\sigma'} d_{-k_F+k\sigma} \Big] \\
+ \frac{1}{2L} \sum_{\sigma\sigma'} \sum_{kk'q} g_{3\sigma\sigma'} \Big[& c^\dagger_{k_F+k+q\sigma} c^\dagger_{k_F+k'-q\sigma'} d_{-k_F+k'\sigma'} d_{-k_F+k\sigma} \\
& + d^\dagger_{-k_F+k+q\sigma} d^\dagger_{-k_F+k'-q\sigma'} c_{k_F+k'\sigma'} c_{k_F+k\sigma} \Big] \\
+ \frac{1}{2L} \sum_{\sigma\sigma'} \sum_{kk'q} g_{4\sigma\sigma'} \Big[& c^\dagger_{k_F+k+q\sigma} c^\dagger_{k_F+k'-q\sigma'} c_{k_F+k'\sigma'} c_{k_F+k\sigma} \\
& + d^\dagger_{-k_F+k+q\sigma} d^\dagger_{-k_F+k'-q\sigma'} d_{-k_F+k'\sigma'} d_{k_F+k\sigma} \Big].
\end{aligned} \tag{A.42}$$

In the bosonization procedure, the terms $g_{1\sigma\sigma'}$ and $g_{3\sigma\sigma'}$ which for $\sigma \neq \sigma'$ are the back-scattering terms which scatter left moving particles into right moving particles

and vice-versa. Therefore, we write (omitting the $q = 0$ scattering processes)

$$\hat{H}_{int} = \frac{1}{2L}\sum_{q\neq 0\sigma\sigma'} g_{2\sigma\sigma'}\left[n_{R\sigma}(-q)n_{L\sigma'}(q) + n_{L\sigma}(-q)n_{R\sigma'}(q)\right]$$

$$+ \frac{1}{2L}\sum_{q\neq 0\sigma\sigma'} g_{2\sigma\sigma'}\left[n_{R\sigma}(-q)n_{R\sigma'}(q) + n_{L\sigma}(-q)n_{L\sigma'}(q)\right]. \tag{A.43}$$

In terms of the boson operators, the interaction can be written as

$$\hat{H}_{int} = \sum_{q\neq 0\sigma\sigma'} \frac{|q|}{4\pi} g_{2\sigma\sigma'}\left(b^{\dagger}_{q\sigma}b^{\dagger}_{-q\sigma'} + b_{-q\sigma}b_{q\sigma'}\right)$$

$$+ \sum_{q\neq 0\sigma\sigma'} \frac{|q|}{4\pi} g_{4\sigma\sigma'}\left(b^{\dagger}_{q\sigma}b_{q\sigma'} + b_{-q\sigma}b^{\dagger}_{-q\sigma'}\right). \tag{A.44}$$

Using the collective charge and spin boson definitions in equation A.39 and A, we can rewrite the Hamiltonian as

$$\hat{H}_{int} = \sum_{q\neq 0} \frac{|q|}{4\pi} g_{2c}\left(b^{\dagger}_{qc}b^{\dagger}_{-qc} + b_{-qc}b_{qc}\right) + \frac{|q|}{4\pi} g_{2s}\left(b^{\dagger}_{qs}b^{\dagger}_{-qs} + b_{-qs}b_{qs}\right)$$

$$+ \sum_{q\neq 0} \frac{|q|}{4\pi} g_{4c}\left(b^{\dagger}_{qc}b_{qc} + b_{-qc}b^{\dagger}_{-qc}\right) + \frac{|q|}{4\pi} g_{4s}\left(b^{\dagger}_{qs}b_{qs} + b_{-qs}b^{\dagger}_{-qs}\right). \tag{A.45}$$

where I have defined the charge and the spin couplings as

$$g_{2c} \equiv g_{2\parallel} + g_{2\perp} \qquad g_{2s} = g_{2\parallel} - g_{2\perp} \tag{A.46}$$

and

$$g_{4c} \equiv g_{4\parallel} + g_{4\perp} \qquad g_{4s} = g_{2\parallel} - g_{4\perp} \tag{A.47}$$

where

$$g_{i\parallel} = g_{i\uparrow\uparrow} = g_{i\downarrow\downarrow} \qquad g_{i\perp} = g_{i\uparrow\downarrow} = g_{i\downarrow\uparrow}. \tag{A.48}$$

So combining this with equation A.41, we can write the Hamiltonian for the Tomonoga-Luttinger *model* as

$$\hat{H}_{TL} = \sum_{q\neq 0} \hbar v_F |q| \left(1 + \frac{g_{4c}}{2\pi\hbar v_F}\right) b^\dagger_{qc} b_{qc} + \frac{|q|}{4\pi} g_{2c} \left(b^\dagger_{qc} b^\dagger_{-qc} + b_{-qc} b_{qc}\right)$$

$$+ \hbar v_F |q| \left(1 + \frac{g_{4s}}{2\pi\hbar v_F}\right) b^\dagger_{qs} b_{qs} + \frac{|q|}{4\pi} g_{2s} \left(b^\dagger_{qs} b^\dagger_{-qs} + b_{-qs} b_{qs}\right). \tag{A.49}$$

Defining dimensionless couplings

$$\tilde{g}_{is,c} \equiv \frac{g_{is,c} g}{2\pi\hbar v_F}, \tag{A.50}$$

we can write equation A as

$$\hat{H}_{TL} = \sum_{q\neq 0} \hbar v_F |q| \left(1 + \tilde{g_{4c}}\right) b^\dagger_{qc} b_{qc} + \frac{|q|}{2} \tilde{g}_{2c} \left(b^\dagger_{qc} b^\dagger_{-qc} + b_{-qc} b_{qc}\right)$$

$$+ \hbar v_F |q| \left(1 + \tilde{g}_{4s}\right) b^\dagger_{qs} b_{qs} + \frac{|q|}{2} \tilde{g}_{2s} \left(b^\dagger_{qs} b^\dagger_{-qs} + b_{-qs} b_{qs}\right). \tag{A.51}$$

Then we can define a Hamiltonian for the collective charge and spin bosons as

$$\hat{H}_{TL,c} \equiv \sum_{q\neq 0} \hbar v_F |q| \left(1 + \tilde{g_{4c}}\right) b^\dagger_{qc} b_{qc} + \frac{|q|}{2} \tilde{g}_{2c} \left(b^\dagger_{qc} b^\dagger_{-qc} + b_{-qc} b_{qc}\right) \tag{A.52}$$

and

$$\hat{H}_{TL,s} \equiv \sum_{q\neq 0} \hbar v_F |q| \left(1 + \tilde{g}_{4s}\right) b^\dagger_{qs} b_{qs} + \frac{|q|}{2} \tilde{g}_{2s} \left(b^\dagger_{qs} b^\dagger_{-qs} + b_{-qs} b_{qs}\right) \tag{A.53}$$

respectively. Each of these Hamiltonians can be diagonalized with a Bogoliubov transformation by defining new operators for the collective charge and spin bosons as

$$\beta_{qc} u_{cq} b_{qc} + v_{cq} b^\dagger_{-qc} \qquad \beta^\dagger_{qc} u_{cq} b^\dagger_{qc} + v_{cq} b_{-qc} \tag{A.54}$$

and

$$\beta_{qs} u_{sq} b_{qs} + v_{sq} b^\dagger_{-qs} \qquad \beta^\dagger_{qs} u_{sq} b^\dagger_{qs} + v_{sq} b_{-qs}. \tag{A.55}$$

The real expansion coefficients $u_{c,sq}$ and $v_{c,sq}$ satisfy the equations

$$u_{c,sq}^2 - v_{c,sq} = 1 \tag{A.56}$$

which required the definition of hyperbolic angles $\theta_{c,sq}$

$$u_{c,sq} = \cosh\theta_{c,sq} \qquad v_{c,sq} = \sinh\theta_{c,sq} \tag{A.57}$$

and gives the inverse transformations of equations A.54 and A.55,

$$b_{qc,s}^\dagger = \beta_{qc,s}^\dagger \cosh\theta_{c,sq} - \beta_{-qc,s}\sinh\theta_{c,sq} \tag{A.58}$$

$$b_{qc,s} = \beta_{-qc,s}\cosh\theta_{c,sq} - \beta_{qc,s}^\dagger \sinh\theta_{c,sq}. \tag{A.59}$$

By putting these results into the Hamiltonian, the terms with $\beta^\dagger\beta^\dagger$ or $\beta\beta$ become zero if the following equation is satisfied

$$\tanh(2\theta_{c,sq}) = \frac{\tilde{g}_{2c,s}}{1+\tilde{g}_{4c,s}}. \tag{A.60}$$

We can therefore define the charge and spin velocities as

$$v_c \equiv v_F\sqrt{(1+\tilde{g}_{4c})^2 + (\tilde{g}_{2c})^2} \tag{A.61}$$

and

$$v_s \equiv v_F\sqrt{(1+\tilde{g}_{4s})^2 + (\tilde{g}_{2s})^2} \tag{A.62}$$

respectively.

This gives us the ability to represent the Hamiltonian for the Tomonoga-Luttinger model as a separate Hamiltonian of collective charge and spin bosons as

$$\hat{H}_{TL} = \hat{H}_c + \hat{H}_s \tag{A.63}$$

where

$$\hat{H}_c = \sum_{q \neq 0} \hbar v_c |q| \beta_{qc}^{\dagger} \beta_{qc} \tag{A.64}$$

and

$$\hat{H}_s = \sum_{q \neq 0} \hbar v_s |q| \beta_{qs}^{\dagger} \beta_{qs} \tag{A.65}$$

where these collective charge and spin bosons travel at different speeds v_c and v_s respectively. The collective charge bosons are referred to as *holons* and the collective spin bosons are referred to as *spinons*.

Appendix B

Linear Response Theory

The following closely follows notes that my advisor Dr. Adolfo Eguiluz gave to me that were necessary for me to perform research for my graduate studies. We want to consider the case where we are *perturbing* the system with a time dependent interaction $\hat{V}_{int}(t)$. By doing so, the total Hamiltonian of the system is

$$\hat{H} = \hat{H}_0 + \hat{V}_{ext}(t), \tag{B.1}$$

Here, $\hat{H}_0$ represents the *exact* Hamiltonian of the system in the absence of the external perturbation and is not meant to represent some non-interacting aspect of a Hamiltonian. The external potential has the form

$$\hat{V}_{ext}(t) = \hat{B}g(t), \tag{B.2}$$

where the time dependence will be assumed to take the form $g(t) = f(t)e^{\eta}t$. The reason for this is we want the potential to be turned on adiabatically in the distant past by take the limit $\eta \to 0^+$ at the end of the calculation. In the presence of the external probe, we want to quantify the *induced* average value of an operator $\hat{A}$, which

corresponds to finding the quantity

$$\delta \langle \hat{A} \rangle (t) \equiv \langle \hat{A} \rangle (t) - \lim_{t_0 \to -\infty} \langle \hat{A} \rangle (t_0). \tag{B.3}$$

To first order in the interaction, $\delta \langle A \rangle (t)$ is given through the linear response equation

$$\delta \langle \hat{A} \rangle (t) = \int_{-\infty}^{\infty} dt' \chi_{AB}(t - t') f(t'), \tag{B.4}$$

where the linear response function is given by the commutators evaluated with respect to the ground state of $\hat{H}_0$.

$$\chi_{AB}(t - t') = \frac{1}{i\hbar} \Theta(t - t') \left\langle [\hat{A}(t), \hat{B}(t')]_- \right\rangle_0 . \tag{B.5}$$

Here, the time-dependence of the operators are given in the interaction picture

$$\hat{A}(t) = e^{\frac{i}{\hbar}\hat{H}_0 t} \hat{A} e^{-\frac{i}{\hbar}\hat{H}_0 t}. \tag{B.6}$$

We can insert a complete set of states between $\hat{A}(t)$ and $\hat{B}(t')$, so

$$\chi_{AB}(t-t') = \frac{1}{i\hbar} \Theta(t-t') \sum_n \langle \psi_0 | \hat{A}(t) | n \rangle \langle n | \hat{B}(t') | \psi_0 \rangle - \langle \psi_0 | \hat{B}(t') | n \rangle \langle n | \hat{A}(t) | \psi_0 \rangle \tag{B.7}$$

$$= \frac{1}{i\hbar} \Theta(t - t') \sum_n e^{\frac{i}{\hbar}(E_0 - E_n)(t-t')} \langle \psi_0 | \hat{A} | n \rangle \langle n | \hat{B} | \psi_0 \rangle - \langle \psi_0 | \hat{B} | n \rangle \langle n | \hat{A} | \psi_0 \rangle \tag{B.8}$$

Since the response function is a function of the *difference* $t - t'$, it is often more convenient to recast equation B.5 in frequency space as

$$\delta \langle \hat{A} \rangle (\omega) = \chi_{AB}(\omega) f(\omega), \tag{B.9}$$

through the Fourier transform

$$\chi_{AB}(\omega) = \int_{-\infty}^{\infty} d(t - t') e^{i\omega(t-t')} \chi_{AB}(t - t'). \tag{B.10}$$

We can write the Fourier transform through the Lehmann representation as

$$\chi_{AB}(\omega) = \sum_n \frac{\langle\psi_0|\,\hat{A}\,|n\rangle\,\langle n|\,\hat{B}\,|\psi_0\rangle}{E_n - E_0 + \hbar(\omega + i\eta^+)}. \tag{B.11}$$

If the operators satisfy $\hat{B} = \hat{A}^\dagger$, then equation B.11 has the form

$$\chi_{AA^\dagger}(\omega) = \sum_n \frac{|\,\langle\psi_0|\,\hat{A}\,|n\rangle\,|^2}{E_n - E_0 + \hbar(\omega + i\eta^+)}, \tag{B.12}$$

so if we take the imaginary part of $\chi_{AA^\dagger}(\omega)$ we obtain

$$\mathrm{Im}\chi_{AA^\dagger}(\omega) \sim \sum_n \delta(E_n - E_0 + \hbar(\omega + i\eta^+)) \tag{B.13}$$

which has resonances at the *exact* excitation spectrum of the system. The η^+ in the denominator comes from the Fourier transform of the step function.

Fluctuation Dissipation Theorem

It is usually the case that spectroscopy measures correlation functions $S_{AA^\dagger}(\omega)$[1] which are given through

$$S_{AA^\dagger}(\omega) = \int_{-\infty}^{\infty} d(t-t')e^{i\omega(t-t')}\,\langle\hat{A}(t)\hat{A}^\dagger(t')\rangle\,. \tag{B.14}$$

Through the fluctuation-dissipation theorem [45] which relies on the cyclic property of a trace of a matrix, we can write the correlation function in terms of the imaginary part of a response function via

$$S_{AA^\dagger}(\omega) = \frac{2\hbar}{1 - e^{-\beta\hbar\omega}} Im\chi_{AA^\dagger}(\omega). \tag{B.15}$$

[1]The operators do not necessarily need to be Hermitian conjugates of each other.

This is a very powerful equation because it allows us to directly measure the excitation spectrum of a system through scattering experiments.

Appendix C

Proof of Hohenberg and Kohn Theorems

Here I give to the proof of the Hohenberg-Kohn theorems in the cases where there is an static external potential $V^{ext}(\vec{x})$ and an static external magnetic field $\vec{B}^{ext}(\vec{x})$. First I consider the case where there is only a static external potential $V^{ext}(\vec{x})$. Recall Hohenberg and Kohn's first theorem:

Hohenberg-Kohn Theorem 1: Given a Hamiltonian of the form of $\hat{H}_{el}$, there exists a one-to-one map between the external potential $V^{ext}(\vec{x})$ and the electron density $n(\vec{x}) \equiv \langle \hat{n}(\vec{x}) \rangle_{el}$. In other words, the external potential is *entirely* determined by the electron density.

proof:
Recall that $\hat{H}_{el}$ has the form $\hat{H}_{el} = \hat{T}_{el} + \hat{V}_{el-el} + \hat{V}_{ext}$. It is obvious that the external potential maps to the electron density $n(\vec{x})$. The proof relies in showing the converse. The proof is by contradiction. Suppose that there are two external potentials $V^{ext,1}(\vec{x})$ and $V^{ext,2}(\vec{x})$ corresponding to two electronic Hamiltonians $\hat{H}_{el}$ and $\hat{H}'_{el}$ that produce the *same* ground state electron density $n(\vec{x})$. From the Rayleigh-Ritz variational

statement, the ground state energy of the unprimed Hamiltonian satisfies

$$E_0 = \langle \Psi_0 | \hat{H}_{el} | \Psi_0 \rangle < \langle \Psi_0' | \hat{H}_{el} | \Psi_0' \rangle . \tag{C.1}$$

such that

$$\langle \Psi_0 | \hat{H}_{el}' | \Psi_0 \rangle = E_0'. \tag{C.2}$$

We can add and subtract $\hat{V}_{ext,2}$ to equation C.1, then we obtain the relation

$$E_0 < E_0' + \langle \Psi_0' | \hat{V}_{ext,1} - \hat{V}_{ext,2} | \Psi_0' \rangle =$$

$$= E_0' + \int d^3x n_0(\vec{x}) \left[V^{ext,1}(\vec{x}) - V^{ext,2}(\vec{x}) \right] . \tag{C.3}$$

We can also make the same but switching $\hat{V}_{ext,1} \leftrightarrow \hat{V}_{ext,2}$. Then we obtain the inequality

$$E_0' < E_0 + \langle \Psi_0' | \hat{V}_{ext,2} - \hat{V}_{ext,1} | \Psi_0' \rangle$$

$$= E_0 + \int d^3x n_0(\vec{x}) \left[V^{ext,2}(\vec{x}) - V^{ext,1}(\vec{x}) \right] . \tag{C.4}$$

If we add equations C.3 and C, we obtain the inequality

$$E_0 + E_0' < E_0' + E_0, \tag{C.5}$$

which is a contradiction. Therefore, the claim that two different external potentials can produce the same electron density must be false.

The proof of the case in an external magnetic field is exactly the same except by replacing equation C.3 with

$$E_0' + \int d^3x n_0(\vec{x}) \left[V^{ext,1}(\vec{x}) - V^{ext,2}(\vec{x}) \right] + \vec{m}_0(\vec{x}) \cdot \left[\vec{B}^{ext,1}(\vec{x}) - \vec{B}^{ext,2}(\vec{x}) \right] \tag{C.6}$$

and equation C with

$$E_0 + \int d^3x n_0(\vec{x}) \left[V^{ext,2}(\vec{x}) - V^{ext,1}(\vec{x}) \right] + \vec{m}_0(\vec{x}) \cdot \left[\vec{B}^{ext,2}(\vec{x}) - \vec{B}^{ext,1}(\vec{x}) \right]. \quad \text{(C.7)}$$

By adding equations C.6 and C.7, we arrive with the same contradiction

$$E_0 + E_0' < E_0' + E_0. \quad \text{(C.8)}$$

Now I will prove the second Hohenberg-Kohn theorem. Recall

Hohenberg-Kohn Theorem 2: As a consequence of theorem 1, a *universal functional* of the electron density can be defined $E[n] \equiv \langle \hat{H}_{el} \rangle_{el}$. The *global* minimum of this functional yields the *exact* ground state energy E_0 and is determined by the *exact interacting* ground state density $n_0(\vec{x})$. The global minimum occurs at the first functional derivative of this functional through

$$\left. \frac{\delta E}{\delta n} \right|_{n=n_0} = \mu. \quad \text{(C.9)}$$

proof

Recall that we can define a functional of the universal interacting electron system

$$F[n(\vec{x})] \equiv \langle \Psi | \hat{T}_{el} + \hat{V}_{el-el} | \Psi \rangle. \quad \text{(C.10)}$$

Then the the total energy functional is defines as

$$E[n(\vec{x})] = F[n(\vec{x})] + \int d^3x n(\vec{x}) V^{ext}(\vec{x}). \quad \text{(C.11)}$$

From theorem one, we know two different external potentials cannot yield the same ground state density. So we know that if $n_0(\vec{x})$ is the ground state electron density, any other electron density $n(\vec{x})$ will satisfy

$$E[n_0(\vec{x})] < E[n(\vec{x})], \tag{C.12}$$

Hence the ground state energy can be obtained by

$$\left.\frac{\delta E}{\delta n}\right|_{n=n_0} = \mu. \tag{C.13}$$

The same holds for the case where there is an external magnetic field except the inequality in equation C.12 becomes

$$E[n_0(\vec{x}), \vec{m}_0(\vec{x})] < E[n(\vec{x}), \vec{m}(\vec{x})], \tag{C.14}$$

and the variational principle is satisfied with

$$\left.\frac{\delta E}{\delta n}\right|_{n=n_0,\vec{m}=\vec{m}_0} = \mu \qquad \left.\frac{\delta E}{\delta \vec{m}}\right|_{n=n_0,\vec{m}=\vec{m}_0} = \vec{0}. \tag{C.15}$$

Appendix D

Proof of the Runge-Gross Theorem

Recall the Runge-Gross theorem

Runge-Gross Theorem: There is a one-to-one correspondence between the time-dependent potential[1] $V^{ext}(\vec{x},t)$ with the time-dependent electron density $n(\vec{x},t)$, *given* that the system was initially in a state $|\psi_0\rangle$.

In proof of the Runge-Gross theorem presented comes from that motivated in references [22, 222, 223]. The proof begins similar to the Hohenberg and Kohn theorems [12] that were proved in appendix C by assuming there are two different time-dependent potentials $V^{ext}(\vec{x},t)$ and $V^{ext,2}(\vec{x},t)$ that produce the *same* time dependent electron density $n(\vec{x},t)$.

The proof will rely on Poisson's equation that will relate the charge density to the external potential

$$\nabla^2 V^{ext}(\vec{x},t) = 4\pi e n(\vec{x},t). \tag{D.1}$$

By integrating this solution, the density at a particular time can be determined by the potential at all previous times. The proof that will be shown for a small time after

[1] It is important to note that the uniqueness of the external potentials must differ by more than just a time dependent factor.

the external potential is turned on at time $t = t_0$ [222] in which a Taylor expansion is well-defined since it could diverge for arbitrary times. Since the system involves conservation of charge, I can invoke the continuity equation

$$\frac{\partial}{\partial t} n(\vec{x}, t) + \vec{\nabla} \cdot \vec{j}(\vec{x}, t) = 0. \tag{D.2}$$

Now applying the Heisenberg equation of motion for the current density $\vec{j}(\vec{x}, t)$

$$i\hbar \frac{\partial}{\partial t} \vec{j}(\vec{x}, t) = \langle \psi(t) | \left[\hat{\mathbf{j}}(\vec{x}), \hat{H}(t) \right]_- | \psi(t) \rangle \,. \tag{D.3}$$

The commutator without the external potential $\hat{T}_{el} + \hat{V}_{el-el}$ does not need to be considered in detail, so I will define the quantity

$$\hat{\mathbf{Q}}(\vec{x}) \equiv \left[\hat{\mathbf{j}}(\vec{x}), \hat{T}_{el} + \hat{V}_{el-el} \right]_- \tag{D.4}$$

, so I can focus on the term which does. I therefore want to focus on the commutator

$$\left[\hat{\mathbf{j}}(\vec{x}), \hat{V}_{ext}(t) \right]_- . \tag{D.5}$$

Since the operator associated with the current density is given by the expression

$$\hat{\mathbf{j}}(\vec{x}) = \frac{\hbar}{2mi} \left[\hat{\psi}^\dagger(\vec{x}) \nabla \hat{\psi}(\vec{x}) - (\nabla \hat{\psi}^\dagger(\vec{x})) \hat{\psi}(\vec{x}) \right] \tag{D.6}$$

and the time-dependent external potential is given by

$$\hat{V}_{ext}(t) = \int d^3x V^{ext}(\vec{x}, t) \hat{n}(\vec{x}), \tag{D.7}$$

then equation D.5 becomes

$$\frac{\hbar}{2mi} \int d^3x' V^{ext}(\vec{x}', t) \left[\hat{\psi}^\dagger(\vec{x}) \nabla \hat{\psi}(\vec{x}) - (\nabla \hat{\psi}^\dagger(\vec{x})) \hat{\psi}(\vec{x}), \hat{n}(\vec{x}') \right]_- . \tag{D.8}$$

using the commutator to anticommutator identity

$$\left[\hat{A}\hat{B},\hat{C}\right]_{-} = -\hat{A}\left[\hat{B},\hat{C}\right]_{+} + \left[\hat{A},\hat{C}\right]_{+}\hat{B}. \tag{D.9}$$

and the property of the gradient of a delta function

$$\nabla[\hat{\psi}(\vec{x}),\hat{\psi}^{\dagger}(\vec{x}')]_{+} = -\nabla'\delta(\vec{x}-\vec{x}'), \tag{D.10}$$

I can integrate by parts to obtain the simplified expression for equation D.8

$$\frac{\partial}{\partial t}\hat{\mathbf{j}}(\vec{x}) = -\frac{1}{m}\nabla\left(V^{ext}(\vec{x},t)\hat{n}(\vec{x})\right) + \hat{\mathbf{Q}}(\vec{x}). \tag{D.11}$$

Now I will take this result and put it into the continuity equation from equation D.2 by taking the average value at time t to obtain the result

$$\frac{\partial}{\partial t}\vec{j}(\vec{x},t) = -\frac{1}{m}\nabla\left(V^{ext}(\vec{x},t)n(\vec{x},t)\right) + \vec{Q}(\vec{x},t). \tag{D.12}$$

I obtain a similar result for the second time-dependent external potential $V^{ext,2}(\vec{x},t)$

$$\frac{\partial}{\partial t}\vec{j}^{(2)}(\vec{x},t) = -\frac{1}{m}\nabla\left(V^{ext,2}(\vec{x},t)n(\vec{x},t)\right) + \vec{Q}^{(2)}(\vec{x},t). \tag{D.13}$$

Now subtracting equation D.12 from D.13, then

$$\frac{\partial}{\partial t}\left(\vec{j}^{(2)}(\vec{x},t) - \vec{j}(\vec{x},t)\right) = -\frac{1}{m}\nabla\left(V^{ext,2}(\vec{x},t) - V^{ext}(\vec{x},t)\right)n(\vec{x},t) + \vec{Q}^{(2)}(\vec{x},t) - \vec{Q}(\vec{x},t). \tag{D.14}$$

Now if I take the divergence of both sides in equation D.14 and use the assumption that

$$\vec{\nabla}\cdot\vec{j}^{(2)}(\vec{x},t) = \vec{\nabla}\cdot\vec{j}^{(2)}(\vec{x},t) = -\frac{\partial n(\vec{x},t)}{\partial t}, \tag{D.15}$$

then I obtain the result

$$\vec{\nabla}\cdot\left(\vec{Q}^{(2)}(\vec{x},t)-\vec{Q}(\vec{x},t)\right)=\frac{1}{m}\vec{\nabla}\cdot\left\{\nabla\left(V^{ext,2}(\vec{x},t)-V^{ext}(\vec{x},t)\right)n(\vec{x},t)\right\}. \tag{D.16}$$

I can define

$$f(\vec{x},t)\equiv\vec{\nabla}\cdot\left(\vec{Q}^{(2)}(\vec{x},t)-\vec{Q}(\vec{x},t)\right) \tag{D.17}$$

which can be expanded about t_0 to obtain the Taylor expansion

$$f(\vec{x},t)=\sum_{k=0}^{\infty}\frac{\partial^k}{(\partial t)^k}\,f(\vec{x},t)|_{t=t_0}\,(t-t_0)^k. \tag{D.18}$$

I will introduce the shorthand notation

$$f_k(\vec{x},t_0)\equiv\frac{\partial^k}{(\partial t)^k}\,f(\vec{x},t)|_{t=t_0}\,, \tag{D.19}$$

so I can rewrite equation D.19 as

$$f(\vec{x},t)=\sum_{k=0}^{\infty}f_k(\vec{x},t_0)(t-t_0)^k. \tag{D.20}$$

I can also expand the right-hand side of equation D.16

$$\frac{1}{m}\vec{\nabla}\cdot\sum_{l,m=0}^{\infty}\left\{\nabla\left(V_l^{ext,2}(\vec{x},t_0)-V_l^{ext}(\vec{x},t_0)\right)n_m(\vec{x},t_0)\right\}(t-t_0)^{l+m}. \tag{D.21}$$

Now letting $l+m=k$ in the dummy summation in equation D.21, then we can rewrite this expression as

$$\frac{1}{m}\vec{\nabla}\cdot\sum_{l,k=0}^{\infty}\left\{\nabla\left(V_l^{ext,2}(\vec{x},t_0)-V_l^{ext}(\vec{x},t_0)\right)n_{k-l}(\vec{x},t_0)\right\}(t-t_0)^{k}. \tag{D.22}$$

Since a Taylor series is equivalent if and only if each of its coefficients in the expansions are the same, then we obtain the relation

$$\frac{1}{m}\vec{\nabla}\cdot\sum_{l=0}^{\infty}\left\{\nabla\left(V_l^{ext,2}(\vec{x},t_0)-V_l^{ext}(\vec{x},t_0)\right)n_{k-l}(\vec{x},t_0)\right\}(t-t_0)^k = f_k(\vec{x},t_0)(t-t_0)^k. \tag{D.23}$$

I can isolate the $l=k$ term on the left-hand side of equation D.23

$$\begin{aligned}
&\frac{1}{m}\vec{\nabla}\cdot\sum_{l=0}^{\infty}\left\{\nabla\left(V_l^{ext,2}(\vec{x},t_0)-V_l^{ext}(\vec{x},t_0)\right)n_{k-l}(\vec{x},t_0)\right\}(t-t_0)^k \\
&= \frac{1}{m}\vec{\nabla}\cdot\left\{\nabla\left(V_k^{ext,2}(\vec{x},t_0)-V_k^{ext}(\vec{x},t_0)\right)n_0(\vec{x},t_0)\right\}(t-t_0)^k \\
&+ \frac{1}{m}\vec{\nabla}\cdot\sum_{l=0}^{k-1}\left\{\nabla\left(V_l^{ext,2}(\vec{x},t_0)-V_l^{ext}(\vec{x},t_0)\right)n_{k-l}(\vec{x},t_0)\right\}(t-t_0)^k.
\end{aligned} \tag{D.24}$$

I then obtain the relation

$$\begin{aligned}
&\frac{1}{m}\vec{\nabla}\cdot\left\{\nabla\left(V_k^{ext,2}(\vec{x},t_0)-V_k^{ext}(\vec{x},t_0)\right)n_0(\vec{x},t_0)\right\} \\
&= f_k(\vec{x},t_0) - \frac{1}{m}\vec{\nabla}\cdot\sum_{l=0}^{k-1}\left\{\nabla\left(V_l^{ext,2}(\vec{x},t_0)-V_l^{ext}(\vec{x},t_0)\right)n_{k-l}(\vec{x},t_0)\right\}.
\end{aligned} \tag{D.25}$$

To prove my claim, I must show that equation D.25 is a contradiction for all integers k. This is done by contradiction. First, the base case $k=0$ is obvious. This is a contradiction unless $V^{ext,2}(\vec{x},t_0)-V^{ext}(\vec{x},t_0) = constant$ in which the statement is true which is equivalent to stating that the ground state from each external potential was the same as stated in the theorem.

Now if we assume that the time-dependent potentials differ by more than just a time-dependent constant $V^{ext,2}(\vec{x},t_0)-V^{ext}(\vec{x},t_0) \neq c(t)$, then there exists some value of k in which equation D.25 will yield a contradiction due to the uniqueness of

a Taylor series. Hence, my original statement of the claim that two different time-dependent potentials can give the same time-dependent density, therefore proving my claim.

Appendix E

Double Fourier Transform of Density Response Function

The purpose of this appendix is to derive the matrix equation for $\chi_{\vec{G}\vec{G}'}(\vec{q},\omega)$ shown in equation 2.78 which is

$$\chi_{\vec{G}\vec{G}'}(\vec{q},\omega) = \sum_{\vec{G}_1} (\chi_0)_{\vec{G}\vec{G}_1}(\vec{q},\omega)[1 - [v(\vec{q}) + f^{xc}(\vec{q},\omega)]\,\chi_0(\vec{q},\omega)]^{-1}_{\vec{G}_1\vec{G}'}. \tag{E.1}$$

Starting with the integral form

$$\chi_{nn}(\vec{x},\vec{x}';t-t') = \chi_0(\vec{x},\vec{x}';t-t') + \int_{-\infty}^{\infty} dt_1 \int_{-\infty}^{\infty} dt_2 \int d^3x_1 \int d^3x_2$$

$$\times\, \chi_0(\vec{x},\vec{x}_1;t-t_1)\left[\frac{e^2}{|\vec{x}_1-\vec{x}_2|}\delta(t_1-t_2) + f_{xc}(\vec{x}_1,\vec{x}_2;t_2-t')\right]\chi(\vec{x}_2,\vec{x}';t_2-t'), \tag{E.2}$$

we can do the Fourier transform over time

$$\int_{-\infty}^{\infty} d(t-t')e^{\imath\omega(t-t')}\chi_{nn}(\vec{x},\vec{x}';t-t') = \int_{-\infty}^{\infty} d(t-t')e^{\imath\omega(t-t')}\chi_0(\vec{x},\vec{x}';t-t')$$

$$+\int_{-\infty}^{\infty} d(t-t')e^{\imath\omega(t-t')}\int_{-\infty}^{\infty} dt_1\int_{-\infty}^{\infty} dt_2\int d^3x_1\int d^3x_2\chi_0(\vec{x},\vec{x}_1;t-t_1)$$

$$\times\left[\frac{e^2}{|\vec{x}_1-\vec{x}_2|}\delta(t_1-t_2)+f_{xc}(\vec{x}_1,\vec{x}_2;t_2-t')\right]\chi(\vec{x}_2,\vec{x}';t_2-t'), \tag{E.3}$$

where we obtain the density-density response function for a given frequency ω

$$\chi_{nn}(\vec{x},\vec{x}';\omega) = \chi_0(\vec{x},\vec{x}';\omega)$$

$$+\int d^3x_1\int d^3x_2\chi_0(\vec{x},\vec{x}_1;\omega)\left[\frac{e^2}{|\vec{x}_1-\vec{x}_2|}+f^{xc}(\vec{x}_1,\vec{x}_2;\omega)\right]\chi(\vec{x}_2,\vec{x}';\omega). \tag{E.4}$$

Now we want to take the double Fourier transform over space, so for $\chi_0(\vec{x},\vec{x}';\omega)$, we have

$$\chi_0(\vec{k},\vec{k}';\omega) = \int d^3x\int d^3x' e^{-i\vec{k}\cdot\vec{x}}\chi_0(\vec{x},\vec{x}';\omega)e^{i\vec{k}'\cdot\vec{x}'}. \tag{E.5}$$

Since we have a periodic system, we have $\chi_0(\vec{x},\vec{x}';\omega) = \chi_0(\vec{x}+\vec{R},\vec{x}'+\vec{R};\omega)$, then we have the relation

$$\chi_0(\vec{k},\vec{k}';\omega) = e^{i(\vec{k}'-\vec{k})\cdot\vec{R}}\chi_0(\vec{k},\vec{k}';\omega). \tag{E.6}$$

so the condition is satisfied if

$$e^{-i(\vec{k}-\vec{k}')\cdot\vec{R}} = 1 \tag{E.7}$$

which is the case when $\vec{k}'-\vec{k} = \vec{H}$, or $\vec{k}' = \vec{k}+\vec{H}$ for a reciprocal lattice vector $\vec{H}$. For any arbitrary wave vector $\vec{k}$, we can relate it to a wave vector in the first Brillouin zone via a reciprocal lattice vector $\vec{G}$, so $\vec{k} = \vec{q}+\vec{G}$. Therefore

$$\chi_0(\vec{k},\vec{k}';\omega) = \chi_0(\vec{q}+\vec{G},\vec{q}+\vec{G}+\vec{H};\omega). \tag{E.8}$$

We can let $\vec{G}' = \vec{G} + \vec{H}$, then

$$\chi_0(\vec{q}+\vec{G},\vec{q}+\vec{G}';\omega) = \int d^3x \int d^3x' e^{-i(\vec{q}+\vec{G})\cdot\vec{x}} \chi_0(\vec{x},\vec{x}';\omega) e^{i(\vec{q}+\vec{G}')\cdot\vec{x}'}, \tag{E.9}$$

where we can conveniently define this as a matrix

$$(\chi_0)_{\vec{G}\vec{G}'}(\vec{q},\omega) \equiv \chi_0(\vec{q}+\vec{G},\vec{q}+\vec{G}';\omega). \tag{E.10}$$

This transformation is invertible, so

$$\chi_0(\vec{x},\vec{x}';\omega) = \frac{1}{V_{BvK}} \sum_{\vec{q}}^{1BZ} \sum_{\vec{G}\vec{G}'} e^{-i(\vec{q}+\vec{G})\cdot\vec{x}} (\chi_0)_{\vec{G}\vec{G}'}(\vec{q},\omega) e^{i(\vec{q}+\vec{G}')\cdot\vec{x}'}, \tag{E.11}$$

and the same holds for the interacting density response χ_{nn}

$$\chi(\vec{x},\vec{x}';\omega) = \frac{1}{V_{BvK}} \sum_{\vec{q}}^{1BZ} \sum_{\vec{G}\vec{G}'} e^{-i(\vec{q}+\vec{G})\cdot\vec{x}} \chi_{\vec{G}\vec{G}'}(\vec{q},\omega) e^{i(\vec{q}+\vec{G}')\cdot\vec{x}'}, \tag{E.12}$$

where I have omitted the nn subscript from this point further. Now I will plug in equation E.10 and E.12 into equation E, and I obtain

$$\frac{1}{V_{BvK}} \sum_{\vec{q}}^{1BZ} \sum_{\vec{G}\vec{G}'} e^{-i(\vec{q}+\vec{G})\cdot\vec{x}} \chi_{\vec{G}\vec{G}'}(\vec{q},\omega) e^{i(\vec{q}+\vec{G}')\cdot\vec{x}'} = \frac{1}{V_{BvK}} \sum_{\vec{q}}^{1BZ} \sum_{\vec{G}\vec{G}'} e^{-i(\vec{q}+\vec{G})\cdot\vec{x}} (\chi_0)_{\vec{G}\vec{G}'}(\vec{q},\omega) e^{i(\vec{q}+\vec{G}')\cdot\vec{x}'}$$

$$+\frac{1}{V_{BvK}} \sum_{\vec{q}}^{1BZ} \sum_{\vec{G}\vec{G}_1} e^{-i(\vec{q}+\vec{G})\cdot\vec{x}} (\chi_0)_{\vec{G}\vec{G}_1}(\vec{q},\omega) \int d^3x_1 \int d^3x_2 e^{i(\vec{q}+\vec{G}_1)\cdot\vec{x}_1} \left(\frac{e^2}{|\vec{x}_1-\vec{x}_2|} + f^{xc}(\vec{x}_1,\vec{x}_2;\omega) \right)$$

$$\times \frac{1}{V_{BvK}} \sum_{\vec{q}'}^{1BZ} \sum_{\vec{G}_2\vec{G}'} e^{-i(\vec{q}'+\vec{G}_2)\cdot\vec{x}_2} \chi_{\vec{G}_2\vec{G}'}(\vec{q}',\omega) e^{i(\vec{q}'+\vec{G}')\cdot\vec{x}'}., \tag{E.13}$$

Looking at the terms in the integral,

$$\frac{1}{V_{BvK}} \sum_{\vec{q}'}^{1BZ} \int d^3x_1 \int d^3x_2 e^{i(\vec{q}+\vec{G}_1)\cdot\vec{x}_1} \left(\frac{e^2}{|\vec{x}_1-\vec{x}_2|} + f_{xc}(\vec{x}_1,\vec{x}_2;\omega) \right) e^{-i(\vec{q}'+\vec{G}_2)\cdot\vec{x}_2} \tag{E.14}$$

Since $e^2/|\vec{x}_1 - \vec{x}_2| + f_{xc}(\vec{x}_1, \vec{x}_2; \omega) = e^2/|\vec{x}_1 + \vec{R} - \vec{x}_2 - \vec{R}| + f^{xc}(\vec{x}_1 + \vec{R}, \vec{x}_2 + \vec{R}; \omega)$, then equation E.14 becomes

$$\frac{4\pi e^2}{\left|\vec{q} + \vec{G}_1\right|^2}\delta_{\vec{G}_1\vec{G}_2} + f^{xc}_{\vec{G}_1\vec{G}_2}(\vec{q}, \omega). \tag{E.15}$$

Therefore, equation E.16 becomes

$$\frac{1}{V_{BvK}}\sum_{\vec{q}}^{1BZ}\sum_{\vec{G}\vec{G}'} e^{-i(\vec{q}+\vec{G})\cdot\vec{x}}\chi_{\vec{G}\vec{G}'}(\vec{q}, \omega)e^{i(\vec{q}+\vec{G}')\cdot\vec{x}'} = \frac{1}{V_{BvK}}\sum_{\vec{q}}^{1BZ}\sum_{\vec{G}\vec{G}'} e^{-i(\vec{q}+\vec{G})\cdot\vec{x}}(\chi_0)_{\vec{G}\vec{G}'}(\vec{q}, \omega)e^{i(\vec{q}+\vec{G}')\cdot\vec{x}'}$$

$$+\frac{1}{V_{BvK}}\sum_{\vec{q}}^{1BZ}\sum_{\vec{G}\vec{G}_1\vec{G}_2\vec{G}'} e^{-i(\vec{q}+\vec{G})\cdot\vec{x}}(\chi_0)_{\vec{G}\vec{G}_1}(\vec{q}, \omega)\left[\frac{4\pi e^2}{\left|\vec{q} + \vec{G}_1\right|^2}\delta_{\vec{G}_1\vec{G}_2} + f^{xc}_{\vec{G}_1\vec{G}_2}(\vec{q}, \omega)\right]$$

$$\times \chi_{\vec{G}_2\vec{G}'}(\vec{q}', \omega)e^{i(\vec{q}'+\vec{G}')\cdot\vec{x}'}. \tag{E.16}$$

Therefore we obtain the *matrix* equation for the matrix *element* $\chi_{\vec{G}\vec{G}'}(\vec{q}, \omega)$

$$\chi_{\vec{G}\vec{G}'}(\vec{q}, \omega) = (\chi_0)_{\vec{G}\vec{G}'}(\vec{q}, \omega)$$

$$+\sum_{\vec{G}_1\vec{G}_2}(\chi_0)_{\vec{G}\vec{G}_1}(\vec{q}, \omega)\left[\frac{4\pi e^2}{\left|\vec{q} + \vec{G}_1\right|^2}\delta_{\vec{G}_1\vec{G}_2} + f^{xc}_{\vec{G}_1\vec{G}_2}(\vec{q}, \omega)\right]\chi_{\vec{G}_2\vec{G}'}(\vec{q}', \omega). \tag{E.17}$$

where we can define the effective interaction

$$V^{eff}_{\vec{G}_1\vec{G}_2}(\vec{q}, \omega) \equiv \frac{4\pi e^2}{\left|\vec{q} + \vec{G}_1\right|^2}\delta_{\vec{G}_1\vec{G}_2} + f^{xc}_{\vec{G}_1\vec{G}_2}(\vec{q}, \omega), \tag{E.18}$$

and upon summing the geometric series, we obtain

$$\chi_{\vec{G}\vec{G}'}(\vec{q}, \omega) = \sum_{\vec{G}_1}(\chi_0)_{\vec{G}\vec{G}_1}(\vec{q}, \omega)\left[1 - V^{eff}(\vec{q}, \omega)\chi_0(\vec{q}, \omega)\right]^{-1}_{\vec{G}_1\vec{G}_2}. \tag{E.19}$$

Now I will explicitly compute $(\chi_0)_{\vec{G}\vec{G}'}(\vec{q},\omega)$. In position space

$$\chi_0(\vec{x},\vec{x}';\omega)=\sum_{\sigma}\psi^*_{\vec{k}j\sigma}(\vec{x})\psi_{\vec{k}'j'\sigma}(\vec{x})\psi^*_{\vec{k}'j'\sigma}(\vec{x}')\psi_{\vec{k}j\sigma}(\vec{x}')\frac{f_{\vec{k}'j'\sigma}-f_{k\vec{j}\sigma}}{\varepsilon_{\vec{k}'j'\sigma}-\varepsilon_{\vec{k}j\sigma}+\hbar(\omega+i\eta^+)}. \tag{E.20}$$

Now

$$(\chi_0)_{\vec{G}\vec{G}'}(\vec{q},\omega)=\int d^3x\int d^3x' e^{-i(\vec{q}+\vec{G})\cdot\vec{x}}\chi_0(\vec{x},\vec{x}';\omega)e^{i(\vec{q}+\vec{G}')\cdot\vec{x}'}, \tag{E.21}$$

so

$$(\chi_0)_{\vec{G}\vec{G}'}(\vec{q},\omega)=\int d^3x e^{-i(\vec{q}+\vec{G})\cdot\vec{x}}\psi^*_{\vec{k}j\sigma}(\vec{x})\psi_{\vec{k}'j'\sigma}(\vec{x})\int d^3x'\psi^*_{\vec{k}'j'\sigma}(\vec{x}')\psi_{\vec{k}j\sigma}(\vec{x}')e^{i(\vec{q}+\vec{G}')\cdot\vec{x}'}$$

$$\times\frac{f_{\vec{k}'j'\sigma}-f_{k\vec{j}\sigma}}{\varepsilon_{\vec{k}'j'\sigma}-\varepsilon_{\vec{k}j\sigma}+\hbar(\omega+i\eta^+)}. \tag{E.22}$$

since $\chi_0(\vec{x},\vec{x}';\omega)=\chi_0(\vec{x}+\vec{R},\vec{x}'+\vec{R};\omega)$, then the two integrands gives

$$e^{-i(\vec{q}+\vec{G})\cdot(\vec{x}+\vec{R})}\psi^*_{\vec{k}j\sigma}(\vec{x}+\vec{R})\psi_{\vec{k}'j'\sigma}(\vec{x}+\vec{R})\psi^*_{\vec{k}'j'\sigma}(\vec{x}'+\vec{R})\psi_{\vec{k}j\sigma}(\vec{x}')e^{i(\vec{q}+\vec{G}')\cdot(\vec{x}'+\vec{R})}$$

$$=e^{-i(\vec{q}+\vec{G})\cdot\vec{x}}\psi^*_{\vec{k}j\sigma}(\vec{x})\psi_{\vec{k}'j'\sigma}(\vec{x})\psi^*_{\vec{k}'j'\sigma}(\vec{x}')\psi_{\vec{k}j\sigma}(\vec{x}')e^{i(\vec{q}+\vec{G}')\cdot\vec{x}'}, \tag{E.23}$$

so, by using Bloch's theorem, we have

$$e^{-i\vec{q}\cdot\vec{R}}e^{-i(\vec{k}-\vec{k}')\cdot\vec{R}}=1 \tag{E.24}$$

which is equivalent to $\vec{k}'=\vec{k}+\vec{q}$. Therefore, we can write equation E.25 as

$$(\chi_0)_{\vec{G}\vec{G}'}(\vec{q},\omega)=\int d^3x e^{-i(\vec{q}+\vec{G})\cdot\vec{x}}\psi^*_{\vec{k}j\sigma}(\vec{x})\psi_{\vec{k}+\vec{q}j'\sigma}(\vec{x})\int d^3x'\psi^*_{\vec{k}+\vec{q}j'\sigma}(\vec{x}')\psi_{\vec{k}j\sigma}(\vec{x}')e^{i(\vec{q}+\vec{G}')\cdot\vec{x}'}$$

$$\times\frac{f_{\vec{k}+\vec{q}j'\sigma}-f_{k\vec{j}\sigma}}{\varepsilon_{\vec{k}+\vec{q}j'\sigma}-\varepsilon_{\vec{k}j\sigma}+\hbar(\omega+i\eta^+)}. \tag{E.25}$$

We can use first quantization notation to symbolize

$$\langle\vec{k}j\sigma|\,e^{-i(\vec{q}+\vec{G})\cdot\hat{\mathbf{x}}}\,|\vec{k}+\vec{q}j'\sigma\rangle\equiv\int d^3x e^{-i(\vec{q}+\vec{G})\cdot\vec{x}}\psi^*_{\vec{k}j\sigma}(\vec{x})\psi_{\vec{k}+\vec{q}j'\sigma}(\vec{x}). \tag{E.26}$$

Then we can write the Kohn sham density response matrix element as

$$(\chi_0)_{\vec{G}\vec{G}'}(\vec{q},\omega) = \langle \vec{k}j\sigma |\, e^{-i(\vec{q}+\vec{G})\cdot\hat{\mathbf{x}}}\, |\vec{k}+\vec{q}j'\sigma\rangle \, \langle \vec{k}+\vec{q}j'\sigma |\, e^{i(\vec{q}+\vec{G})\cdot\hat{\mathbf{x}}}\, |\vec{k}j\sigma\rangle$$

$$\times \frac{f_{\vec{k}+\vec{q}j'\sigma} - f_{k\vec{j}\sigma}}{\varepsilon_{\vec{k}+\vec{q}j'\sigma} - \varepsilon_{\vec{k}j\sigma} + \hbar(\omega + i\eta^+)}. \tag{E.27}$$

Appendix F

$\chi^t_{\vec{G}\vec{G}'}(\vec{q},\omega)$ in the Wannier basis

In this appendix, I will derive the target response $\chi^t_{\vec{G}\vec{G}'}(\vec{q},\omega)$ in the Wannier basis. Using the matrix for the target response

$$(\chi^t)^{\sigma\sigma'}_{\vec{G}\vec{G}'}(\vec{q},\omega) = \delta_{\sigma\sigma'}(\chi^t_0)^{\sigma}_{\vec{G}\vec{G}'}(\vec{q},\omega) + \sum_{\sigma_1}\sum_{\vec{G}_1\vec{G}_2}(\chi^t_0)^{\sigma}_{\vec{G}\vec{G}_1}(\vec{q},\omega)\tilde{V}^{\sigma\sigma_1}_{\vec{G}_1\vec{G}_2}(\vec{q},\omega)(\chi^t)^{\sigma_1\sigma'}_{\vec{G}_2\vec{G}'}(\vec{q},\omega) \tag{F.1}$$

where

$$\tilde{V}^{\sigma\sigma_1}_{\vec{G}_1\vec{G}_2}(\vec{q},\omega) = \tilde{v}^{\sigma\sigma_1}_{\vec{G}_1\vec{G}_2}(\vec{q},\omega) + (f^{xc})^{\sigma\sigma_1}_{\vec{G}_1\vec{G}_2}(\vec{q},\omega) \tag{F.2}$$

and

$$\tilde{v}^{\sigma\sigma_1}_{\vec{G}_1\vec{G}_2}(\vec{q},\omega) = \frac{4\pi e^2}{\left|\vec{q}+\vec{G}_1\right|^2}(\varepsilon^r)^{-1}_{\vec{G}_1\vec{G}_2}(\vec{q},\omega). \tag{F.3}$$

The first step in the derivation is to expand $(\chi^t_0)^{\sigma}_{\vec{G}\vec{G}'}(\vec{q},\omega)$ in the Wannier basis. In the Bloch basis,

$$(\chi^t_0)^{\sigma}_{\vec{G}\vec{G}'}(\vec{q},\omega)$$
$$= \sum_{\vec{k}}^{1BZ}\sum_{jj'}\langle\vec{k}j\sigma|\, e^{-i(\vec{q}+\vec{G})\cdot\hat{\mathbf{x}}}\,|\vec{k}+\vec{q}j'\sigma\rangle\,\frac{f_{\vec{k}+\vec{q}j'\sigma}-f_{\vec{k}j\sigma}}{\varepsilon_{\vec{k}+\vec{q}j'\sigma}-\varepsilon_{\vec{k}j\sigma}+\hbar(\omega+i\eta^+)}\,\langle\vec{k}+\vec{q}j'\sigma|\, e^{i(\vec{q}+\vec{G}')\cdot\hat{\mathbf{x}}}\,|\vec{k}j\sigma\rangle\,. \tag{F.4}$$

Using the transformation from the Bloch to the Wannier basis

$$|\vec{k}j\sigma\rangle = \frac{1}{\sqrt{N_{BvK}}} \sum_{\vec{R}} e^{i\vec{k}\cdot\vec{R}} \sum_{n} c_{jn\sigma}(\vec{k}) \, |W_{n\sigma}(\vec{R})\rangle \,, \tag{F.5}$$

we can express the charge fluctuation matrix elements $\langle \vec{k}j\sigma| \, e^{-i(\vec{q}+\vec{G})\cdot\hat{\mathbf{x}}} \, |\vec{k}+\vec{q}j'\sigma\rangle$ as

$$\langle \vec{k}j\sigma| \, e^{-i(\vec{q}+\vec{G})\cdot\hat{\mathbf{x}}} \, |\vec{k}+\vec{q}j'\sigma\rangle = \sum_{\vec{R}_1\vec{R}_2} e^{-i\vec{k}\cdot\vec{R}_1} e^{i(\vec{k}+\vec{q})\cdot\vec{R}_2} \sum_{n_1 n_2} c^*_{n_1 j\sigma}(\vec{k}) c_{j' n_2\sigma}(\vec{k}+\vec{q})$$

$$\times \langle W_{n_1\sigma}(\vec{R}_1)| \, e^{-i(\vec{q}+\vec{G})\cdot\hat{\mathbf{x}}} \, |W_{n_2\sigma}(\vec{R}_2)\rangle \,, \tag{F.6}$$

where I will introduce the notation

$$A^{\sigma}_{n_1\vec{R}_1,n_2\vec{R}_2}(\vec{q}+\vec{G}) \equiv \langle W_{n_1\sigma}(\vec{R}_1)| \, e^{-i(\vec{q}+\vec{G})\cdot\hat{\mathbf{x}}} \, |W_{n_2\sigma}(\vec{R}_2)\rangle \,. \tag{F.7}$$

Then we can rewrite equation F.4 as

$$(\chi^t_0)^{\sigma}_{\vec{G}\vec{G}'}(\vec{q},\omega) = \frac{1}{(N_{BvK})^2} \sum_{\vec{R}_1\vec{R}_2\vec{R}_3\vec{R}_4} \sum_{n_1 n_2 n_3 n_4} e^{i\vec{q}\cdot(\vec{R}_2-\vec{R}_4)} A^{\sigma}_{n_1\vec{R}_1,n_2\vec{R}_2}(\vec{q}+\vec{G}) \sum_{\vec{k}}^{1BZ} e^{-i\vec{k}\cdot\left[(\vec{R}_1-\vec{R}_2)-(\vec{R}_3-\vec{R}_4)\right]}$$

$$\sum_{jj'} c^*_{n_1 j\sigma}(\vec{k}) c_{j' n_2\sigma}(\vec{k}+\vec{q}) \frac{f_{\vec{k}+\vec{q}j'\sigma} - f_{\vec{k}j\sigma}}{\varepsilon_{\vec{k}+\vec{q}j'\sigma} - \varepsilon_{\vec{k}j\sigma} + \hbar(\omega + i\eta^+)} c^*_{n_4 j'\sigma}(\vec{k}+\vec{q}) c_{j n_3\sigma}(\vec{k}) A^{\sigma *}_{n_3\vec{R}_3,n_4\vec{R}_4}(\vec{q}+\vec{G}'). \tag{F.8}$$

Here, I will define the quantity

$$(\chi^t_0)^{\sigma n_3\vec{R}_3,\sigma n_4\vec{R}_4}_{\sigma n_1\vec{R}_1,\sigma n_2\vec{R}_2}(\vec{q},\omega) \equiv \frac{1}{(N_{BvK})^2} e^{i\vec{q}\cdot(\vec{R}_2-\vec{R}_4)} \sum_{\vec{k}}^{1BZ} e^{-i\vec{k}\cdot\left[(\vec{R}_1-\vec{R}_2)-(\vec{R}_3-\vec{R}_4)\right]}$$

$$\times \sum_{jj'} c^*_{n_1 j\sigma}(\vec{k}) c_{j' n_2\sigma}(\vec{k}+\vec{q}) \frac{f_{\vec{k}+\vec{q}j'\sigma} - f_{\vec{k}j\sigma}}{\varepsilon_{\vec{k}+\vec{q}j'\sigma} - \varepsilon_{\vec{k}j\sigma} + \hbar(\omega + i\eta^+)} c^*_{n_4 j'\sigma}(\vec{k}+\vec{q}) c_{j n_3\sigma}(\vec{k}). \tag{F.9}$$

Then equation F.4 becomes

$$(\chi^t_0)^{\sigma}_{\vec{G}\vec{G}'}(\vec{q},\omega) = \sum_{\vec{R}_1\vec{R}_2\vec{R}_3\vec{R}_4} \sum_{n_1 n_2 n_3 n_4} A^{\sigma}_{n_1\vec{R}_1,n_2\vec{R}_2}(\vec{q}+\vec{G}) (\chi^t_0)^{\sigma n_3\vec{R}_3,\sigma n_4\vec{R}_4}_{\sigma n_1\vec{R}_1,\sigma n_2\vec{R}_2}(\vec{q},\omega) A^{\sigma *}_{n_3\vec{R}_3,n_4\vec{R}_4}(\vec{q}+\vec{G}'). \tag{F.10}$$

We can introduce shorthand notation in terms of a super index $1 \equiv (n_1 \vec{R}_1)$

$$(\chi_0^t)^{\sigma}_{\vec{G}\vec{G}'}(\vec{q},\omega) = \sum_{\bar{1}\bar{2}\bar{3}\bar{4}} A^{\sigma}_{\bar{1}\bar{2}}(\vec{q}+\vec{G})(\chi_0^t)^{\sigma}_{\bar{1}\bar{2}\bar{3}\bar{4}}(\vec{q},\omega)A^{\sigma *}_{\bar{3}\bar{4}}(\vec{q}+\vec{G}'), \tag{F.11}$$

where we can use the convention that terms with a bar over them are summed over, so

$$(\chi_0^t)^{\sigma}_{\vec{G}\vec{G}'}(\vec{q},\omega) = A^{\sigma}_{\bar{1}\bar{2}}(\vec{q}+\vec{G})(\chi_0^t)^{\sigma}_{\bar{1}\bar{2}\bar{3}\bar{4}}(\vec{q},\omega)A^{\sigma *}_{\bar{3}\bar{4}}(\vec{q}+\vec{G}'). \tag{F.12}$$

Now looking at the first order term in the geometric series in equation F.1

$$\sum_{\vec{G}_1\vec{G}_2} (\chi_0^t)^{\sigma}_{\vec{G}\vec{G}_1}(\vec{q},\omega)\tilde{V}^{\sigma\sigma'}_{\vec{G}_1\vec{G}_2}(\vec{q},\omega)(\chi_0^t)^{\sigma'}_{\vec{G}_2\vec{G}'}(\vec{q},\omega) \tag{F.13}$$

$$= \sum_{\vec{G}_1\vec{G}_2} A^{\sigma}_{\bar{1}\bar{2}}(\vec{q}+\vec{G})(\chi_0^t)^{\sigma}_{\bar{1}\bar{2}\bar{5}\bar{6}}(\vec{q},\omega)A^{\sigma *}_{\bar{5}\bar{6}}(\vec{q}+\vec{G}_1)\tilde{V}^{\sigma\sigma'}_{\vec{G}_1\vec{G}_2}(\vec{q},\omega)A^{\sigma'}_{\bar{7}\bar{8}}(\vec{q}+\vec{G}_2)(\chi_0^t)^{\sigma'}_{\bar{7}\bar{8}\bar{3}\bar{4}}(\vec{q},\omega)A^{\sigma' *}_{\bar{3}\bar{4}}(\vec{q}+\vec{G}')$$

$$\times A^{\sigma' *}_{\bar{3}\bar{4}}(\vec{q}+\vec{G}') \tag{F.14}$$

$$= A^{\sigma}_{\bar{1}\bar{2}}(\vec{q}+\vec{G})(\chi_0^t)^{\sigma}_{\bar{1}\bar{2}\bar{5}\bar{6}}(\vec{q},\omega) \sum_{\vec{G}_1\vec{G}_2} \left(A^{\sigma *}_{\bar{5}\bar{6}}(\vec{q}+\vec{G}_1)\tilde{V}^{\sigma\sigma'}_{\vec{G}_1\vec{G}_2}(\vec{q},\omega)A^{\sigma'}_{\bar{7}\bar{8}}(\vec{q}+\vec{G}_2)\right)$$

$$\times (\chi_0^t)^{\sigma'}_{\bar{7}\bar{8}\bar{3}\bar{4}}(\vec{q},\omega)A^{\sigma' *}_{\bar{3}\bar{4}}(\vec{q}+\vec{G}'), \tag{F.15}$$

where we can define the *effective* interaction in the Wannier basis

$$\tilde{V}^{\sigma\sigma'}_{1234}(\vec{q},\omega) \equiv \sum_{\vec{G}_1\vec{G}_2} A^{\sigma *}_{12}(\vec{q}+\vec{G}_1)\tilde{V}^{\sigma\sigma'}_{\vec{G}_1\vec{G}_2}(\vec{q},\omega)A^{\sigma'}_{34}(\vec{q}+\vec{G}_2), \tag{F.16}$$

which allows us to write the first order term as

$$A^{\sigma}_{\bar{1}\bar{2}}(\vec{q}+\vec{G})(\chi_0^t)^{\sigma}_{\bar{1}\bar{2}\bar{5}\bar{6}}(\vec{q},\omega)\tilde{V}^{\sigma\sigma'}_{\bar{5}\bar{6}\bar{7}\bar{8}}(\vec{q},\omega)(\chi_0^t)^{\sigma'}_{\bar{7}\bar{8}\bar{3}\bar{4}}(\vec{q},\omega)A^{\sigma' *}_{\bar{3}\bar{4}}(\vec{q}+\vec{G}'). \tag{F.17}$$

Now looking at the second order term in the geometric series in equation F.1

$$\sum_{\sigma_1}\sum_{\vec{G}_1\vec{G}_2\vec{G}_3\vec{G}_4}(\chi_0^t)^{\sigma}_{\vec{G}\vec{G}_1}(\vec{q},\omega)\tilde{V}^{\sigma\sigma_1}_{\vec{G}_1\vec{G}_2}(\vec{q},\omega)(\chi_0^t)^{\sigma_1}_{\vec{G}_2\vec{G}_3}(\vec{q},\omega)\tilde{V}^{\sigma_1\sigma'}_{\vec{G}_3\vec{G}_4}(\vec{q},\omega)(\chi_0^t)^{\sigma'}_{\vec{G}_4\vec{G}'}(\vec{q},\omega) \quad \text{(F.18)}$$

$$=\sum_{\sigma_1}\sum_{\vec{G}_1\vec{G}_2\vec{G}_3\vec{G}_4}A^{\sigma}_{\bar{1}\bar{2}}(\vec{q}+\vec{G})(\chi_0^t)^{\sigma}_{\bar{1}\bar{2}\bar{5}\bar{6}}(\vec{q},\omega)A^{\sigma*}_{\bar{5}\bar{6}}(\vec{q}+\vec{G}_1)\tilde{V}^{\sigma\sigma_1}_{\vec{G}_1\vec{G}_2}(\vec{q},\omega)A^{\sigma_1}_{\bar{7}\bar{8}}(\vec{q}+\vec{G}_2)$$

$$\times(\chi_0^t)^{\sigma}_{\bar{7}\bar{8}\bar{9}\bar{1}\bar{0}}(\vec{q},\omega)A^{\sigma_1*}_{\bar{9}\bar{1}\bar{0}}(\vec{q}+\vec{G}_3)\tilde{V}^{\sigma_1\sigma'}_{\vec{G}_3\vec{G}_4}(\vec{q},\omega)A_{\bar{1}\bar{1}\bar{1}\bar{2}\sigma'}(\vec{q}+\vec{G}_4)(\chi_0^t)^{\sigma}_{\bar{1}\bar{1}\bar{1}\bar{2}\bar{3}\bar{4}}(\vec{q},\omega)A^{\sigma'*}_{\bar{3}\bar{4}}(\vec{q}+\vec{G}')$$

$$=\sum_{\sigma_1}A^{\sigma}_{\bar{1}\bar{2}}(\vec{q}+\vec{G})(\chi_0^t)^{\sigma}_{\bar{1}\bar{2}\bar{5}\bar{6}}(\vec{q},\omega)\sum_{\vec{G}_1\vec{G}_2}\left(A^{\sigma*}_{\bar{5}\bar{6}}(\vec{q}+\vec{G}_1)\tilde{V}^{\sigma\sigma_1}_{\vec{G}_1\vec{G}_2}(\vec{q},\omega)A^{\sigma_1}_{\bar{7}\bar{8}}(\vec{q}+\vec{G}_2)\right)$$

$$\times(\chi_0^t)^{\sigma}_{\bar{7}\bar{8}\bar{9}\bar{1}\bar{0}}(\vec{q},\omega)\sum_{\vec{G}_1\vec{G}_2}\left(A^{\sigma_1*}_{\bar{9}\bar{1}\bar{0}}(\vec{q}+\vec{G}_3)\tilde{V}^{\sigma_1\sigma'}_{\vec{G}_3\vec{G}_4}(\vec{q},\omega)A_{\bar{1}\bar{1}\bar{1}\bar{2}\sigma'}(\vec{q}+\vec{G}_4)\right)$$

$$\times(\chi_0^t)^{\sigma}_{\bar{1}\bar{1}\bar{1}\bar{2}\bar{3}\bar{4}}(\vec{q},\omega)A^{\sigma'*}_{\bar{3}\bar{4}}(\vec{q}+\vec{G}') \quad \text{(F.19)}$$

$$=\sum_{\sigma_1}A^{\sigma}_{\bar{1}\bar{2}}(\vec{q}+\vec{G})(\chi_0^t)^{\sigma}_{\bar{1}\bar{2}\bar{5}\bar{6}}(\vec{q},\omega)\tilde{V}^{\sigma\sigma_1}_{\bar{5}\bar{6}\bar{7}\bar{8}}(\vec{q},\omega)(\chi_0^t)^{\sigma}_{\bar{7}\bar{8}\bar{9}\bar{1}\bar{0}}(\vec{q},\omega)\tilde{V}^{\sigma_1\sigma'}_{\bar{9}\bar{1}\bar{0}\bar{1}\bar{1}\bar{2}}(\vec{q},\omega)$$

$$\times(\chi_0^t)^{\sigma}_{\bar{1}\bar{1}\bar{1}\bar{2}\bar{3}\bar{4}}(\vec{q},\omega)A^{\sigma'*}_{\bar{3}\bar{4}}(\vec{q}+\vec{G}'). \quad \text{(F.20)}$$

This manipulation is continued to infinite order, so the target response is now cast in the form

$$(\chi^t)^{\sigma\sigma'}_{\vec{G}\vec{G}'}(\vec{q},\omega)=A^{\sigma}_{\bar{1}\bar{2}}(\vec{q}+\vec{G})\Big[\delta_{\sigma\sigma'}(\chi_0^t)^{\sigma}_{\bar{1}\bar{2}\bar{3}\bar{4}}(\vec{q},\omega)+(\chi_0^t)^{\sigma}_{\bar{1}\bar{2}\bar{5}\bar{6}}(\vec{q},\omega)\tilde{V}^{\sigma\sigma'}_{\bar{5}\bar{6}\bar{7}\bar{8}}(\vec{q},\omega)(\chi_0^t)^{\sigma'}_{\bar{7}\bar{8}\bar{3}\bar{4}}(\vec{q},\omega)$$

$$+\sum_{\sigma_1}(\chi_0^t)^{\sigma}_{\bar{1}\bar{2}\bar{5}\bar{6}}(\vec{q},\omega)\tilde{V}^{\sigma\sigma_1}_{\bar{5}\bar{6}\bar{7}\bar{8}}(\vec{q},\omega)(\chi_0^t)^{\sigma}_{\bar{7}\bar{8}\bar{9}\bar{1}\bar{0}}(\vec{q},\omega)\tilde{V}^{\sigma_1\sigma'}_{\bar{9}\bar{1}\bar{0}\bar{1}\bar{1}\bar{2}}(\vec{q},\omega)(\chi_0^t)^{\sigma}_{\bar{1}\bar{1}\bar{2}\bar{3}\bar{4}}(\vec{q},\omega)+\ldots\Big]$$

$$\times A^{\sigma'*}_{\bar{3}\bar{4}}(\vec{q}+\vec{G}'). \quad \text{(F.21)}$$

If we sum over the geometric series, we obtain the result

$$(\chi^t)^{\sigma\sigma'}_{\vec{G}\vec{G}'}(\vec{q},\omega) = A^{\sigma}_{\bar{1}\bar{2}}(\vec{q}+\vec{G})(\chi^t_0)^{\sigma}_{\bar{1}\bar{2}\bar{5}\bar{6}}(\vec{q},\omega)\left[\{(1-\tilde{V}(\vec{q},\omega)\chi^t_0(\vec{q},\omega)\}^{-1}\right]^{\sigma\sigma'}_{\bar{5}\bar{6}\bar{3}\bar{4}} A^{\sigma'*}_{\bar{3}\bar{4}}(\vec{q}+\vec{G}'). \tag{F.22}$$

Here, we can define the interacting Kohn-Sham electron-hole 'propagator' $(\chi^t)^{\sigma\sigma'}_{1234}(\vec{q},\omega)$

$$(\chi^t)^{\sigma\sigma'}_{1234}(\vec{q},\omega) \equiv (\chi^t_0)^{\sigma}_{12\bar{3}\bar{4}}(\vec{q},\omega)\left[\{(1-\tilde{V}(\vec{q},\omega)\chi^t_0(\vec{q},\omega)\}^{-1}\right]^{\sigma\sigma'}_{\bar{3}\bar{4}34}, \tag{F.23}$$

which allows us to obtain the final result for the target density response

$$(\chi^t)^{\sigma\sigma'}_{\vec{G}\vec{G}'}(\vec{q},\omega) = A^{\sigma}_{\bar{1}\bar{2}}(\vec{q}+\vec{G})(\chi^t)^{\sigma\sigma'}_{\bar{1}\bar{2}\bar{3}\bar{4}}(\vec{q},\omega)A^{\sigma'*}_{\bar{3}\bar{4}}(\vec{q}+\vec{G}'). \tag{F.24}$$

Vita

Casey J. Eichstaedt was born to James R. and Terri S. Eichstaedt in Daytona Beach, FL as an only child. He attended Sweetwater Elementary School, Creekside Middle School and Spruce Creek High School in Port Orange, FL. After completetion of secondary school, he attended Daytona State College to obtain an Associate of Arts degree. After completion of the Associate of Arts degree, he attended the University of Central Florida with a dual major in mathematics and physics. He studied under Professor Michael Leuenberger studying the theory of photonic crystals and their application to fast switching in opto-electronic devices. After completion of his Bachelor of Science degrees at UCF, he was married to his wife Olivia Kaiser and decided to pursue a doctorate of philosophy degree at the University of Tennessee, Knoxville. At the University of Tennesse Knoxville, he was under the supervision of Professor Adolfo G. Eguiluz. While at UTK, he has had two legitimate daughters, Layla J. and Bradley Q. Eichstaedt.